Molecular Transport, Reactivity and Structure in Organic Crystals

A thesis submitted to Cardiff University
by
Javier Martí Rujas

In candidature of Doctor of Philosophy

October 2005

School of Chemistry
Cardiff University

ProQuest LLC
789 East Eisenhower Parkway
P.O. Box 1346
Ann Arbor, MI 48106-1346

Abstract

The work presented in this thesis is based on studies concerning structural properties of molecular solids, and is composed of three different parts.

First, structural aspects of solid state dimerization reactions have been studied using ^{1}H NMR and powder X-ray diffraction. The experiments are based on the photoreactions of cinnamic acids in the solid state. These materials show photochemical behaviour upon irradiation by UV light. The β-phase (photoreactive polymorph) of 4-chloro-*trans*-cinnamic acid was chosen as the primary material for study, and a combination of powder X-ray diffraction and solution state ^{1}H NMR spectroscopy techniques have been used to follow the evolution of the solid-state photoreaction, and to determine the structural evolution of the photoproduct. In addition, the structure of a photoreactive material (the β-phase of 4-fluoro-*trans*-cinnammic acid) that cannot be prepared as a single crystal suitable for single crystal X-ray diffraction has been determined directly from powder X-ray diffraction data. This research exploits modern developments in the application of powder X-ray diffraction techniques in order to obtain new levels of understanding of a classical solid state reaction.

The second part of this thesis is based on the investigation of transport of molecules through linear tunnels in solid organic inclusion compounds (host-guest systems). This project is focused on incommensurate inclusion compounds in which guest molecules are contained within a system of one-dimensional tunnels (with a diameter of about 5.5 Å) in a crystalline urea host structure. It was shown previously that net transport of guest molecules in one direction along the crystal can be achieved by insertion of new guest molecules at one end of the crystal (by dipping it into the liquid phase of another potential guest), with the original guest molecules expelled from the other end of the crystal. Such phenomena have considerable potential as the basis of selective micro-scale separation techniques, based on discrimination of molecular size, shape and chirality. In the present work, the spatial distribution of the guest molecules in the crystal has been studied together with the changes in the spatial distribution of the guest molecules as a function of time during the transport process. This process has been investigated directly by using confocal Raman

microspectrometry as an *in situ* probe of the molecular transport process. The data obtained from such experiments have provided access to information on the kinetics of the transport process and the time-dependence of the spatial distribution of guest molecules within the channel system. A model has been developed to understand the kinetics of the transport process, leading to detailed mechanistic insights.

The last part of the thesis is focused on the design of hydrogen-bonded organic complexes. Underlying all structural aspects of organic molecular crystals is the fundamental question of what factors control the molecular packing arrangement, and an important related issue is how to apply an understanding of these factors in the design of crystals with desired structural properties. The work has focused on the study of components with hydrogen bonding capability (urea/diols and *p*-phenylenediamine/diols), with a view to the formation of hydrogen-bonded complexes with predictable structural features.

Optical microscopy, single crystal X-ray diffraction, powder X-ray diffraction and confocal Raman microspectroscopy have been applied in this work.

Dedicated to Kyoko,
my parents and my grandmother

Acknowledgements

I would like to thank all the people who have made this PhD possible. First, I would like to thank my supervisor, Prof. Kenneth Harris, for welcoming me as a member of his research group. His help, enthusiasm and guidance during my PhD were always helpful and motivating.

I am very grateful to Dr François Guillaume and Dr Arnaud Desmedt who helped me with my Raman experiments at Université de Bordeaux 1 during the seven moths I spent in Bordeaux. Their supervision and encouragement were always a source of motivation. Merci beaucoup! My special thanks also to Dr Eugènia Estop, from Universitat Autònoma de Barcelona for giving me the advice and support to start my PhD.

I would like to thank Dr Eugene Cheung, who has helped me from the first day I arrived in the Harris group. I would also like to thank Dr Colan Hughes who enthusiastically guided me during the last months of my PhD. Thanks Colan!

I would like to thank Dr Liling-Ooi and Dr Benson Kariuki for their help during my experiments involving single crystal X-ray diffraction and Rob Jenkins for his help with the ^{1}H NMR.

Part of my research work would not have been possible without the technical support of Jean-Luc Bruneel and David Talaga from Bordeaux who always made the long Raman experiments possible.

Many thanks to the whole Structural Chemistry group, both past and present, Dr David Albesa-Jové, Dr Sang-Ok Lee, Dr Scott Habershon, Dr Mao-Hsun Chao, Dr Siwaporn Meejoo, Dr Zhigang Pan, Dr Mingcan Xu, Dr Veronique Siegler, Dr Colan Hughes, Dr Eugene Cheung, Andrew Hanson, Fang Guo, Gianina Tutoveanu, Nathan Dedman, Hasmerya Maarof, Anabel Morte, Lianne Davis and Zornitza Glavcheva.

I would like to thank all the people who helped me to enjoy during my stay in Bordeaux, both scientifically and gastronomically, Dr Arnaud Desmedt, Dr Raphael Moreau, Dr Cédric Crespo, Stephanie Palmier, Nicolas and Aurelie. I hope I did not forget anyone.

I am really grateful to all the people who welcomed and helped me in Cardiff, Elisenda Reixac, Paula Janeiro and Meritxell Casadesus.

I would like to thank The University of Birmingham, Cardiff University and the European Union for my Marie Curie Fellowship training at Université de Bordeaux i for funding my research.

I would like to thank my parents and my family for their help and support during these three years of PhD.

Finally, I would like to thank Kyoko Nakagawa for encouragement and help through these three years. Arigatou gozaimasu Kyoko!

Table of Contents

Chapter 1 Introduction

1.1 Overview of this Thesis

Solid-state chemistry is nowadays a well established subject. It appeared in the late 1960's as a new branch of modern chemistry, related to the development of high technology materials. Solid-state chemistry, as a branch of science that studies the physical properties of solids, presents an important overlap between Physics (in particular Solid-State Physics), Earth Sciences, Materials Science and Engineering. Solid-state science focuses on understanding and modifying the properties of solids from the viewpoint of the fundamental physics of the atomic and electronic structure (Figure 1.1). Inorganic solid-state chemistry focuses in the synthesis of novel materials as well as investigating new uses of existing materials in electronics, communications and computers. This has intensified the demand for a systematic approach to the problem of relating properties to structure and necessitates a multidisciplinary approach. Organic solid-state chemistry, on the other hand, is very important for studying crystalline stability of some solid materials (e.g., in the pharmaceutical industry). A deep knowledge of the molecular arrangement in molecular solid crystals is a key point to understand polymorphism[1] and phase transformations, often very important processes

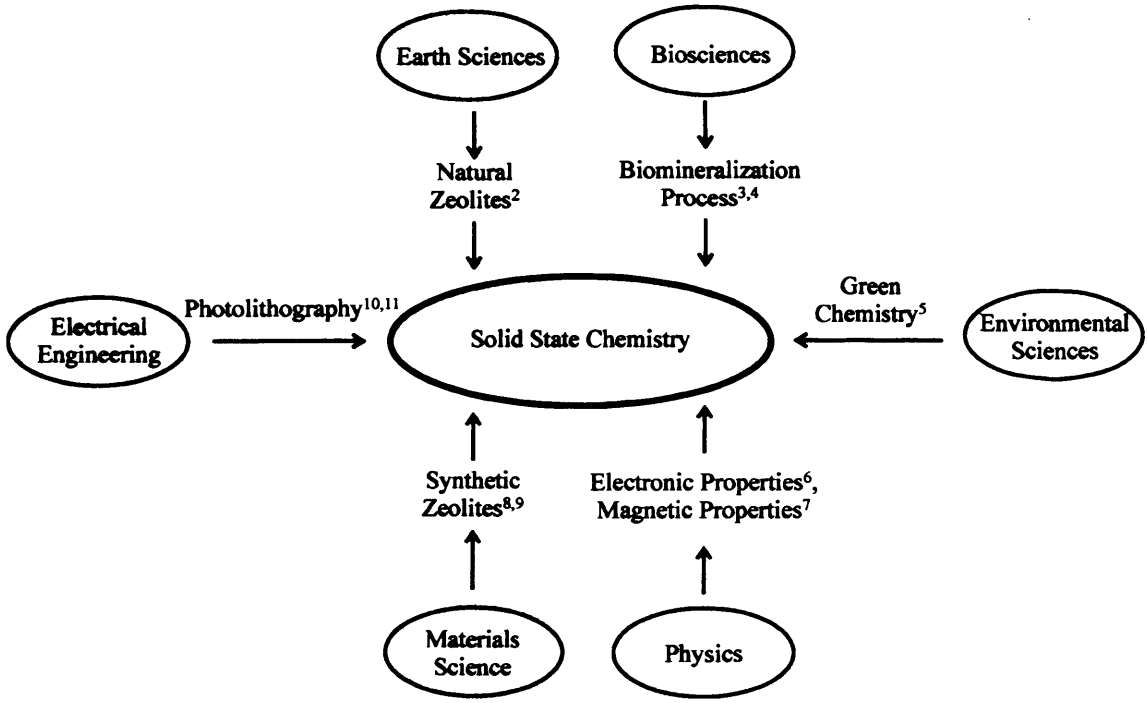

Figure 1.1. Diagram showing the multidisciplinarity of different fields usually required in solid state chemistry.

in drugs. Crucially, a particular drug substance administered in different polymorphic forms may have very different properties. It is also very interesting to be able to control the solubility and the conditions for handling and administration.

The work presented in this thesis is the result of three years of research in solid-state chemistry. It can be divided, according to the research field, into three parts: *i*) molecular transport of linear molecules (alkanes) in a host-guest system, *ii*) synthesis and structure determination of novel molecular crystals applying the concept of *Crystal Engineering*, and *iii*) study of solid-state reactivity with interests in structure determination, lattice parameters evolution and phase separation. In this Chapter, an introduction related to the three fields of solid state chemistry which have been covered in this thesis is given.

1.2 Photoinduced Reactions Under Crystalline Environments

The majority of crystalline solids are stable both thermally and photochemically. Reactivity in the solid state is more complicated than the reactions in the liquid state. Firstly, molecules have to move in order to react properly, which is fairly simple in the liquid or gas state but this is not the case in the solid state, where there is less motional freedom. Nevertheless, organic photoreactions in the solid state have been studied widely and date back to the middle of the last century. The main experimental difficulty was probably the identification of photoreactive crystals. The technique of X-ray crystallography has proved to be a very important tool for establishing structure-reactivity correlations. Early observations of photoreactive crystals suggested that the intrinsic photochemical properties of organic molecules are relegated to second place and their solid-state photochemistry is controlled by the periodic environment of the crystal structure. Such reactions are referred to as *topochemical reactions*. The topochemical postulate[12] states that reactions in crystals may occur within a minimum of atomic and molecular motion. Another way to classify a reaction as topotactic is to consider the variation in the lattice parameters during the reaction. Thus, if a reaction occurs so as to retain one or more of the crystallographic axes of the reactant and a particular orientation of the product lattice is retained relative to that of the reactant, then this reaction can be called topotactic.

A proper distance and orientation between potentially reactive partners is an important requirement if reactivity is to be expected. In the case of bimolecular reactions, the reactivity of the system depends on the packing arrangement, whilst unimolecular rearrangements occur with less atomic and molecular movement. Most bimolecular reactions occur between molecules that are identical. The restrictions on the number of components allowed in crystalline phases and the precise distances and orientations necessary for bimolecular reactivity are the major limitations imposed by the crystalline media for photoreaction to occur. Photochemical reactions in unimolecular crystals do not depend on the nature and location of their closest neighbours. Therefore, molecular rearrangements in unimolecular crystals may be investigated with less concern for packing arrangements. In unimolecular reactions, structural changes of the reactant toward that of the product can be limited by repulsive non-bonded interactions which determine whether or not the reaction is energetically feasible.

A very interesting type of photoreaction are so called single-crystal-to-single-crystal reactions, in which a single crystal of starting material transforms into a single crystal of product, without any loss of crystallinity throughout the reaction. Structural similarity between reactant and product are usually very high in this kind of reaction. Due to the formation of the product within the lattice of the reactant, most solid state reactions destroy the crystal lattice of the reactant phase. Although single-crystal-to-single-crystal reactions are not very common, the cases where they do occur can be studied by X-ray diffraction which provides information on the structural changes. Single-crystal-to-single-crystal reactions are usually homogeneous, i.e., the reaction occurs throughout all the crystal, not only at localized spots.

Although some reactions occur by phase separation mechanisms to the stable form of the product, others may lead to metastable phases that are not available by crystallization from solution, sublimation or the melt. It is likely that many solid-state reactions will involve metastable phases and phase separation and recrystallization will be highly dependent on whether the reaction is carried out in large crystals or small crystals (e.g., in a microcrystalline powder). Since phase separation and recrystallization require a great deal of molecular motion,

solubility limits in the solid-state reaction may exceed those observed by equilibrium co-crystallization of the components. It is likely that efficient solid-to-solid reactions will require very high solubility of the product in the crystalline phase of the starting material. Although it is expected that disordered phases should result in loss of control, it is possible that product-like phases may have a similar influence on the reaction as does the phase of the reactant.

1.3 Solid Inclusion Compounds

Solid inclusion compounds can be classified as solid materials forming a framework architecture that contains empty spaces within which other molecules can be included or incorporated. The framework-building molecule is usually called the "host", whereas the molecules included in the cavities are referred to as the "guest". Solid inclusion compounds are common in nature. As inorganic materials, solid inclusion compounds are formed in aluminosilicate minerals such as zeolites. In these materials, the host framework is constructed from SiO_4 and AlO_4 tetrahedra, interconnected by corner-sharing to form "sponge-like" materials but with a very regular structure and pore sizes which are typically of molecular dimensions. Each AlO_4 unit is associated with a negative charge, which is balanced by a positive ion, usually H^+. These protons form acidic (Brønsted) sites, which behave in a similar way as the protons in acidic solution. Many important properties of zeolites depend on the Si/Al ratio, as this clearly dictates the number of extra-framework cations. Due to the geometrical arrangement of the tetrahedral building blocks, zeolites can form inclusion spaces with different topologies, ranging from tunnels to cages, which can be parallel (one-dimensional) or interconnected, forming two- and three-dimensional networks. Since the 1960's, zeolites have been applied in an increasing number of ways, most involving catalytic processes. One important advantage of using zeolites is that, due to the great variety and specific structure of the pores and cages, not all products are formed in a catalytic process, enhancing the selectivity of the reaction. For example, zeolites are used in applications involving catalysis of crude oil to produce gasoline, kerosene and other smaller hydrocarbons.

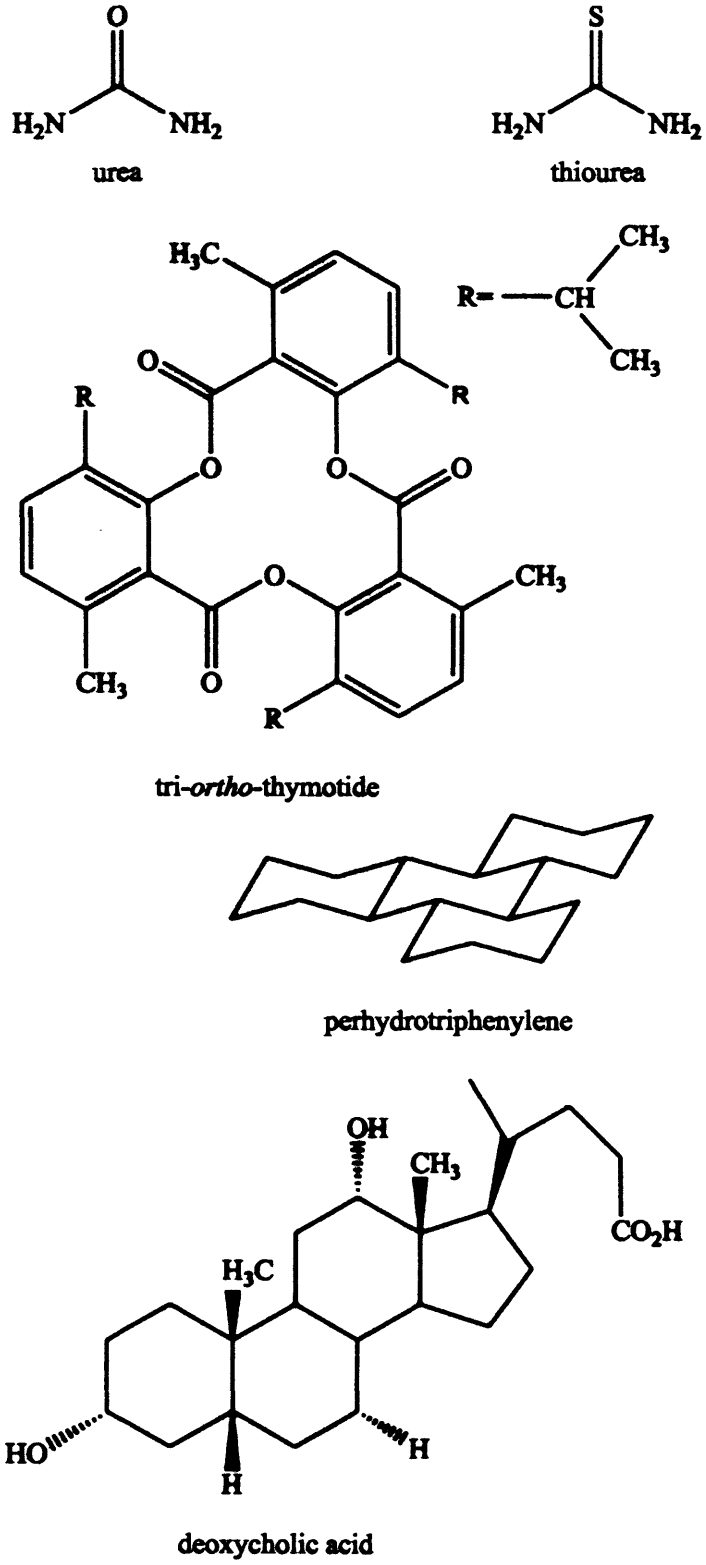

Figure 1.2. Potential organic molecules that can form host structures with determined guest molecules.

Solid inclusion phenomena are not only a subject regarding inorganic materials. Host structures constructed from the crystal packing of organic molecules also can form solid inclusion compounds. Urea, thiourea, tri-*ortho*-thymotide, perhydrotriphenylene and deoxycholic acid are organic molecules that can form porous frameworks (Figure 1.2). Solid

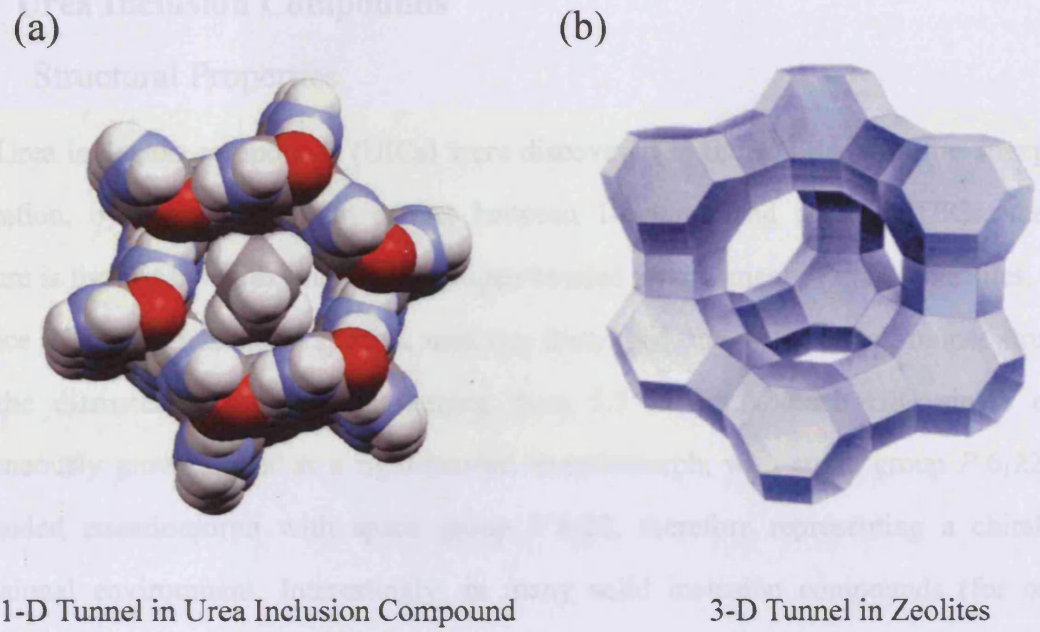

Figure 1.3. Two different porous structures showing (a) one-dimensional tunnels (Urea Inclusion Compound) and (b) three dimensional tunnels (Zeolites).

inclusion compounds can be subdivided into two categories,[13] depending on how the structure behaves after removing the guest molecules. In organic inclusion compounds, the host structure is often unstable if the guest molecules are removed. Removal of guest molecules implies collapsing of the host framework. Collapse of the host structure is often irreversible. This type of framework is called a "soft" host (Figure 1.3a). On the other hand, if the host remains stable after removal of the guest molecules, such as in zeolites, the structure is referred as a "hard" host (Figure 1.3b). The structural properties of the soft hosts often vary substantially depending on the structural and chemical characteristics of the guest molecules and in general the properties of these inclusion compounds cannot be understood adequately in terms of the separate behaviour of the host and guest components. The region of contact between the host and guest components in a solid inclusion compound can be regarded as an interface and many properties of inclusion compounds are dictated by the nature of the interface. In the next section some basic structural features of urea inclusion compounds are presented, since an important part of this work is based on these materials. In addition, urea can also form specific complexes with a variety of organic and inorganic molecules and ions. Chapter 6 is dedicated to the study of molecular complexes formed between urea and diols.

1.4 Urea Inclusion Compounds

1.4.1 Structural Properties

Urea inclusion compounds (UICs) were discovered in the 1940's, with the unexpected preparation, by Bengen,[14] of an adduct between 1-octanol and urea. In UICs, the host structure is formed by an extensively hydrogen-bonded arrangement of urea molecules. In the presence of appropriate guest species, urea can form this, one-dimensional, tunnel structure, with the diameter of the tunnels ranging from 5.5 to 5.8 Å. Each UIC single crystal spontaneously grows either as a right-handed enantiomorph, with space group $P\,6_122$, or a left-handed enantiomorph with space group $P\,6_522$, therefore representing a chiral one-dimensional environment. Interestingly, in many solid inclusion compounds (for organic molecular hosts), the host structure is chiral. Although, in some cases, the building blocks of the host structure are themselves chiral (therefore the construction of a chiral host structure is obligatory), in many cases chirality is introduced by spontaneous assembly of achiral building blocks into a chiral packing arrangement in the host structure, as in UICs. Clearly, chiral host structures can exert an important influence on the structural and chemical properties of chiral guest molecules. A remarkable fact is that the vast majority of different UICs containing different guest molecules have essentially the same urea host structure, which is hexagonal at room temperature with lattice parameters $a = b = 8.227$ Å, $c = 11.017$ Å; $\alpha = \beta = 90$, $\gamma = 120°$.

1.4.2 Guest Molecules in UICs

The factor that determines whether or not a molecule is appropriate as a guest species to form a UIC is the ability to fit into the space in the tunnel. Due to the "effective diameter" of the tunnel, urea can only form UICs with guest molecules based on a sufficiently long alkane chain, with a limited degree of substitution of this chain allowed. Therefore, the length of the guest molecule and the degree of branching are two key features for the formation of urea inclusion compounds. In early studies[15] it was believed that UICs could only be formed with *n*-alkanes and their linear derivatives. Now it is known that other UICs can be formed but with restrictions concerning the degree of branching allowed. Size, position and number of the substituents are crucial factors. Bulky atoms in the middle of an alkane chain will not form a

UIC, whereas the same alkane chain with the same substituents at the chain-ends might be able to form a UIC[16].

In UICs, the guest molecules are densely packed along the tunnels and generally exhibit sufficient positional ordering to allow an average three-dimensional guest lattice to be defined.[17,18] An important property of tunnel inclusion compounds concerns the degree of registry between the host and the guest substructures along the tunnel. In many one-dimensional inclusion compounds, the guest molecules are arranged in a periodic manner (with a periodic distance c_g) along the tunnel and it is then important to consider the relationship between c_g and the repeat distance c_h of the host structure along the tunnel (Figure 1.4). If there are no sufficiently small integers p and q for which the $pc_h \approx qc_g$, the UIC is said to be *incommensurate*, whereas, if such integers can be found to satisfy the relationship, the UIC is said to be *commensurate*. For an incommensurate system, every guest molecule along the tunnel occupies a slightly different position with respect to the unit cell of the host substructure. In fact, the vast majority of UICs are incommensurate and are called *conventional* UICs. These are typified by n-alkane/urea inclusion compounds, where the guest molecules are well ordered along a single tunnel[18] and have some degree of ordering between adjacent tunnels (i.e., there is an overall three-dimensional ordering). The positional correlations between guest molecules in different tunnels are stronger for some UICs than others. Some UICs are, however, commensurate, allowing complete structure determination from single crystal X-ray diffraction (e.g., 1,6-dibromohexane/urea[19] and 1,4-dichlorobutane/urea[20]). Interestingly, for commensurate UICs, the host structure is often distorted to a lower symmetry than for the conventional UICs.

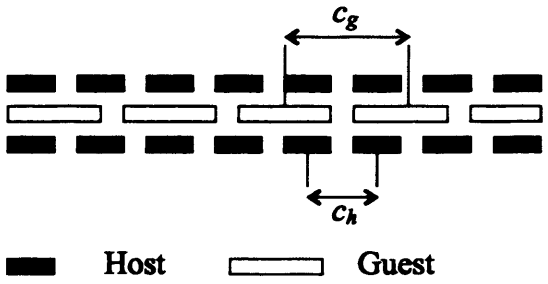

Figure 1.4. Schematic representation of the host (c_h) and guest (c_g) periodicity in one single tunnel of a urea inclusion compound viewed perpendicular to the tunnel axis.

In many cases, a given single crystal contains different domains of the guest substructure; each domain has an identical packing of guest molecules but has a different (although equivalent) orientation relative to the host structure. Although diffraction data allow the average periodicity and symmetry of the basic guest structure to be determined, dynamic disorder of the guest molecules in conventional UICs can limit the ability to obtain detailed information about the guest structure. One consequence of the dynamic disorder of the guest molecules is the appearance of different forms of diffuse scattering in diffraction patterns of urea inclusion compounds. Other experimental and computational approaches can be used to obtain direct information on local structural properties of the guest molecules, the interactions between guest molecules within the tunnel and the orientational distribution of the guest molecules.

Raman spectroscopy has been used[21] to probe conformational properties of α,ω-dihalogenoalkane guest molecules [$X(CH_2)_nX$; $n = 8$ for X = Cl; n = 7-11 for X = Br; $n = 8$ for X = I] in UICs. The C – X stretching vibrations were used to assess the relative amounts of *trans* and *gauche* end groups as a function of the length (n) of the guest molecule, the identity of the terminal substituent X, temperature and pressure. These results suggest that there is no well-defined relationship between the proportion of end groups in the *gauche* conformation and the length of the $Br(CH_2)_nBr$ guest molecules. High resolution solid-state ^{19}F-NMR spectroscopy was employed[22] to study the interaction between adjacent guest molecules in a UIC containing 1,10-difluorodecane guest molecules.

Bromine K-edge extended X-ray absorption fine structure (EXASF) experiments were carried out[23] to investigate a variety of local structural properties of UICs containing α,ω-dibromoalkane guest molecules, including the intramolecular geometry around the bromine atom, based on the Br···C(3) distances for the three intramolecular carbon atoms closest to the bromine atom. The value of the Br···C(3) distance indicates that the bromine end groups exist predominantly in the *trans* conformation, in agreement with results from Raman spectroscopy.

Interactions between guest molecules in UICs containing α,ω-diiodoalkane $I(CH_2)_nI$ guest molecules have been analysed[24] to establish the intensity distribution of diffuse sheets in

X-ray diffraction patterns. These diffuse sheets are often observed in X-ray diffraction patterns of UICs and correspond to one-dimensional ordering of guest molecules along the tunnel axis. Thus, analysis of the intensities of the diffuse sheets provides information on the structural properties of the periodic linear array of guest molecules along an individual tunnel.

1.4.3 Synthesis of UICs.

UICs are usually easy to obtain, although in many cases it is not easy to obtain large, good quality crystals. Preparation of the UICs is usually done by slow cooling, using a thermal bath or incubator, from a methanolic solution from 55°C to 25-20°C. Sometimes it may be necessary to use mixtures of solvents to obtain a homogeneous solution containing both the host and guest species, e.g., tert-amyl-alcohol (which is too bulky to be included in the urea tunnels)[25] and methanol. Once the single crystals are removed from the solution, it is necessary to wash the surface of the single crystal. The solvent used to wash the crystals is 2,2,4-trimethylpentane (TMP) which does not dissolve the urea host structure and is too big to fit into the tunnel structure of the UIC.

The stability of the UICs depends on the type of guest molecules. For *n*-alkanes and their linear derivatives, liquid or solid at room temperature, the UICs generally remain stable at ambient temperature. For *n*-alkanes, the minimum chain length required for inclusion is C_6[26], at room temperature and pressure. Schlenck[27] reported one explanation for the existence of a minimal chain length. His approach states that, when the guest molecules are too short, regions between two adjacent guest molecules represents a big proportion of the tunnel length, hence destabilizing the urea framework due to a lack of host-guest interaction. It has been demonstrated[26] that UICs can be formed by polymers with molecular weights as high as 4×10^6. More information regarding the variety of guest molecules that can form UICs can be found elsewhere.[16,25] If a volatile or very bulky guest species is included, the UIC may be unstable, usually collapsing the porous structure to form a more dense and tetragonal structure, corresponding to pure urea molecules. This is visible by eye, as the single crystal becomes cloudy. Conventional UICs can be easily identified by optical microscopy which reveals the typical hexagonal shape of the UIC needle-like crystals. Using powder X-ray diffraction, UICs can be routinely characterized.

1.4.4 Crystal Growth

On a macroscopic scale, most UICs form long hexagonal needles. However, it has been found that certain molecules (notably ketones) form flat plate crystals instead. During the crystal growth process, the first stage is the protrusion of guest molecules above the surface of the crystal, around which host molecules collect. This in turn provides a large, longitudinal surface area to which other guest molecules can attach, which in turn attracts more host molecules and so on. However, if there is a strong host-guest interaction, the first step is inhibited and lateral growth is preferred. Crystal growth is generally governed by kinetic factors and to alter the crystal morphology requires control of the relative rates of crystal growth in different directions. A general strategy has been reported[28] to control the crystal morphology of tunnel inclusion compounds, and demonstrated for alkane/urea inclusion compounds. It has been shown that it is possible to dictate the shape of the crystal form long-needle to flat-plate if the rate of crystal growth along the tunnel direction is reduced by using a selective inhibitor in the crystallization solution.

1.5 The Design of Desired Molecular Structures

The last part of this thesis focuses on the design of novel organic complexes. Underlying all structural aspects of organic molecular crystals is the fundamental question of what factors control the molecular packing arrangement. An important related issue is how to apply an understanding of these factors in the design of crystals with desired structural properties. Schmidt, during his studies of photodimerization of cinnamic acids and derivatives, introduced the concept of crystal engineering.[29] The objective was to design organic molecules in order to adopt a particular molecular packing, leading to structures with high regioselective and stereoselective reactivity. Therefore, crystal engineering is the understanding of intermolecular interactions in the context of crystal packing and the utilisation of such knowledge in the design of new solids with desired physical and chemical properties.

The term "crystal engineering" means to design a supramolecular structure on the basis of intermolecular interactions, such as hydrogen bonding and Van der Waals interactions. This focus on the identification of determined patterns of intermolecular motifs, which can be

found in crystals such as ribbons, layers, chains and tunnels, can be applied to act as a template for desired chemical and physical purposes (e.g., catalysis, photoreactivity, proton conduction and nonlinear optics). In crystal engineering, it is very important to be able to predict the molecular network structure (i.e., one-, two-, or three- dimensionality) of the desired crystal. The conventional O–H···O and N–H···O hydrogen bonds have been considered the building blocks of the molecular architecture, whereas weaker interactions such as C–H···O, C–H···N, have been proposed to be determining the course of crystallization.

Weakness of interaction does not mean lack of specificity. The roles played by some of the weaker interactions during crystallization could be of specific nature. For hydrocarbons, the interactions are exclusively of the Van der Waals type, which means that crystal structures may be easily predicted assuming a close-packing model, without interference from anisotropic and stronger interactions. In heteroatom containing structures, however, the interactions are much more complex, with different strengths, directionalities and distance

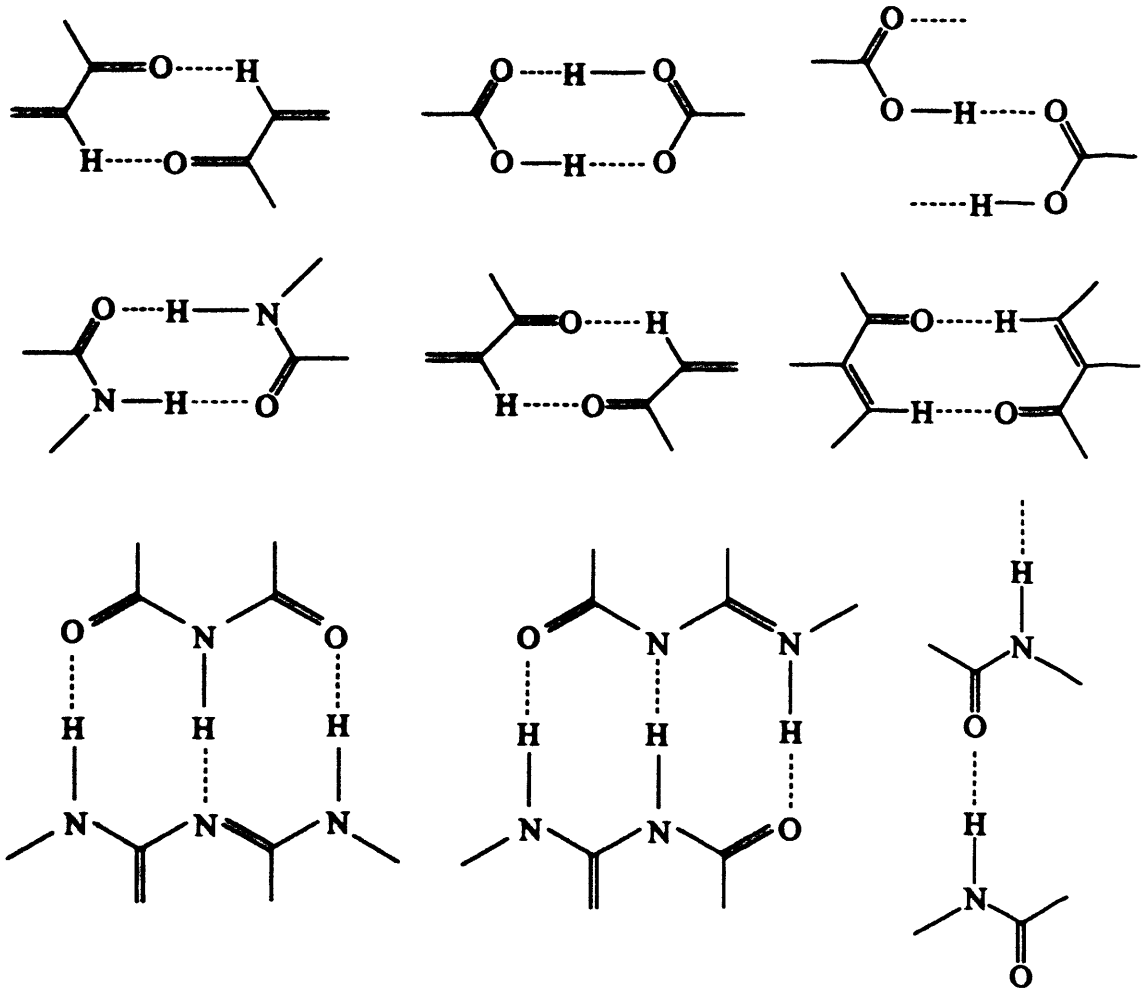

Figure 1.5. Examples of supramolecular synthons.

dependencies. In such situations, direct and simple extrapolations from molecules to crystal structure are difficult in the best cases and impossible in the worst. The situation becomes even more challenging if one is dealing with flexible molecules and if solvent inclusion is a possibility. Supramolecular synthons are structural units which can be generated by synthesis-like operations involving intermolecular interactions. Supramolecular synthons are spatial combinations of molecular interactions as design elements for the solid-state architecture. An example of supramolecular synthons is shown in Figure 1.5.

For recognition between identical molecules, as is the case of most crystal structures, it is the dissimilar parts that come into close contact and not the similar surfaces-bumps fit into hollows just as keys fit into locks. Conversely, identical parts of neighbouring molecules tend to avoid one another. Therefore, space groups containing only rotation axes and mirror planes are found much less frequently compared to those containing inversion centres, screw axes and glide planes. Centro-symmetric close packing is preferred even for molecules that do not possess an inversion centre. Geometrical preferences of the common heteroatom interactions reinforce the close-packing tendencies, with the result that there is a dominance of a small number of space groups which contain translational symmetry elements. Because the typical organic molecule has an irregular shape, low symmetry crystal systems (triclinic, monoclinic, and orthorhombic) are preferred over the high-symmetry ones. Kitaigorodskii's close-packing principle states that molecules undergo a "shape simplification" as they progress towards dimers, higher aggregates and ultimately crystals.[30] Shape is a very effective tool for molecular recognition. Supramolecular arrays in a crystal structure have simpler shapes than the constituent molecular species, and their packing patterns may be easier to predict.

In summary, crystal engineering is the design of crystal structures for specific purposes and applications. Crystal structures are determined by intermolecular interactions and so the study and understanding of interactions, such as the hydrogen bond, are of considerable importance in the developments of this subject. The description of a crystal as a supramolecular entity has had a direct impact on crystal engineering, for if a crystal is a super molecule, crystal engineering is supramolecular synthesis in the solid state. Instead of

building molecules with atoms and covalent bonds, one builds crystals (supermolecules) with molecules and non-covalent interactions according to a predetermined protocol.

The utilization of weak hydrogen bonds in crystal engineering strategies follows directly from their known important role in crystal packing and also in the formation of bicomponent species such as host-guest systems. Host-guest complexes are of importance in supramolecular chemistry because the very fact that two different molecular components have crystallized together is significant. When the interactions responsible for the co-crystallization are strong hydrogen bonds, one is more confident that such interactions can, in turn, be used for the design of new crystal structures.

References for Chapter 1

[1] J. Bernstein, R. J. Davey and J.–O. Henck, *Angew. Chem. Int. Ed.*, **1999**, *38*, 3440.

[2] D. L. Bish and D. W. Ming, *Natural Zeolites: Occurrence, Properties, Applications.* Review in Mineralogy and Geochemistry, Washington DC, **2001**, 45.

[3] R. E. Sours, A. Z. Zellelow and J. A. Swift, *J. Phys. Chem. B*, **2005**, *109*, 9989.

[4] M. C. Frincu, C. E. Fogarty and J. A. Swift, *Langimur*, **2004**, *20*, 6524.

[5] A. Albini and M. Fagnoni, *Green Chem.*, **2004**, *6*, 1.

[6] G. D. Stucky and J.E. MacDougall, *Science*, **1990**, *247*, 669.

[7] J. S. Miller, A. J. Epstein and W. M. Reiff, *Chem. Rev.*, **1988**, *88*, 201.

[8] C. T. Kresge, M. E. Leonowicz, W. J. Roth, J. C. Vartuli and J. S. Beck, *Nature*, **1992**, *359*, 710.

[9] J. M. Thomas, *Nature*, **1994**, *368*, 289.

[10] E. K. Lin, C. L. Soles, D. L. Goldfarb, B. C. Trinque, S. D. Burns, R. L. Jomes, J. L. Lenhart, M. Angelopoulos, C. G. Willson, S. K. Satija, and W. Wu, *Science*, **2002**, *297*, 372.

[11] E. Reichmains and O. Nalamasu, *Science*, **2002** *297*, 349.

[12] W. H. Kohlshutter, *Anorg. Allg. Chem.*, **1918**, *105*, 121.

[13] K. D. M. Harris in *Monographs on Chemistry for the 21st Century: Interfacial Chemistry*, (Editor: M. W. Roberts), I.U.P.A.C/Blackwell Science, **1997**, 21 –55.

[14] M. F. Bengen, (I. G. Farbenindustrie). *Ger. Pat. Appl.*, OZ 123438, **1940**.

[15] M. F. Bengen, *Angew. Chem.*, **1951**, *63*, 207

[16] L. C. Fetterly, *"Non-stoichiometric compounds"*, L. Mandelcorm, Ed., Academic press,.**1964,** 491.

[17] K. D. M. Harris, *J. Mol. Struct.*, **1996**, *374*, 241.

[18] K.D.M. Harris and J.M. Thomas, *J. Chem. Soc. Faraday Trans.*, **1990**, *86*, 2985.

[19] S. P. Smart, *PhD. Thesis*, The University of St. Andrews, Scotland, **1993.**

[20] J. Otto, *Acta Crystallogr Sect .B*, **1972,** *28*, 543.

[21] S. P Smart, A. ElBaghdadi, F. Guillaume and K. D. M. Harris, *J. Chem. Soc., Faraday Trans.*, **1994**, *90*, 1313.

[22] A. Nordon, E. Hughes, R. K. Harris, L. Yeo and K. D. M. Harris, *Chem. Phys. Lett.*, **1998**, *289*, 25.

[23] I. J. Shannon, K. D. M. Harris, A. Mahdyarfar, P. Johnston and R. W. Joyner, *J. Chem. Soc., Faraday Trans.*, **1993**, *89*, 3099.

[24] M.–H. Chao, K. D. M. Harris, B. M. Kariuki, C. L. Bauer and B. M. Foxman, *J. Phys. Chem. B*, **2002**, *106*, 4032

[25] M. D. Hollingsworth and K. D. M. Harris, *"Comprehensive Supramolecular Chemistry"*, D. D. MacNicol, F. Toda and R. Bishop, Eds., Pergamon Press, Elmsford, NY, USA, **1996**, *6*, 77.

[26] F. E. Bailey, H. G. France, *J. Polym. Science*, **1961**, *41*, 397.

[27] W. Schlenck, *Liebigs Ann. Chem.*, **1949**, *565*, 204.

[28] S.–O. Lee and K. D. M. Harris, *Chem. Phys. Lett.*, **1999**, *307*, 327.

[29] G. M. Schmidt, *Pure. Appl. Chem.*, **1971**, *27*, 647.

[30] C. N. R. Rao and K. J. Rao, *Phase Transitions in Solids: An Approach to the Study of the Chemistry and Physics of Solids*, McGraw-Hill, New York, **1973**.

Chapter 2 Experimental Techniques

2.1 Introduction

The purpose of this chapter is to describe the background theory of the techniques that have been used in this research and focuses particularly on the methods employed. The different experimental techniques used in this thesis range from single crystal X-ray diffraction to powder X-ray diffraction and Raman microspectrometry.

2.2 Diffraction by Crystals

Since the development of X-ray diffraction, there has been a great advance in the knowledge of crystalline structures of solid materials. A deep understanding of the structure of both molecular and non-molecular materials is one of the fundamental aims of chemistry and is essential for a deeper understanding of the physical and chemical properties of the materials. The term structure can be considered as the relative positions of ions, atoms or molecules which form the substance under study and therefore a description in a geometrical basis in terms of bond lengths and angles, torsional angles, non-bonded distances and other geometrical arrangements of interest. This knowledge makes possible the pictorial representation of chemical structures. Knowledge of the structure may be sought simply as a means of identifying a newly synthesised compound and gaining an understanding of growth mechanisms, or detailed geometry may be important for further investigations of reactivity, bonding, structure-energy relationships, etc.

A crystalline material is characterized by its high degree of internal order where the atoms, ions or molecules of which a crystal is composed are arranged in a regular manner that is repeated periodically in the three-dimensional space. The simplest portion of the structure which is repeated and shows its full symmetry is called the unit cell. The unit cell is defined by three axes a, b, and c and three angles α, β, and γ (Figure 2.1). Diffraction methods provide a way to obtain a detailed image of the contents of a crystal at the unit cell level.

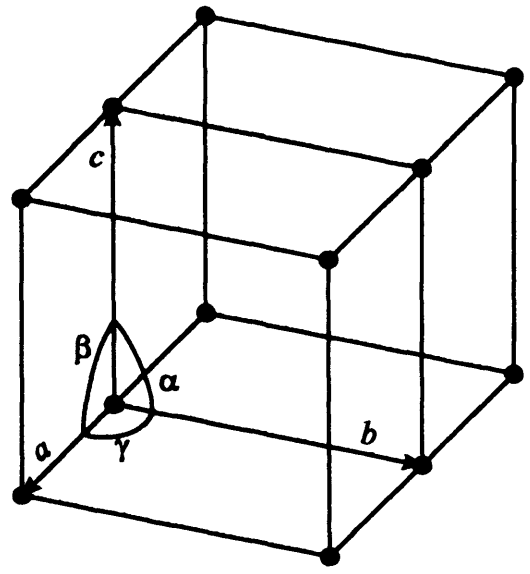

Figure 2.1. Geometrical representation of two unit cells.

The first experiments involving the scattering, or diffraction, of X-rays by crystals were initiated by von Laue in 1912. It is well known that similar effects with visible light can be achieved with a ruled diffraction grating, provided that the rulings are spaced at about the same order of magnitude as the wavelength of the light. The analogy in the crystalline state is that the wavelength range of the X-rays must be of the same order of magnitude as the distance between the scattering units in the crystal. These scattering units are the electron clouds associated with the atoms in the structure and their regularity is provided by the crystal lattice. Hence, a crystal acts as a three dimensional grating, capable of diffraction with a wavelength of the order of a few Ångströms (0.7 Å to 2.0 Å), i.e., X-rays. The resulting diffraction pattern can then be analysed by various methods and provides a space averaged and time averaged representation of the atomic, ionic or molecular arrangement within the crystal.

2.2.1 X-Ray Radiation Sources

X-rays are electromagnetic radiation with a wavelength of the order 0.1-100 Å and are situated energetically between γ-rays and UV radiation. In conventional laboratory X-ray sources, X-rays are produced when high energy electrons (emitted from a heated filament) collide with a metal target, often copper or molybdenum. The electrons are slowed down or stopped by the collision and some of their lost energy is converted into electromagnetic

radiation. This process gives 'white radiation' which is independent of the metal used.[1] In addition, when the electrons bombarding the metal reach certain critical energies, they can remove electrons from the innermost K shell in the target metal. These vacancies are subsequently filled by electrons from the outer L or M shells, with the emission of energy as X-rays. The transition energies have fixed values and so the wavelength of the X-ray generated has a fixed value depending on the transition that has occurred.

For copper, the $L \rightarrow K$ transition, called K_α, has a wavelength of 1.5418 Å and the $M \rightarrow K$ transition, K_β, has a wavelength of 1.3922 Å. The K_α(Cu) transition occurs much more frequently than the K_β, transition and the more intense K_α radiation is often used in diffraction experiments. In fact, the K_α transition is a doublet, $K_{\alpha 1} = 1.5405$ Å and $K_{\alpha 2} = 1.5443$ Å, because the transition has a slightly different energy for the two possible spin states of the $2p$ electron which makes the transition; the K_β transition is also a doublet ($K_{\beta 1}$, $K_{\beta 2}$). As the atomic number (Z) of the target element increases, the characteristic lines shift to shorter wavelengths, and one can select a target to give almost any desired value for the K_α line. In practice, the transition elements ($Z = 21 - 30$ and $39 - 48$ in the periodic table) have characteristic radiation in the region that is most useful for X-ray diffraction experiments. Cu X-ray sources generally produce a higher flux of X-rays than Mo and are diffracted more efficiently. Thus Cu radiation is useful for small or weakly diffracting crystals. The longer wavelength of Cu radiation is preferred over Mo radiation when studying crystals with large lattice parameters, as the greater wavelength minimizes problems due to overlap of reflections in the diffraction pattern. Mo radiation is preferred to study organometallic materials due to the absorption effect caused by heavier atoms (i.e., less absorption for Mo that Cu radiation).

Most X-ray tubes used for X-ray diffraction studies are operated under conditions which give a wide band of white radiation on which is superimposed a characteristic spectrum of K_β, $K_{\alpha 1}$ and $K_{\alpha 2}$ lines, with perhaps some contaminating K or L lines from target (window, etc.) impurities. Many diffraction techniques preferentially require a monochromatic beam. K_α fulfils this requirement but the presence of the accompanying K_β is inconvenient. Fortunately, K_β can be removed by a selective filter (an element of atomic number $Z - 1$).[2,3] An alternative method of obtaining monochromatic X-rays is by the use of a crystal monochromator.[4] In this

case, the direct beam from the X-ray tube is diffracted from a large single crystal of a suitable material before being used. Because of the nature of X-ray diffraction, only a very narrow band of wavelengths appears at a given crystal setting and so the resulting beam is very nearly monochromatic. A crystal monochromator is used in most modern X-ray diffractometers.

2.2.2 The Geometry of X-Ray Diffraction. Bragg's Law

W. L. Bragg developed a description which is universally used as the basis for X-ray diffraction geometry (Figure 2.2). Bragg showed in 1913 that the angular distribution of scattered radiation could be understood by considering that the diffracted beams behave as if they are reflected from planes passing through points of the crystal lattice. This "reflection" is analogous to that from a mirror, for which the angle of incidence is equal to the angle of reflection. Waves scattered from adjacent lattice planes are in phase only for certain angles of scattering. From such considerations, Bragg derived the famous equation that now bears his name

$$2d \sin\theta = n\lambda \tag{2.1}$$

where λ is the wavelength of the radiation used, n is an integer (analogous to the order of diffraction from a grating so that $n\lambda$ is the path difference between waves), d is the perpendicular spacing between the lattice planes in the crystal and θ is the complement of the angle of incidence of the X-ray beam. The Bragg equation can be derived by considering that

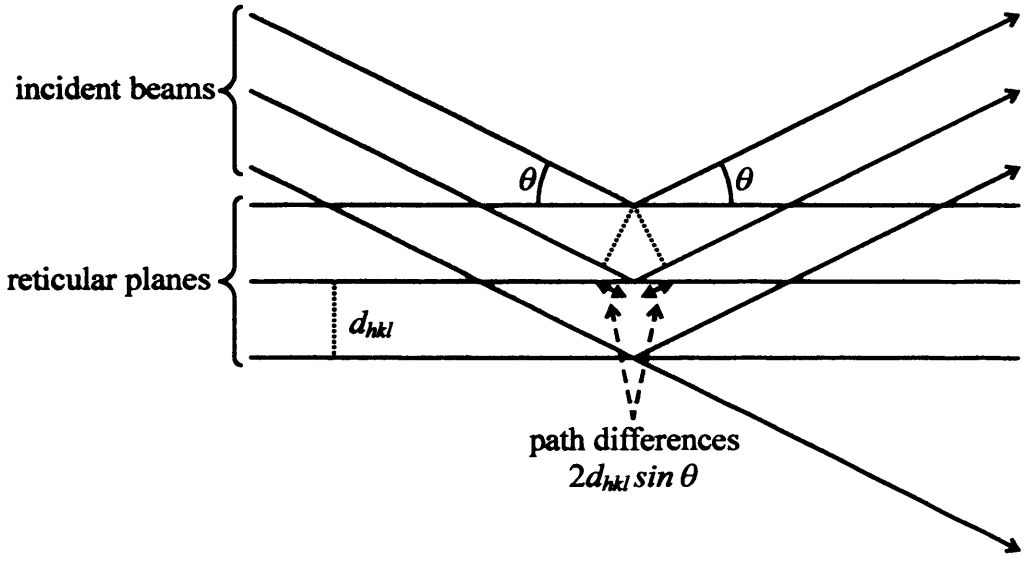

Figure 2.2. Construction for Bragg reflection of X-rays from two (*hkl*) lattice planes with an interplanar spacing *d*.

the path difference between waves scattered from adjacent parallel lattice planes must be an integral number in wavelengths. Diffraction maxima occur only when the relation of wavelength, interplanar spacing and angle of incidence of the X-ray beam is satisfied by equation 2.1.

2.2.3 The Structure Factor

Since the electrons are the only components of the atom that scatter X-rays significantly and since they are distributed over atomic volumes with dimensions comparable to wavelengths of X-rays used in diffraction experiments, X-rays scattered from one part of an atom interfere with those scattered from another at all angles of scattering greater than 0°. At $\theta = 0°$, all electrons in the atom scatter in phase and the scattering power of an atom at this angle, expressed relative to the scattering power of a free electron, is just equal to the number of electrons present (the atomic number for neutral atoms). The amplitude of scattering for an atom is known as the atomic scattering factor, *f*. The atomic scattering factor falls off with increasing scattering angle or, more precisely, increasing values of $\sin(\theta/\lambda)$. Since the diffraction pattern is the sum of the scattering from all unit cells, vibrations or disorder may be considered the equivalent of smearing out of the electron density, so that there is a greater fall-off at higher $\sin(\theta/\lambda)$.

The two numerical values associated with each reflection in a crystal diffraction pattern are the amplitude $|F|$ and the phase ϕ of the diffracted wave

$$F = |F|e^{i\phi} \tag{2.2}$$

Each reflection is labelled by its three Miller indices *h*, *k* and *l* so, for each reflection

$$F(hkl) = |F(hkl)| \exp\{i\phi(hkl)\} \tag{2.3}$$

The structure factor for a given reflection, $F(hkl)$, depends on the electron density. As the electron density is repeated periodically through the unit cell, it is possible to represent the electronic distribution by addition of periodic functions. For this purpose, we use the Fourier transform of the electron density which can be expressed as

$$F(hkl) = \int_{cell} \rho(xyz) \exp\{2\pi i(hx + ky + lz)\} dV \tag{2.4}$$

where $\rho(xyz)$ is the electron density at position (x, y, z) in the unit cell. The expression in Eq. (2.4) shows the contribution of each portion of the structure. The total diffraction pattern of a crystal is just the Fourier transform of the contents of the unit cell, multiplied by a scale factor between the observed and the calculated set of amplitudes. The scaling factor reproduces all the unit cells in the crystal. This equation is a continuous function $\rho(xyz)$ which is not convenient for calculation. Expressing the electron density instead in terms of individual atoms, the calculation becomes more straightforward. The Fourier transform expressed as a function of discrete atoms becomes

$$F(hkl) = \sum_j f_j \exp\left\{-8\pi^2 U_j \sin^2(\theta_{hkl})/\lambda^2\right\} \exp\{2\pi i(hx_j + ky_j + lz_j)\} \tag{2.5}$$

where f_j is the scattering amplitude for atom j (which depends on $\sin^2(\theta_{hkl})/\lambda^2$ for X-rays), x_j, y_j, and z_j are the fractional coordinates of atom j within the unit cell and U_j is the displacement parameter of atom j (representing its average distribution around the point (x_j, y_j, z_j)). The displacement parameter can be considered as either isotropic or anisotropic.

The reverse Fourier transform (FT^{-1}) is the electron density of a given structure which consists of discrete reflections. This Fourier transform is thus a summation rather than an integral. Therefore the expression given in Eq. (2.4) can be expressed as

$$\rho(xyz) = \frac{1}{V} \sum_{hkl} F(hkl) \exp\{-2\pi i(hx + ky + lz)\} \tag{2.6}$$

From the experimental data, the amplitude $|F(hkl)|$ can be measured from the diffraction pattern but the phases of the reflections unfortunately cannot be measured experimentally, so the determination of $\rho(xyz)$, and hence determination of the structure, cannot be carried out straightforwardly. This is known as the phase problem. Methods devised to overcome the phase problem are presented in the following sections.

2.3 Single Crystal X-Ray Diffraction

Following this introduction of the fundamentals of the X-ray diffraction process, we now consider how the method of crystal structure determination works by considering single crystal X-ray diffraction. The result of the collection of X-ray diffraction data is a relative intensity, I, for each "reflection" with indices, h, k and l, together with the corresponding value of the scattering angle, 2θ, for that reflection. The angular positions at which scattered radiation is observed depend only on the dimensions of the crystal lattice, while the intensities of the different diffracted beams depend only on the nature and arrangement of the atoms within each unit cell. Nowadays, the data required for structure determination is recorded on a diffractometer, which produces a set of observed structure factor amplitudes $|F(hkl)|$. The main steps in the process of structure determination from single crystal diffraction data are: determination of lattice parameters and space group, structure solution and finally structure refinement.

2.3.1 Determination of Lattice Parameters and Space Group Assignment

The unit cell type of a crystal is defined by three lengths a, b, c and three angles α, β, γ. With area detector diffractometers, several X-ray photographs are recorded for a crystal oscillating about the direct lattice axis oriented perpendicular to the incident X-ray beam. Indexing the diffraction pattern consists of assigning the correct indices hkl to each maximum in the diffraction pattern. This process is carried out by indexing programs that take into consideration the observed positions of the diffraction maxima. With this information, data collection can proceed covering the total range of 180° rotation of the crystal through a series of frames, each over a restricted oscillation range. The optimum oscillation range per frame and optimum exposure time per frame depend on the nature of the crystal being investigated. Once a good set of unit cell parameters has been obtained, they are refined by least squares methods.

To assign the space group it is necessary to identify the systematic absences in the indexed diffraction pattern. From the patterns of systematic absence, it is possible to derive the lattice type (body centred, face centred, etc) and whether or not the crystal possesses elements of space symmetry, i.e., screw axis and/or glide planes.

2.3.2 Structure Determination

Determination of a crystal structure of an unknown crystalline material is carried out by solving a set of simultaneous equations. The unknowns in the equations are the atomic coordinates and the observations are the experimental intensity data. In general, it is necessary to have more observations than variables in order to obtain good quality structure determination. Unfortunately, there is an intrinsic problem within the structure solution process. From the experimental data, only the amplitudes $|F(hkl)|$ are known, rather than $F(hkl)$, and the experimental data does not contain information on the phase associated with each reflection. Thus, direct solution of the crystal structure is not possible. This inability to extract the phases from the experimental data is known as the phase problem. Knowledge of the phase of each structure factor is necessary to estimate the electron density as a function of position (x, y, z) within the unit cell. Several methods have been developed in order to tackle this problem. The most common methods are the Patterson technique[5] and direct methods.[6,7]

The Patterson method is suitable for structures containing a few heavy atoms that dominate the scattering. A Fourier series using values of $|F(hkl)|^2$ as coefficients instead of $F(hkl)$ produces a so-called Patterson map. In this map, the magnitude and direction of peaks from the origin corresponds to a vector between pairs of atoms in the structure. The locations of these atoms can then be deduced, representing an approximate structure. Direct methods involves selecting the most important reflections (those which contribute most to the Fourier transform), and working out the probable relationships between the phases of these reflections. For the most promising combinations, Fourier transforms are calculated from the observed amplitudes and trial phases, and these are examined for recognizable molecular features.

2.3.3 Structure Refinement

Once we have solved the phase problem and have obtained a reasonable structure solution, the atomic positions in the unit cell can be refined by least square methods (the structure solution only gives approximate coordinates). During the refinement process, slight variations in the atomic positions (and other parameters) will produce variations in the values of the calculated structure factors. The best agreement between the calculated and observed

structure factor amplitudes corresponds to that given by the best set of structural parameters. The most convenient measures of the correctness of a structure are given by the "reliability factor" or *R*-factor

$$R = \frac{\sum_{hkl} \left| \left| F_{hkl}^{obs} \right| - \left| F_{hkl}^{calc} \right| \right|}{\left| F_{hkl}^{obs} \right|} \times 100\% \qquad (2.7)$$

where $|F_{hkl}^{obs}|$ and $|F_{hkl}^{calc}|$ are the observed and calculated structure factor amplitudes, respectively and the weighted *R*-factor, R_w, which is defined as

$$R_w = \frac{\sum_{hkl} w_{hkl} \left| \left| F_{hkl}^{obs} \right| - \left| F_{hkl}^{calc} \right| \right|}{\sum_{hkl} w_{hkl} \left| F_{hkl}^{obs} \right|} \times 100\% \qquad (2.8)$$

where w_{hkl} is a weighting factor for each *hkl* reflection. The value of the *R*-factor is typically about 12 % after the structure solution but after refinement of the model it usually falls to 5% or less.

2.4 Powder X-Ray Diffraction Structure Determination

The most important and powerful technique used for crystal structure determination of solid materials is single crystal X-ray diffraction, but this technique requires that a single crystal of appropriate dimensions must be available. If the single crystal is not big enough, or if the material cannot be crystallized, then it is convenient instead to consider the use of powder X-ray diffraction (PXRD) for structure elucidation. Powder diffraction also has important uses in chemical analysis (identification of crystalline phases, determination of sample purity, study of phase transformations, etc.) and for the identification of materials, since all crystalline solids have a unique powder X-ray diffraction pattern. In mixtures of phases, each crystalline phase will contribute to the observed powder diffraction pattern, and the relative intensity of the contribution of a given phase will depend on the amount in which it is present.

If several single crystals of the same material in different orientations are irradiated simultaneously by X-rays, each of them gives its own diffraction pattern, and for a powder, these separate diffraction patterns are superimposed. As the composite sample is rotated, any particular reflection will be generated by each of the individual crystals at a different time as the Bragg equation is satisfied; the Bragg angle and intensity will be the same in each case (assuming equal sizes of crystals) but the direction of the diffracted beam will vary, while always being inclined at 2θ to the direction of the incident beam. On a flat detector perpendicular to the incident beam and on the opposite side of the sample, the set of corresponding reflections from the multiple crystals appear as identical spots on a circle. With an increasing number of identical and randomly oriented crystals, more such spots appear, all lying on the same circle, which is where a cone of diffracted radiation hits the detector. A microcrystalline powder consists of an essentially infinite number of tiny crystals and this produces a complete circle for a particular reflection.

The same occurs for every Bragg reflection, each one giving a cone of radiation with semi-angle 2θ and hence producing a circle on the detector. The overall result is a set of many concentric circles (Figure 2.3), with radii dictated by the Bragg equation and hence the unit cell geometry, and with intensities closely related to those that would be produced by one single crystal. The effect of using a microcrystalline powder instead of a single crystal is to

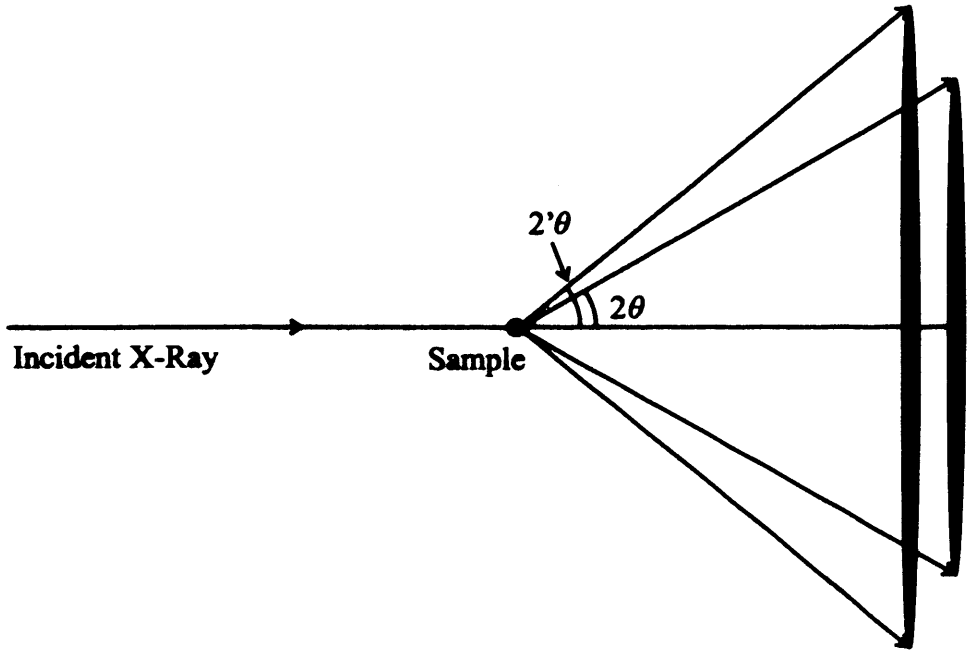

Figure 2.3. Scattering of X-rays generated by a microcrystalline (powder) sample.

compress the full three-dimensional diffraction pattern into a one-dimensional pattern (the only geometric variable is θ).

Essentially the same information is contained in single crystal and powder diffraction patterns but in the former case this information is distributed in three-dimensional space whereas in the latter case the three-dimensional diffraction data are compressed into one dimension and peak overlap occurs. The ambiguity in the data creates particular problems in the determination of the unit cell and the application of Patterson techniques and direct methods for structure solution. Sophisticated methods are currently being developed that have guided to a possible approach to determine crystal structures of organic solids directly from powder X-ray diffraction.[8] Considering the potential of powder X-ray diffraction for determining crystal structures from those crystalline materials that are inappropriate for single crystal X-ray diffraction, there is a great opportunity to make a considerable impact in structural sciences. For this reason, much research activity in recent years has been devoted to the development and application of new techniques for carrying out structure determination directly from powder diffraction data and has led to significant advances in the scope and power of techniques in this field.[9-11]

2.4.1 Stages of the Structure Determination Process

Crystal structure determination from powder diffraction data can be divided into three stages (Figure 2.4): 1) unit cell determination (indexing) and symmetry determination (space-group assignment), 2) structure solution and 3) structure refinement.

2.4.1.1 Unit Cell Determination (Indexing)

Indexing the powder pattern is the first step after collecting the data from the diffractometer. The goal of indexing is to find values for the lattice parameters (a, b, c, α, β, γ) so that every observed peak satisfies a particular combination of Miller indices. Several programs are routinely used to determine the lattice parameters from diffraction data (ITO,[12] TREOR,[13] DICVOL[14] and CRYSFIRE[15]). These programs consider the peak intensity at low diffraction angles since peak overlap at high diffraction angles is considerable. Once the correct lattice parameters are known, the space group can be assigned by examining systematic absences.

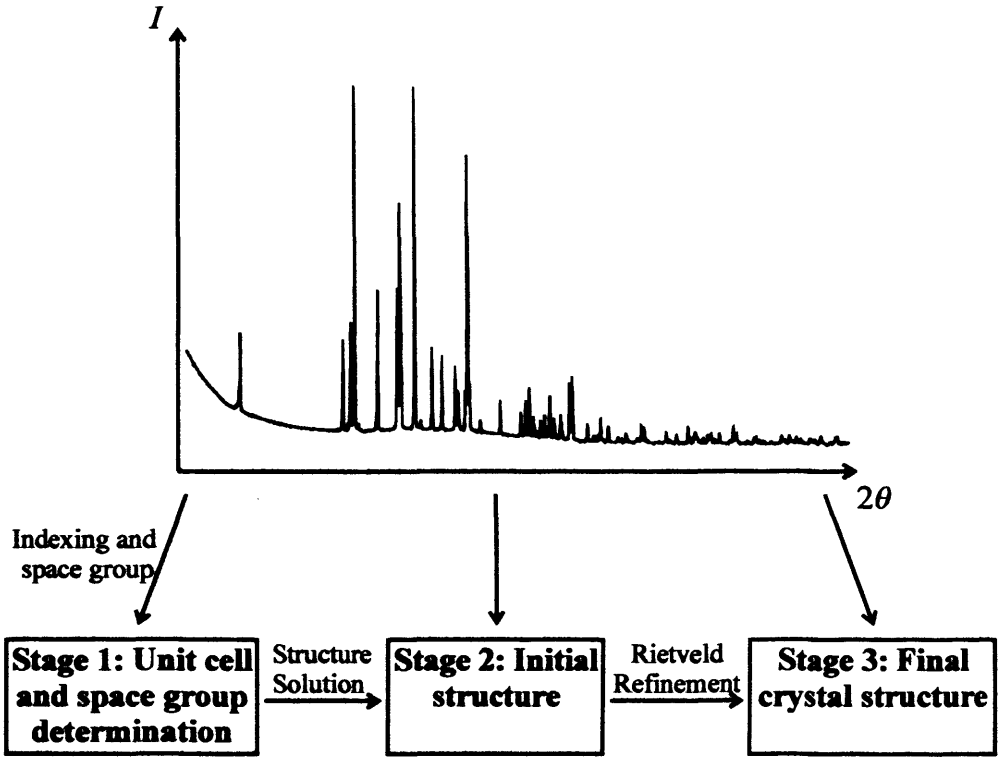

Figure 2.4. Schematic diagram to illustrate the different stages involved in complete structure determination from powder diffraction data.

2.4.1.2 Structure Solution

The techniques that are currently used for structure solution from powder diffraction data can be subdivided into two categories: traditional and direct-space approaches. The traditional approach follows a close analogy to the analysis of single crystal diffraction data, in that the intensities of individual reflections are extracted directly from the diffraction pattern and are then used in the types of structure calculation (e.g., direct or Patterson methods) that are used for single crystal diffraction data.

The direct-space approach[16], on the other hand, follows a close analogy to global optimization procedures, which find applications in many areas of science. In the direct-space approach, trial structures are generated in direct space (independently of the experimental powder diffraction data), with the suitability of each trial structure assessed by directly comparing the powder diffraction pattern calculated for the trial structure and the experimental powder diffraction pattern. The comparison can be quantified using the *R*-factor, R_p

$$R_p = \frac{\sum \left| y_j^{obs} - y_j^{calc} \right|}{\sum \left| y_j^{obs} \right|} \times 100\% \qquad (2.9)$$

where y_j^{obs} is the intensity of the jth observed point in the experimental powder diffraction profile, y_j^{calc} is the intensity of the jth corresponding point in the calculated powder diffraction profile. The weighted profile R-factor R_{wp} is defined as

$$R_{wp} = \frac{\left[\sum w_j \left(y_j^{obs} - y_j^{calc} \right)^2 \right]^{1/2}}{\left[\sum w_j \left(y_j^{obs} \right)^2 \right]^{1/2}} \times 100\% \qquad (2.10)$$

where w_j is a weighting factor for the jth point in the powder diffraction profile. The value of R_{wp} decreases as the level of agreement between the experimental and calculated powder diffraction patterns improves. Importantly, R_p and R_{wp} consider the whole digitized intensity profile and thus implicitly take care of peak overlap.

In the direct-space approach, the structure is generally defined by a structural fragment, which represents an appropriately chosen collection of atoms within the asymmetric unit. The direct-space strategy involves exploring an n dimensional R_{wp} hypersurface (Figure 2.5) (where n is the number of variables) to find the best structure solution (lowest R_{wp}). In principle any technique for global optimization may be used to find the lowest point on the R_{wp} hypersurface and much success has been achieved using Monte Carlo/Simulated Annealing[16-23] and Genetic Algorithm (GA)[24-36] methods.

Our GA technique for structure solution from powder diffraction data is implemented in the program EAGER[9] that is being developed in our laboratory. The GA technique is based on the principles of evolution and involves familiar evolutionary operations such as mating, mutation, and natural selection, to optimize the quality of a population of structures. A schematic flow-chart of our implementation of the GA[25] is shown in Figure 2.6.

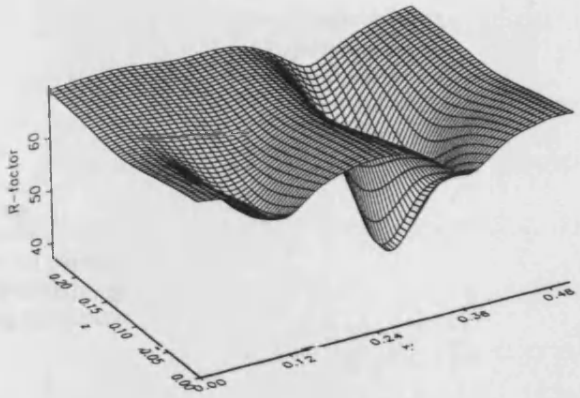

Figure 2.5. A two-dimensional section through an R_{wp} hypersurface. The deep minimum in R_{wp} corresponds to the correct structure solution but the plot clearly shows the existence of other significant local minima.

The fitness (F) of a structure is a measure of its quality with respect to the property being optimized. In our application of the GA technique in structure solution from powder diffraction data, structures giving rise to good agreement between experimental and calculated diffraction data, (i.e., low R_{wp}) have high fitness. In the evolution of the GA, the structures of highest fitness have the best chance of passing on their characteristics (genetic information) to the next generation.

Our GA works as follows. Each structure is described as a set of variables (Γ), such as the fractional coordinates (x, y, z) of the centre of mass or a defined pivot atom, the rotation angles (θ, ϕ, ψ) around a set of orthogonal axes and the intramolecular geometry specified as a set of n variable torsional angles $\{\tau_1, \tau_2, \ldots \tau_n\}$. The set of variables $\Gamma = (x, y, z, \theta, \phi, \psi, \tau_1, \tau_2, \ldots \tau_n)$ represents the "genetic code". A number (n) of trial structures are randomly generated to create the first population, P_0. From this initial population, a number (N_M) of mating operations are carried out, in each of which two "parent" structures are selected and their "genetic codes", Γ, are combined with each other to generate two offspring giving a total of $2N_M$ offspring in each generation. These offspring together with all N_p structures from the previous generation give rise to an intermediate population of (N_p+$2N_M$) structures.

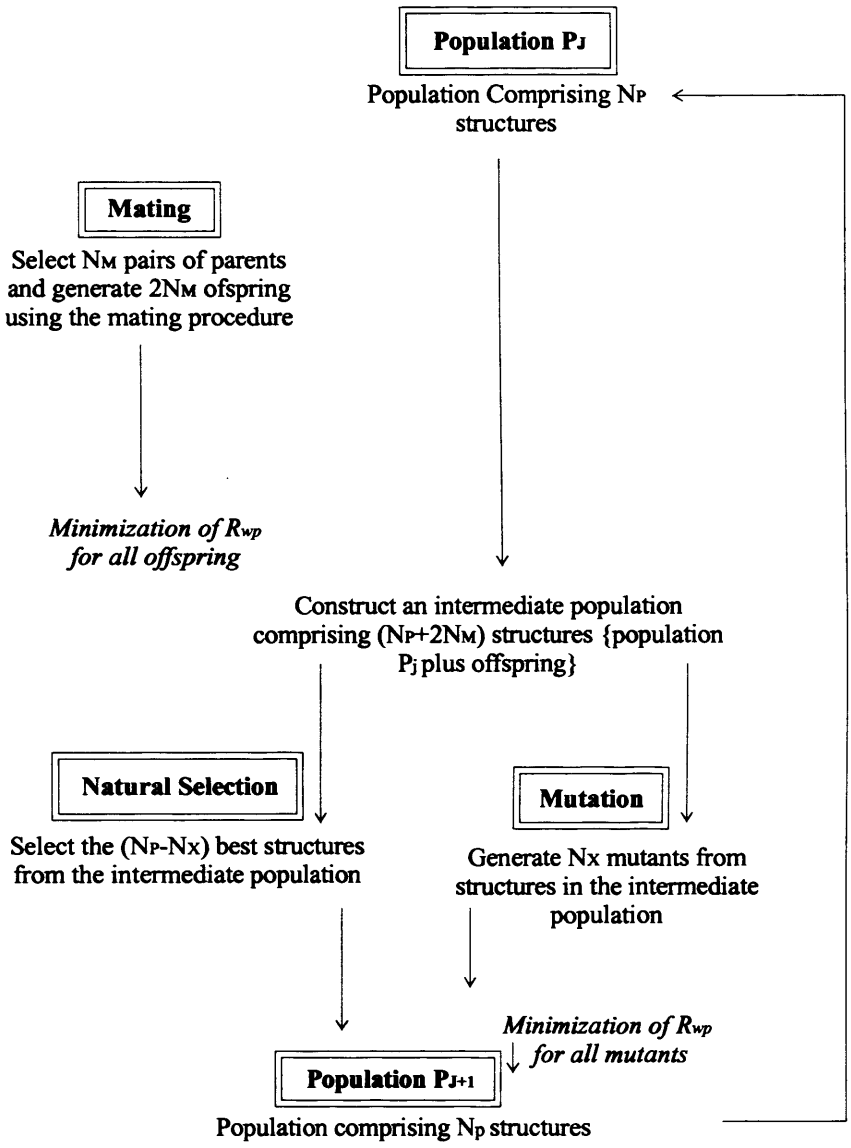

Figure 2.6. Flow chart representing the steps during the evolution of the population from one generation (population P_j) to the next generation (population P_{j+1}) in the GA for powder structure solution.

In the mutation procedure, structures are selected randomly from the population and random changes are made to parts of their genetic information to generate new structures, called mutants. There are two different types of mutation, so-called static and dynamic mutation. In static mutation, a subset of the variables in the "genetic code" is randomly selected and new random values are assigned to them. In dynamic mutation, the change involves random displacements of the selected variables from their existing values. The introduction of mutants within the population is necessary to maintain genetic diversity (i.e., to prevent in-breeding within the population) and to prevent the GA calculation converging on

a non-optimal structure, (stagnation). The introduction of mutants within the population allows new regions of the hypersurface to be explored.

Each new structure generated during the calculation is subjected to local minimization of R_{wp}, and only these minimized structures are used subsequently in the evolution of the population. This minimization is analogous to Lamarckian evolution, which differs from Darwinian evolution and is based on the assumption that characteristics acquired by an individual during its life can be passed to the next generation. The overall quality of the population increases from one generation to the next.

The EAGER program also allows the use of the multi-population approach to parallelization. In this approach, N_{sub} different sub-populations, each comprising N_{pop} structures, are present on N_{sub} processors. In each population, the evolutionary operations are carried out as in the normal, serial GA approach. In the parallel genetic algorithm (PGA) method, a further evolutionary operation (mixing) is involved in the calculation. This operation involves the transfer of structures between the sub-populations in order to produce N_{sub} new sub-populations. The method that is used in this mixing procedure is known as migration. In this method, each sub-population generates a random number κ (where $0 \leq \kappa \leq 1$) at the beginning of each generation and compares it to a user-defined exchange probability, ε. If $\kappa \leq \varepsilon$, then N_{send} structures are selected from the current population, with selection biased towards fitter members of the population. The N_{send} selected structures are then copied into the intermediate population of another randomly chosen sub-population.

2.4.1.3 Structure Refinement

Structure refinement is the last stage of crystal structure determination. Starting from the structure solution, which is quite close to the actual structure, parameters of the structural model are refined using the Rietveld technique.[37,38] In Rietveld refinement, the variables that define the structural model are adjusted by least squares methods in order to obtain a better fit between the experiment and calculated powder diffraction patterns. In general, the weighted powder profile *R*-factor, R_{wp}, is used to assess the fit between the experimental and calculated powder diffraction patterns. For successful Rietveld refinement, the initial structural model

(obtained from the structure solution stage) must be a sufficiently good representation of the correct structure.

As Rietveld refinement can often suffer from problems of instability, it is generally necessary to use geometric restraints based on standard molecular geometries to ensure stable convergence of the refinement calculation. The structural model obtained in the structure solution stage can sometimes be an incomplete representation of the true structure. In such cases, difference Fourier techniques can be used in conjunction with Rietveld refinement in order to complete the structural fragment. A properly refined crystal structure from powder diffraction data provides reliable information on the arrangement of atoms and molecules in the crystal structure that are of interest to chemists (such as details of the molecular packing arrangement and identification of the molecular interactions).

2.5 Raman Spectroscopy

The Raman effect was discovered in 1928 by Sir C. V. Raman and since the development of Fourier transform methods and powerful laser sources, Raman spectroscopy has been used routinely for studying vibrational properties of molecules. Raman scattering experiments involve shifts in the wavelength of an incident monochromatic beam. In Raman spectroscopy, the spectrum between 100 cm^{-1} and 4000 cm^{-1} is obtained in one experiment. Raman spectra can usually be recorded non-destructively and can be recorded from samples in a closed ampoule.

2.5.1 Theoretical Background

2.5.1.1 Molecular Vibrations

Molecules consist of atoms which have a certain mass and which are connected by elastic bonds. As a result, they can perform periodic motions. All motions of the atoms in a molecule relative to each other are a superposition of so-called normal vibrations, in which all atoms are vibrating with the same phase and frequency. The amplitudes are described by a normal coordinate. Polyatomic molecules with n atoms possess $3n-6$ (i.e., for non-linear molecules) normal vibrations which define their vibrational spectra. These spectra depend on:

(*i*) the masses of the atoms, (*ii*) their geometrical arrangement and (*iii*) the strength of their chemical bonds.

Each atom can move independently along each of the axes of a Cartesian Coordinate system. If n atoms constitute a molecule, there are $3n$ degrees of motional freedom. Three of these degrees of freedom (the translational ones) involve moving of all atoms simultaneously in the same direction parallel to the axes of a Cartesian coordinate system. Another three degrees of freedom also do not change the distance between atoms, as they describe molecular rotations, e.g., about the principal axes of the inertial ellipsoid of the molecule. For a non-linear molecule, the remaining $3n-6$ degrees of freedom are motions which change the distances between atoms: the lengths of the chemical bonds and the angles between them. Since these bonds are elastic, periodic motions occur. All vibrations of an idealized molecule result from superposition of $3n-6$ non-interacting, normal vibrations.

Since the centre of gravity is immobile when a molecule vibrates, the amplitudes are inversely proportional to the masses of the atoms. The force necessary to move the atom to a certain distance x from an equilibrium position is proportional to the force constant f, a measure of the strength of the bond. This is Hooke's law

$$F = -fx \tag{2.11}$$

The potential energy, V, of a molecule which obeys Hooke's law is obtained by integrating Eq. 2.11

$$V = \tfrac{1}{2} fr^2 \tag{2.12}$$

in which $r = x - x_e$, x_e is the Cartesian coordinate of the potential minimum. The graph of this function is a parabola; it is referred to as a "harmonic" potential because the model performs a "harmonic" vibration. The atoms move with a definite frequency, according to the cosine function

$$x = x_0 \cos(2\pi\nu t + \phi) \tag{2.13}$$

that describes the motion of the atom as a harmonic oscillation. Here ν is the vibrational frequency and ϕ is the phase angle. The bonds in actual molecules, however, do not obey Hooke's law exactly. The force to compress a bond by a definite distance is larger than the force required to stretch this bond. According to classical mechanics, a harmonic oscillator may vibrate with any amplitude, which means that it can possess any amount of energy, large or small. Quantum mechanics, however, shows that molecules can only exist in definite energy states. In the case of harmonic potentials, these states are equally spaced in energy

$$E_i = h\nu(\upsilon_i + \tfrac{1}{2}) \qquad \text{where } \upsilon_i = 0, 1, 2, ..., n \tag{2.14}$$

For anharmonic potentials, the distances between energy levels decrease with increasing energy. These energy levels are numbered υ_i, the vibrational quantum number. At $\upsilon_i = 0$, the vibrational energy has its lowest value.

For polyatomic molecules the frequency of normal vibrations may be calculated by applying the Lagrange equation of the kinetic and potential energy of the molecule. The kinetic energy of a molecule is given by the masses (m_i) of the atoms and their velocities (v_i)

$$E_k = \frac{1}{2}\sum_i m_i v_i^2 \tag{2.15}$$

Generally, the potential function of a polyatomic molecule can be described by a Taylor series

$$V(r) = V_0 + \sum_i f_i r_i + \tfrac{1}{2}\sum_{i,j} f_{ij} r_i r_j + \tfrac{1}{6}\sum_{i,j,k} f_{ijk} r_i r_j r_k + \ldots \tag{2.16}$$

where the r_i are suitable displacement coordinates from the equilibrium geometry at a potential minimum and the constants

$$f_i = \left(\frac{\partial V}{\partial r_i}\right)_0 ; f_{ij} = \left(\frac{\partial^2 V}{\partial r_i \partial r_j}\right)_0 ; f_{ijk} = \left(\frac{\partial^3 V}{\partial r_i \partial r_j \partial r_k}\right)_0 \tag{2.17}$$

are called linear, quadratic and cubic, force constants. The potential can be defined such that $V_0 = 0$. By definition, the second term in Eq. 2.16 is equal to zero, because the molecule is regarded as being in equilibrium

$$\sum_i f_i r_i = 0 \tag{2.18}$$

The cubic and higher terms are difficult to determine; they have many components with a comparatively small value. Therefore, to a good approximation, an acceptable potential function has the form

$$\begin{aligned} V &= \tfrac{1}{2}\sum_{i,j}\left(\frac{\partial^2 V}{\partial r_i \partial r_j}\right)_0 r_i r_j \\ &= \tfrac{1}{2}\sum_{i,j} f_{ij} r_i r_j \end{aligned} \tag{2.19}$$

The off diagonal force constants (f_{ij} with $i \neq j$) describe the change of the elastic properties of one bond when another bond is deformed. Thus, the force constant of the bonds, the masses of the atoms and the molecular geometry determine the frequencies and the relative motions of the atoms.

In the following sections, it is useful to keep in mind that molecular potentials are not exactly harmonic but that the harmonic approximation is generally sufficient. We have seen that classical mechanics describes molecular vibrational frequencies but only quantum mechanics can specify the change of energy of the vibrational states and the interaction with the light quanta which is absorbed, emitted or scattered by a molecule.

2.5.1.2 The Molecular Polarizability Tensor

We consider a sample irradiated by an intense monochromatic radiation, such as a laser beam, such that the frequency ν_0 does not correspond to any characteristic vibrational or electronic frequency of the molecule. The electric field $\vec{E}$ of the incoming electromagnetic radiation perturbs the electronic cloud of the molecule and consequently creates an induced dipole moment $\vec{P}$ defined by

$$\vec{P} = \vec{\vec{\alpha}}\,\vec{E} \tag{2.20}$$

where $\vec{\vec{\alpha}}$ is the molecular polarizability tensor of rank two.

2.5.1.3 Raman Scattering

During the vibrations of the molecule about its equilibrium position, n atoms of the molecule vibrate at the same frequency and each atom passes through its equilibrium position at the same time. As a consequence, the centre of gravity of the molecule does not change. The polarizability of the molecule can thus be described in a fixed reference frame related to the molecule. The polarizability tensor of the molecule may then be expressed as a function of the normal coordinates of vibration, Q_i, of the molecule, $\vec{\vec{\alpha}}(Q_1, Q_2, Q_3, ..., Q_{3n-6})$. It can be shown[39,40] that $\vec{\vec{\alpha}}$ may be written as a function of Q such that

$$\vec{\vec{\alpha}} = \vec{\vec{\alpha}}_0 + \left(\frac{\partial \vec{\vec{\alpha}}}{\partial Q}\right)_{Q_0} Q + \frac{1}{2}\left(\frac{\partial^2 \vec{\vec{\alpha}}}{\partial Q^2}\right)_{Q_0} Q^2 + ... + \frac{1}{n!}\left(\frac{\partial^n \vec{\vec{\alpha}}}{\partial Q^n}\right)_{Q_0} Q^n \tag{2.21}$$

where $\vec{\vec{\alpha}}_0$ is the molecular polarizability at the equilibrium and Q_0 is the normal coordinate at equilibrium.

In the harmonic approximation, all but the first two terms of equation (2.21) become negligible and we can then write the polarizability tensor as

$$\vec{\vec{\alpha}} = \vec{\vec{\alpha}}_0 + \vec{\vec{\alpha}}' Q \tag{2.22}$$

where

$$\vec{\vec{\alpha}}' = \left(\frac{\partial \vec{\vec{\alpha}}}{\partial Q}\right)_{Q_0} \tag{2.23}$$

Although the incoming monochromatic radiation of frequency ν_0 does not correspond to any molecular energy transition, the electric field $\vec{E}$ (described as $\vec{E} = \vec{E}_0 \cos(2\pi\nu_0 t)$), gives rise to an induced molecular dipole. Remembering that in the classical description, the normal coordinates may be written $Q = Q_0 \cos(2\pi\nu t)$, equation (2.20) can be written as

$$\vec{P} = \vec{\vec{\alpha}}_0 \vec{E}_0 \cos 2\pi\nu_0 t + \vec{\vec{\alpha}}' Q_0 \vec{E}_0 \cos(2\pi\nu t)\cos(2\pi\nu_0 t) \tag{2.24}$$

which can be rearranged to give

$$\vec{P} = \vec{\vec{\alpha}}_0 \vec{E}_0 \cos 2\pi\nu_0 t + \tfrac{1}{2}\vec{\vec{\alpha}}' Q_0 \vec{E}_0 (\cos 2\pi(\nu_0 + \nu)t + \cos 2\pi(\nu_0 - \nu)t) \qquad (2.25)$$

and contains terms of frequency $(\nu_0 + \nu_k)$ and $(\nu_0 - \nu_k)$. Thus, for each normal mode of vibration of frequency ν, the induced dipole re-emits a polychromatic electromagnetic signal composed of three different emissions with frequencies ν_0, $(\nu_0 + \nu_k)$ and $(\nu_0 - \nu_k)$.

These three frequencies belong to two different types: the Rayleigh activity, which depends on the permanent polarizability tensor α_0 and gives rise to ν_0, and the Raman activity, which depends on the derivative of the polarizability tensor and gives rise to $(\nu_0 + \nu_k)$ and $(\nu_0 - \nu_k)$. Figure 2.7 shows that when excited by the incoming photon $h\nu_0$, the molecule cannot reach a stable and quantified higher energy level. Upon incidence of photon $h\nu_0$, the molecule passes through a virtual excited level and can follow three different relaxational scattering processes in order to return to the fundamental energy level.

In Rayleigh scattering, the molecule returns to its initial energy level through emission of a photon $h\nu_0$. This scattering therefore occurs without change of frequency with respect to the incident monochromatic wave (elastic scattering). In Raman Stokes scattering, the molecule returns to a level through emission of energy $h\nu_S$. The change in molecular energy is

$$h\nu_R^- = h\nu_0 - h\nu_S \text{ with } h\nu_S < h\nu_0 \qquad (2.26)$$

In Raman anti-Stokes scattering, the molecule returns to a level of lower energy than the original level, with release of energy $h\nu_S$. The change in molecular energy is

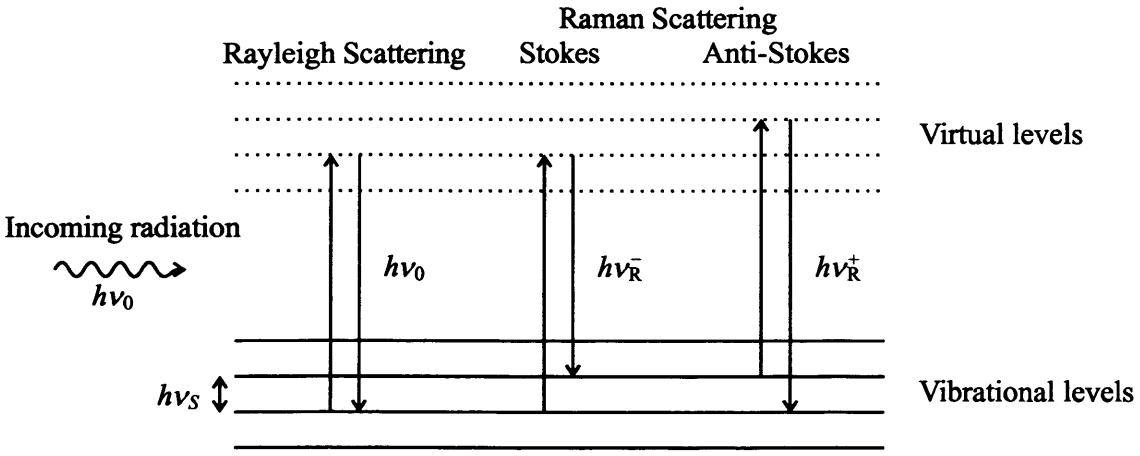

Figure 2.7. Rayleigh and Raman processes.

$$h\nu_R^+ = h\nu_S - h\nu_0 \text{ with } h\nu_S > h\nu_0 \quad (2.28)$$

The two scattering processes correspond to different initial energy levels. The Boltzmann distribution shows that, at a given temperature, the respective populations of these two initial energy levels can be significantly different. For a given transition between two energy levels, the lower level is the initial level for the Raman Stokes band and the upper level is the initial level for the Raman anti-Stokes band. The lower energy level is more populated and thus the Raman Stokes band is more intense. Therefore, the Raman Stokes spectrum is mainly used in Raman vibrational analysis.

2.5.2 Polarisation of Radiation

We use the reference system of Porto[41], in which the sample is situated at the centre O of the reference frame defined by the system of orthogonal axes (*X, Y, Z*). The *X* axis is defined as the direction of the incident laser beam and the *Y* axis is defined as the direction of observation of the radiation scattered by the sample. The *XY* plane is known as the scattering plane. The polarisation state of the radiation (incident or scattered) is defined with respect to the scattering plane. Normally, the radiation is either polarised vertically or horizontally (i.e., perpendicular or parallel to the scattering plane) and its intensity is then denoted I_V or I_H, respectively. The polarisation of the observed radiation is expressed by a notation that describes the polarisation of the incident radiation and the polarisation of the scattered radiation. If the incident laser beam is polarised vertically, the scattered beam may be polarised vertically or horizontally and the corresponding intensities of the observed radiations are denoted I_{VV} and I_{VH} respectively. In a similar manner, if the incident laser beam is polarised horizontally, the scattered beam may be polarised vertically or horizontally and the corresponding intensities of the observed radiations are denoted I_{HV} and I_{VH} respectively (Note that, in theory, $I_{VH} = I_{HV}$).

2.5.3 Experimental Set-up for Raman Scattering

Four different elements comprise a typical Raman spectrometer: the laser, the transfer deck, the monochromator (double or triple) and the detector (photomultiplier or bank of diodes). Figure 2.8 displays the general experimental set-up for direct geometry. Lasers are

the most widely used radiation sources as they provide the high density monochromatic radiation necessary to observe the Raman scattering effect. The gas used in the laser device can either be neutral atoms such as He-Ne, or ions such as Ar^+ or Kr^+. The laser beam is nearly parallel and, in general, is vertically polarised by construction (I_V). In order to turn its polarisation by 90°, to give horizontal polarisation (I_H), a half wave crystal is placed before the transfer deck. The transfer deck comprises the sample holder and two optical devices designed to focus the laser beam onto the sample and to focus and concentrate the scattered radiation onto the entrance slit of the monochromator.

Raman scattering is usually observed at an angle of 90° with respect to the direction of the incident laser beam and this observation set-up is termed direct geometry. As the scattered radiation can have any polarisation, a polarizer is generally placed after the transfer deck to select either the vertical or the horizontal polarisation. Finally, in order to avoid an anisotropic response of the monochromator to the vertically or horizontally polarised scattered rays, a quarter wave crystal (or quartz scrambler) is placed between the polarizer and the monochromator. This crystal circularises all possible polarisations, allowing a consistent comparison of the Raman intensities obtained from experiments involving different polarisations.

The monochromator analyses the radiation and provides a corresponding intensity for each wavelength resolution unit. The monochromator is based on the combination of two or three diffraction gratings. Upon hitting the reflecting surface of the diffraction grating, composed of a series of closely and regularly spaced grooves each acting as an individual slit,

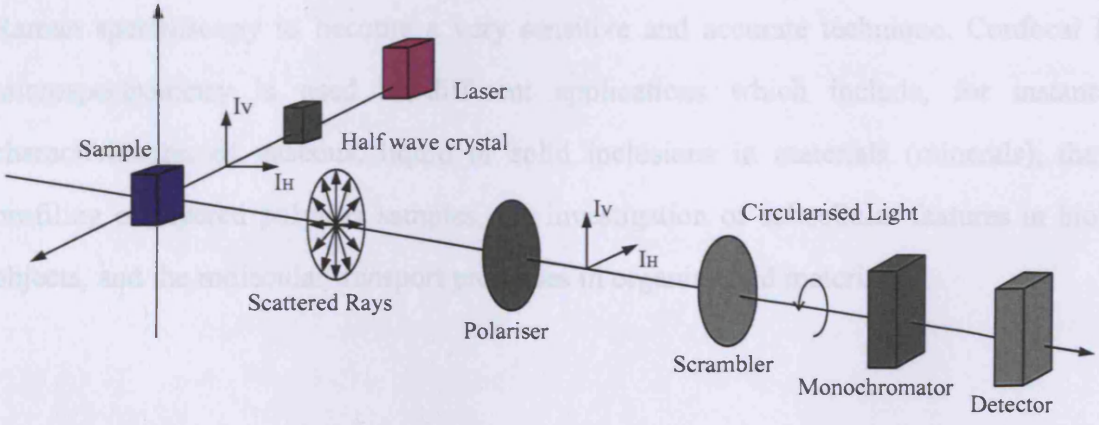

Figure 2.8. Instrumental set-up for a direct geometry Raman experiment.

5the scattered light that comes through the entrance slit is diffracted at various angles towards the exit slit. Only the diffracted radiation leaving the grating at a specific angle can then pass through the exit slit towards the detector. Entrance and exit slits are equal in size, which determines the spectral resolution. The detector is generally a photomultiplier placed after the exit slit of the monochromator. The photomultiplier collects the incoming light generating an electric signal proportional to the amount of photons striking its surface. The signal is then processed by a computer to generate the spectrum.

2.5.4 Confocal Raman Microspectrometry (CRM)

Raman microspectrometry[42] is a well-known, routine, non-destructive analytical technique which offers a unique combination for probing the chemical and structural properties of a sample on a micrometric length scale. This is achieved by using very efficient optical filtering, a high brightness spectrometer, optically matched to a wide-aperture microscope, and very sensitive detection charge-coupled device (CCD) components. With confocal Raman microspectrometry (CRM), the spectral resolution is improved markedly depending on the entrance slit used and depending on the grating selected to perform the analysis. The spatial resolution is determined by the confocal apertures of the objective used.

Most Raman spectrometers for material characterization use a microscope to focus the laser beam to a small spot (1 – 100 μm diameter). The scattered light from the sample passes back through the microscope optics into the spectrometer at an angle of 180° with respect to the direction of the incident laser beam (backscattering geometry) and is detected with a CCD detector. A computer is used for data acquisition and curve fitting. These factors have helped Raman spectroscopy to become a very sensitive and accurate technique. Confocal Raman microspectrometry is used in different applications which include, for instance, the characterization of gaseous, liquid or solid inclusions in materials (minerals), the depth profiling of layered polymer samples, the investigation of subcellular features in biological objects, and the molecular transport processes in organic solid materials.

References for Chapter 2

[1] D. Schwarzenbach. *Crystallography*. John Wiley & Sons, **1993.**

[2] G. H. Stout and L. H. Jensen. *X-ray Structure Determination*. John Wiley & Sons, second edition, **1989**.

[3] C. H. Macgillavry and G. D. Rieck, editors. *International Tables*, volume III. The Kynoch Press, **1962.**

[4] C. H. Macgillavry and G. D. Rieck, editors. *International Tables*, volume III. The Kynoch Press, **1962.**

[5] J. P. Glusker, K. N. Trueblood, *Crystal Structure Analysis-A Primer,* Oxford University Press, Oxford, **1985.**

[6] H. Hauptman and J. Karle, *The Solution of the Phase Problem I. The centrosymmetrical Crystal,* ACA Monograph, N° 3. Polycrystal Book Service. New York, **1953.**

[7] J. D. Dunitz, *X-Ray Analysis and the Structures of Organic Molecules,* VHCA, Basel, **1995.**

[8] K. D. M. Harris and M. Tremayne, *Chem. Mater.*, **1996**, *59*, 131.

[9] S. Habershon, G. W. Turner, B. M. Kariuki, E. Y. Cheung, A. Hanson, E. Tedesco, D. Albesa-Jové, M. H. Chao, O. J. Lanning, R. L. Johnston and K. D. M . Harris, *EAGER*, Computer Program for Structure Solution from Powder Diffraction Data, Cardiff University and University of Birmingham, **2004**.

[10] S. Habershon, E. Y. Cheung, K. D. M. Harris and R. L. Johnston, *Chem. Phys. Lett.*, **2004,** *390*, 394.

[11] E. Y. Cheung, K. D. M. Harris and B. M. Foxman, *Cryst. Growth Des.*, **2003**, *3*, 705.

[12] J. W. Visser, *J. Appl. Crystallogr.*, **1969**, *2*, 89.

[13] P. E. Werner, L. Eriksson and M. Westdhal, *J. Appl. Crystallogr.*, **1985**, *18*, 367.

[14] A. Boultif and D. Louër, *J. Appl. Crystallogr.*, **1991**, *24*, 987.

[15] R. A Shirley, *CRYSFIRE*, Suite of Programs for Indexing Powder Diffraction Patterns, University of Surrey, **2002**.

[16] K. D. M. Harris, M. Tremayne, P. Lightfoot and P. G. Bruce, *J, Am. Chem. Soc.*, **1994**, *116*, 3543.

[17] D. Ramprasad, G.B. Pez, B. H. Toby, T. J. Markley and R. M. Pearlstein, *J. Am. Chem. Soc.*, **1995**, *117*, 10694.

[18] B. M. Kariuki, D. M. S. Zin, M. Tremayne and K. D. M. Harris, *Chem. Matter.*, **1996**, *8*, 565.

[19] M. Tremayne, B. M. Kariuki and K. D. M. Harris. *Angew. Chem., Int. Ed. Engl.*, **1997**, *36*, 770.

[20] C. M. Freeman, A. M. Gorman and J. M. Newsam, in *Computer Modelling in Inorganic Crystallography*. (Editor: C. R. A. Catlow), Academic Press, San Diego, **1997**.

[21] Y. G. Andreev, P. Lightfoot and P. G. Bruce, *J. Appl. Crystallogr.*, **1997**, *30*, 294.

[22] G. E. Engel, S. Wilke, O. König, K. D. M. Harris and F. J. J. Leusen, *J. Appl. Crystallogr.*, **1999**, *32*, 1169.

[23] E. J. MacLean, M. Tremayne, B. M. Kariuki, K. D. M. Harris, A. F. M. Iqbal and Z. Hao, *J. Chem. Soc., Perkin Trans.*, **2000**, *2* 1513.

[24] B. M. Kariuki, H. Serrano-Gonzalez, R. L. Johnston and K. D. M. Harris, *Chem. Phys. Lett.*, **1997**, *280*, 189.

[25] K. D. M. Harris, R. L. Johnston and B. M. Kariuki, *Acta Crystallogr., Sect. A*, **1998**, *54*, 632.

[26] B. M. Kariuki, P. Calcano, K. D. M. Harris, D. Philp and R. L. Johnston, *Angew. Chem., Int. Ed. Engl.*, **1999**, *38*, 831.

[27] B. M. Kariuki, K. Psallidas, K. D. M. Harris, R. L. Johnston and R. W. Lancaster, S. E. Stainforth and S. M. Cooper, *Chem. Comm.*, **1999**, *17*, 1677.

[28] G. W. Turner, E. Tedesco, K. D. M. Harris, R. L. Johnston and B. M. Kariuki, *Chem. Phys. Lett.*, **2000**, *321*, 183.

[29] E. Tedesco, G. W. Turner, K. D. M. Harris, R. L. Johnston and B. M. Kariuki, *Angew. Chem., Int. Ed. Engl.*, **2000**, *39*, 4488.

[30] E. Tedesco, K. D. M. Harris, R. L. Johnston, G. W. Turner, K. M. P. Raja and P. Balaram, *Chem. Comm.*, **2001**, *16*, 1460.

[31] E. Y. Cheung, E. E. McCabe, K. D. M. Harris, R. L. Johnston, E. Tedesco, K. M. P. Raja and P. Balaram, *Angew. Chem., Int. Ed. Engl.*, **2002**, *41*, 494.

[32] S. Habershon, K. D. M. Harris and R. L. Johnston, *J. Comput. Chem.*, **2003**, *24*, 1766.

[33] E. Y. Cheung, S. J. Kitchin, K. D. M. Harris, Y. Imai, N. Tajima and R. Kuroda, *J. Am. Chem. Soc.*, **2003**, *125*, 14658.

[34] D. Albesa-Jové, B. M. Kariuki, S. J. Kitchin, L. Grice, E. Y. Cheung and K. D. M. Harris, *ChemPhysChem*, **2004**, *5*, 414.

[35] K. D. M. Harris, R. L. Johnston and S. Habershon, *Struct. Bonding,* **2004**, *110*, 55.

[36] K. Shankland, W. I. F. David and T. Csoka, *Z. Kristallogr.*, **1997**, *212*, 550.

[37] R. A. Young (Editor), *The Rietveld Method,* International Union of Crystallography, Oxford, **1993**.

[38] H. M. Rietveld, *J. Appl. Crystallogr.*, **1969**, *2*, 89.

[39] LSMC, Laboratoire de Spectroscopie Moléculaure et Cristalline (CNRS), *Manuel de la session de initiation"*, Université de Bordeaux I, France, **1991**.

[40] N. B. Colthup, L.H Daly and S. E. Wiberley, *"Introduction to Infrared and Raman spectroscopy"*, **1990**, 3rd edition, Academic press, San Diego. USA.

[41] T. C. Damen, S. P. S Porto and B. Tell, *Phys. Rev.* **1966**, *142*, 570.

[42] J. L. Bruneel, J. C. Lassègues, and C. Sourisseau, *J. Raman Spectrosc.* **2002**, *33*, 815 - 828.

Chapter 3 Aspects of Solid-State Photodimerization Reactions

3.1 Introduction

Structure-reactivity correlations require an understanding of the initial reactant crystal structure. The *β*-phase of 4-fluoro-*trans*-cinnamic acid had an unknown structure. Using powder X-ray diffraction, we solved the crystal structure. In this work, we monitored the solid-state photodimerization of the *β*-phase of 4-chloro-*trans*-cinnamic acid (of known structure) and the *β*-phase of 4-fluoro-*trans*-cinnamic acid under UV irradiation and we followed the structural evolution of the reactant and product phases by powder X-ray diffraction. With this study, we were able to observe the behaviour of the crystal structure at different stages of the photoreaction which will help us to understand phase separation mechanisms between reactant and product.

3.2 Solid-State Photoreactions

Environmental and economic concerns in avoiding the expensive cost of recovering polluted air and water as well as the intellectual motivation of the desire to show that chemical processes can be carried out in a cleaner and safer way are important aspects of the so called green chemistry. Green chemistry is the effort to reduce or eliminate the use or generation of hazardous substances in the design, manufacture and application of chemical products.[1] One of the techniques available to green chemistry is photochemistry. The use of light as an energy source, and as an agent of chemical change, can allow very mild reaction conditions that will lead to a cleaner, less polluted, solvent-free chemistry. In this regard, solid-state photochemistry has contributed to the idea of green chemistry.

Photochemistry of organic crystals has been studied extensively[2-5] in the last 40 years or so. The basic concepts in organic solid state reactions were first established by Schmidt and co-workers.[5] They systematically studied (in the early 1960's) the factors that govern the course of organic solid state reactions, especially photoinduced reactions. From the work carried out by Schmidt and co-workers in the photochemistry of cinnamic acids, they confirmed the topochemical postulate[6] established in 1918 by Kohlshutter, which states that

reactions in the crystalline solid-state proceed with the minimum amount of atomic and molecular movement. In a topochemical reaction, the constraining crystalline environment controls the nature and properties of the products of the reaction. Therefore, the reactions in the crystalline state are very different from those reactions that take place in solution or gas phase photochemistry, because the crystalline environment can induce a high degree of regio-selectivity, and stereo-selectivity, resulting in a high degree of control. As a result of the work of Schmidt and co-workers, some important principles have been established. These principles state that the intrinsic reactivity of a molecule is less important that the nature of the packing of neighbouring molecules around the reactant, and the separation distance, mutual orientation and space symmetry of reactive functional groups are crucial.

In crystalline solids, there are very few conformations (usually just one) taken up by molecules which, in the dispersed state, are very flexible. Organic molecular crystals display a rich variety of polymorphic forms, in each of which a particular conformer or particular symmetry and separation of functional groups prevails. A polymorphic system comprises a set of crystalline materials with the same chemical composition but different crystal structures. Thus, in the case of molecular solids, polymorphism arises when a given type of molecule can form different crystal structures. The phenomenon of polymorphism[7-9] is of considerable interest in the field of organic solid state chemistry since by crystal structure comparison of different polymorphs we can understand relationships between physical properties of the particular polymorph and its crystal structure.

[2+2] photodimerization reactions in crystalline *trans*-cinnamic acid and its derivatives represent the classic example of a set of solid-state reactions which conform to the topochemical principle. The *trans*-cinnamic acids and their derivatives crystallize in one or more of three possible types[10] (α, β, or γ), which may be distinguished by the product of their photoreactions (Figure 3.1). In crystals of the α-type, the double bond of the molecule in one stack overlaps with that of a centrosymmetrically related molecule in an adjacent stack. The distance between the double bonds related by translation is greater that 5.5 Å but that between the double bonds related across the inversion centre is about. 4.2 Å. Upon irradiation of this type of crystal a centrosymmetric dimer is obtained. In the β-type structure, potentially

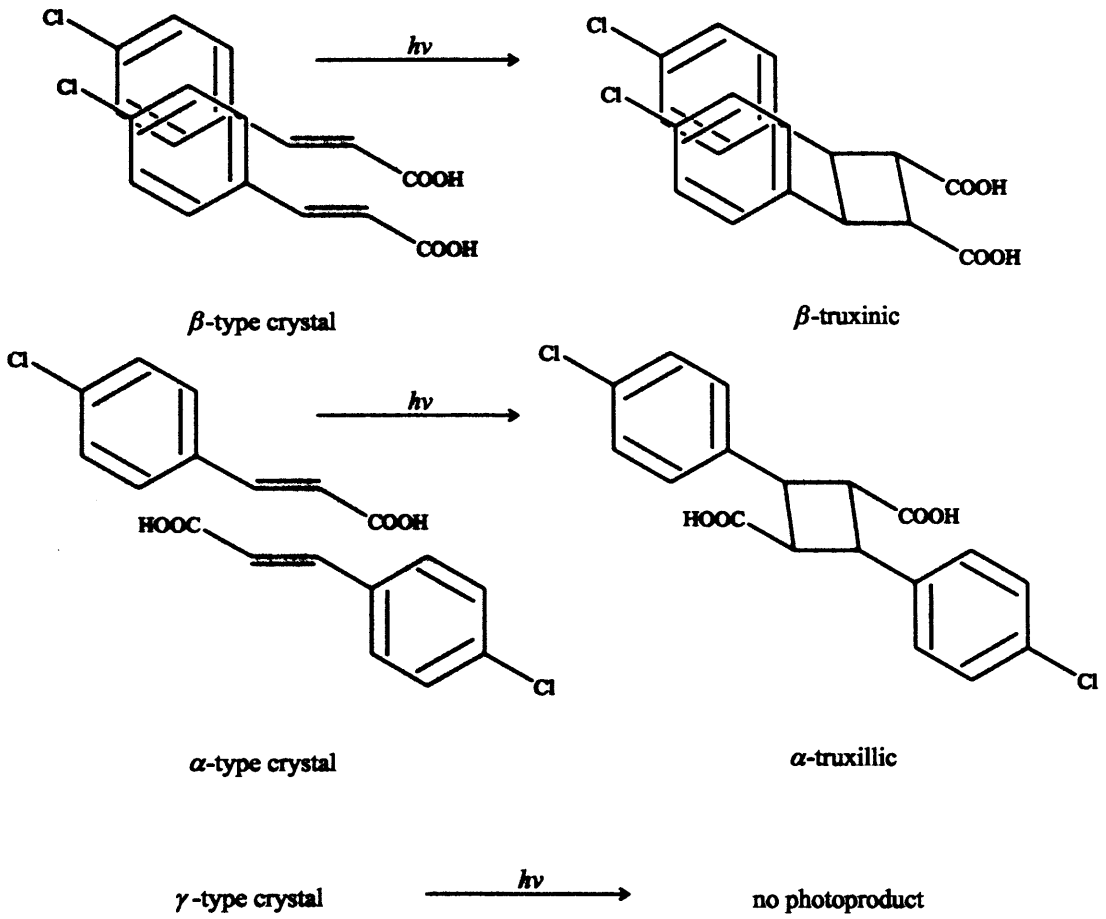

Figure 3.1. Classification of crystals of *trans*-cinnamic acid derivatives according to their behaviour upon UV irradiation. Note, that as shown, potentially dimerizable monomer molecules in α-type crystals are related across a crystallographic center of symmetry, whereas potentially dimerizable monomer molecules in β-type crystals are related crystallographically by translation. This results in the production of a β-truxinic acid following topochemical dimerization in β-type crystals.

reactive molecules are related by translation and are separated by a short repeat distance of 3.8-4.2 Å, thus neighbouring molecules along the stack are translationally equivalent and show considerable face to face overlap. All cinnamic acids which crystallize in this structure react photochemically to give products of the same stereochemistry (mirror symmetric dimers).

The single-crystal X-ray diffraction studies of Schmidt demonstrated well-defined correlations between crystal structure and photoreactivity in these materials. In the γ-type structures, adjacent molecules are offset, so that the potentially reactive double bonds do not overlap and, furthermore, the distance between them is large (4.8-5.2 Å). Crystals of this type are photostable. [2+2] photodimerization reactions of *trans*-cinnamic acid and its derivates

have also been analyzed by Raman spectroscopy.[11-14] Using vibrational spectroscopy, it is possible to monitor the Raman intensity of the double bond of the monomer as a function of conversion.

In our work, we have chosen the reactive phases (*β*-phases) of 4-chloro-*trans*-cinnamic (CLCN) acid and 4-fluoro-*trans*-cinnamic (FLCN) acid. We also have determined the crystal structure of FLCN acid using PXRD data (see section 3.5.1). ^{1}H NMR showed that this polymorph of FLCN was a photoreactive phase. By crystal structure determination, we demonstrate that this is the *β*-phase of FLCN that will enable us to study its structural properties under UV irradiation and to compare it with the CLCN case. Here, we demonstrate correlations between crystal structure and photoreactivity, with a particular interest in understanding, by means of powder X-ray diffraction, the structural evolution of the system on passing from the reactant phase to the product phase. One of the main challenges in solid-state photochemistry is to protect the single crystal from degradation by the reaction. Crystallinity may degrade gradually during the photoreaction, for example through fracturing of the single crystal to produce a polycrystalline product phase. Using powder X-ray diffraction, the ability to monitor structural changes during the reaction is not affected by the reaction proceeding in a "single-crystal to polycrystalline" manner. Indeed, by exploiting this technique, we have the opportunity to monitor the evolution of structural changes associated with such reactions.

3.3 Methodology

3.3.1 Solid Solutions

The first stages of any solid-state reaction can be described as a dilute mixed crystal of the product in the crystal phase of the reactant. Mixed crystals or solid solutions are structurally regular solid-state phases with a crystal structure characteristic of one of the two components. Mixed crystals do not have precise stoichiometric composition like inclusion complexes or clathrates, but they can exist over an extended and continuous range of compositions. Nevertheless, they may have limited co-solubilities with compositions beyond which they may not exist. The extent and possibility of mixed crystallization is still determined by the similarity between the reactant and product. It is interesting to note that

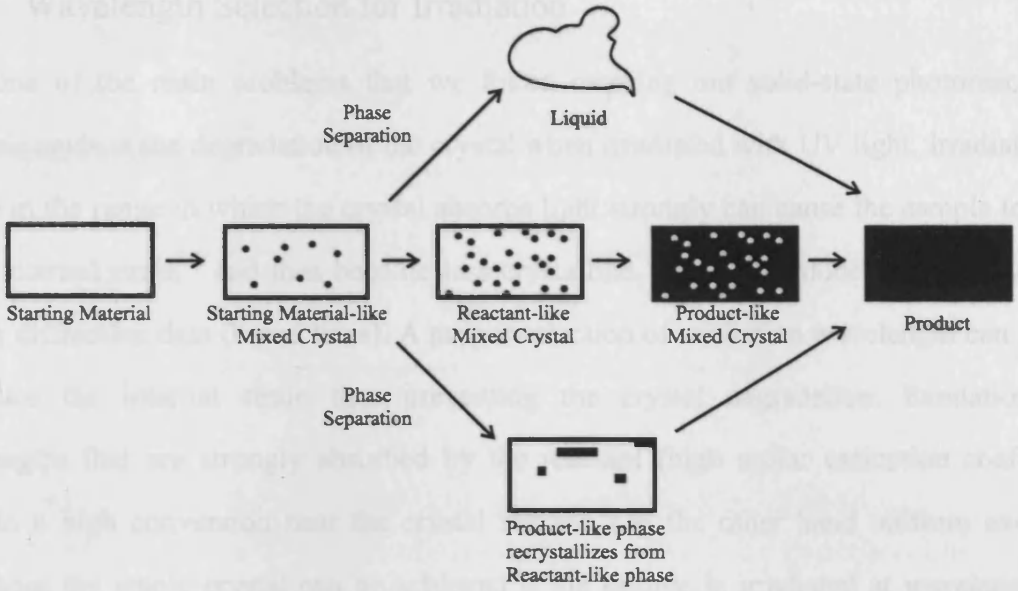

Figure 3.2. Accumulation of product can occur in a continuous mixed crystal (center), or by phase separation to a liquid (top) of a bi-phasic (bottom) solid.

structural factors facilitating solid-state reaction (such as complementarity between the product molecule and the reaction cavity in the reactant crystal) may also facilitate the formation of a mixed crystalline phase of the product in the lattice of the reactant. Solid-state reactions having a reactant ideally predisposed to form a given product will be favoured in this regard. Products that cause small perturbation to the crystal lattice of the reactant should be tolerated and allow for high conversion values, producing mixed product/reactant crystals across a wide composition range. Limited solid-state solubility, on the other hand, can cause severe crystal lattice perturbations, leading to large numbers of defect sites. Such reactions are likely to proceed to low conversion limits or to lead to rapid loss of selectivity.

The evolution of a solid-state reaction occurring throughout the bulk of a crystal following the formation of a dilute mixed crystalline phase should depend on: *i*) the solubility of the product in the crystal phase of the reactant, *ii*) their phase separation mechanisms and *iii*) the influence of intermediate and final solid phases on the reactivity of the starting material. While the number of possible scenarios may be large, one may distinguish three general pathways (see Figure 3.2) that depend on the overall changes that occur as the composition of the crystal changes from reactant to product.

3.3.2 Wavelength Selection for Irradiation

One of the main problems that we found carrying out solid-state photoreaction in cinnamic acids is the degradation of the crystal when irradiated with UV light. Irradiating the sample in the range in which the crystal absorbs light strongly can cause the sample to suffer strong internal strain[15] and thus become less crystalline. This fact reduces the quality of the powder diffraction data (broad lines). A proper selection of excitation wavelength can help us to reduce the internal strain thus preventing the crystal degradation. Excitation with wavelengths that are strongly absorbed by the reactant (high molar extinction coefficient) result in a high conversion near the crystal surface. On the other hand uniform excitation throughout the whole crystal can be achieved if the sample is irradiated at wavelengths for which the molar extinction coefficient of the reactant is as small as possible and that of the product is zero. The wavelength chosen for irradiation has been shown to be extremely important for maintaining the homogeneity of the reaction.[16] Frequently, this occurs at the "tail" of the UV-Vis spectrum of the reactant.

3.3.3 Homogeneous and Heterogeneous Reactions

In a homogeneous reaction, it might be presumed that initial product formation occurs randomly throughout the bulk of the crystal but this is not always the case. Wegner[17] has introduced a useful distinction between heterogeneous and homogeneous solid-state reactions. Heterogeneous reactions show preferential product formation at distinct nucleation sites, defined by defects or a surface. The resulting product distribution leads most often to the separation of a new phase when the product locally reaches the limit of its solid-state solubility. Homogeneous reactions are those in which the product is distributed randomly in the crystal throughout the reaction. These proceed by way of a solid solution of product in the reactant crystal, without ever undergoing phase separation. The strict requirement of random product distribution implies that no photoreaction can be truly homogeneous, since absorption at the surface will always be greater that in the interior. Here, we use "homogeneous" to mean reactions that proceed by way of a continuous solid solution that preserves the mixed-crystalline nature of the reacting crystal throughout the transformation.

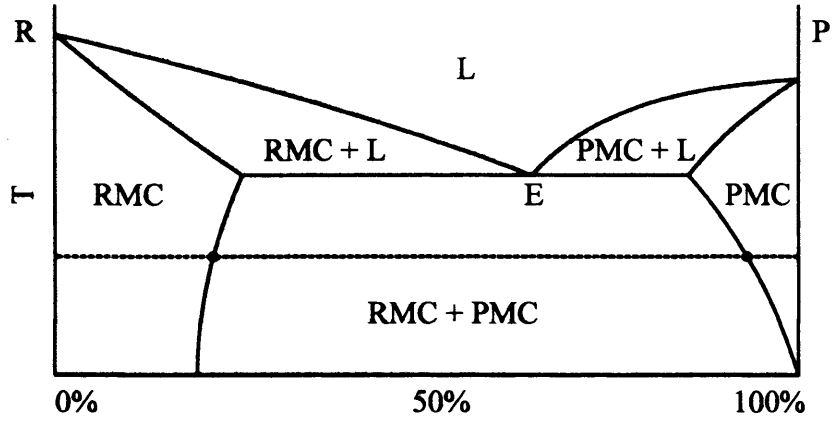

Pure Reactant: R	Reactant-like Mixed Crystal: RMC	Liquid: L
Pure Product: P	Product-like Mixed Crystal: PMC	Eutectic Point: E

Figure 3.3. Possible phase diagram representing the solid state solubility of a binary system.

Thus, homogeneous reactions maintain the structure of the reactant crystal, but with the reactant molecules gradually replaced by product molecules. Such reactions can be followed by X-ray crystallography and the structure of the as-formed product can be determined *in situ*.[18,19] Single-crystal-to-single-crystal reactions are rare, as most solid state reactions disrupt the lattice hosting the reaction to some extent. Some reactions destroy the crystallinity of the medium to give liquid or amorphous phases and some reactions lead to new crystalline phases by poorly understood reconstructive mechanisms. In principle, the evolution of a reacting system, from a phase transformation point of view, may be followed according to the phase diagram of the reactant and the product(s). A solid-to-solid reaction along the dotted line in the hypothetical phase diagram (Figure 3.3) would start with formation of reactant-like mixed crystals (RMC). In the example in Figure 3.3, the reaction would continue within the RMC phase until the solubility limit of the product was reached, for example at about 20% conversion in Figure 3.3. After this, the RMC no longer tolerates the product, and phase separation would occur. Segregation of the reactant and the product would result in recrystallization into the RMC phase and "product-like" mixed crystal phase (PMC). Conversion values between 20 and 90% would involve a weighted mixture of crystals with compositions given by the solubility limits of the two allowed solid phases and, at the end, the reaction would reach completion within the PMC phase.

Potentially the preferred product from the solid state reaction can change as a function of conversion. While dimerization is favoured at low conversion values, rearrangement can become increasingly important as the reaction proceeds. However, as the reaction proceeds, the local structure may be altered, so that potential reaction partners may no longer exist or may not have the required orientation.

3.4 Experimental

Samples of CLCN and FLCN were obtained from Aldrich and recrystallized from ethanol before irradiation. For the irradiation experiments, single crystals of CLCN and FLCN acid were spread over a glass slide to form a thin layer of single crystals. We then introduced the sample into a UV lamp housing and the sample was irradiated with an Oriel ultra-high-pressure 200 W (Hg(Xe)) UV lamp. The power used to irradiate the crystals was 40 W and the time was varied between 1 and 34 hours. We used a CVI Technical Optics 305 nm filter to control the wavelength used in our experiments. In our samples, the optimum wavelength to be used is at 305 nm, as shown in Figure 3.4. The starting material in both cases was colourless, but turned yellowish on irradiation with UV light.

Once the reaction was finished, we immediately ground the sample using a pestle and mortar until a fine crystalline powder was obtained. This sample was packed into a capillary

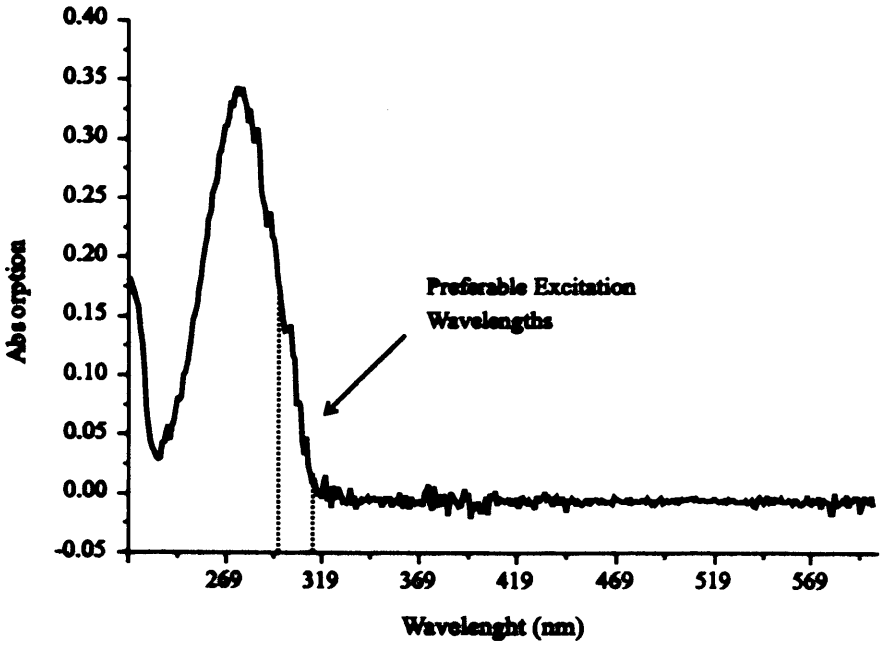

Figure 3.4. Preferable excitation wavelengths used for β-phase of 4-chloro-*trans*-cinnamic acid.

glass tube which was mounted into a goniometer head to perform the PXRD analysis. It is important to highlight that we performed the PXRD just after the solid-state reaction was finished, as we noticed that the photoproduct was unstable and further recrystallization processes were observed. The same samples used for the PXRD analysis were removed from the capillary tube and dissolved in DMSO-d_6 to carry out solution state ^{1}H NMR study in order to assess the conversion from reactant to product. The changes in the lattice parameters of the reactant and product were followed by a series of Le Bail refinements using the GSAS package.

3.5 Results and Discussion

In this section, the crystal structure of the β-phase of FLCN, solved from PXRD data, is presented. This is followed by the description of the evolution of the lattice parameters of CLCN and FLCN acid upon UV irradiation.

3.5.1 Structure Solution of 4-Fluoro-*trans*-cinnamic acid using PXRD

The powder X-ray diffractogram was measured at ambient temperature on a Siemens D5000 diffractometer (operating in transmission mode using Ge-monochromatized Cu $K_{\alpha 1}$ radiation). The data were recorded for 2θ in the range 3.5-70° and the total data collection time was 10 h. The diffractogram was indexed by the program DICVOL to give a monoclinic unit cell a = 31.706(4) Å, b = 6.489(5) Å, c = 3.878(1) Å; β = 94.74(0)°; V = 795.132(35) Å^3; Z = 4. The Pawley[20] fit gives an agreement factor of R_{wp} = 5.5 %, representing an acceptable fit of the whole powder diffraction profile using this unit cell and allowing reliable peak width and peak shape parameters to be determined for use in our subsequent GA structure solution calculations. From systematic absences, the space group was assigned as $P2_1/a$ and from density considerations, there is one molecule in the asymmetric unit.

The structure solution was carried out using the "direct-space" methodology with a Genetic Algorithm search method. The molecular fragment used in the structure solution calculation is depicted in Figure 3.5. Each structure was defined by a total of six variables (x, y, z, θ, ϕ, φ) as there are no variable torsional angles (the molecule is constrained to be planar).

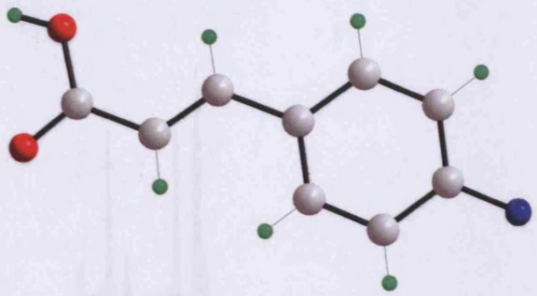

Figure 3.5. Structural fragment used in the GA structure calculation of the β-phase of 4-fluoro-trans-cinnamic acid.

The program EAGER, using the multi-population approach to parallelization, was used to solve the structure involving evolution of 2 sub-populations, each containing 500 structures. The mating rate was set at 50% and 30 mutants were allowed per generation. In the mating procedure, coordinates and orientation angles were kept as blocks and spliced to generate offspring. Figure 3.6 depicts the best (R_{min}), the average (R_{ave}) and the worst (R_{max}) R_{wp} values as a function of generation number, reaching the minimum value of 16.42 %.

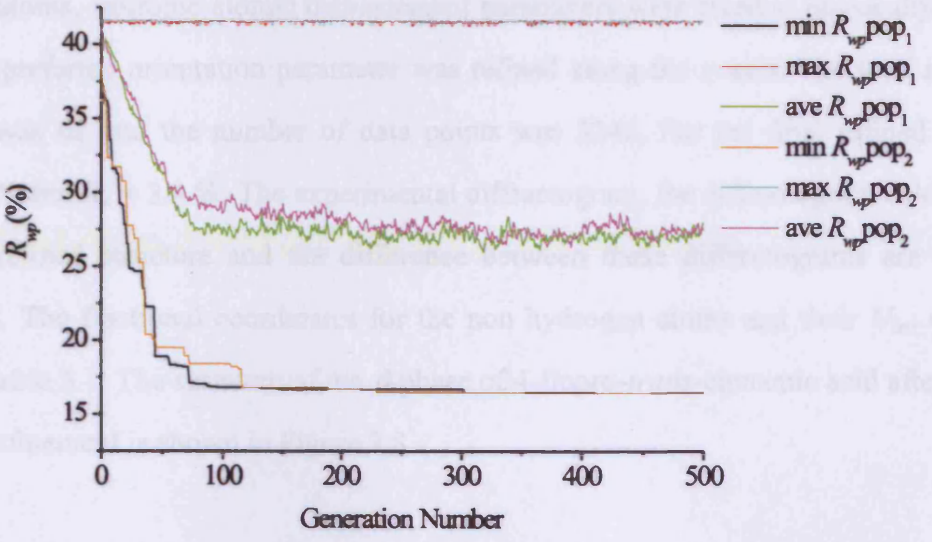

Figure 3.6. Evolutionary progress plot for the GA calculation showing the minimum, maximum and the average values of R_{wp} for two sub-populations as a function of generation of the β-phase of 4-fluoro-*trans*-cinnamic acid.

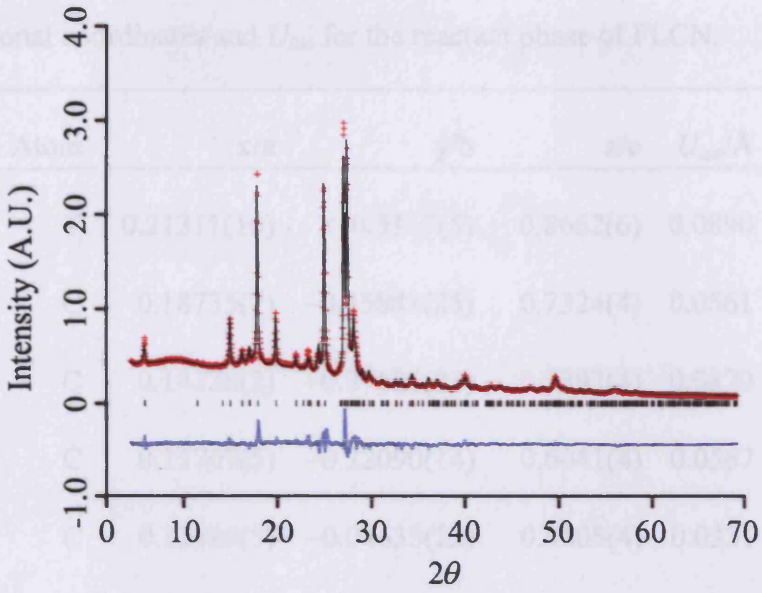

Figure 3.7. Experimental (+ marks), calculated (black solid line) and difference (blue lower line) powder X-ray diffraction profiles for the final Rietveld refinement for 4-fluoro-*trans*-cinnamic acid.

Rietveld refinement calculations were then carried out using the GSAS program package, taking the structure solution corresponding to $R_{wp} = 16.42$ % as the starting structural model. Soft constraints were applied to the geometry of the molecule and hydrogen atoms were added to the structure in positions consistent with standard geometry. For the non-hydrogen atoms, isotropic atomic displacement parameters were fixed at physically plausible values. A preferred orientation parameter was refined along the *a* axis. The total number of variables was 62 and the number of data points was 3245. For the final refined structure, $R_{wp} = 4.6$ % and $R_p = 3.4$ %. The experimental diffractogram, the diffractogram calculated for the fully refined structure and the difference between these diffractograms are shown in Figure 3.7. The fractional coordinates for the non hydrogen atoms and their U_{iso} values are given in Table 3.1. The structure of the β-phase of 4-fluoro-*trans*-cinnamic acid after the final Rietveld refinement is shown in Figure 3.8.

Table 3.1. Fractional coordinates and U_{iso} for the reactant phase of FLCN.

Atom	x/a	y/b	z/c	U_{iso}/Å
F	0.21311(10)	–0.5117(5)	0.8662(6)	0.0890
C	0.18735(7)	–0.35881(25)	0.7324(4)	0.0561
C	0.14328(2)	–0.37626(23)	0.7393(4)	0.0870
C	0.11707(5)	–0.22090(14)	0.6041(4)	0.0567
C	0.13385(5)	–0.04633(22)	0.4605(4)	0.0331
C	0.17809(3)	–0.03049(23)	0.4538(4)	0.0850
C	0.20438(5)	–0.18762(13)	0.5915(4)	0.0850
C	0.10437(3)	0.1184(6)	0.3216(20)	0.0600
C	0.06244(3)	0.1092(8)	0.3343(22)	0.0300
C	0.03400(5)	0.26935(35)	0.1956(5)	0.0374
O	0.04786(5)	0.44289(29)	0.0377(4)	0.0850
O	-0.00372(11)	0.2468(4)	0.2132(6)	0.0826

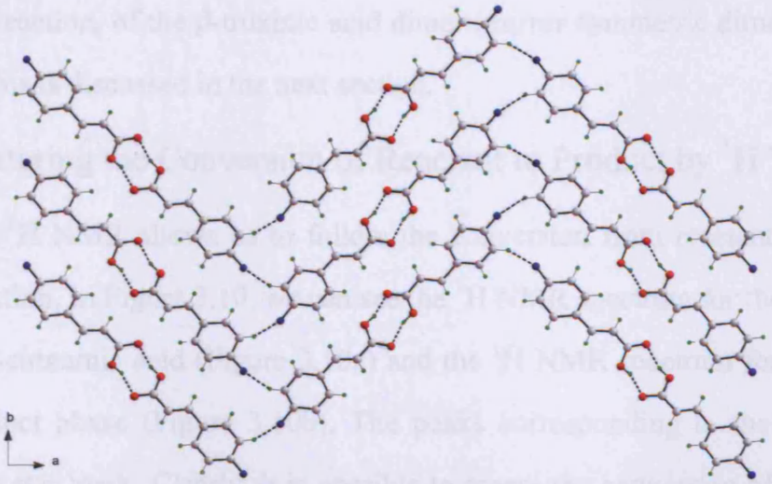

Figure 3.8. View along the *c* axis of the molecular arrangement in the FLCN.

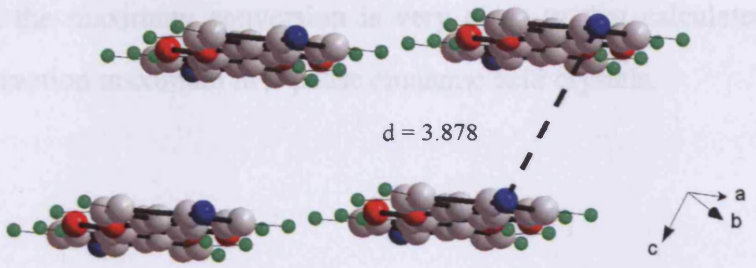

Figure 3.9. Stacking pattern in the β-phase of 4-fluoro-*trans*-cinnamic acid showing adjacent molecules in different sheets.

3.5.1.1 Crystal Structure

The packing of the β-phase of 4-fluorocinnamic acid is very similar to the structure observed in the β-phase of 4-chloro-*trans*-cinnamic acid.[21] The molecules of FLCN are planar and pairs of molecules are related to each other by an inversion centre (the carboxylic acid dimer motif) (Figure 3.8) involving the formation of hydrogen bonds between carboxylic acid groups. These hydrogen bonds are formed between FLCN molecules that are coplanar and involve the OH group of one monomer with the OH of the adjacent monomer. The geometry of this hydrogen bond is O–H···O: 162.30° and O···O: 2.586 Å.

The FLCN molecules form stacks parallel to the *c* axis (the shortest unit cell axis) with adjacent molecules related by translation (3.878 Å) as shown in Figure 3.9. This close distance between the double bonds and the head-to-head packing favours the formation, via a topochemical reaction, of the β-truxinic acid dimer (mirror symmetric dimer) under exposure of UV light. This is discussed in the next section.

3.5.2 Monitoring the Conversion of Reactant to Product by ^{1}H NMR

Solution ^{1}H NMR allows us to follow the conversion from reactant to product in the solid-state reaction. In Figure 3.10, we can see the ^{1}H NMR spectrum for the reactant phase of 4-chloro-*trans*-cinnamic acid (Figure 3.10a) and the ^{1}H NMR spectrum for both the reactant and photoproduct phase (Figure 3.10b). The peaks corresponding to the photoproduct are labelled with a star mark. Clearly, it is possible to assess the conversion of the photoreaction by ^{1}H NMR. Integrating these intensities, we calculate the ratio that corresponds to the

photoproduct and the maximum conversion is very close to that calculated by theoretical approaches[22] for reaction maximum in β-phase cinnamic acid crystals.

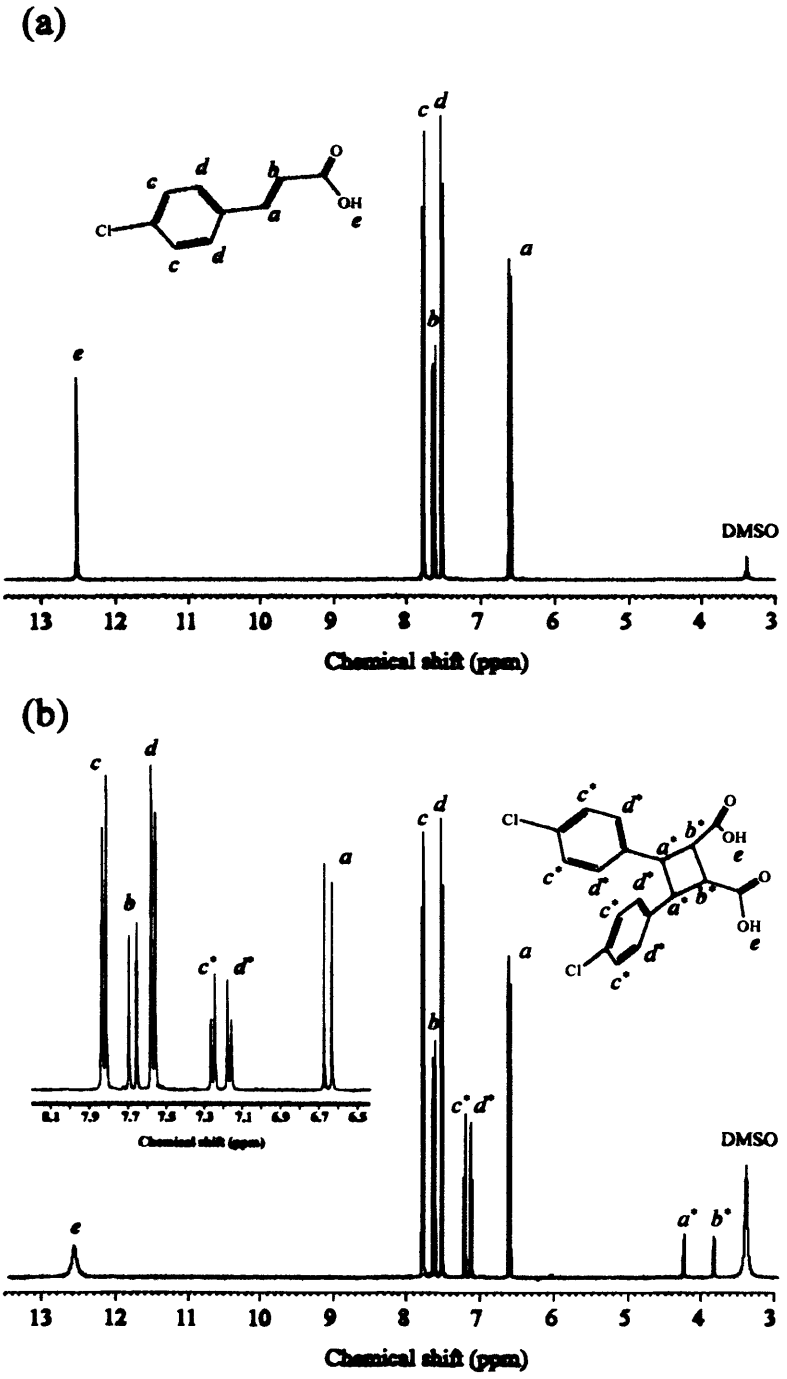

Figure 3.10. (a) Solution ^{1}H NMR spectra for the reactant 4-chloro-*trans*-cinnamic acid and (b) the mixture of 4,4'-dichloro-β-truxinic acid and 4-chloro-*trans*-cinnamic acid obtained for the photoproduct after 8 hours of photoreaction. Expanded region shown in the inset.

As mentioned in Section 3.2, this kind of reaction corresponds to a reaction along a stack of monomer molecules to produce a mirror-symmetric dimer, and the theoretical maximum conversion calculated for a β-phase structure is 86.46 %. The α- and β- phase differ

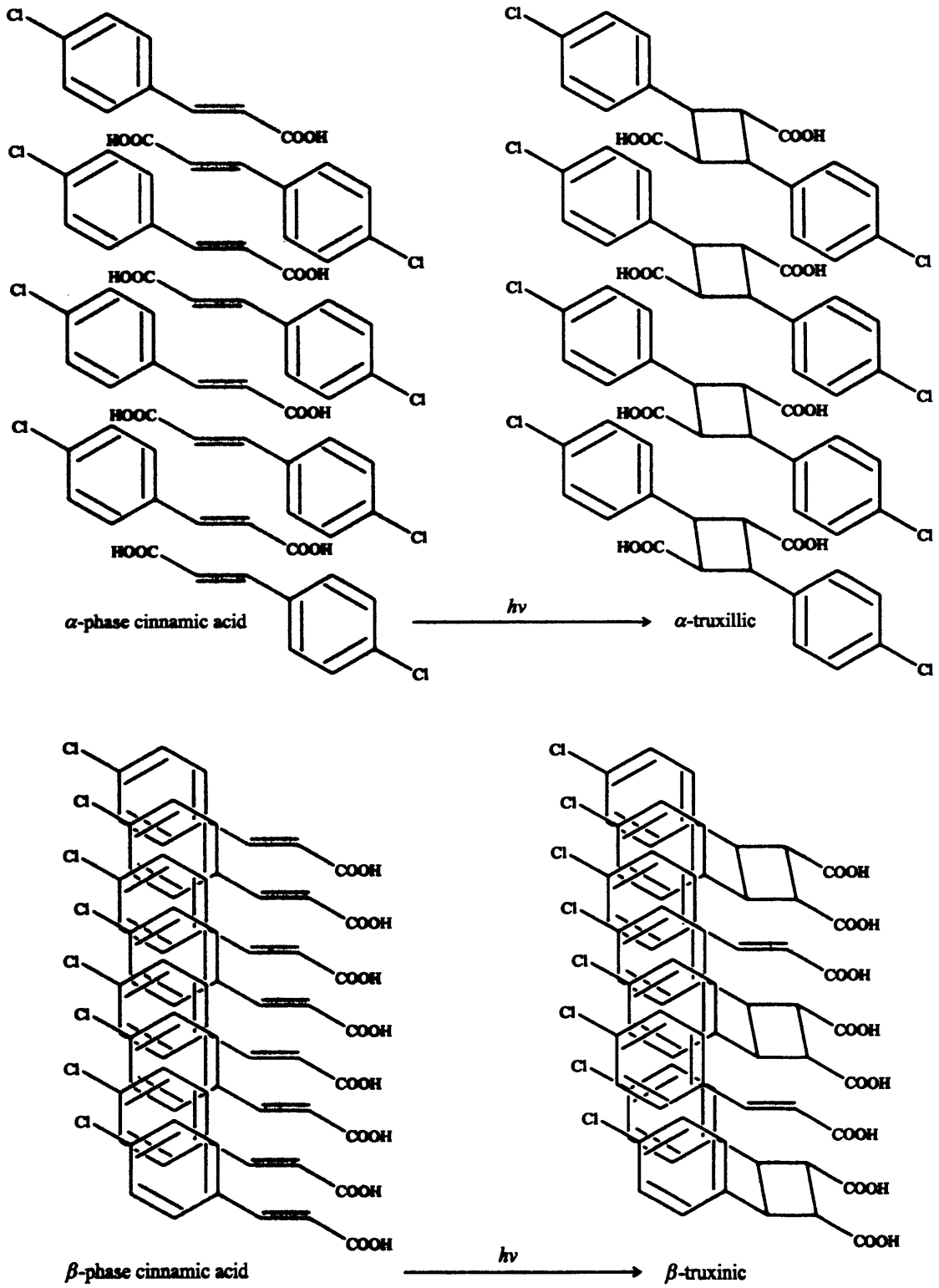

Figure 3.11. Illustration of dimerization in β- and α- phase cinnamic acids, showing that, by the end of the reaction, certain monomer molecules can remain unreacted ('isolated') in the β-phase, whereas for α- phase structures all monomer molecules can react.

in the theoretical maximum possible conversion into dimer. Whereas in the α-phase, two monomer units are paired (across the crystallographic centre of symmetry) and are therefore capable of dimerization so long as they can maintain this alignment, irrespective of progress of dimerization elsewhere in the lattice, in the β-phase, a monomer molecule may find itself eventually isolated (Figure 3.11): a parallel stack designated by M...M...M...M...M may react to form M_2...M...M_2 in which the remaining monomer molecule is unable to react. Such "isolated" monomer molecules are only able to react subsequently if a solid state recrystallization mechanism is operative.

Photodimerization in many β-phase *trans*-cinnamic acids is thought to occur according to a dimerization-followed-by-recrystallization mechanism. In summary, the mechanism proceeds as follows. Dimerization within the monomer crystal will produce a dimer/monomer solid solution and, after a certain extent of dimerization (when the concentration of dimer in this crystal has reached its solubility limit), phase separation will occur to give a monomer-rich (or pure monomer) phase and a dimer-rich (or pure dimer) phase:

$$\{M_z\}_M \xrightarrow{\text{dimerization}} \{M_xD_y\}_M \xrightarrow{\text{recrystallization}} \{M_aD_b\}_M + \{M_dD_c\}_D$$

M and D represent monomer and dimer, respectively, $\{\ \}_M$ and $\{\ \}_D$ denote the monomer and dimer crystal structures. The important question here concerns the identity of the monomer phase produced following the recrystallization step. If the β-phase is generated, then in further

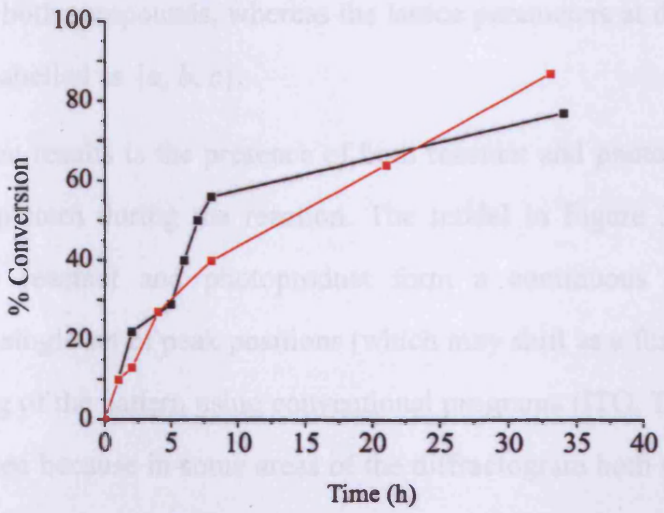

Figure 3.12. Product conversion as a function of time for CLCN (red line) and FLCN (black line).

dimerization-followed-by-recrystallization steps, the monomer-to-dimer conversion in the system as a whole will progressively increase. If the monomer recrystallizes out as the γ-phase, then this monomer can not take part in further reaction. In our experiments, the maximum rate of conversion for β-CLCN acid was obtained after 33 hours of photoreaction with a yield of 86.6 %. In the case of β-FLCN acid, the maximum conversion was 77 % and was achieved after 34 hours of photoreaction (Figure 3.12).

3.5.3 Monitoring the Evolution of the Lattice Parameters by PXRD

Powder X-ray diffraction patterns are valuable because they contain information relating to the changes in structure. Using this technique, we can follow the evolution of the lattice parameters corresponding to the reactant and product phases. As far as we know, this is the first time that the photoreaction in a cinnamic acid crystalline phase has been evaluated using PXRD. First of all, we demonstrate that the photoproduct obtained after irradiation could not be described using only one phase, thus, it was necessary to use a second phase (dimer) to fit the experimental data. We also checked that it was not possible to fit the data using only product phase. Two phases, reactant and product phase, were necessary to monitor the structural evolution of the system. In order to follow the evolution of the lattice parameters, we carried out a series of Le Bail refinements. The first Le Bail refinement was carried out for the original phases of β-CLCN and β-FLCN which provided us with the starting point in our calculations. The lattice parameters were labelled as $\{a_0, b_0, c_0\}$ for the starting unit cell for both compounds, whereas the lattice parameters at different stages of the photoreaction were labelled as $\{a, b, c\}$.

A feature of the results is the presence of both reactant and photoproduct peaks in the powder diffraction pattern during the reaction. The model in Figure 3.11 for the β-phase implies that if the reactant and photoproduct form a continuous solid solution after dimerization, then a single set of peak positions (which may shift as a function of conversion) is expected. Indexing of the pattern using conventional programs (ITO, TREOR, DICVOL) is extremely complicated because in some areas of the diffractogram both sets of peaks overlap and distinguishing between product and reactant peaks is difficult. For this type of solid-state reaction, we expect to observe a doubling of the lattice parameter along the direction in which

the stacking pattern of the monomer phase takes place (shortest unit cell axis). Once we had established the lattice parameters corresponding to the dimer phase, we carried out Le Bail refinements always using the previous photoproduct (i.e., from the previous value of conversion) as the starting point. With this approach, we can monitor the evolution of the lattice parameters of both reactant and product phases, and hence detect phase separations, as a function of conversion.

3.5.3.1 Solid-State Dimerization of 4-Chloro-trans-Cinnamic Acid

Single crystals of CLCN acid were irradiated for different periods of time. The maximum conversion (86.6 %) was obtained after 33 hours of reaction. The lattice parameters for the reactant phase were: $a_0 = 32.813$ Å, $b_0 = 3.890$ Å, $c_0 = 6.538$ Å; $\beta_0 = 95.94°$; $V_0 = 830.30$ Å. The space group was $P2_1/a$. Even in the early stages of the photoreaction ($\approx$10 % conversion), there is already a second phase present in the sample. Thus, in the PXRD diffractogram, there is a shoulder in the main peak ($2\theta \approx 18.5°$) that is not predicted for the starting unit cell (see Figure 3.13). Therefore, a second phase must be introduced to match this peak, indicating that phase separation occurs in the early stages of the photoreaction for CLCN acid (Figure 3.14). The unit cell used to predict the peak position corresponding to the photoproduct was: $a = 32.813$ Å, $b = 6.90$ Å, $c = 6.538$ Å; $\beta = 95.94°$; $V = 1476.96$ Å (the space group assumed for the Le Bail fit used was $P2$). Using this unit cell, we could exactly predict all the peaks due to the dimer phase. This unit cell was refined using the Le Bail method and was used as a starting unit cell for the photoproduct at the next value of conversion. In carrying out the mixtures of reactant and product phases, the reactant unit cell was refined while the product unit cell was held fixed and *vice versa*, until optimal fit was obtained. This method was applied to analyze the materials cells obtained at all stages of this solid-state photoreaction.

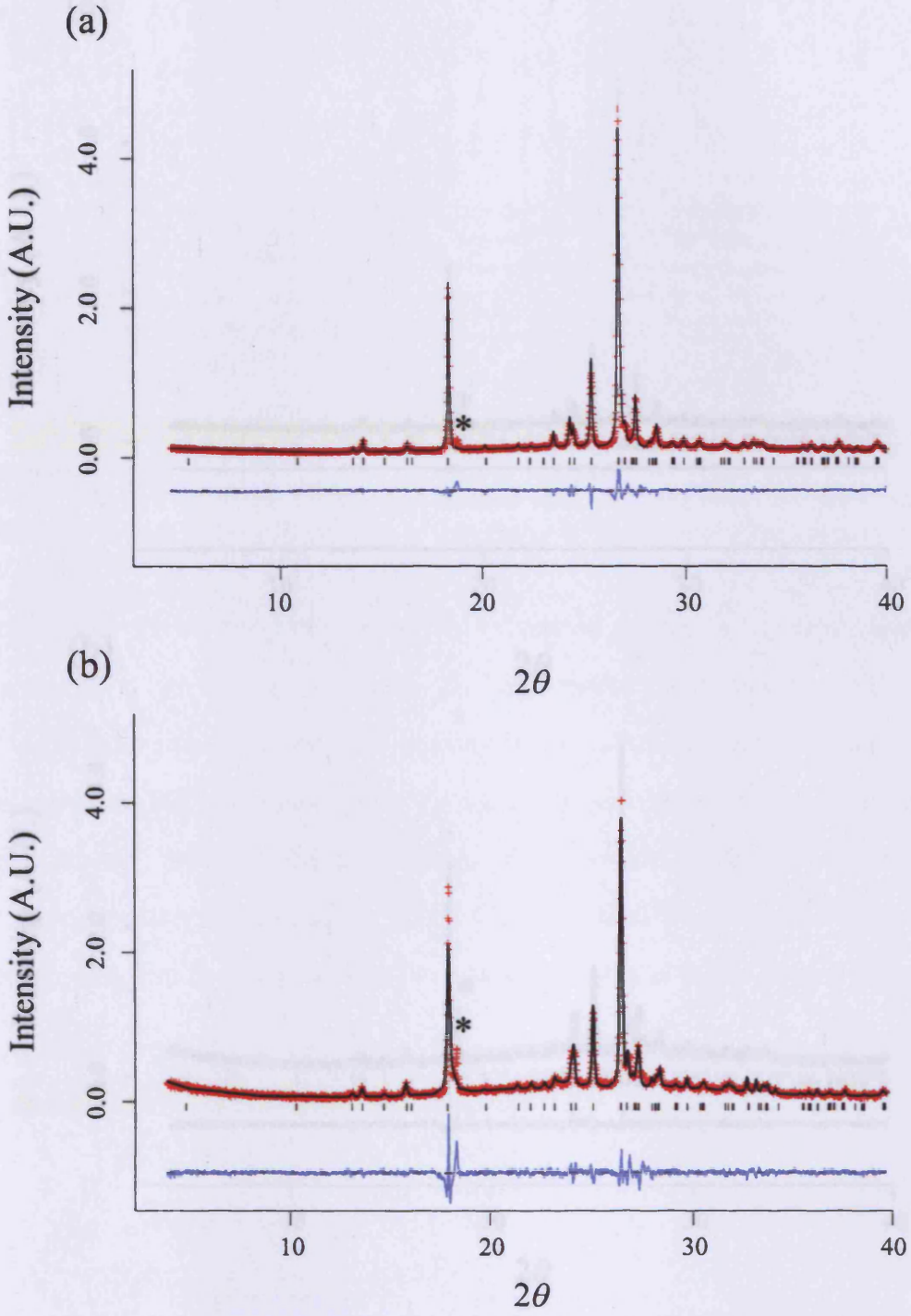

Figure 3.13. Phase separation is observed from the early stages of photoreaction. (a) At 10 % conversion, using one phase for unit cell refinement is already inadequate –a shoulder peak has appeared at $2\theta \approx 18.5°$. (b) At high conversion (26 %), the discrepancy in the difference plot (blue line) especially ~18.5° is much greater. Clearly, as shown in the difference plots, the experimental diffraction pattern cannot be fitted using only one phase.

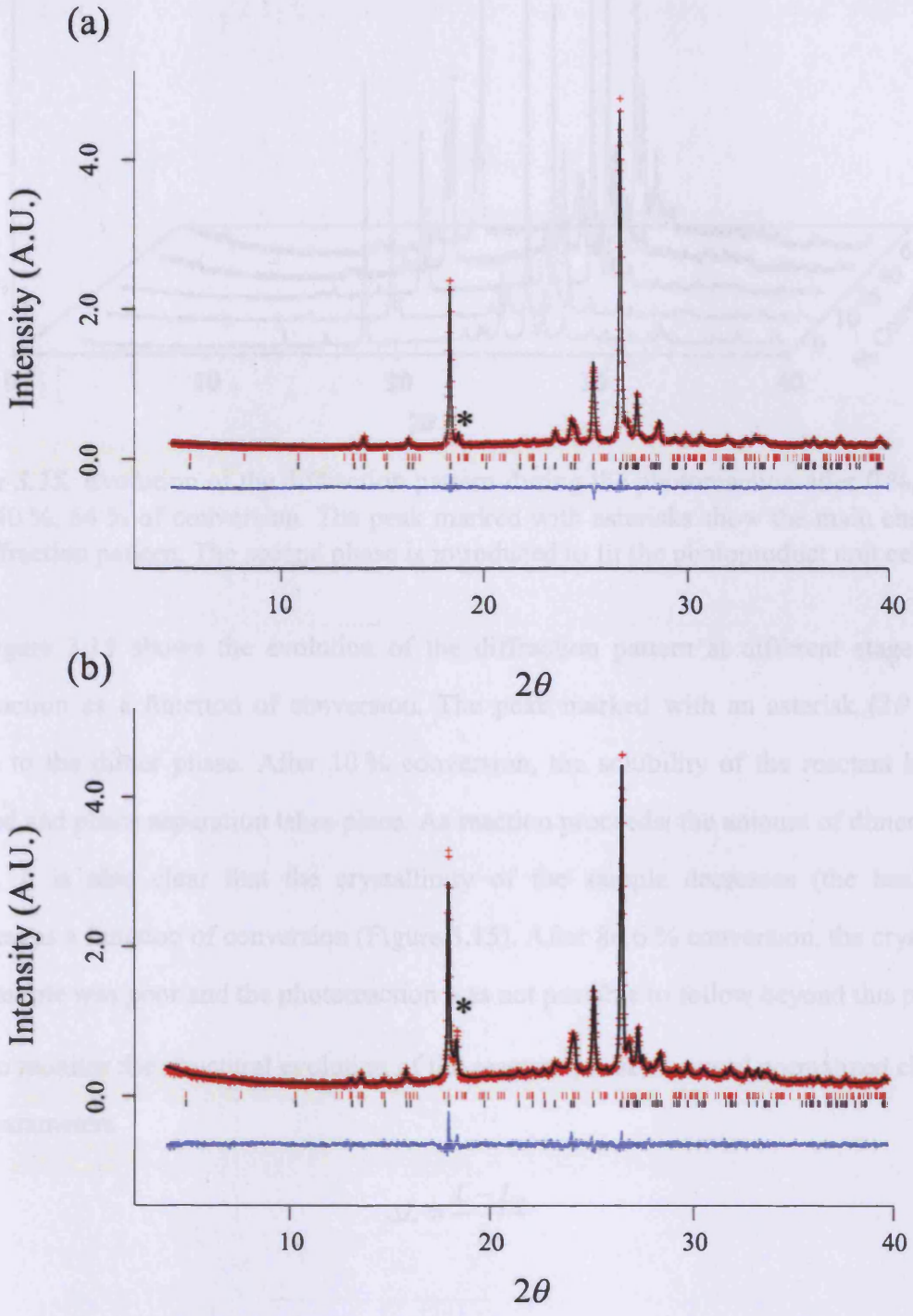

Figure 3.14. Introduction of a second phase (red tick marks) significantly improves the difference plot at both high and low conversion. (a) The unit cell refinement for reactant and product phases at 10 % conversion. (b) The unit cell refinement for reactant and product phases at 26 % conversion.

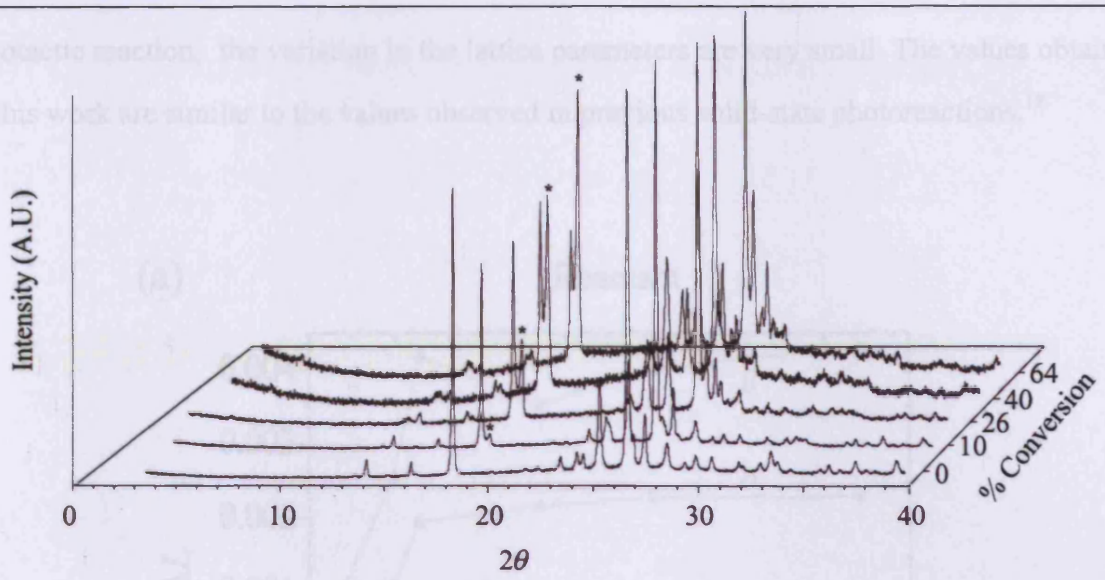

Figure 3.15. Evolution of the diffraction pattern during the photoreaction after 0 %, 10 %, 26 % 40 %, 64 % of conversion. The peak marked with asterisks show the main change in the diffraction pattern. The second phase is introduced to fit the photoproduct unit cell.

Figure 3.15 shows the evolution of the diffraction pattern at different stages of the photoreaction as a function of conversion. The peak marked with an asterisk ($2\theta = 18.5°$) belongs to the dimer phase. After 10 % conversion, the solubility of the reactant has been exceeded and phase separation takes place. As reaction proceeds, the amount of dimer is more evident. It is also clear that the crystallinity of the sample decreases (the background increases) as a function of conversion (Figure 3.15). After 86.6 % conversion, the crystallinity of the sample was poor and the photoreaction was not possible to follow beyond this point.

To monitor the structural evolution of the reactant phase, we used normalized change in lattice parameters

$$\Delta L = \frac{L - L_0}{L_0} \tag{3.1}$$

where L is the lattice parameter (a, b, c, β or V) and L_0 is the initial value. For the product phase, the lattice were obtained from a Le Bail refinement.

The absolute values of the lattice parameters are given in Tables 3.2 and 3.4, whilst the values of ΔL are given in Tables 3.3 and 3.5 and are plotted in Figure 3.16. The normalized changes in the unit cell parameters are of the order of 0.005 - 0.05. As expected for a

topotactic reaction, the variation in the lattice parameters are very small. The values obtained in this work are similar to the values observed in previous solid-state photoreactions.[18]

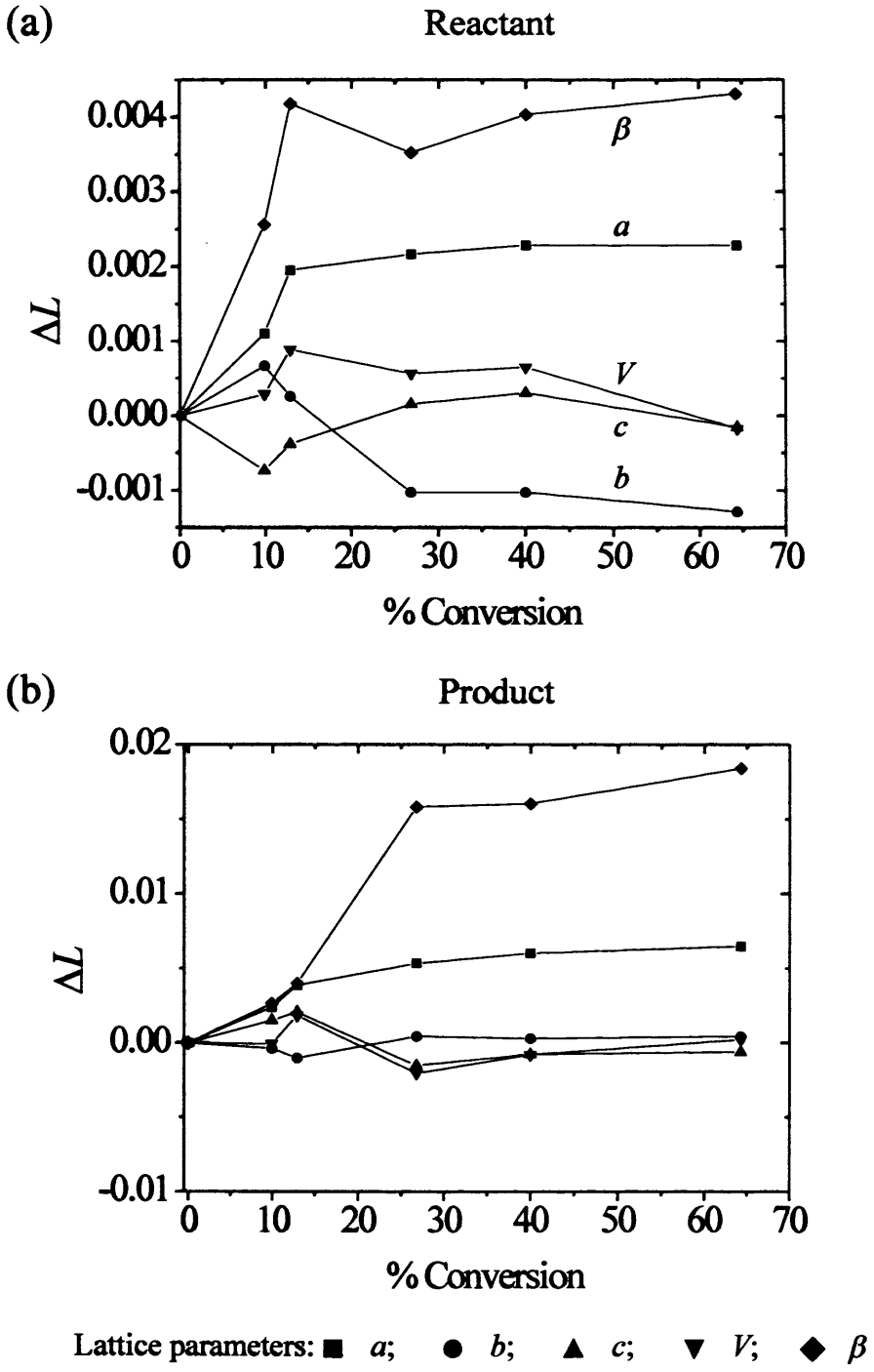

Figure 3.16. Lattice evolution for (a) reactant and (b) product phase of CLCN.

Table 3.2. Lattice parameters for the reactant phase of CLCN during conversion.

% Conversion	a (Å)	b (Å)	c (Å)	β (°)	V (Å^3)
0	32.813	3.89	6.538	95.94	830.30
10	32.8491	3.893	6.533	96.186	830.54
13	32.877	3.891	6.536	96.341	831.04
27	32.884	3.886	6.539	96.278	830.77
40	32.888	3.886	6.54	96.327	830.84
64	32.888	3.885	6.537	96.354	830.16

Table 3.3. Normalized change of lattice parameters for the reactant phase of CLCN.

% Conversion	Δa	Δb	Δc	$\Delta\beta$	ΔV
0	0	0	0	0	0
10	0.0011	0.00066	–0.00073	0.0026	0.00028
13	0.00195	0.00026	–0.00038	0.0042	0.00089
27	0.00216	–0.0010	0.00015	0.0035	0.00056
40	0.00229	–0.0010	0.00030	0.0040	0.00065
64	0.00229	–0.00129	–0.00015	0.0043	–0.00017

Table 3.4. Lattice parameters for the product phase of CLCN during conversion.

% Conversion	a (Å)	b (Å)	c (Å)	β (°)	V (Å^3)
0	32.813	6.9	6.538	95.94	1476.956
10	32.892	6.8974	6.5479	96.194	1476.85
13	32.94	6.893	6.5515	96.323	1479.677
27	32.988	6.903	6.528	97.457	1473.947
40	33.01	6.902	6.533	97.479	1475.788
64	33.026	6.903	6.534	97.707	1477.263

Table 3.5. Normalized change of lattice parameters for the product phase of CLCN.

% Conversion	Δa	Δb	Δc	$\Delta\beta$	ΔV
0	0	0	0	0	0
10	0.00241	–0.00038	0.00151	0.0265	–0.00007
13	0.00387	–0.00101	0.00206	0.0399	0.00184
27	0.00533	0.000435	–0.00153	0.01581	–0.00204
40	0.0060	0.000290	–0.00076	0.01604	–0.00079
64	0.00649	0.00437	–0.00061	0.01842	0.000208

3.5.3.2 Solid-State Dimerization of 4-Fluoro-trans-Cinnamic Acid

Single crystals of FLCN acid were irradiated for different periods of time. For this compound, the maximum conversion of 77 % was obtained after 34 hours of reaction. The initial lattice parameters for the reactant phase were: $a_0 = 31.706$ Å, $b_0 = 6.489$ Å, $c_0 = 3.878$ Å; $\beta_0 = 94.74°$ and $V_0 = 795.132$ Å. The space group was $P2_1/a$. The PXRD analysis showed that the changes in the diffraction pattern are not as evident as in the case of CLCN acid. Mainly the peaks with *hk*0 shifted towards lower 2θ values, reflecting the increase in size of the photoproduct. For FLCN, the introduction of a second phase was not required until 50% of conversion. This fact reflects that the solubility of the product in the FLCN phase is higher than that of the CLCN. The unit cell used to predict the peak position corresponding to the photoproduct was: $a_0 = 31.706$ Å, $b_0 = 6.489$ Å, $c_0 = 6.942$ Å; $\beta_0 = 95.74°$ and $V_0 = 1421.09$ Å and for the Le Bail fitting, the space group was assumed to be *P*2. Using this unit cell, we could predict exactly all the peaks that belonged to the dimer phase.

We only monitored the evolution of the lattice parameters corresponding to the reactant phase, since phase separation took place at a very advanced stage of the photoreaction. The

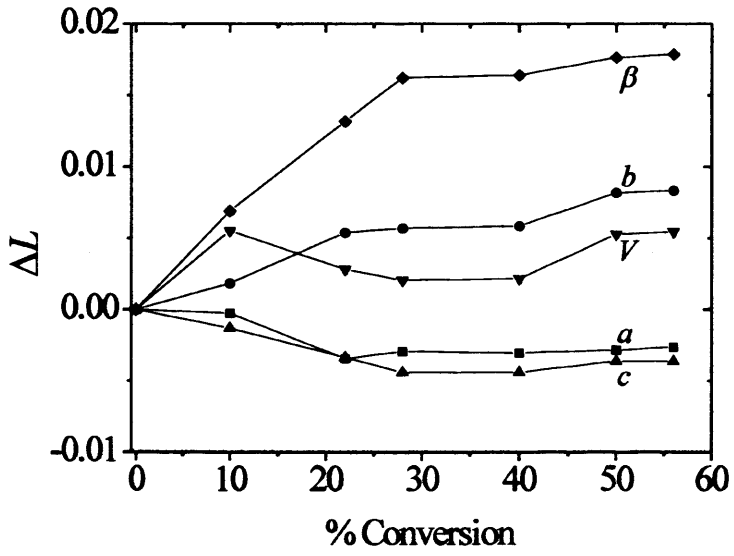

Figure 3.17. Lattice evolution for the reactant phase of FLCN.

same approach as in the CLCN case was used here to follow the lattice evolution. The variation of the lattice parameters is given in Tables 3.6 (absolute) and 3.7 (normalized) and plotted in Figure 3.17. As expected for this type of solid-state reaction, the changes in the lattice parameters are small but consistent for a topotactic reaction.

Table 3.6. Lattice parameters for the reactant phase of FLCN during conversion.

% Conversion	*a* (Å)	*b* (Å)	*c* (Å)	*β* (°)	*V* (Å^3)
0	31.706	6.489	3.878	94.742	790.061
10	31.698	6.501	3.873	95.395	794.424
22	31.597	6.524	3.865	95.991	792.285
28	31.613	6.526	3.861	96.280	791.691
40	31.610	6.527	3.861	96.297	791.773
50	31.616	6.542	3.864	96.414	794.232
56	31.623	6.543	3.864	96.434	794.345

Table 3.7. Normalized change of lattice parameters for the reactant phase of FLCN.

% Conversion	Δ*a*	Δ*b*	Δ*c*	Δ*β*	Δ*V*
0	0	0	0	0	0
10	–0.000252	0.001849	–0.001289	0.006892	0.005522
22	–0.003438	0.005394	–0.003352	0.013173	0.002815
28	–0.002933	0.00570	–0.004384	0.016234	0.002064
40	–0.003028	0.005856	–0.004384	0.016413	0.002166
50	–0.002839	0.008168	–0.003610	0.017648	0.005279
56	–0.002618	0.008322	–0.003610	0.017859	0.005422

3.5.4 Evolution of Lattice Parameters

In Figure 3.16, the evolution of lattice parameters for the reactant and product phases of CLCN acid show that the main change in the unit cell of the reactant takes place in the early stages of the photoreaction, 0-12% conversion. The lattice parameters show no significant variation in the further stages of the reaction. For the product phase, we see that between 0 and 26 % conversion, the lattice parameters of the new phase have undergone a major variation (particularly β) due to the phase separation process. After this, the product phase does not show significant changes. We interpret that after phase separation, the reactant phase does not change as there is no more solid-state reaction within the reactant unit cell. In the photoproduct case, since phase separation occurs at 12 % and it is possible to observe changes in the lattice parameters until 26 %. In the early stages of the reaction (i.e., from 12 % to 26 %) is where the main changes are observed due to the dimerization involving the doubling of the shortest unit cell axis (stacking pattern direction). After 26 % of conversion the product phase does not change significantly since the main change in the lattice parameters has already been carried out.

Figure 3.17 shows the evolution of lattice parameters for FLCN as a function of conversion. Interestingly, in this case the reactant phase seems to accommodate the photoproduct within the reactant unit cell better than the case of CLCN acid. Phase separation was observed only after 50 % conversion and, as observed in Figure 3.17, the lattice parameters are stable after approximately 30% conversion. The solubility of the photoproduct phase in the reactant crystal is clearly higher for FLCN than for CLCN.

3.6 Conclusions

The topochemical principle states that reaction in the solid state occurs with a minimum amount of atomic or molecular movement. This implies that a certain amount of motion of various atoms in the crystal is tolerable. In cinnamic acids, the double bonds in the crystal do not stack precisely on top of each other.[21] We understand the variation of the lattice parameters, some structural reorganization is required to accommodate the product mixture reactant crystal. Even under ideal conditions, movement of double bonds towards each other is essential for dimerization to take place. The criterion of less than 4.2 Å of separation

implicitly assumes that such a motion can be accommodated in the crystal. Using PXRD we have successfully determined the crystal structure of the β-phase 4-fluoro-*trans*-cinnamic acid. This structure conforms to that of other β-phase of cinnamic acids with a short repeat distance of 3.878 Å. Therefore, it was an ideal sample to be used in the study of its physical properties under UV light.

In this experiment we have observed how the lattice parameters for both CLCN and FCNA acids vary between 0.004-0.02 Å during the photodimerization reaction. Such variation can be explained on the grounds of structural reorganization required for the reaction to occur and to accommodate product molecules within the monomer crystal, at least up to the solubility limit. We observed that this small variation is consistent with this type of process which appears to be very similar to other photoreactions studied previously. As far as we know, this process has not been analyzed previously using PXRD technique. Using PXRD we can study solid-state photoreactions even if the reaction proceeds in a single-crystal to polycrystalline manner with the possibility to study systems that are not possible to investigate by single crystal X-ray diffraction.

Unfortunately we did not succeed in obtaining the crystal structure corresponding to the pure product phase using PXRD. The presence of two phases in the photoproduct represents a hindrance to structure determination. Therefore, we cannot know the final molecular arrangement of the photoproduct. Recrystallization of the product phase from solution can provide one way to determine the structure of the dimer phase, although the recrystallized phase could be a different polymorph from that obtained directly by the solid state reaction. Further experiments geared towards a better understanding of the product phase as well as crystal structure solution, will enable us to elucidate the reactivity of molecular crystals under UV light. Solid state chemistry in crystalline organic materials provides a promise for materials applications, for carrying out selective synthetic transformations and for use as tool in studying fundamental aspects of organic reactivity. A better knowledge on phase-separation mechanisms and how microscopic reactivity is related to macroscopic phase changes is an important objective to fully exploit the potential of organic solid-state chemistry.

References for Chapter 3

[1] P. Tundo, P. Anastas, D. C. Black, J. Breen, T. Collins, S. Memoli, J. Miyamoto, M. Polyakof and W. Timas, *Pure Appl. Chem.*, **2000**, *72*, 1207.

[2] H. D. Roth, *Angew. Chem. Int. Ed. Engl.*, **1989**, *28*, 1193.

[3] C. Ramamurthy and K. Vankatesan, *Chem. Rev.*, **1987**, *87*, 433.

[4] J. R. Scheffer, M. Garcia-Garibay and O. Nalamasu, *Org. Photochem.*, **1989**, *8*, 249.

[5] M .D. Cohen, G. M. J. Schmidt and F. I. Sonntag, *J. Chem. Soc.*, **1964**, 2000.

[6] W. H. Kohlshutter, *Anorg. Allg. Chem.*, **1918**, *105*, 121.

[7] J. D. Dunitz, *Pure Appl. Chem.*, **1991**, *63*, 177.

[8] M. R. Caira, *Top. Curr. Chem.*, **1998**, *198*, 164.

[9] J. Bernstein, R. J. Davey and J.–O. Henck, *Angew. Chimie, Int. Ed.*, **1999**, *38*, 3441.

[10] G. Kaupp, *Angew. Chem. Int. Ed. Engl.*, **1992**, 31, 592.

[11] M. Gosh, T. K. Mandal and S. Chakrabarti, *J. Raman Spectrosc.*, **1998**, *29*, 807.

[12] M. Gosh, S. Chakrabarti and T. N. Misra, *J. Phys. Chem. Solids,*, **1996**, *57*, 1891.

[13] S. Chakrabarti, A. K. Maity and T. N. Misra, *J. Polymer Sci. Part A*, **1992**, *30*, 1625.

[14] S. D. M. Allen, M. J. Almond, J. L. Bruneel, A. Gilbert, P. Hollins and J. Mascetti., *Spectroch. Acta Part A*, **2000**, *56*, 2423.

[15] H. Hosomi, Y. Ito and S. Ohba, *Acta Crystallogr.*, **2000**, *5*, 224.

[16] V. Enkelmann, G. Wegner, K. Novak and K. B. Wegener, *J. Am. Chem. Soc.*, **1994**, *115*, 10390.

[17] G. Wegner, *Pure Appl. Chem.*, **1977**, *49*, 443.

[18] S. Ohba and Y. Ito, *Acta Crystallogr B*, **2003**, *59*, 149.

[19] Y. Ohashi, *Acta Crystallogr A*, **1998**, *54*, 842.

[20] G. S. Pawley, *J. Appl. Crystallogr.*, **1981**, *14*, 357.

[21] J. P. Glusker, D. E. Zacharias and H. L. Carrell., *J. Chem. Soc.Perkin II*, **1975**, *65*. 68.

[22] K. D. M. Harris, J. M. Thomas and D. W. Williams., *J. Chem. Soc.Faraday Trans.*, **1991**, *87*, 325.

Chapter 4 Exploring Molecular Transport Processes in Solid Organic Tunnel Structures

4.1 Introduction

In this chapter, the molecular transport of linear molecules (alkanes) along one-dimensional channels is presented. The material is based on an incommensurate urea inclusion compound, in which guest molecules are contained within a system of parallel, one-dimensional channels in a crystalline urea host structure. It has been demonstrated previously that exchange of guest molecules in one direction along the urea channel system can occur by inserting new guest molecules at one end of the crystal (by putting in contact with the liquid of another potential guest), with the original guest molecules expelled from the other end of the crystal. To understand details of the transport process in this system, it is essential to understand the spatial distribution of the two types of guest molecule within the crystal and the variation of the spatial distribution of the two types of guest molecule as a function of time during the transport process. This molecular transport is studied *in situ* in this chapter using confocal Raman microspectrometry, yielding information on the spatial distribution of guest molecules, including its time dependence.

4.2 Molecular Transport in Incommensurate Solids

Many important processes, including several of biological[1,2], industrial[3], and nanotechnological[4,5] interest, rely upon the transport of molecules or ions through channel systems. Although details of the transport process clearly differ from one system to another, well defined model systems have an important role to play in furnishing a general fundamental understanding of such processes. In this regard, the design of a molecular-scale capillary, capable of selective molecular transport process, was demonstrated.[6] The material is based on an incommensurate inclusion compound, in which guest molecules are contained within a system of one dimensional channels (diameter ca. 5.5 Å) in a crystalline urea host structure.[7-9]

4.2.1 Basic Properties of Incommensurate Solids

In a conventional crystal, atoms or molecules are arranged in a periodic manner throughout a macroscopic region of three-dimensional space, with the translational symmetry characterised by three non-coplanar lattice vectors $\{a, b, c\}$. If a crystal requires more than three lattice vectors to define its structural periodicity, the crystal is described as "aperiodic". To describe an incommensurate intergrowth material, it is necessary to define two basic structures, each with three dimensional periodicity and characterized by the sets of lattice vectors $\{a, b, c_1\}$ and $\{a, b, c_2\}$. Incommensurate, intergrowth structures are a class of aperiodic crystals[10-13] and comprise at least two interpenetrating substructures with the property that, along at least one direction, the two substructures have different repeat distances. In the simplest case, the c_1 and c_2 vectors are parallel and the ratio $|c_1|/|c_2|$ is not equal to a low-denominator rational number. This is the case studied here. Conversely, if this ratio is equal to a low-denominator rational number, the composite system can be described by a single repeat distance. As a result of the interactions between the two systems, each substructure has a periodic modulation, the periodicity of which is the same as the periodicity of the other basic structure. Therefore, substructure 1 has an incommensurate modulation with period c_2 and substructure 2 has an incommensurate modulation with period c_1. A substructure is based on a basic structure and a modulation. In terms of dimensionality, four lattice vectors a, b, c_1 and c_2 are required to define the translational symmetry of the complete incommensurate system (Figure 4.1).

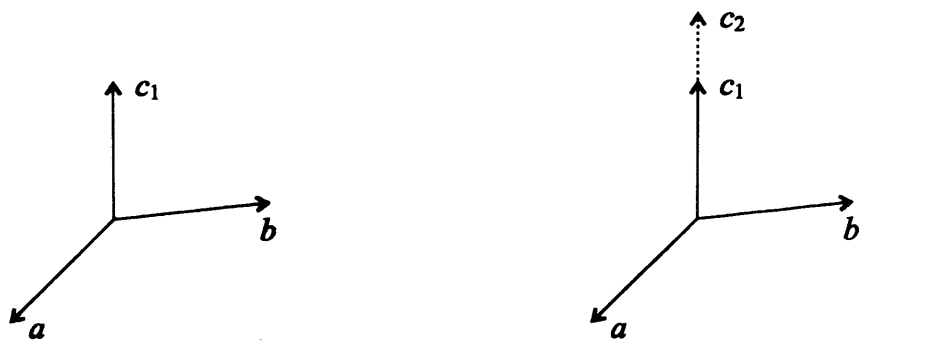

Periodic Crystal (a, b, c_1) **Aperiodic Crystal (a, b, c_1, c_2)**

(a) **(b)**

Figure 4.1. Schematic representation of the lattice vectors in a periodic crystal (a) and for the case of an aperiodic crystal (b).

Conventional urea inclusion compounds[7-9] are a well known family of incommensurate intergrowth materials. In these solids, long-chain alkane or substituted alkane guest molecules are arranged within one-dimensional host tunnels, formed by a helical hydrogen-bonded network of urea molecules (Figure 4.2). The tunnels run the length of the crystal (along the *c*-axis). There is an incommensurate relationship between the periodicities (c_h and c_g respectively) of the basic host structure and the basic guest structure along the tunnel direction.

Incommensurate intergrowth materials, can also be classified by considering the fluctuation in energy associated with translating one substructure relative to the other substructure.[14,15] We consider the magnitude of variations in the average host-guest interaction energy per guest molecule as the guest substructure (with fixed c_g) is translated along the one-dimensional host tunnel structure. If the variations are sufficiently small, the inclusion compound can be classified as an incommensurate material. If the variation in the average host-guest interaction energy is significant, an energetic "lock in" will occur for a specific position of the guest substructure relative to the host substructure. For the incommensurate case, on the other hand, the energy of the inclusion compound is essentially independent of the position of the guest substructure relative to the host substructure, giving rise to the concept of *activationless translation* of the guest substructure along the host tunnel.

Figure 4.2. View along the tunnel axis of a single urea channel filled with one alkane guest molecule with an arbitrary orientation. The diameter of the tunnel is about 5.5 Å. Colour code: carbon-grey; hydrogen-white; oxygen-red; nitrogen-blue.

Interestingly, for an incommensurate system, the fluctuation in the host-guest interaction energy for a single guest molecule translated along the host tunnel can be significant, even though the fluctuation in the average host-guest interaction energy for the complete set of guest molecules is negligible.

4.2.2 Exchange of Guest Molecules

Solid inclusion compounds can be classified depending on the stability of the host structure upon removal of the guest molecules. Hard hosts are stable after the guest molecules are removed from the tunnels. Zeolites are an example of hard inclusion compounds which are often used in applications involving exchange of guest molecules. Soft host are those structures that collapse after guest molecules are removed from the inclusion cavity. Usually, the host recrystallizes to form a more compact and denser structure that does not contain cavities. Thus, for soft hosts, the guest component generally acts as an essential template for the formation of the host structure as well as an essential buttress for maintaining the stability of the host structure; the collapse of the host structure on removal of the guest component is often an irreversible process. In urea inclusion compounds, the urea host structure is unstable in the absence of guest molecules and if the guest molecules are removed, the tunnels collapse and re-crystallize as the crystal structure of pure urea (which does not contain empty tunnels). The fact that the empty urea tunnel structure is unstable limits the scope for applications based on urea inclusion compounds. For example, applications such as those exploited for microporous inorganic hosts[16,17] involving diffusion of guest molecules into, within and out of the empty host structure are not feasible.

However, it has been shown[6] that, for soft hosts such as urea inclusion compounds, exchange of the "original" guest molecules (G_1) can be carried out by inserting "new" guest molecules (G_2) at one end of the tunnel and expelling the original guest at the other end of the tunnel, providing that the structure remains filled throughout the transport process. Figure 4.3 shows how the exchange of guest molecules can be carried out by putting a urea inclusion compound containing "original" guest molecules in contact with an environment containing a potential "new" guest molecule (liquid). After some time, the "new" guest molecules will replace the "original" molecules that will be extruded at the other end of the tunnels. The

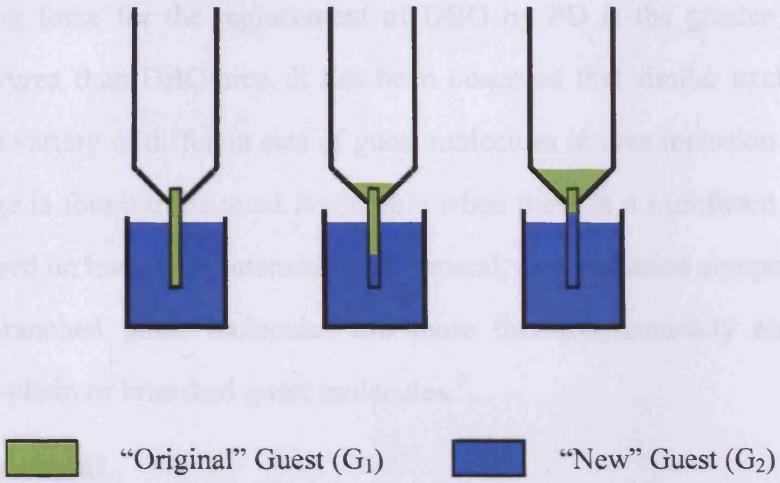

Figure 4.3. Schematic representation of molecular exchange by dipping a single crystal into a liquid containing potential new guest molecules.

efficacy of this exchange process should depend on properties of both the inclusion compound and the external environment. The most important property of the internal environment should be the relative affinity of the host structure for the two guest molecules, which depends mainly on host-guest interactions. The most important property of the external environment should be the chemical potentials of the guest molecules, the surface properties of the crystal at the ends of the tunnels and the differences in the chemical potentials at the two ends of the crystal.

While the occurrence of this transport process was demonstrated[6] on the basis of visual observation, chemical analysis and X-ray diffraction, these previous studies did not investigate the spatial distribution of the two types of guest molecules within the crystal nor its variation as a function of time. To address these issues, the present work demonstrates that confocal Raman microspectrometry[18] can be used successfully as an *in situ* probe of the molecular transport process, yielding information on the spatial distribution of guest molecules and its time dependence. Although several different combinations of guest molecules are of interest, the focus here is on the system in which the "original" and "new" guest molecules are 1,8-dibromooctane (DBO) and pentadecane (PD), respectively, as the C–Br stretching vibration can be used to assess the relative amounts of DBO and PD guest molecules in different regions of the urea inclusion compound single crystal and this can be studied in a spatially resolved and time-resolved manner during the transport process within the channel system.

The driving force for the replacement of DBO by PD is the greater thermodynamic stability for PD/urea than DBO/urea. It has been observed that similar exchange processes occur for a wide variety of different sets of guest molecules in urea inclusion compounds and that the exchange is found to be most favourable when there is a significant thermodynamic driving force based on host guest interaction. In general, urea inclusion compounds containing long-chain, unbranched guest molecules are more thermodynamically stable than those containing short-chain or branched guest molecules.[9]

4.3 Experimental

Single crystals of the DBO/urea inclusion compound were prepared using standard procedures. An excess amount of the guest species (excess with respect to the expected molar guest/host ratio in the inclusion compound) was added to a saturated solution of urea in methanol at 50°C. On obtaining a homogeneous solution, it was cooled slowly (for 120 hours) to 20°C. Experiments were performed using a Labram II spectrometer (Jobin-Yvon), an Ar/Kr 2018 Spectra-Physics laser (514.5 nm) and a grating of 1800 lines/mm (spectral resolution $\sim 6\ cm^{-1}$). The laser was focused on the sample through a microscope (50× Olympus objective) of 0.55 numerical aperture and the diameter of the confocal pinhole was 700 μm. The radial and axial resolutions were 10 μm and 50 μm, respectively.

Single crystal X-ray diffraction was performed using graphite-monochromated Cu-Kα radiation ($\lambda = 1.54178$ Å) on a Bruker SMART diffractometer equipped with a CCD area detector. Differential scanning calorimetric (DSC) data were recorded for all samples on a TA differential scanning calorimeter.

The laboratory reference frame in our Raman experiments is defined in Figure 4.4, with the Z axis collinear to the direction of the incident laser beam. The direction of polarization of the incident laser beam defines the X axis. The scattered light was collected in the same direction as the incident light (backscattering geometry) and was analyzed through a polarizer along the X direction. A single crystal of DBO/urea was attached (using septum and Araldite as a sealant) to a reservoir containing liquid PD (Figure 4.4). The long axis (tunnel direction) of the needle-shaped crystal was aligned parallel to the X axis of the reference frame and polarized spectra ($(Z(XX)\bar{Z}$ in Porto notation[19]) were recorded.

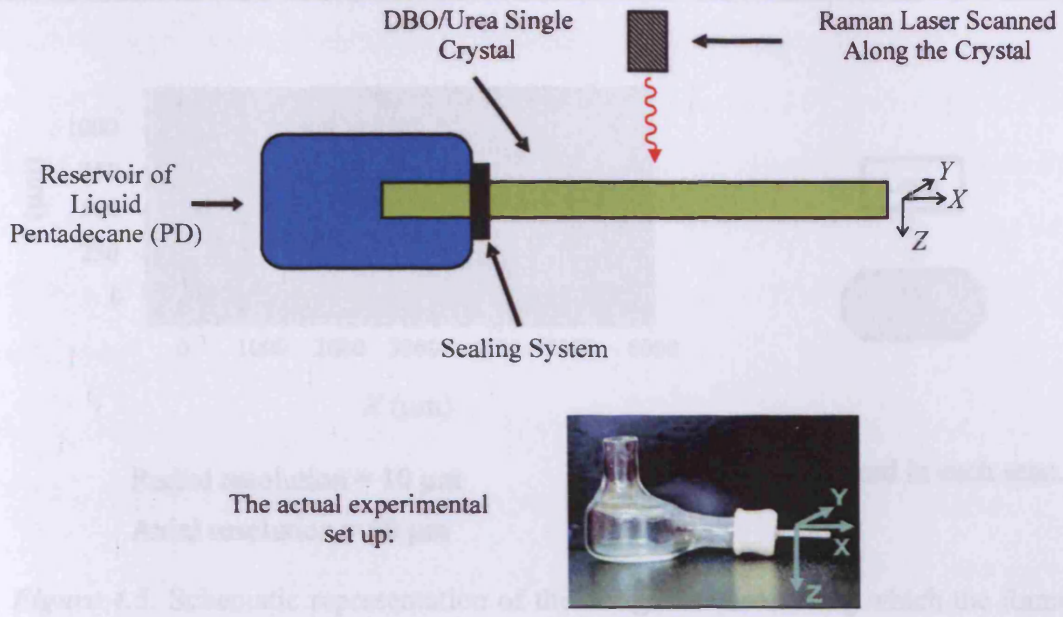

Figure 4.4. Schematic diagram of the experimental assembly, comprising the DBO/urea inclusion compound crystal and reservoir containing liquid PD.

The DBO/urea single crystal and reservoir of liquid PD were mounted on an *X,Y*-motorized microscope table (the (100) face of the crystal was aligned parallel to the *XY* plane). Increasing positive values of *X* correspond to the direction of transport of PD. Spectra were recorded by scanning a rectangular slice of length 5200 μm (along *X*) by width 600 μm (along *Y*) (Figure 4.5) at a fixed depth of 175 μm below the top surface of the crystal (along *Z*). The time to record the entire Raman image of the probed area was about 28 min.

To perform these molecular transport experiments, we established a protocol to ensure that the set up was correct during the whole process (usually around 3 days). First of all, urea inclusion compound single crystals were analyzed by optical microscopy. Those single crystals of highest quality were selected to perform the experiment. Secondly, the integrity of the UIC was analyzed using confocal Raman microspectrometry (CRM). Focusing on the spectral region 950 cm^{-1} - 1050 cm^{-1}, allowing an assessment of whether the urea inclusion compound had recrystallized to pure urea (see next section) or if it still had the pure urea inclusion compound structure.

Following this assessment, a digitized picture of the crystal was recorded to determine the crystal dimensions. The next step was to attach the crystal to the reservoir containing liquid PD. The reservoir was glued to a circular plate which was screwed to a goniometer.

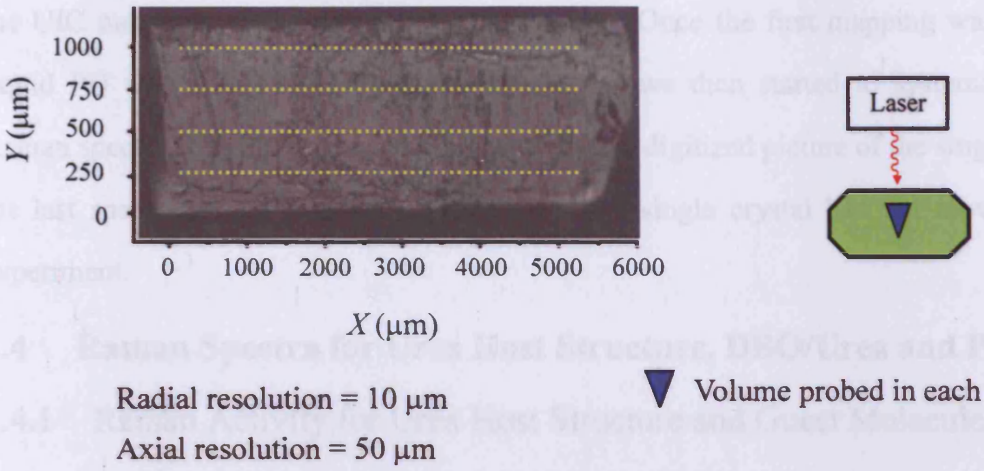

Figure 4.5. Schematic representation of the designated area along which the Raman scans were carried out. Each confocal Raman microspectrometry is probing a small volume of single crystal (bulk of sample).

The UIC crystal was then attached to the reservoir. Special attention was taken to confirm that the single crystal was horizontal. In the case that further alignment was required, it was performed using the goniometer. Once the single crystal was attached to the reservoir, the goniometer with the single crystal-reservoir set up was mounted on the motorized microscope table. The long axis (tunnel direction) of the needle-shaped crystal was aligned along the *X* axis of the laboratory reference frame. The ratio *R* (defined in Section 4.4.3) was used to assess any misalignment of the crystal. A well aligned crystal gave a ratio $R = 0.35$. Values of *R* less than 0.35 were considered as an indicator of misaligned crystals. This arises from the fact that the laser was polarized along the *X* direction of our reference frame. Since the guest molecules are confined within the urea tunnel, which is oriented along the *X* direction of the reference frame, the C–Br stretching vibration of the DBO has a significant component along the *X* direction, and any misalignment of the crystal can be detected by a decrease of the value of *R*. Once the crystal was well aligned, we recorded a second picture of the single crystal which was compared to a third and last picture once the experiment was finished. This is an important check that indicates if the alignment changed during the experiment.

The next step was to define the area, depth and time required to record each spectrum. The time needed for each spectrum was dictated by the quality of the single crystal. After the dimensions and time were set up, a first mapping was recorded. This first mapping contains

the information which is necessary to determine the relative amount of guest molecules within the UIC once the molecular transport has started. Once the first mapping was finished, the liquid PD was introduced into the reservoir and we then started to systematically record Raman spectra. The last step was to record the third digitized picture of the single crystal after the last spectrum was recorded to check that the single crystal had not moved during the experiment.

4.4 Raman Spectra for Urea Host Structure, DBO/Urea and PD/Urea

4.4.1 Raman Activity for Urea Host Structure and Guest Molecules

In the Raman spectra, bands due to urea modes are sharp and most modes due to the guest molecules are also easily observable. Earlier studies[20-22] showed that only a few spectral regions, such as 2750 cm^{-1} - 3000 cm^{-1} (C–H stretching modes) and 1300 cm^{-1} - 1500 cm^{-1} (CH_2 and CH_3 bending modes) can be used to observe specific modes due to alkane guest molecules. For α,ω-dibromoalkane guest molecules, the C–Br stretching modes for the conformations with trans and gauche end-groups have different characteristic frequencies in the 300 – 1000 cm^{-1} region of the Raman spectrum.[23] In all cases, the vibrations of the guest molecules give rise to bands that are weaker that those for the urea modes. Raman microspectrometry is thus an appropriate technique for studying in detail the spatial distribution of guest molecules in UICs.

4.4.2 Spectral Region for Monitoring *In Situ* the Molecular Transport Process

In the Raman spectrum, some urea internal vibrations are characteristic of UICs[24]. In the range 950 cm^{-1} - 1050 cm^{-1}, there is a very strong band at 1025 cm^{-1} at room temperature due to the symmetric C–N stretching vibration. This C–N stretching band shifts to higher wavenumber as temperature is decreased. For the pure tetragonal phase of urea, this vibration occurs at 1010 cm^{-1}. The C–N stretching mode at 1025 cm^{-1} is therefore a reliable test of the phase purity of UICs. Likewise, in the 500 cm^{-1} - 650 cm^{-1} spectral window, two bands at 533 cm^{-1} and 610 cm^{-1} are observed in the spectra of UICs and are attributed to the N–C=O deformation mode. Concerning other spectral regions, the 3100 cm^{-1} - 3500 cm^{-1} range contains the N–H stretching modes, and the 20 cm^{-1} - 200 cm^{-1} range contains the urea lattice modes. These modes can also be used to distinguish pure urea and UICs, although

these spectral regions are not discussed further. Further details concerning modes characteristic of the urea molecules in conventional UICs may be found elsewhere.[25-27]

Polarized Raman spectra of α,ω-dibromoalkane/urea and alkane/urea inclusion compounds studied previously[28,29] allow us to establish the Raman peaks that are useful for monitoring the transport process. Figure 4.6 shows the Raman spectrum of the DBO/urea inclusion compound measured at room temperature. The C–Br stretching vibration ν(CBr) of DBO (which mainly adopts the all-trans conformation within the urea channel) gives an intense $(Z(XX)\bar{Z})$ polarized peak at about 620 cm^{-1}. Figure 4.7 shows the Raman spectrum of the PD/urea inclusion compound, measured at room temperature. From Figure 4.7 it is possible to distinguish the methyl rocking vibration $r(CH_3)$ for the all-trans PD which is at 900 cm^{-1}.

4.4.3 Ratio of Integrated Intensities

The Raman bands of the urea host structure are identical for both the DBO/urea and PD/urea inclusion compounds (the average urea host structures in the DBO/urea and PD/urea inclusion compounds are essentially identical at ambient temperature (see Figures 4.6 and 4.7)). In particular, the symmetric C–N stretching vibration ν_s(CN) of urea gives a very intense $(Z(XX)\bar{Z})$ polarized Raman band at 1024 cm^{-1}. Thus, variation in the amount of DBO guest molecules in a single crystal can be probed by measuring the ratio $R = I(\text{CBr})/I(\text{CN})$ of the integrated intensities (denoted I(CBr) and I(CN), respectively) of the ν(CBr) and ν_s(CN) Raman bands. In this way, the transport process may be evaluated by measuring R as a function of position in the crystal. For a single crystal of DBO/urea, the ratio R is about 0.35. This value is therefore used to determine the alignment of the crystal (Section 4.3). In practice, we used the normalized ratio $R_N = R/R_0$, where R_0 is the value of R (averaged over the probed area) for the original crystal of DBO/urea (before starting the transport process). Thus, $R_N = 1$ if the inclusion compound contains only DBO guest molecules, and $R_N = 0$ if it contains only PD guest molecules. The value of R_N, measured as a function of position therefore allows the spatial distribution of the two types of guest molecules (DBO and PD) to be assessed.

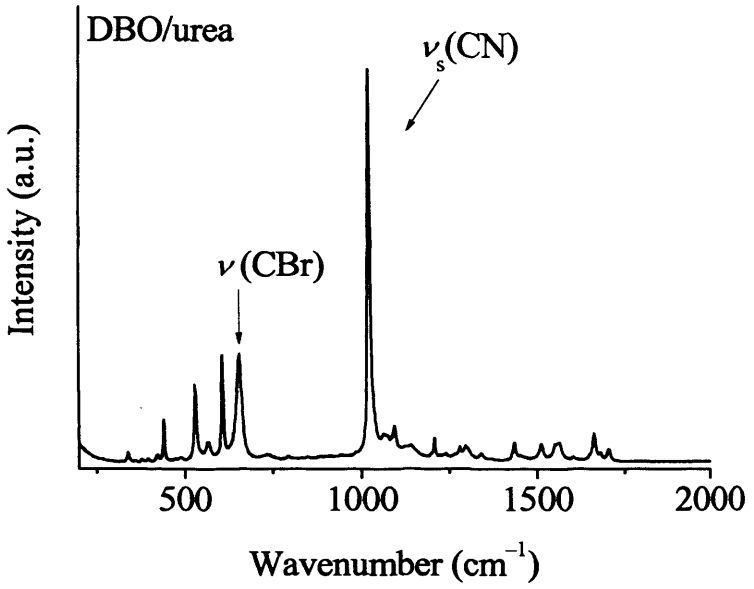

Figure 4.6. Raman spectrum for the DBO/urea inclusion compound in the 200 cm^{-1} - 2000 cm^{-1} region.

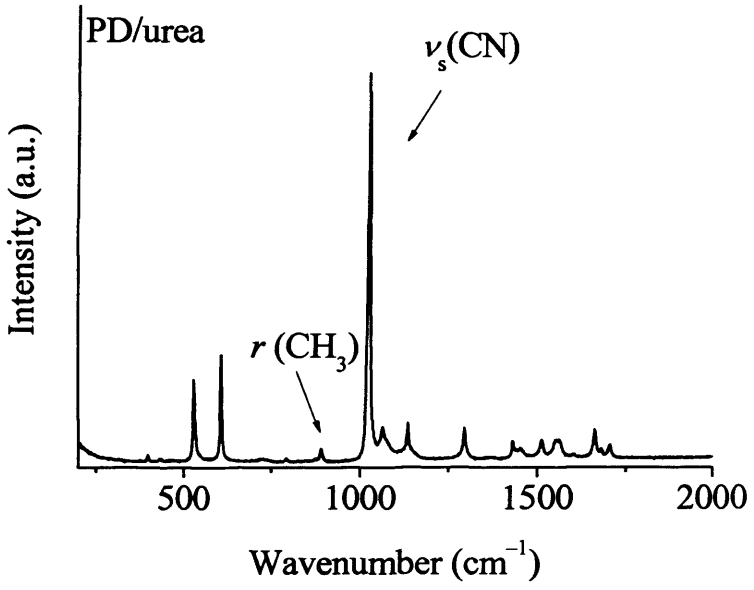

Figure 4.7. Raman spectrum for the PD/urea inclusion compound in the 200 cm^{-1} - 2000 cm^{-1} region.

4.5 Results

The occurrence of molecular transport inside the UIC is clearly evident from Figure 4.8, which shows the probed area at 18, 29 and 40 h, after commencing the transport process (i.e., after one end of the crystal had been put in contact with liquid PD). At 18 h, it is clear (from consideration of the $r(CH_3)$ and ν(CBr) modes) that both DBO and PD are present near the end of the crystal in contact with liquid PD ($R_N \approx 0.3$), whereas only DBO guest molecules are present at the other end of the crystal ($R_N \approx 1$). At 40 h, the results show that PD guest molecules are present over the full length of the crystal. Interestingly, this experiment (including studies over longer periods of time than those explained above) suggest that complete exchange does not occur and the ratio R_N typically does not fall below 0.1 even for long periods of time. Thus, a proportion of the original DBO guest molecules are unable to take part in the exchange process and it is reasonable to propose that transport in some channels may be impeded as a result of structural defects.

To assess the variation in the spatial distribution of the guest molecules as a function of time, we consider one-dimensional scans (along X) through each of the images shown in Figure 4.8 (with the scan taken at the same fixed Y value in each case). For each of these scans, the value of R_N is plotted as a function of X in Figure 4.9. An approximately sigmoidal distribution is observed and at the earlier stages of the process (18 h), there is a comparatively narrow boundary region (with width of the order of 1000 μm) between the DBO-rich ($R_N \approx 1$) and PD-rich ($R_N \approx 0.3$) regions of the crystal.

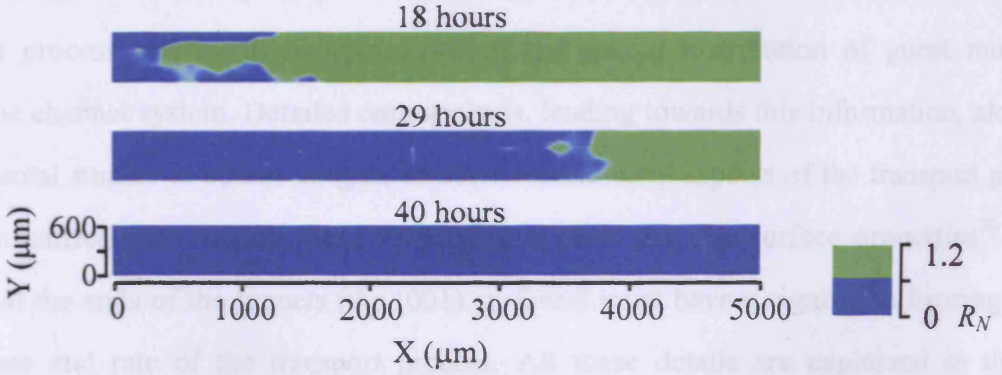

Figure 4.8. Raman spectra recorded during the transport process at different times after the commencement of the transport process (green: DBO-rich regions, $R_N \geq 0.5$; blue: PD-rich regions, $R_N < 0.5$).

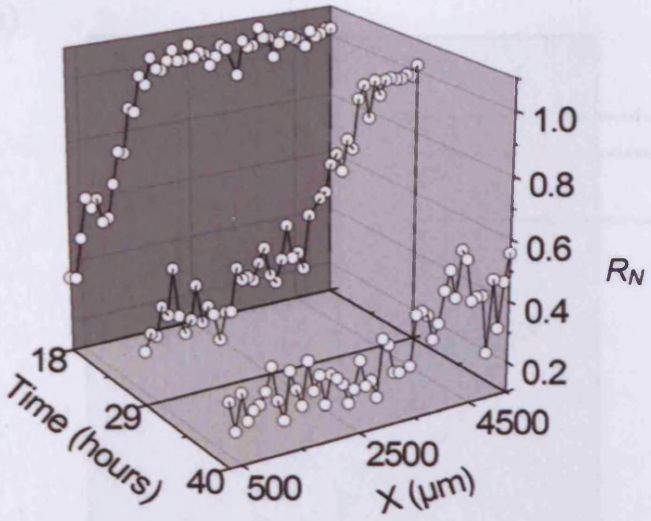

Figure 4.9. Plots of R_N as a function of position X along the channel direction at different times after the commencement of the transport process. The same fixed value Y value was used for each scan.

Interestingly, the Raman bands assigned to the urea host structure remain unchanged throughout the period of time investigated, suggesting that the urea host structure is not significantly affected by the transport process. In the course of the present work, we have also carried out single crystal X-ray diffraction measurements, which confirm the previous results.[6] From these studies, it is clear that the exchange process is not associated with any loss of integrity of the urea inclusion compound single crystal (only a slight increase in the mosaicity of the crystal during the exchange process is evident from Figure 4.10). As time progresses, translation of the centroid of the distribution along the crystal and spreading of the boundary region are evident. It is clear that such data, recorded as a function of both position within the crystal and time, can give access to quantitative information on the kinetics of the transport process and the time-dependence of the spatial distribution of guest molecules within the channel system. Detailed data analysis, leading towards this information, alongside experimental studies to obtain insights of other fundamental aspects of the transport process, has been carried out. Among these aspects, it is clear that the surface properties[30] of the crystals at the ends of the tunnels (the (001) surfaces) must have a significant bearing on the occurrence and rate of the transport process. All these details are explained in the next chapter.

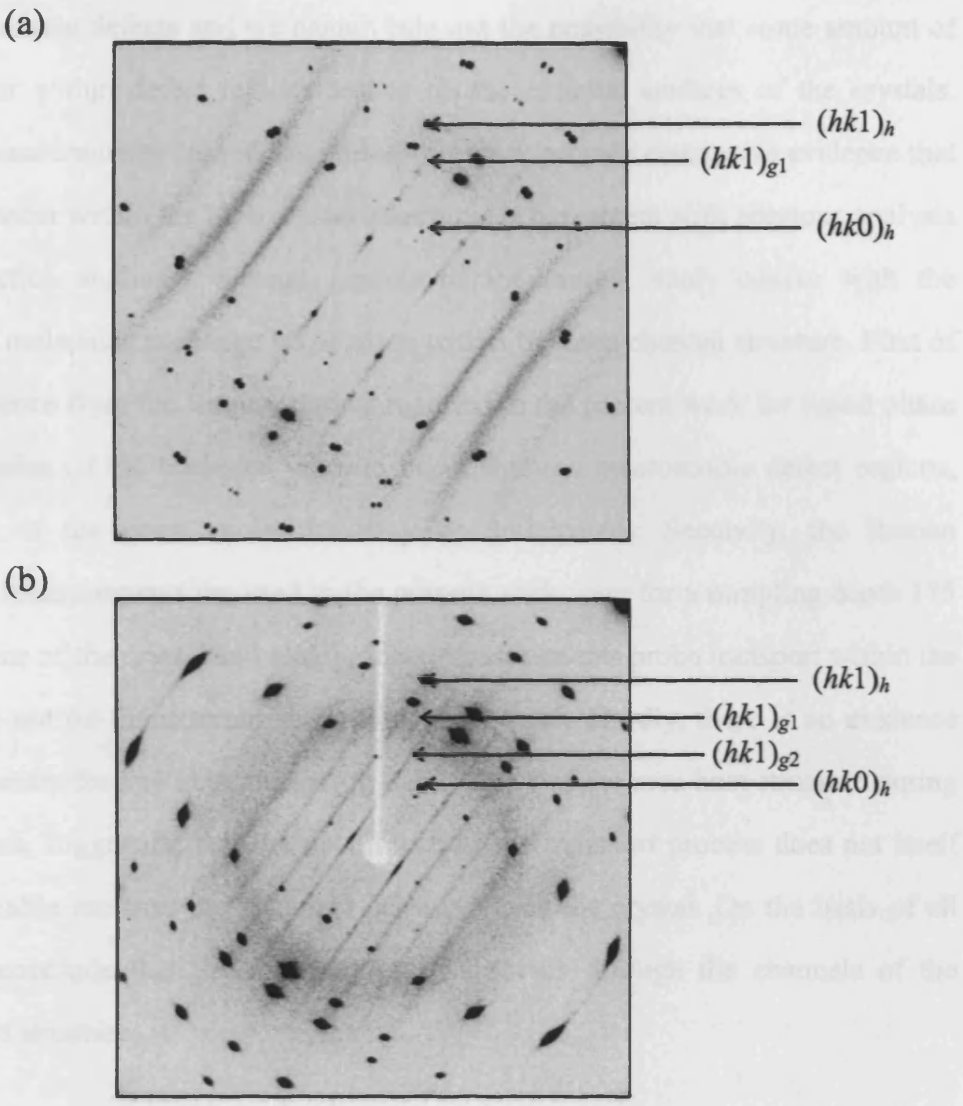

Figure 4.10. Single crystal X-ray diffraction oscillation photographs recorded at ambient temperature for DBO/urea inclusion compound crystal: (a) before the molecular exchange; (b) the same crystal after the exchange experiment. The spots corresponding to the host structure have become towards an elliptical shape due to the mosaicity. Layer lines arising from the guest components[6] are labelled as g_1 for DBO and g_2 for PD are also observed.

4.6 Conclusions

We have demonstrated, by using *in situ* confocal Raman microspectrometry, that it is possible to obtain information on the spatial distribution of the guest molecules and variation of the spatial distribution as a function of time during the transport process. Both of these aspects are crucial for understanding fundamentals of the transport process, including its kinetics. The present work shows conclusively that these aspects can be investigated directly by using confocal Raman microspectrometry as an *in situ* probe of the transport process.

All crystals contain defects and we cannot rule out the possibility that some amount of transport may occur within defect regions and/or on the external surfaces of the crystals. However, Raman measurements carried out during this work provide conclusive evidence that the transport does occur within the bulk crystal structure (in agreement with previous analysis from X-ray diffraction studies[6]). Several aspects of the present study concur with the conclusion that the molecular exchange takes place within the urea channel structure. First of all, there is no evidence from the Raman studies reported in the present work for liquid phase of the guest molecules (if the transport were to occur through macroscopic defect regions, liquid-like spectra of the guest molecules may be anticipated). Secondly, the Raman microspectrometry measurements reported in the present work were for a sampling depth 175 μm below the surface of the crystal and clearly these measurements probe transport within the bulk of the crystal, not on the external surfaces of the crystal. Thirdly, there is no evidence from the Raman spectra for any deterioration in the integrity of the urea host structure during the transport process, suggesting that the occurrence of the transport process does not itself lead to any appreciable increase in the defect density within the crystal. On the basis of all these factors, we conclude that the transport process occurs through the channels of the crystalline urea host structure.

References for Chapter 4

[1] G. M. Preston, T. P. Carroll, W. B. Guggino and P. Agre, *Science*, **1992**, *256*, 385.

[2] D. A. Doyle, J. Morais Cabral, R. A. Pfuetzner, A. Quo, J. M. Gulbis, S. L. Cohen, B. T. Chait and R. Mackinnon, *Science*, **1998**, *280*, 69.

[3] J. M. Thomas, *Angew. Chemie Int. Ed.*, **1999**, *38*, 3588.

[4] O. Hod, E. and Rabani, *Proc. Nat. Acad. Sci.*, **2003**, *100*, 14661.

[5] A. Kalra, S. Grade and G. Hummer, *Proc. Nat. Acad. Sci.*, **2003**, *91*, art. no. 235901.

[6] A. A. Khan, S. T. Bramwell, K. D. M. Harris, B. M. Kariuki and M. R. Truter, *Chem. Phys. Lett.*, **1999**, *307*, 320.

[7] A. E. Smith, *Acta Crystallogr.*, **1952**, *5*, 224.

[8] K. D. M Harris and J. M. Thomas, *J. Chem. Soc. Faraday Trans.*, **1990**, *86*, 2985.

[9] M. Hollingsworth and K. D. M. Harris, *"Comprehensive Supramolecular Chemistry"*, D. D. MacNicol, F. Toda and R. Bishop, Eds., Pergamon Press, Elmsford, NY, USA, **1996**, *6*, 77.

[10] J. D. Axe and P. Bak, *Phys. Rev B.*, **1982**, *26*, 4963.

[11] S. Van Smaalen, *Crystallogr. Rev.*, **1995**, *4*, 79.

[12] D. Schmicker and S. Van Smaalen, Int. *J. Mod. Phys. B*, **1996**, *10*, 2049.

[13] S. Van Smaalen and K. D. M. Harris, *Proc. Roy. Soc. A*, **1996**, *452*, 677.

[14] A. J. O. Rennie and K. D. M. Harris, *Proc. Roy. Soc. A*, **1990**, *430*, 615.

[15] A. J. O. Rennie and K. D. M. Harris, *J. Chem. Phys. Lett.*, **1992**, *96*, 7117.

[16] J. M. Thomas, *Angew. Chemie Int. Ed.*, **1988**, *27*, 1673.

[17] J. M. Thomas, *Angew. Chemie Int. Ed.*, **1994**, *33*, 913.

[18] J. L. Bruneel, J. C. Lassègues and C. Sourisseau, *J. Raman Spectrosc.*, **2002**, *33*, 815.

[19] T. C. Damen, S. P. S. Porto and B. Tell, *Phys. Rev.*, **1966**, *142*, 570.

[20] P. H. H. Fisher and C. A. McDowell, *Can. Chem.*,**1960**, *38*, 187.

[21] G. B. Rarlow and P. J. Corish, *J. Chem. Soc.*, **1959**, 1706.

[22] R. A. Durie and R. J. Garisson, *Spectrochim. Acta*, **1962**, *18*, 1505

[23] F. R Dollish, W. G. Fateley and F. F. Bentley, *Characteristic Raman Frequencies of Organic Compounds,* Wiley, New York, **1974**.

[24] L. Elizabe, PhD Thesis, **1998**, *The Univesity of Birmingham*, England.

[25] S. P. Smart, PhD Thesis, **1993**, *University of St. Andrews*, Scotland.

[26] L. Le Brumant, M. Jaffarin and G. Lacrampe, *J. Phys. Chem.*, **1984**, *88*, 1584.

[27] A. ElBaghdadi, PhD Thesis, **1993**, *Université de Bordeaux I*, France.

[28] S. P Smart, A. ElBaghdadi, F. Guillaume and K. D. M. Harris, *J. Chem. Soc., Faraday Trans.*, **1994**, *90*, 1313.

[29] A. ElBaghdadi and F. Guillaume, *J. Raman Spectrosc.*, **1995**, *26*, 155.

[30] M. D. Hollingsworth, M. E. Brown, A. Hillier, B. D. Santarsiero and J. D. Chaney, *Science*, **1996**, *273*, 1355.

Chapter 5 Molecular Transport in Urea Inclusion Compounds: A Kinetic Study

5.1 Introduction

The aim of this chapter is to determine the time dependence of guest transport within the host architecture of urea inclusion compounds. Confocal Raman microspectrometry (CRM) has been used to perform a number of experiments using three different guests: 1,8-dibromooctane (DBO), dodecane (DD) and pentadecane (PD). We studied the dependence of the kinetics on the identity of the "original" and "new" guests. The surface properties at the ends of the tunnels and the molecular exchange from both ends of the tunnels were also investigated. A kinetic model for the transport process is defined. A general conclusion of the results obtained through this work is presented.

The results obtained in this work provide insights into the time dependence of the molecular transport process studied. We can divide the process into three stages: *i*) the molecules are introduced into the tunnels, involving the opening up of the tunnels (we believe that urea molecules can reorganize at the ends of the tunnels to effectively "close" the tunnels, and therefore opening up of the tunnels is required before "new" guest molecules can enter the tunnels); *ii*) the molecules are transported along the tunnels and *iii*) the expulsion of guest molecules at the other end of the crystal, which will also require reconstructive processes of the urea molecules at the surface. The time dependence of these three different stages of the reaction may be very different from one another, and one may act as a rate-determining step. Therefore, to be able to assign a model for this process, we need to obtain sufficient understanding of the kinetics of the process, as described in this chapter.

5.2 Background to Molecular Transport Processes in Zeolites and UICs.

Molecular diffusion processes have been studied considerably, because for example it is a key step in the catalytic cycle in zeolites.[1] In this process, molecules have to move through the channel architecture of the zeolite in order to reach the reaction site in the tunnel, then the molecules must move out of the tunnel to leave the pore empty, allowing the cycle to start again. Due to the great variety of tunnel frameworks displayed by these inorganic solids,

zeolites are the prototype material for studying molecular transport processes such as diffusion. They can form a wide variety of architectural frameworks, including one-, two- and three-dimensional tunnels, which can also vary in size and shape.

Diffusion of guest molecules can occur in zeolites because they belong to the "hard" type of inclusion compounds, in which the host structure remains stable upon removal of the guest molecules. Hence, it is not surprising to find many studies related to molecular transport processes in zeolites. On the other hand, substantially less research has been devoted to studying molecular transport processes within organic solids such as urea inclusion compounds (UICs). Hitherto, exchange processes have not been applied in UICs because they belong to the "soft" type of inclusion compounds. For soft hosts, the "empty" host structure is unstable and it is usually necessary to build up the inclusion compound by crystal growth in the presence of the potential guests. Moreover, applications in which an increase of temperature is necessary are not possible either, as this will also destroy the crystalline structure through loss of the guest molecules and, consequently, its physical properties.

Nevertheless, UICs have the potential to be used in a considerable number of applications, including nanoscale separation techniques based on molecular size, shape and chirality. Chemists studying fatty acids, for example, routinely use UICs to carry out separations. Among industrial examples, UIC formation has been used by the petroleum industry in the dewaxing of certain oil fractions, although zeolites are nowadays routinely used in such applications. A number of important applications requiring molecular transport in organic materials are found in medicine and biochemistry.

5.3 Diffusion Processes in Solids

Diffusion in liquids, gases and solids has been studied for more than a century. It is caused by the thermal motion and subsequent collisions of the molecules. Diffusion can be related to a microscopic quantity called the mean-square displacement (MSD), as shown by Einstein in his contribution on Brownian motion.[2] The mean square displacement is a measure of the average square of the distance a molecule travels and is defined as

$$\left\langle r^2(t)\right\rangle = \left\langle \left|\vec{r}(t)-\vec{r}(0)\right|^2 \right\rangle = \frac{1}{N}\sum_{i=1}^{N}\left(\vec{r}_i(t)-\vec{r}_i(0)\right)^2 \qquad (5.1)$$

In this equation, $\vec{r}_i(t) - \vec{r}_i(0)$ is the (vector) distance travelled by molecule i over some time interval t. The squared magnitude of this vector is averaged (as indicated by the angular brackets) over many such time intervals and molecules.

Considering a simple random walk model for a one-dimensional system, it can be shown that, for sufficiently long time, the molecular mean square displacement will be linearly dependent on time, i.e.,

$$\left\langle \vec{r}^{\,2}(t) \right\rangle = 2D_s t \tag{5.2}$$

The factor of 2 results from the one-dimensional nature of the motion, and D_s is the diffusion constant.

Diffusion in microporous materials, such as UICs and zeolites, differs from ordinary diffusion, since molecules have to move through channels of molecular dimensions (5-20 Å). Hence, there is constant interaction between the diffusing molecules and the host framework. The molecular motion is thus strongly influenced by the size and shape of the cavities within the framework, by the temperature and by the concentration. It is also possible that the neighbouring molecules in one tunnel may have some influence on the transport process. For one-dimensional structures such as zeolites, the transport of molecules along the tunnels is called single-file diffusion.[3-7] This type of diffusion arises from the fact that the guest molecules may be unable to pass each other in the narrow pores of the tunnel structure. This reduces the mobility of the molecules. As the mutual passage of particles is prohibited in single-filing systems, the movement of individual particles are correlated, even at long time periods, because the displacement of a given particle over a long distance necessitates the motion of many other particles in the same direction. This correlation is reflected in the long-time behaviour of the molecular transport process, which is predicted for an infinite system to be[8-13]

$$\left\langle \left| \vec{r}^{\,2}(t) \right| \right\rangle = 2F\sqrt{t} \tag{5.3}$$

where the F is the single-file mobility. Single-file processes, in contrast to one and three-dimensional self-diffusion (observed in systems like zeolites or colloidal systems),[14,15] cannot be described by a diffusion coefficient.

While, in the case of gases and liquids, the behaviour and exact value of the diffusivity can be calculated with relative ease, the diffusivity values are much more difficult to determine in zeolites. The interactions between molecules and the pore wall lead to large differences in the diffusivities of different alkanes. In the case of zeolites, it is possible to study the diffusivity of branched alkanes.

The present work is the first time that transport of guest molecules has been studied in UICs. Due to the structural differences between zeolites and UICs, we cannot say that single file process is expected to be observed in UICs. Therefore, the aim of this work is to study the kinetics of the transport process of alkanes within the host structure of UICs. In Figure 5.1 a graphic representation of the classical and single-file diffusion is shown.

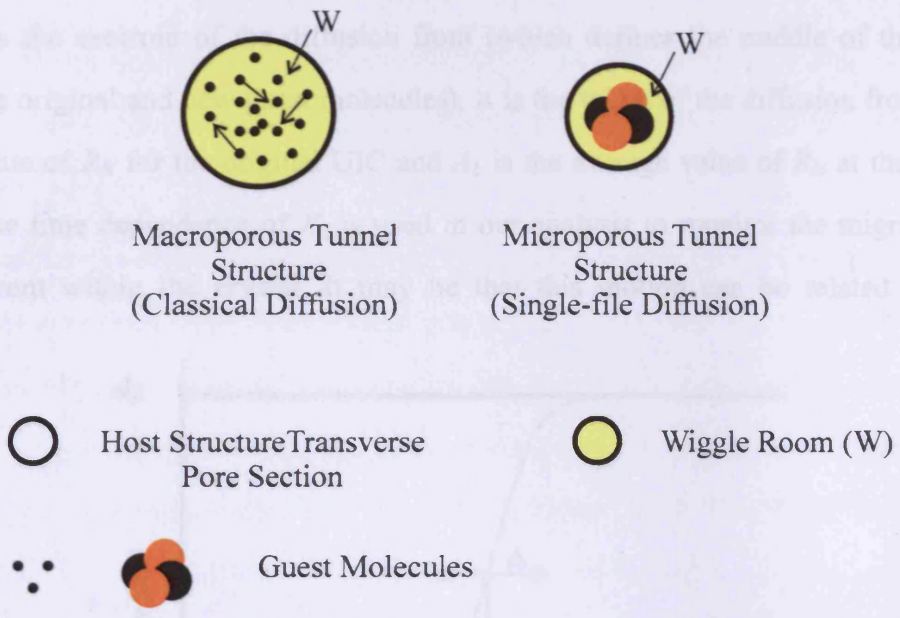

Figure 5.1. Representation of classical and single-file diffusion process showing the space available for the guest molecules to diffuse along one-dimensional tunnels.

5.4 Development of a Kinetic Model

In this work, molecular exchange within the UIC leads to a spatial distribution of the new and original guest molecules that varies as a function of time. This is analysed by measuring the intensity corresponding to the Raman bands of the "original" guest molecules and the host structure (see Section 4.4.3). In our calculations we used the normalized ratio of integrated intensities, $R_N = R/R_0$, where the R_0 is the value of R (averaged over the probed area) for the original DBO/urea crystal before starting the guest exchange process. Therefore, $R_N = 1$ if the crystal contains only DBO guest molecules and $R_N = 0$ if the crystal contains only PD guest molecules (i.e., complete guest exchange).

The shape of this distribution is a front, to be approximately described by a sigmoidal distribution. Thus, the experimental data has been analysed by means of the following function, illustrated in Figure 5.2

$$R_N(X,t) = \frac{A_1 - A_2}{1 + \exp[(X - X_0(t))/\Delta(t)]} + A_2 \qquad (5.4)$$

where X_0 is the centroid of the diffusion front (which defines the middle of the boundary between the original and new guest molecules), Δ is the width of the diffusion front, A_2 is the average value of R_N for the original UIC and A_1 is the average value of R_N at the end of the process. The time dependence of X_0 is used in our analysis to monitor the migration of the diffusion front within the crystal. It may be that this motion can be related to time by

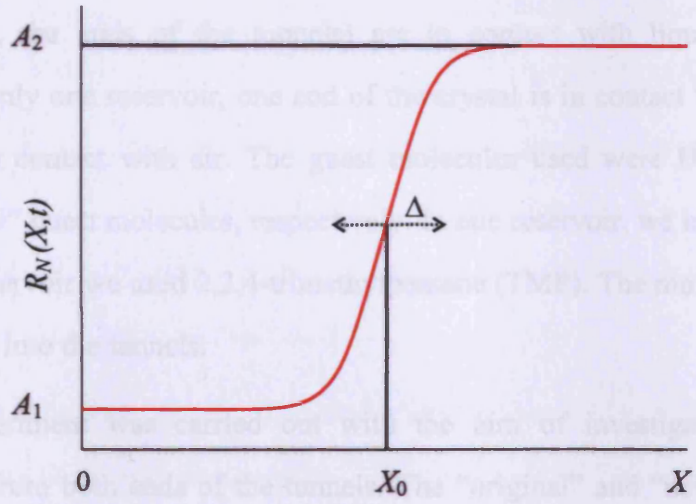

Figure 5.2. Sigmoidal distribution of $R_N(X,t)$ versus X at a specific value of time.

considering a random walk model for the new guest molecules in each tunnel. By analogy with the arguments above, the movement of the diffusion front may be described by

$$X_0^2(t) \propto t \tag{5.5}$$

for classical diffusion or

$$X_0^2(t) \propto t^{1/2} \tag{5.6}$$

for a single file-diffusion process. During the fitting procedure, we held the values of A_2 and A_1 fixed, whereas X_0 and Δ were varied. During the kinetic analysis, we consider both classical and single file processes, but other models will be also considered.

5.5 Strategy

It has been demonstrated in Chapter 4 that CRM can be used to monitor *in situ* the exchange of guest molecules within the host tunnel architecture in UICs.[16] In the following work, several different experiments were performed to study the kinetics of the molecular transport process. The first experiment presented here consists of a system using 1,8-dibromooctane (DBO) and pentadecane (PD) as the "original" and "new" guest molecules, respectively. The experimental set up used only one reservoir (containing the liquid phase of PD).

The second experiment was carried out to study the surface properties at the ends of the tunnels. Two reservoirs were used in this experiment. Using this set up, both ends of the single crystal (i.e., the ends of the tunnels) are in contact with liquid, whereas in the experiment using only one reservoir, one end of the crystal is in contact with liquid whereas the other end is in contact with air. The guest molecules used were DBO and PD as the "original" and "new" guest molecules, respectively. In one reservoir, we introduced liquid PD and in the other reservoir we used 2,2,4-trimethylpentane (TMP). The molecular size of TMP is too large to enter into the tunnels.

A third experiment was carried out with the aim of investigating the molecular exchange process from both ends of the tunnels. The "original" and "new" guest molecules

were DBO and PD, respectively. We used two reservoirs each containing liquid PD. Clearly, PD molecules can enter the tunnel at both ends of the crystal.

The last experiment reported in this chapter is focused on the case in which the original and new guest molecules are members of the *same* homologous series, and differ only in chain length. In particular, we demonstrate in this work the occurrence of alkane-alkane guest exchange within the urea channel structure, focusing on the UIC containing dodecane (DD) as the "original" guest and pentadecane PD as the "new" guest. To monitor the guest exchange process by confocal Raman microspectrometry, fully deuterated pentadecane (PD-d_{32}) was used in order to provide discrimination in the Raman spectrum between the regions of the crystal containing the original and new guest molecules. We note that, within the homologous series of alkane UICs, the thermodynamic stability is greater the longer the guest molecule and there is therefore a thermodynamic driving force for the PD guest molecules to replace DD guest molecules within the urea channel system.

5.6 Experimental Methods

Crystals of the DBO/urea and DD/urea inclusion compound were prepared using standard procedures. An excess amount of the guest species (excess with respect to the expected molar guest/host ratio in the inclusion compound) was added to a saturated solution of urea in methanol in a flask at 50°C. On obtaining a homogeneous solution, the flask was placed in a thermal bath at 50°C, then left to cool slowly over a period of several days to 20°C. Needle-shaped crystals with hexagonal cross-section were collected with a diameter between 1 and 2 mm and typical length of between 20 and 40 mm. The surfaces of the crystal were washed with 2,2,4-trimethylpentane (TMP) prior to each experiment.

Confocal Raman Microspectrometry experiments were performed with a Labram II spectrometer (Jobin-Yvon), an Ar/Kr 2018 Spectra-Physics laser (514.5 nm) and a grating of 1800 lines/mm (spectral resolution ~ 6 cm^{-1}). The laboratory reference frame in our Raman experiments is defined in Chapter 4, Section 4.3.

The laser was focused on the different samples through a microscope using 10× Olympus objective of 0.25 numerical aperture, respectively, and the diameter of the confocal pinhole was 700 μm. With this setting, the diameter of the area probed by the laser was

50 μm. Each sample was analyzed between 100 and 300 μm below the surface. This range of depths was used to avoid the roughness of the crystal surface, since it was observed that at some points due to defects it was possible to find hollows.

Variation in the amount of DBO guest molecules in the crystal during their replacement with PD guest molecules can be probed by measuring the ratio $R = I(\text{CBr})/I(\text{CN})$ of the integrated intensities of the $\nu(\text{CBr})$ and $\nu_s(\text{CN})$ Raman bands (denoted $I(\text{CBr})$ and $I(\text{CN})$, respectively), which was converted to the normalized ratio R_N defined in Section 5.4. The ratio of integrated intensities, $R_N(x)$, at a given point (x) of the single crystal is related to the concentration of DBO guest molecules C_{DBO} by

$$R_N(x) = 1 - p\, C_{DBO}(x) \tag{5.7}$$

A transport coefficient has been determined by considering three possibilities. First, we plotted the data assuming the conventional Einstein law ($X_0^2 \propto t$), and second, assuming a single-file diffusion process ($X_0^2 \propto t^{1/2}$). According to the physical properties of the system studied, the molecular transport process can behave differently from a classical or single file diffusion process and, a third, linear model was also considered,

$$X_0(t) \propto t \tag{5.8}$$

The data obtained from these plots will be used to determine the rate of transport (by measuring the gradient), and to assess if there is an induction time before commencement of the exchange process.

5.7 Experimental Results

5.7.1 Molecular Exchange of DBO by PD Using One Reservoir.

For the *in situ* confocal Raman microspectrometry, we used a single crystal of the DBO/urea inclusion compound (needle shaped with dimensions 1 × 1 × 38 mm^3). The single crystal was attached to a reservoir using Araldite. The single crystal and its reservoir were mounted on the *X,Y*-motorized table of the confocal microscope.

The in-depth analysis was performed inside the crystal at coordinate $Z = 175$ μm. The diameter of the laser beam was 10 μm (using 140 μm diameter pinhole due to experimental

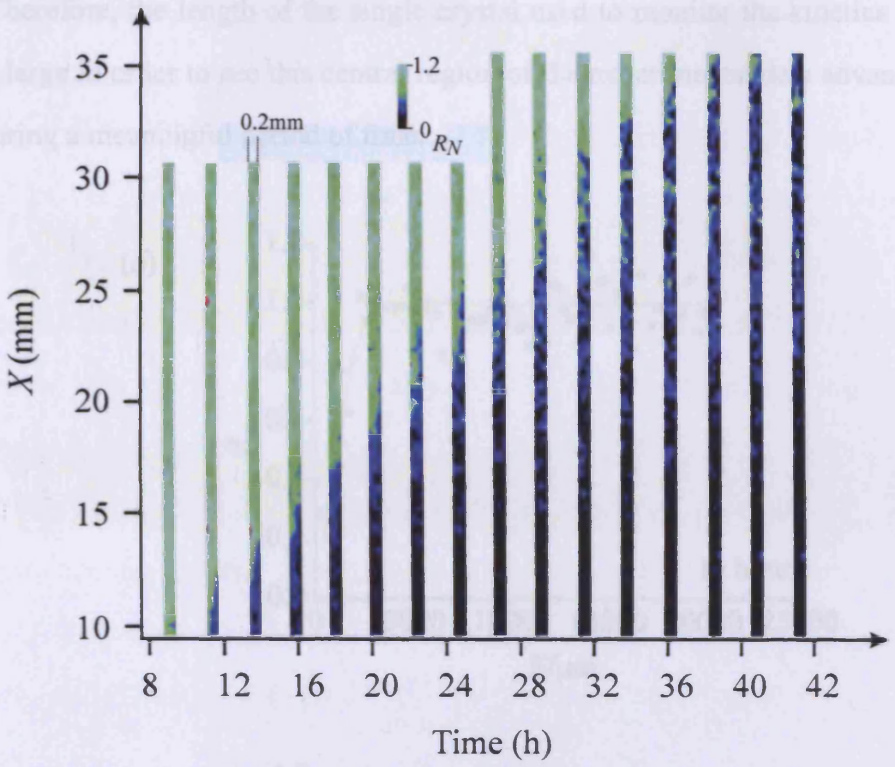

Figure 5.3. Raman images of the probed area of the single crystal at different times after the commencement of the transport process. The regions of the crystal rich in DBO are in green ($R_N \geq 0.5$) and those rich in *n*-pentadecane are in dark blue ($R_N < 0.5$).

conditions). The Raman spectra were collected along the X coordinates with step 300 μm and over 3 lines at Y coordinates separated by 100 μm. The acquisition time for each Raman spectrum was 2 s, so that the time taken to record each line was about 15 min and the time required to record the entire Raman image of the probed area (several examples of these Raman images are shown in Figure 5.3) was about 1 hour and 40 min. In the following, we consider that the time needed to record the Raman spectra along one line of the single crystal is negligible compared to the overall time of the experiment (about two days).

Before we introduced the liquid PD to the reservoir, we performed the first scan, which gave us an $R = 0.37$. This is the value expected for a single crystal of DBO/urea that is well aligned. The last mapping carried out after 33 hours gave $R = 0.04$. An example of the experimental data obtained in this experiment is shown in Figure 5.4, which can clearly be fitted by a sigmoidal function. Interestingly, from this figure it is possible to observe how, after 19 hours, there is a comparatively narrow boundary region (defined by the width of the diffusion front (Δ)) between the DBO-rich ($R_N \approx 1$) and the PD-rich ($R_N \approx 0.1$) regions of the

crystal. Therefore, the length of the single crystal used to monitor the kinetics of the process has to be large in order to see this central region of the experimental data advancing along the crystal during a meaningful period of time.

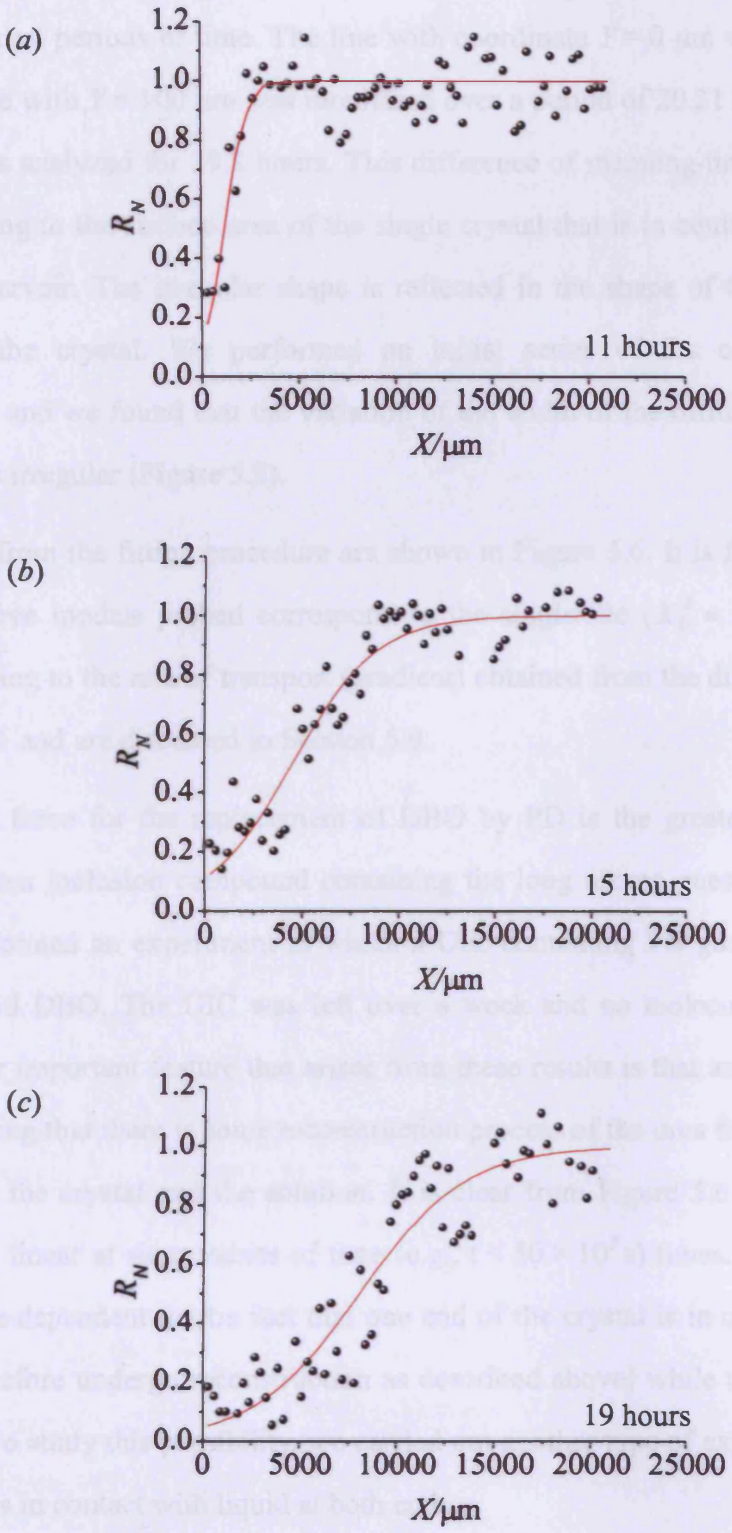

Figure 5.4. The experimental data can be fitted by a sigmoidal function. Translation of the centroid of the diffusion front along the crystal as a function of time is evident.

The experimental data was analyzed using the function defined in Equation 5.4. During the fitting procedure, we held the values corresponding to the parameters A_2 and A_1 fixed, whereas the X_0 and Δ were allowed to vary. The values corresponding to A_2 are ~ 0.37 while A_1 are ~ 0.04 for the three lines studied in this experiment. The three different lines were followed for different periods of time. The line with coordinate $Y = 0$ μm was followed over 18.5 hours, the line with $Y = 100$ μm was monitored over a period of 20.31 hours and the line at $Y = 200$ μm was analyzed for 29.8 hours. This difference of mapping-time arises from the shape corresponding to the surface area of the single crystal that is in contact with the liquid PD inside the reservoir. The irregular shape is reflected in the shape of the diffusion front travelling along the crystal. We performed an initial series of fits of Eq. 5.4 to the experimental data and we found that the variation of the width of the diffusion front (Δ) as a function of time is irregular (Figure 5.5).

The results from the fitting procedure are shown in Figure 5.6. It is found that the best fits among the three models probed correspond to the single-file ($X_0^2 \propto t^{1/2}$) process. The values corresponding to the rate of transport (gradient) obtained from the different models are shown in Table 5.1 and are discussed in Section 5.9.

The driving force for the replacement of DBO by PD is the greater thermodynamic stability for the urea inclusion compound containing the long alkane guest molecules. Note that we have performed an experiment in which a UIC containing PD guest molecules was immersed in liquid DBO. The UIC was left over a week and no molecular exchange was observed. Another important feature that arises from these results is that an induction time is observed, suggesting that there is some reconstruction process of the urea framework near the interface between the crystal and the solution. It is clear from Figure 5.6 that the transport process cannot be linear at short values of time (e.g., $t < 50 \times 10^3$ s) times. It may be argued that the results are dependent on the fact that one end of the crystal is in contact with liquid PD (and may therefore undergo reconstruction as described above) while the other end is in contact with air. To study this possibility, we carried out another type of experiment in which the single crystal is in contact with liquid at both ends.

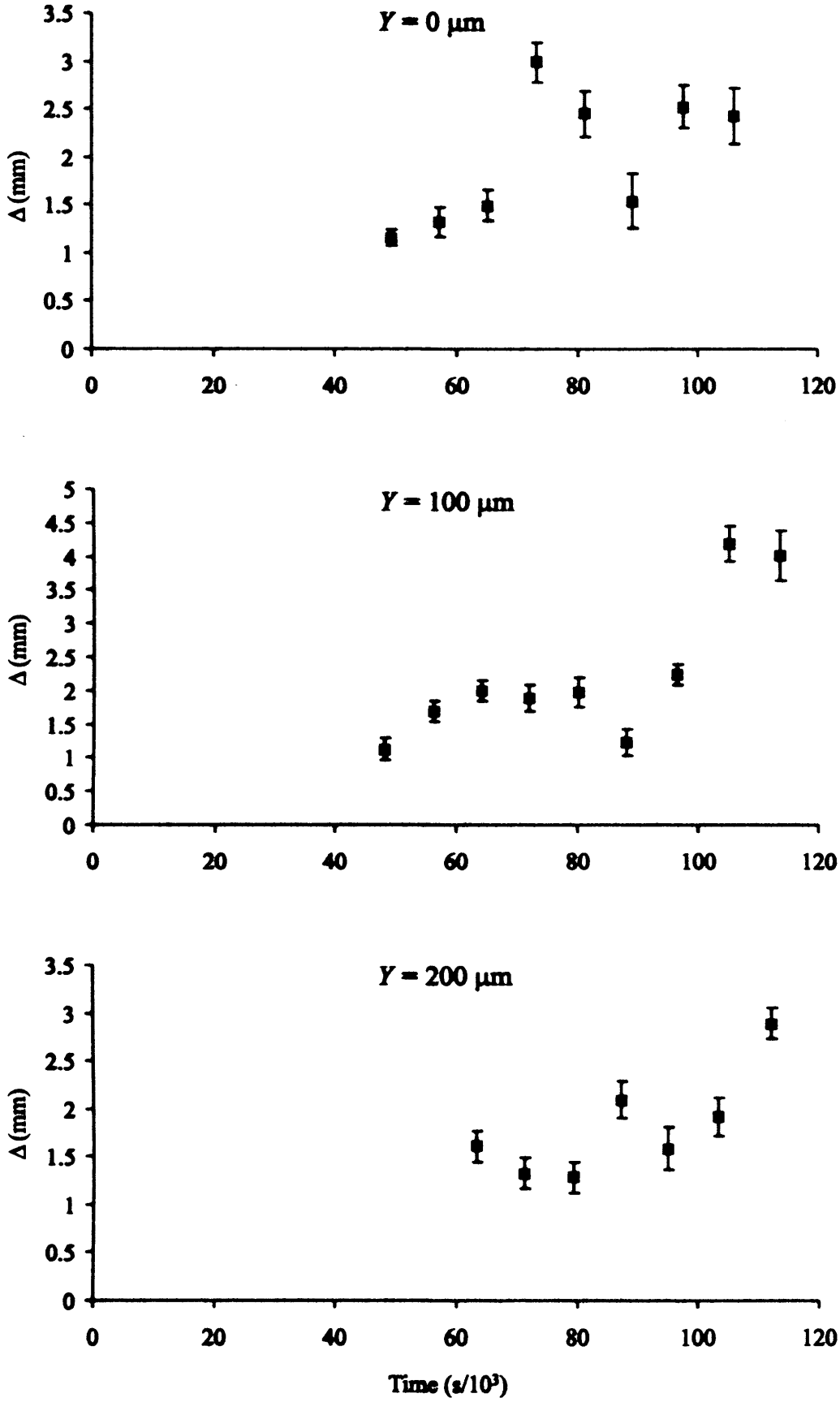

Figure 5.5. Evolution of Δ as a function of time during the molecular exchange of DBO by PD (using one reservoir) showing an irregular time dependence.

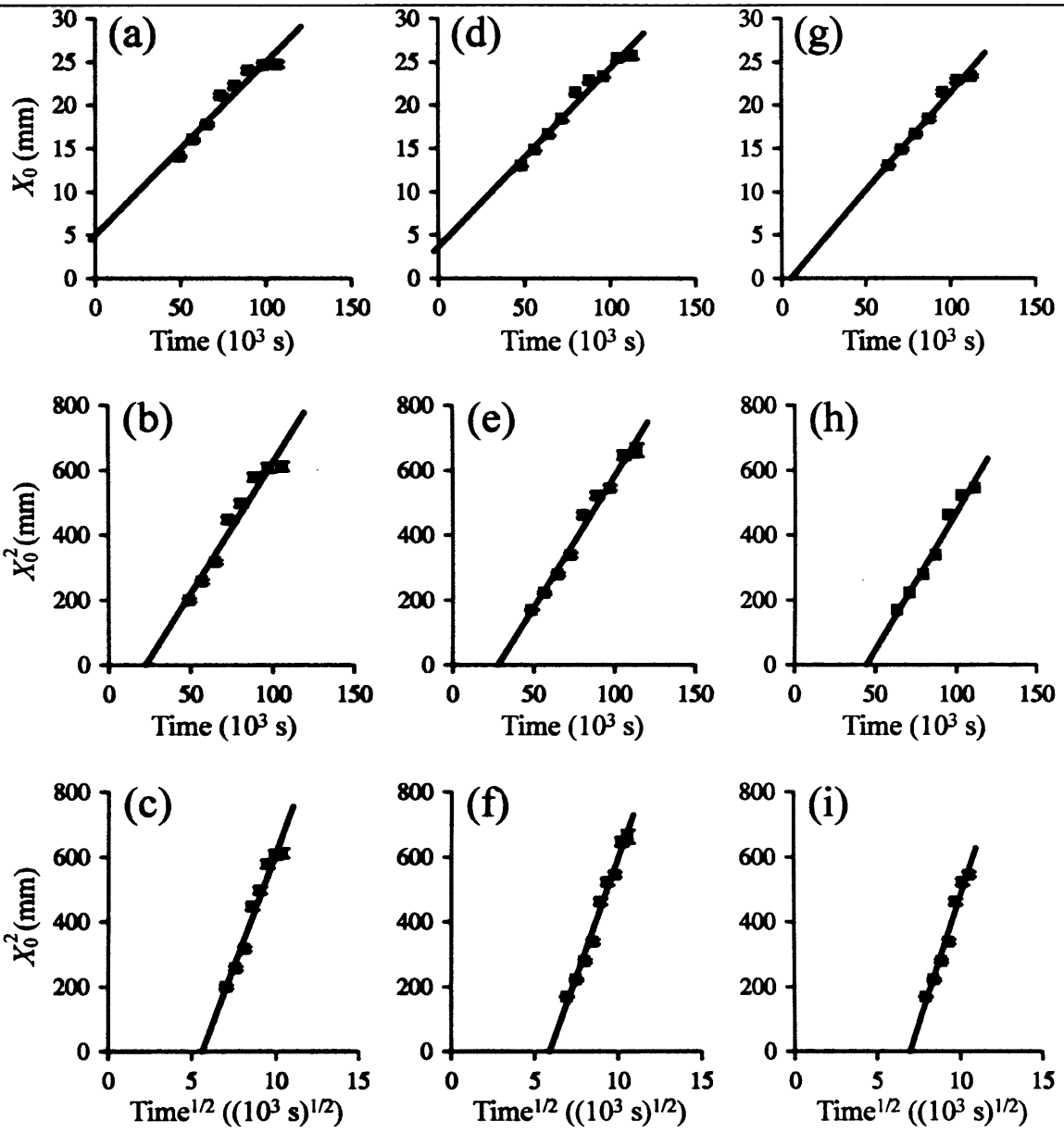

Figure 5.6. Fittings of the front positions, X_0, in the three lines analyzed during molecular exchange of DBO by PD (using one reservoir). The lines were (a), (b) and (c); Y = 0 μm, (d), (e) and (f); Y = 100 μm and (g), (h) and (i) Y = 200 μm. The fitting models were (a), (d) and (g); $X_0 \propto t$, (b), (e) and (h); $X_0^2(t) \propto t$ and (c), (f) and (i); $X_0^2(t) \propto t^{1/2}$.

5.7.2 Molecular Exchange of DBO by PD Using Two Reservoirs Filled with PD and TMP respectively.

The purpose of this experiment is to study the effect of having liquid in contact with the crystal at *both* ends of the tunnels, using two reservoirs containing PD guest molecules in one and TMP in the other. With this set up, both ends of the crystal are in contact with liquid. To follow the experiments *in situ*, we used a single crystal of the DBO/urea inclusion compound (needle shaped with dimensions $1 \times 1.6 \times 38$ mm^3). The single crystal was sealed to two reservoirs using Araldite.

The experimental set up is depicted in Figure 5.7. The in-depth Raman analysis was performed at 200 μm below the surface along three lines separated by 100 μm. The step (Δx) between measurements along each line was of 300 μm. The diameter of the laser beam was 50 μm (using 700 μm diameter pinhole). The time needed to record the micrograph across the entire probed area was 97 min. Each line took approximately 14 minutes to be scanned. The spatial and spectral resolutions are the same as those used in the previous experiment.

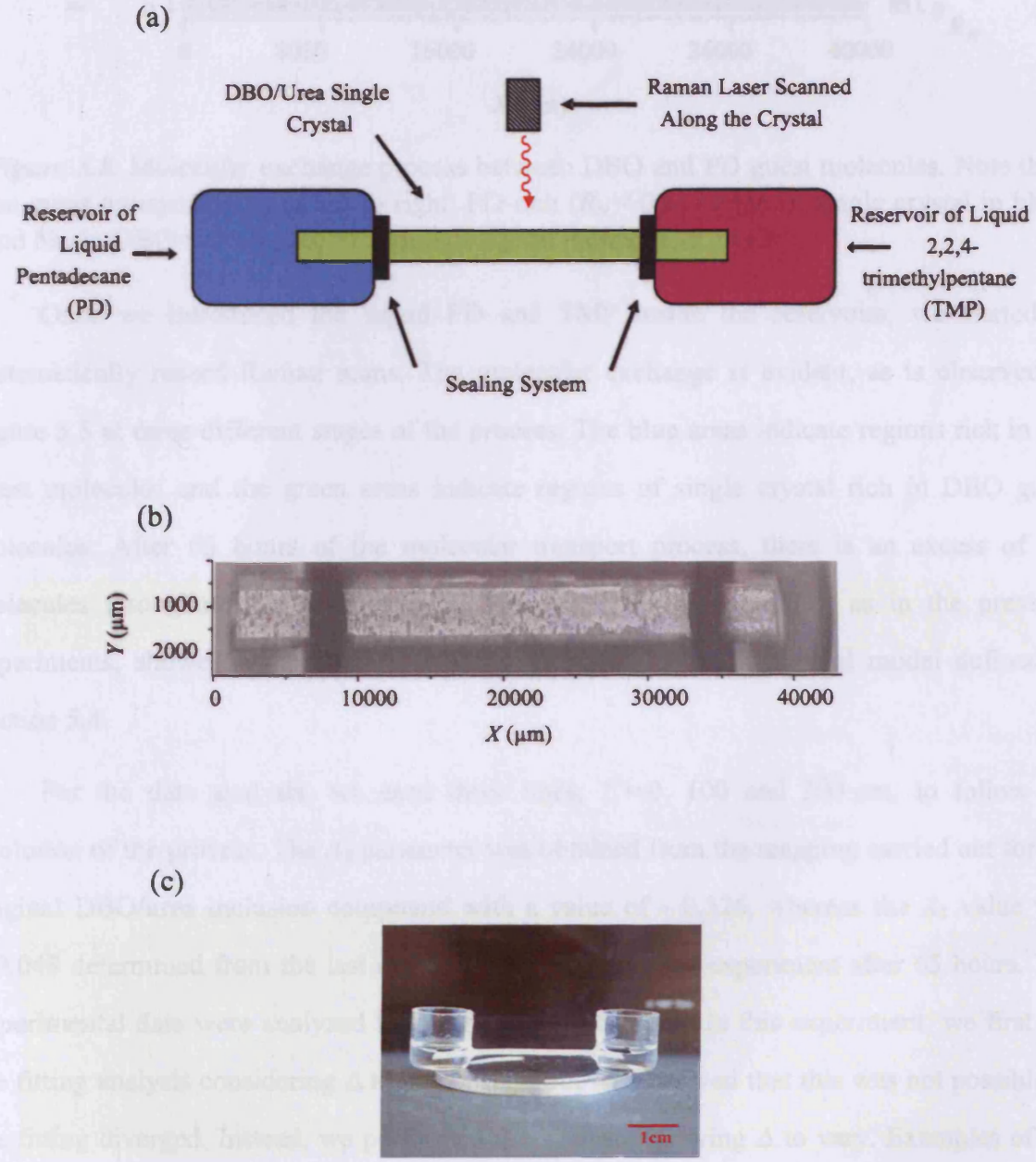

Figure 5.7. (a) Schematic diagram of the experimental assembly, comprising the DBO/urea inclusion compound crystal and two reservoirs containing liquid PD and 2,2,4-trimethylpentane (TMP); (b) single crystal of the DBO/urea inclusion compound attached to two reservoirs (black strips correspond to the glue); (c) actual experimental set up with the single crystal attached to both reservoirs.

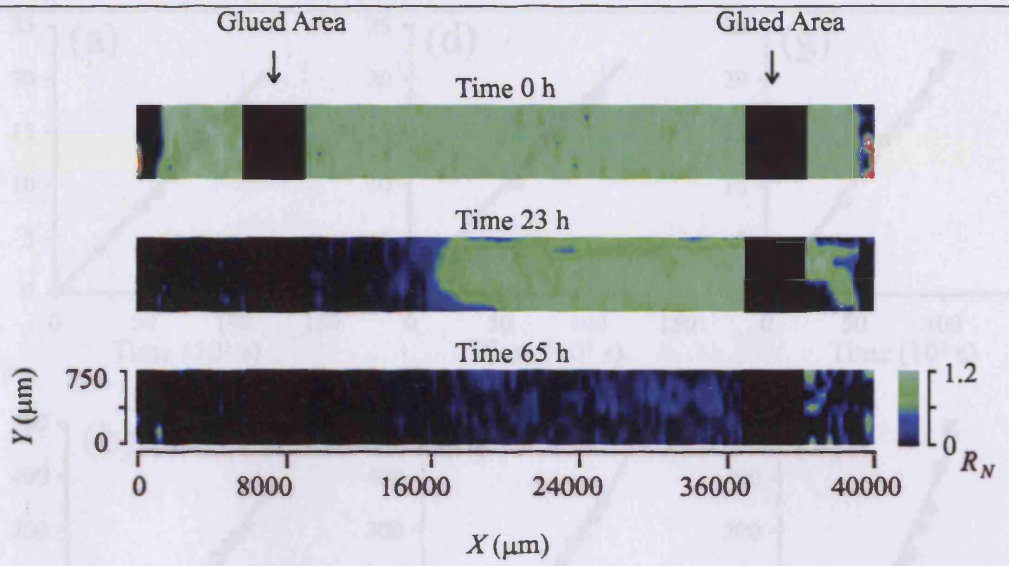

Figure 5.8. Molecular exchange process between DBO and PD guest molecules. Note that the guest transport is from left to right. PD-rich ($R_N < 0.5$) region of single crystal in blue and black; DBO-rich ($R_N \geq 0.5$) region of crystal indicated in green.

Once we introduced the liquid PD and TMP inside the reservoirs, we started to systematically record Raman scans. The molecular exchange is evident, as is observed in Figure 5.8 at three different stages of the process. The blue areas indicate regions rich in PD guest molecules and the green areas indicate regions of single crystal rich in DBO guest molecules. After 65 hours of the molecular transport process, there is an excess of PD molecules throughout the scanned area. The experimental data $R(x)$, as in the previous experiments, showed a distribution that can be fitted by the sigmoidal model defined in Section 5.4.

For the data analysis, we used three lines, $Y = 0$, 100 and 200 μm, to follow the evolution of the process. The A_2 parameter was obtained from the mapping carried out for the original DBO/urea inclusion compound with a value of ~ 0.326, whereas the A_1 value was ~ 0.048 determined from the last mapping carried out in our experiment after 65 hours. The experimental data were analyzed by means of Equation 5.4. In this experiment, we first did the fitting analysis considering Δ to be constant but we observed that this was not possible as the fitting diverged. Instead, we performed the analysis allowing Δ to vary. Examples of the three different fitted models are shown in Figure 5.9. The rate of exchange is very close to the previous experiment and the induction time is also very similar. From the fitting analysis, we observed that the time dependence of X_0 is well explained by assuming a single-file process.

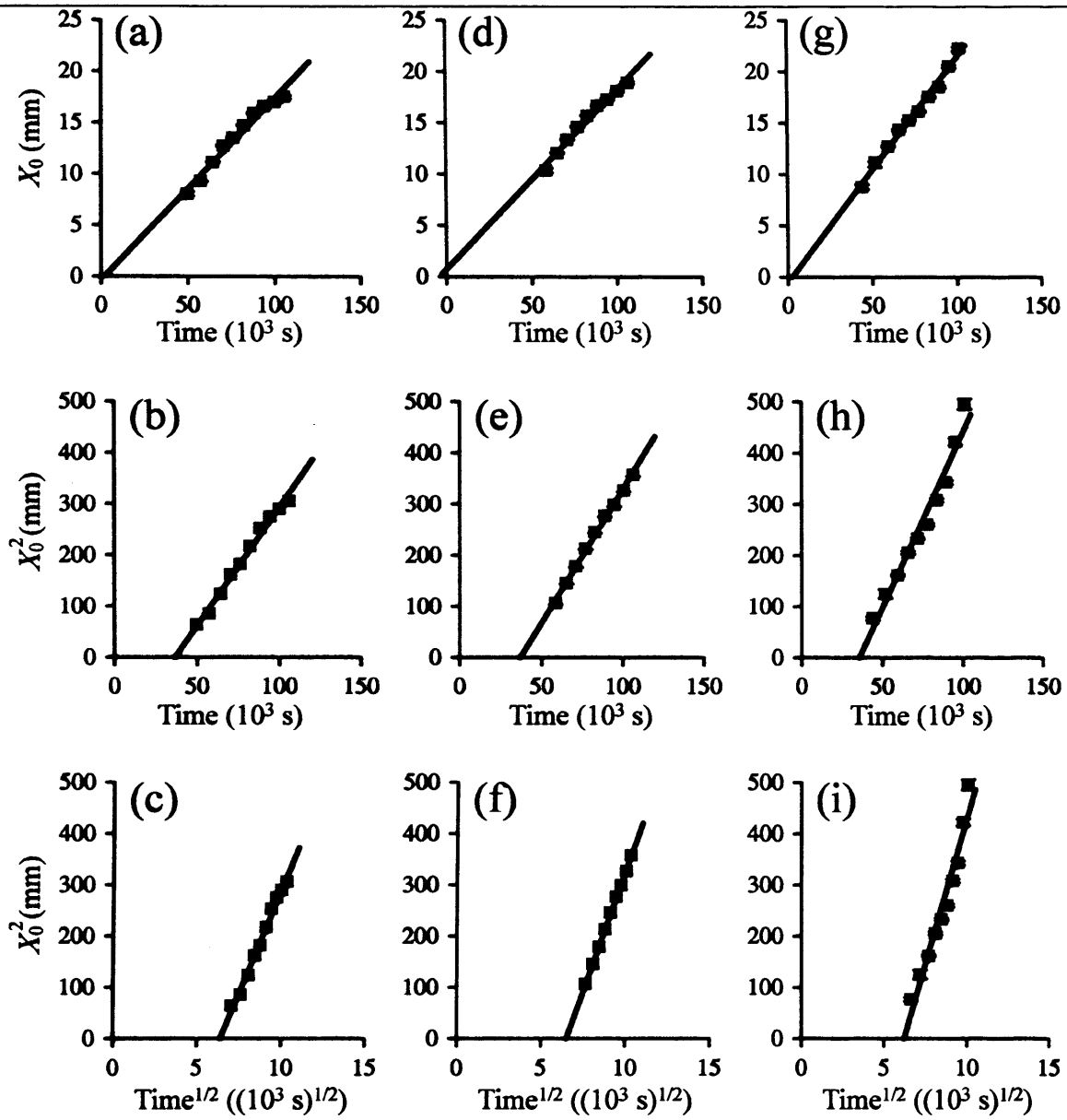

Figure 5.9. Fittings of the front positions, X_0, in the three lines analyzed during molecular exchange of DBO by PD (using one PD reservoir and one TMP reservoir). The lines were (a), (b) and (c); Y = 0 μm, (d), (e) and (f); Y = 100 μm and (g), (h) and (i) Y = 200 μm. The fitting models were (a), (d) and (g); $X_0 \propto t$, (b), (e) and (h); $X_0^2(t) \propto t$ and (c), (f) and (i); $X_0^2(t) \propto t^{1/2}$.

From Figure 5.10, we observe that Δ has a different behaviour from the previous experiment (with only one reservoir). Here, we observe a slight increase of Δ towards the end of the process. Values of rate of exchange and induction time are given in Table 5.1.

We have demonstrated with this experiment how there is no influence on the transport process by having the single crystal in contact with liquid at the end of the tunnel at which the "original" guest molecules are expelled. The main difference compared to the previous experiment is that the width of the diffusion front increases with time. We have also observed

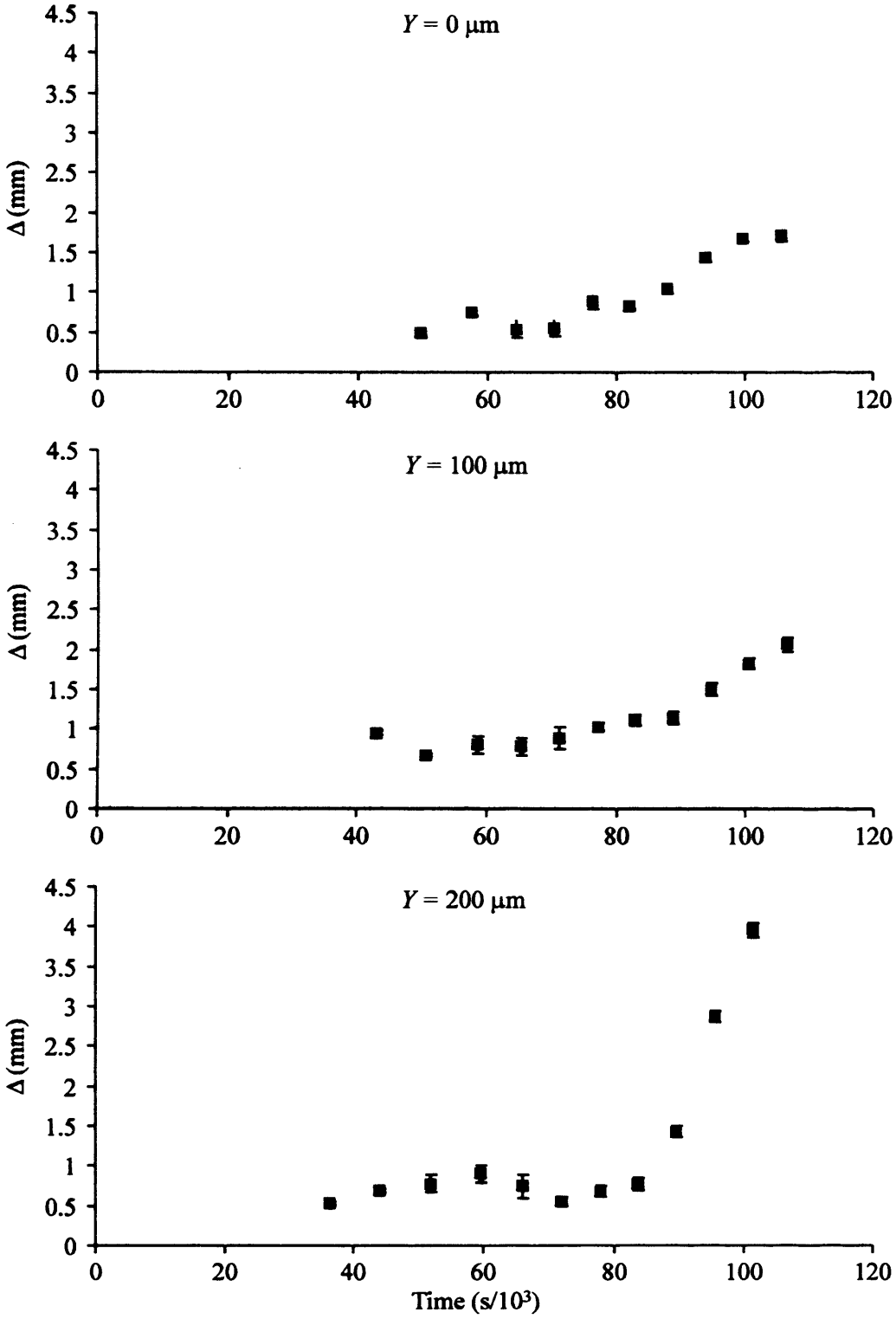

Figure 5.10. Values of Δ obtained for the three monitored lines in the experiment with two reservoirs and TMP. We can see how there is an increase of Δ towards the last experiental values.

that the exchange between DBO and PD guest molecules is never complete. After several days of the exchange process, there remains some amount of the original (DBO) guest molecules throughout the crystal.

5.7.3 Molecular Exchange of DBO by PD Using Two Reservoir

In this experiment, we are investigating if molecular transport is possible by insertion of PD guest molecules from both ends of the tunnels at the same time. The kinetics of this process will also be evaluated. To follow the experiments *in situ*, we used a single crystal (needle-like shaped with dimensions 1 × 1.5 × 35 mm^3) of the DBO/urea inclusion compound. This long single crystal was sealed to two reservoirs using Araldite. The experimental set up is the same as the one depicted in Figure 5.7 but with the difference that liquid PD is introduced into both reservoirs. Clearly, the molecular transport process is expected to occur from both ends of the tunnels.

The in-depth Raman analysis was performed at 100 μm below the surface along three lines ($Y = 0$, $Y = 150$ and $Y = 300$ μm) with a distance between each line of 150 μm. The diameter of the laser beam was 50 μm (using 700 μm diameter pinhole). The step between points was of 300 μm. The time needed to record a map was 81 min. Each line took approximately 14 min. to be scanned. Spatial and spectral resolutions were the same as used in previous experiments.

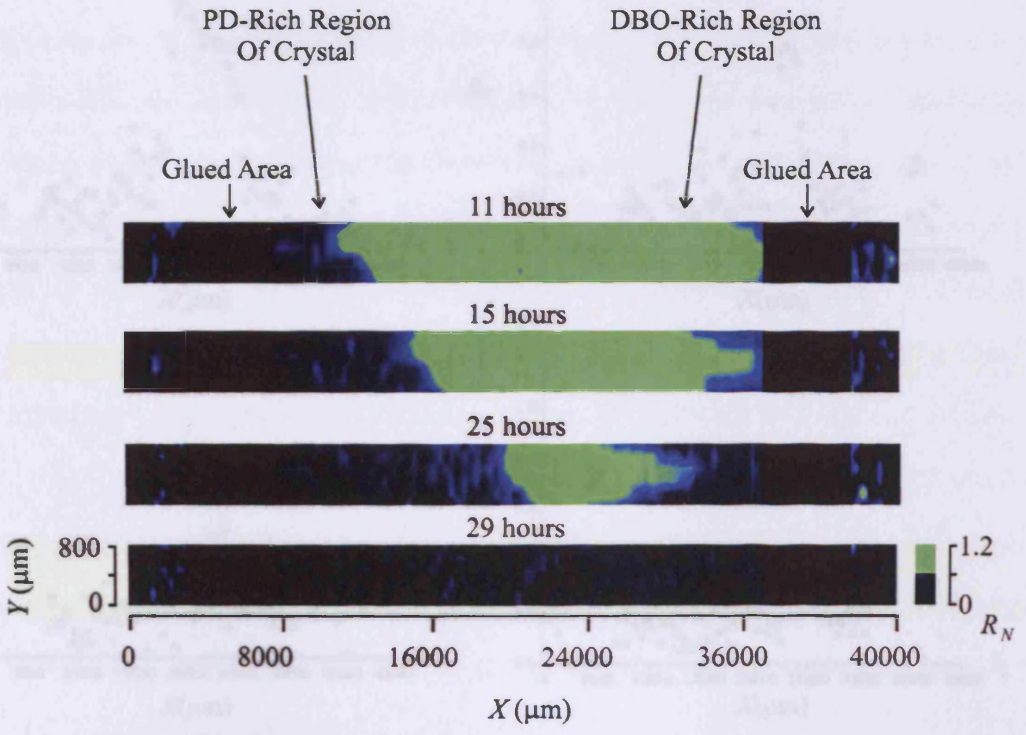

Figure 5.11. Exchange process in PD experiment with PD molecular transport from both ends. The regions of the crystal rich in DBO are in green ($R_N \geq 0.5$) and those rich in *n*-pentadecane are in dark blue ($R_N < 0.5$).

Three different lines were used to perform the analysis. The values corresponding to A_2 and A_1 obtained for the three different lines studied in this experiment are 0.326 and 0.05 respectively. The A_2 parameter was obtained from the mapping carried out for the DBO/urea inclusion compound before the start of the process, whereas the A_1 value was determined from the last measurement carried out after 29 hours. From Figure 5.11, it is evident that the molecular transport process occurs from both ends of the single crystal since molecular transport is now measured from left to right (L-R) and right to left (R-L) at the same time. As

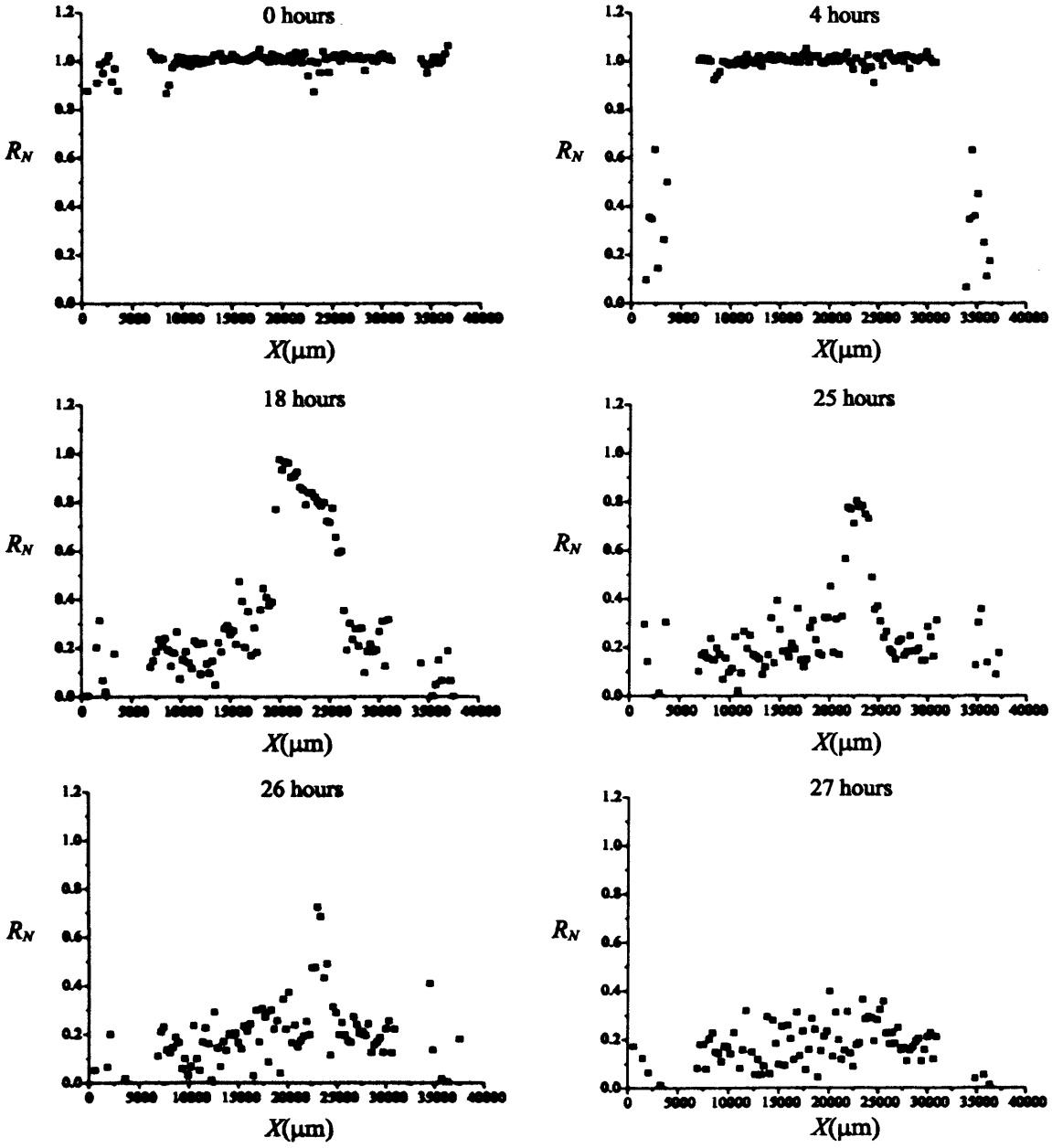

Figure 5.12. Evolution of R_N as a function of time for the PD from both ends experiment. It is clear from the picture how the exchange of guest molecules is from both ends of the single crystal at the same time.

shown in Figure 5.11, the process does not appear to be symmetrical (i.e., the encounter of both diffusion fronts does not take place at the middle point of the crystal).

In Figure 5.12, we observe how the ratio R_N decreases from both ends of the tunnels at the same time (i.e., with transport occurring from left to right and from right to left) and a double-sigmoidal distribution of experimental points is observed. Hence, the molecular transport process can be evaluated using the Eq. 5.4.

We performed a first fitting process keeping Δ constant but we observed that the fits did not converge, so we decided to allow Δ to vary. For the analysis of the kinetics, we used the three different models as in the previous experiments. For the transport process from left to right and right to left, the best fitting corresponded to the linear process ($X_0 \propto t$). The gradient obtained in both cases was very similar, indicating that the molecular exchange is not affected by the fact that there are two fronts moving in opposite directions at the same time. It is also observed (see Table 5.1) that the gradient obtained in this experiment is very close to the previous experiments discussed above. An example of the fits for the three models is shown in Figure 5.13.

In this experiment, the probabilities to start the molecular transport process at both ends of one single tunnel are the same *ca.* 50% (Figure 5.14). Once the process has started at one end of a given tunnel, this implies that the first PD to enter the tunnel "pushes" the entire row of DBO guest molecules until one DBO and a fraction of a second DBO molecule have been "pushed out" or extruded at the other end of the tunnel. Therefore, the energy of that single tunnel is now more favourable containing both DBO and PD rather than only DBO. A molecular exchange in the same tunnel but starting from the opposite end is also possible. The energy of the UIC will be the same if the molecular exchange process starts either from left to right or from right to left (Figure 5.14). If, for the same tunnel, there is now a PD molecule pushing in the opposite direction to get inside the tunnel, the energy that this PD has to overcome is too large, thus it is easier to keep the transport process proceeding from the side where the first PD has been introduced.

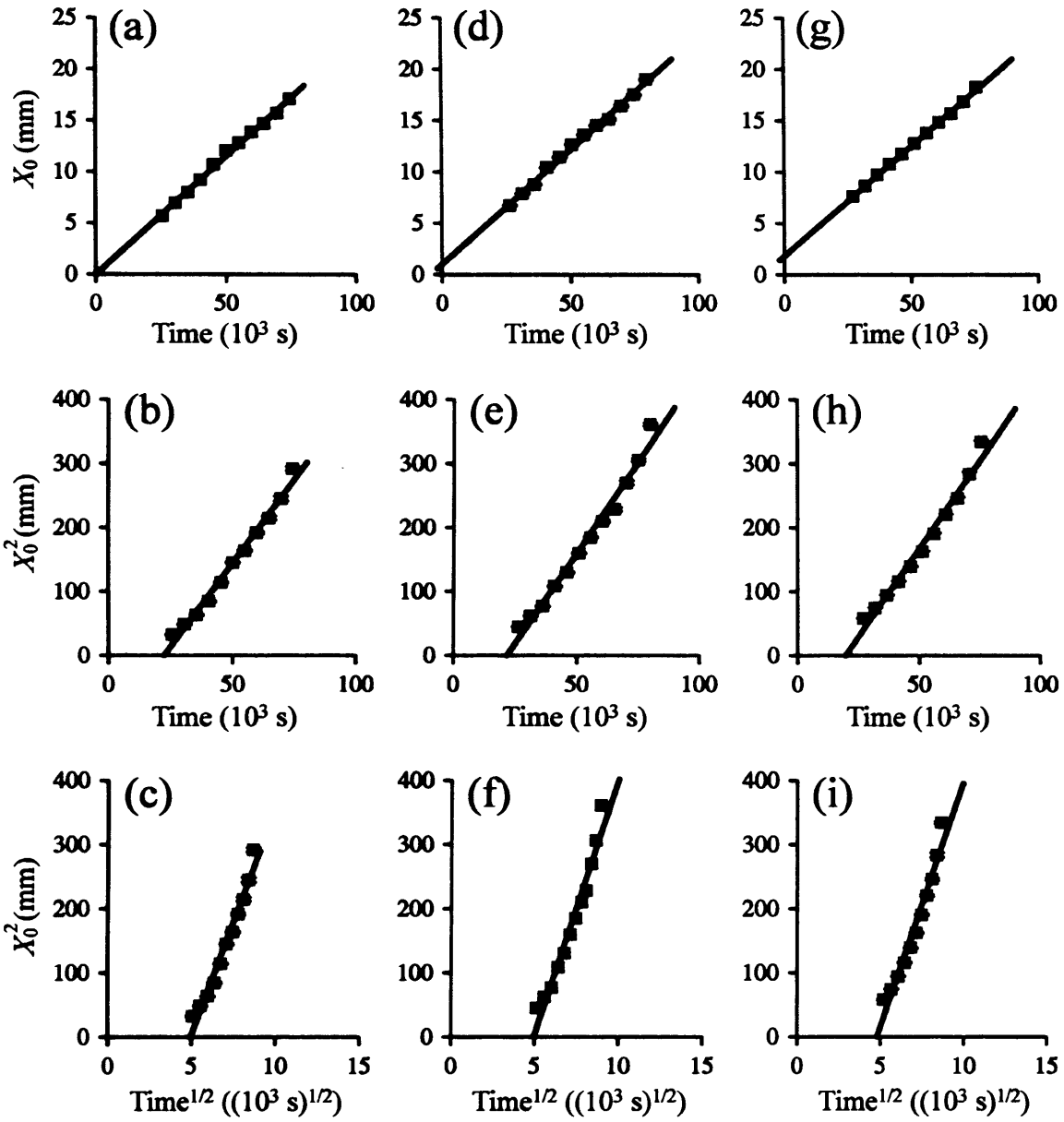

Figure 5.13. Fittings of the front positions, X_0, in the three lines analyzed during molecular exchange of DBO by PD (using two PD reservoirs). The lines were (a), (b) and (c); Y = 0 μm, (d), (e) and (f); Y = 100 μm and (g), (h) and (i) Y = 200 μm. The fitting models were (a), (d) and (g); $X_0 \propto t$, (b), (e) and (h); $X_0^2(t) \propto t$ and (c), (f) and (i); $X_0^2(t) \propto t^{1/2}$.

According to the explanation stated above, it is expected for this process to observe five different stages: (*i*) a flat line with $R_N = 1$ (before molecular exchange begins); (*ii*) two fronts moving in opposite directions $1 > R_N > 0.5$ (Figure 5.15a); (*iii*) a flat line with $R_N = 0.5$ when the two fronts meet (Figure 5.15b), (*iv*) two fronts moving in opposite directions $0 < R_N < 0.5$ (Figure 5.15c); and (*v*) a flat line following complete exchange with $R_N = 0$.

In our experiments, we do initially observe two fronts moving in opposite directions and these two fronts converge to form a flat line. However, we do not observe stages (*iv*) and (*v*).

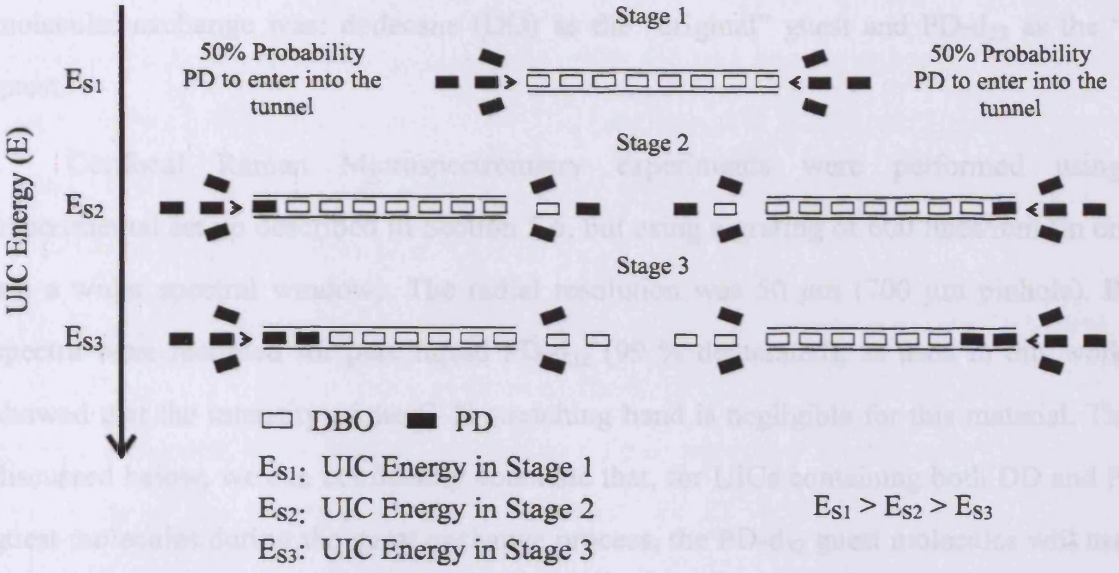

Figure 5.14. Representation showing the equal probability to start the exchange process at both ends of one single tunnel. The UIC is more energetically favourable containing PD guest molecules (black boxes).

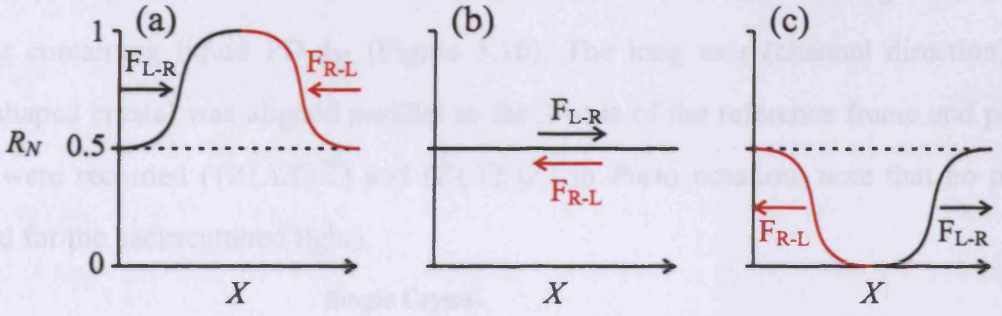

Figure 5.15. Schematic representation for the two diffusing fronts (L-R) and (R-L) moving in opposite directions at three different stages of the molecular exchange process: (a) for values $1 > R_N > 0.5$ behind the two fronts, (b) values of $R_N = 0.5$ after the two fronts have converged into a flat line and, (c) fronts moving in opposite directions $0 < R_N < 0.5$.

5.7.4 Molecular Exchange of *n*-Alkanes

In this work, we study the dependence on the kinetics of the identity (different lengths) of the guest molecules used in the exchange process. Hence, the system used to perform the molecular exchange was: dodecane (DD) as the "original" guest and PD-d_{32} as the "new" guest.

Confocal Raman Microspectrometry experiments were performed using the experimental set up described in Section 5.6, but using a grating of 600 lines/mm (in order to see a wider spectral window). The radial resolution was 50 μm (700 μm pinhole). Raman spectra were recorded for pure liquid PD-d_{32} (99 % deuterated), as used in this work, and showed that the intensity of the C–H stretching band is negligible for this material. Thus, as discussed below, we can confidently conclude that, for UICs containing both DD and PD-d_{32} guest molecules during the guest exchange process, the PD-d_{32} guest molecules will make no significant contribution to the observed C–H stretching band.

The confocal Raman microspectrometry experiments used a single crystal of dodecane/urea (dimensions $1 \times 1 \times 16$ mm^3), which was attached (using Araldite) to a reservoir containing liquid PD-d_{32} (Figure 5.16). The long axis (channel direction) of the needle-shaped crystal was aligned parallel to the X-axis of the reference frame and polarized spectra were recorded ($(Z(XX)\bar{Z}$) and ($Z(XY)\bar{Z}$) in Porto notation; note that no polarizer was used for the backscattered light).

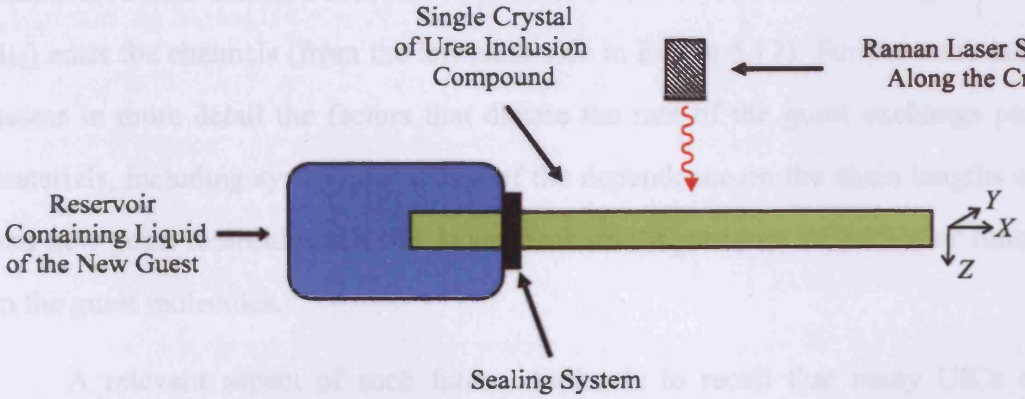

Figure 5.16. Schematic representation of the experimental assembly, comprising the single crystal of the urea inclusion compound (green), initially containing DD guest molecules, attached to a reservoir containing liquid PD-d_{32}. The laboratory reference frame (X, Y, Z) is also defined.

The analysis was performed at a depth $Z = 175$ μm beneath the upper surface of the crystal. The Raman spectra were collected in scans along the *X*-axis with a step size of 400 μm and a total scan range of 14 mm; six separate scans of this type were carried out at *Y*-coordinates separated by 75 μm (the "width" of each scan along *Y*, determined by the spatial resolution, was *ca.* 50 μm). The acquisition time for each Raman spectrum was 2 s, and the time to record each scan was about 70 s. The time to record the complete Raman micrograph of the probed area was thus about 7 min, which is significantly shorter than the overall timescale of the guest exchange process.

To monitor the exchange of guest molecules, the C–H stretching band (2900 cm^{-1}) due to the DD guest molecules was compared to the N–H stretching vibration (3300 cm^{-1}) due to the urea molecules in the host structure. The ratio of integrated intensities $R = I(C–H)/I(N–H)$ was measured and converted to the normalized ratio $R_N = R/R_0$, where R_0 is the value of R (averaged over the probed area) for the original DD/UIC crystal (before starting the guest exchange process). Thus, $R_N = 1$ if the crystal contains only DD guest molecules and $R_N = 0$ if the crystal contains only PD-d_{32} guest molecules (i.e., complete exchange). The value of R_N allows an assessment of the relative amount of DD guest molecules as a function of position in the crystal and as a function of time.

In the results shown in Figure 5.17, it is clear that alkane-alkane guest exchange occurs in this system, with the proportion of the original guest molecules (DD) decreasing as a function of time and as a function of position in the crystal as the new guest molecules (PD-d_{32}) enter the channels (from the left-hand side in Figure 5.17). Further work is in progress to assess in more detail the factors that dictate the rate of the guest exchange process in such materials, including systematic studies of the dependence on the chain lengths of the original and new guest molecules and the dependence on the presence of particular functional groups in the guest molecules.

A relevant aspect of such future studies is to recall that many UICs exhibit three-dimensional ordering of the guest molecules. The inter-channel ordering of guest molecules (characterized by the offset Δ_g shown in Figure 5.18) depends on the functional groups present in the guest molecule and different homologous families of guest molecules exhibit

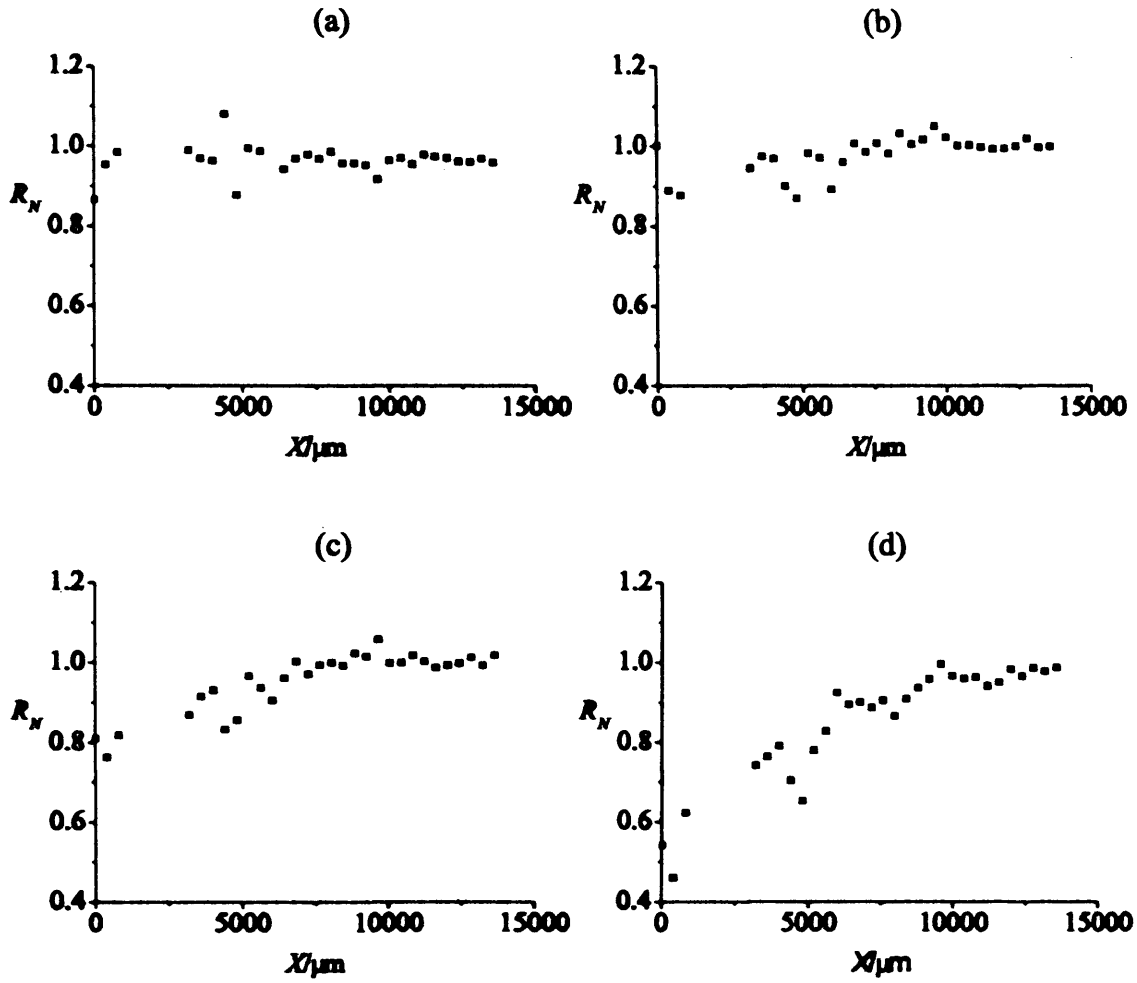

Figure 5.17. Graphs showing the variation of R_N as a function along the tunnel axis (X-axis) for different values of time after commencement of the guest exchange process: (a) 0 hours, (b) 3.6 hours, (c) 10.4 hours, and (d) 19 hours. The crystal is in contact with liquid PD-d_{32} at $X = 0$, and thus the transport of PD-d_{32} guest molecules occurs from left-to-right in the graphs shown. Note that the region of the crystal between about $X = 1200$ μm and $X = 2800$ μm is "hidden" by the sealing system.

characteristic modes of inter-channel ordering. For example, at ambient temperature, $\Delta_g = 0$ Å for alkane/UICs, whereas for α,ω-dibromoalkane/urea inclusion compounds, Δ_g depends on the periodic repeat (c_g) of the guest molecules along the channel by the following relationship: $\Delta_g = c_g/3$.[17]

In our previous experiments involving exchange of 1,8-dibromooctane guest molecules by pentadecane, there is a mismatch in the value of Δ_g between the original and new guest molecules, whereas for alkane-alkane exchange, the original and new guest molecules have the same value of Δ_g. This issue may have an important bearing on the local structure at the interface between the original and new guest molecules in the inclusion compound, and may

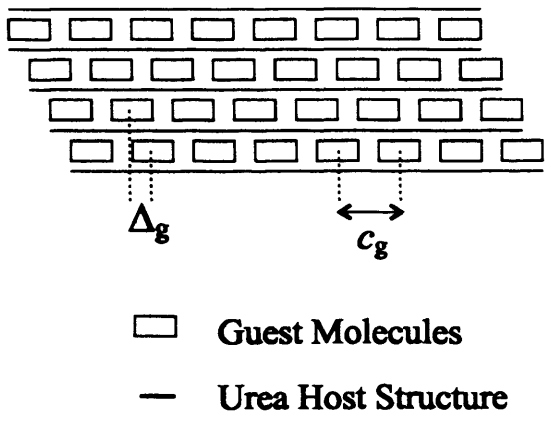

Figure 5.18. Schematic two-dimensional representation of a urea inclusion compound, viewed perpendicular to the channel axis, indicating the definitions of c_g and Δ_g.

therefore have important implications for several aspects of the guest exchange process. Systematic studies of this issue are also central to our on-going research in this field.

In summary, the preliminary results reported in this work provide direct evidence for the occurrence of alkane-alkane guest exchange in urea inclusion compounds, with the alkane of longer chain length (in this case PD) replacing the alkane of shorter chain length (in this case DD). The confocal Raman microspectrometry technique employed in this work, with appropriate deuteration of one of the alkane guest components, represents a viable strategy for *in situ* characterization of the guest exchange process.

5.8 A Theoretical Model

In collaboration with a member of our group (Dr. Hughes), a simple theoretical model has been developed to attempt to predict and understand the transport process under investigation. It is based on treating the insertion of each new guest molecule as a separate step with a rate. To begin with, each rate of insertion was taken to be equal. A set of differential equations was generated and solved to give the concentration as a function of time and position in the crystal. From this, plots corresponding to those presented for the experimental data can be produced. Values of X_0 and Δ can be determined by identifying the point of inflection of plots of concentration against position which are analogous to the values determined experimentally using a sigmoidal fitting procedure. The calculations predict a linear dependence of X_0 upon time, with a gradient equal to k, where k is the rate of insertion

of each new guest molecule. The value of Δ is found to increase with time. A positive induction time is observed.

More complex models have also been employed. First, the rate for the insertion of the first new guest molecule was made different from the rate for all subsequent insertions. Second, an additional, reverse process is considered, in which new guest molecules are expelled by the reintroduction of old guest molecules. Neither of these modifications affect the linearity of the time dependence of X_0, although the gradient and induction time are affected. The value of Δ is again found to increase with time.

5.9 Comparison of Results

Extensive experimental data has been obtained from the four different experiments reported in this chapter as shown in Table 5.1. From this table, we have the values of the rate, the induction time for each process and the values of the standard deviation (R^2) in each case.

From the three different models considered, classical diffusion, single-file diffusion and the linear process, it appears that the best results correspond to the linear process (Eq. 5.8). It is true that there are also good fits corresponding to classical and single-file diffusion but the linear process most commonly gives the best fit to the data. It is interesting to note that the actual transport process itself is single-file, but the kinetics of the overall process depends not only on the transport along the tunnel but also on the processes at the ends of the tunnel. A physical description of the occurrence of this linear process will be presented in the following section.

As mentioned previously, the transport process in UICs is different from that observed in zeolites, therefore, it is not correct to compare the molecular transport process in UIC with that in zeolites. However, to have an approximate idea of how close this process is to the zeolites case, we compared these cases by assuming a single-file model. From this comparison, it is observed that the single-file displacement of guest molecules inside UICs is faster than in zeolites. The calculated value of F in UICs is ~ 10^{-7} $mm^2/s^{1/2}$ and for zeolites is ~ 10^{-12} $mm^2/s^{1/2}$.[18]

Table 5.1. Values corresponding to the linear fittings obtained to determine the induction time (t_0), the transport coefficients considering three models: linear process (X_0 *vs.* t), classical diffusion (X_0^2 *vs.* t) and single-file difussion (X_0^2 *vs.* $t^{1/2}$). Best fittings (R^2) are highlighted in bold.
DBO/PD - Molecular exchange of DBO by PD using one reservoir.
TMP - Molecular exchange of DBO by PD using one PD reservoir and one TMP reservoir.
PD L-R - Molecular exchange (left to right) of DBO by PD using two PD reservoirs.
PD R-L - Molecular exchange (right to left) of DBO by PD using two PD reservoirs.

		Linear			Classical			Single File		
Experiment.	Y (μm)	t_0 (s)	R^2	Grad. (mm/s)	t_0 (s)	R^2	D (mm^2/s)	t_0 (s)	R^2	F (mm^2/s$^{1/2}$)
DBO/PD	0	-2.509×10^{4}	0.9345	2.01×10^{-4}	2.263×10^{4}	0.9509	8.01×10^{-3}	**5.603×10^{3}**	**0.9648**	**1.40×10^{-1}**
	100	-1.798×10^{4}	0.9706	2.05×10^{-4}	2.782×10^{4}	0.9816	8.12×10^{-3}	**5.913×10^{3}**	**0.9834**	**1.44×10^{-1}**
	200	5.144×10^{3}	0.9762	2.27×10^{-4}	**4.419×10^{4}**	**0.9764**	**8.40×10^{-3}**	6.977×10^{3}	0.9753	1.56×10^{-1}
TMP	0	1.865×10^{3}	0.9728	1.77×10^{-4}	3.655×10^{4}	0.9890	4.64×10^{-3}	**6.397×10^{3}**	**0.9909**	**7.68×10^{-2}**
	100	-4.417×10^{3}	0.9819	1.75×10^{-4}	3.670×10^{4}	0.9967	5.20×10^{-3}	**6.502×10^{3}**	**0.9992**	**8.60×10^{-2}**
	200	**2.454×10^{3}**	**0.9914**	**2.20×10^{-4}**	3.551×10^{4}	0.9681	6.84×10^{-3}	6.219×10^{3}	0.9483	1.04×10^{-1}
PD L-R	0	**3.689×10^{1}**	**0.9952**	**2.30×10^{-4}**	2.231×10^{4}	0.9878	5.24×10^{-3}	4.955×10^{3}	0.9693	8.63×10^{-2}
	150	**-4.664×10^{3}**	**0.9959**	**2.22×10^{-4}**	2.163×10^{4}	0.9818	5.67×10^{-3}	4.947×10^{3}	0.9599	7.96×10^{-2}
	300	**-8.550×10^{3}**	**0.9987**	**2.14×10^{-4}**	1.956×10^{4}	0.9809	5.48×10^{-3}	4.784×10^{3}	0.9586	7.59×10^{-2}
PD R-L	0	**-6.330×10^{4}**	**0.9906**	**2.16×10^{-4}**	-6.925×10^{2}	0.9872	11.76×10^{-3}	3.853×10^{3}	0.9823	1.84×10^{-1}
	150	**-4.256×10^{4}**	**0.9959**	**2.41×10^{-4}**	1.012×10^{4}	0.9937	12.25×10^{-3}	4.584×10^{3}	0.9909	1.97×10^{-1}
	300	**-6.858×10^{4}**	**0.9998**	**1.87×10^{-4}**	2.765×10^{3}	0.9939	9.17×10^{-3}	3.801×10^{3}	0.9952	1.46×10^{-1}

Interestingly, it has been found that the width of the diffusion front is not constant during the course of molecular exchange. An increase of Δ towards the end of the process is observed. It has been observed that there is an induction time, that is, at early stages of the process, there is a delay before any significant amount of exchange is observed. The induction time, according to the kinetic model defined in Section 5.4, is expected to be positive but, due to the difficulties in determining the exact position of $X = 0$ (e.g., due to the rough shape of the end of the crystal) this induction time can appear to be negative.

The values of the gradient assuming a linear process are similar in all experiments, $\sim 2\times10^{-4}$ mm/s. It is important to notice that, within a given single crystal, the time dependence of the molecular transport process is homogeneous, that is, that we do not observe large differences in the kinetics in different regions of the crystal. No major differences in the kinetics of the process have been observed between the experiments in which the single crystal was in contact with liquid at only one end or both ends. It seems that the molecular transport process depends more upon the details of the insertion rather than expulsion of guest molecules.

A considerable effect upon the kinetics of the transport process has been observed depending on the identity of the guest molecules. For alkane-alkane exchange (using dodecane (DD) as the "original" guest and pentadecane (PD) as the "new" guest), the kinetics of the exchange is considerably slower than in the case for DBO as the original guest and PD as the new guest. Clearly a wider range of experiments is needed before the underlying reason for this observation can be understood. The much slower rate of exchange may be dependent on the fact that the energy difference between compounds is less for the DD/PD case than the DBO/PD case (on account, probably, of the more similar lengths of the guest molecules in the former case), but such a conclusion must wait until systematic studies of the effect of chain length have been carried out.

5.10 Conclusions

As far as we know, this is the first time that *in situ* studies of guest exchange in UICs have been carried out. It has been demonstrated how this molecular exchange process is reproducible. During these experiments, different set ups for studying the transport of guest

molecules using confocal Raman microspectrometry have been designed and constructed. Two different set ups have been developed: *i*) one reservoir set-up, in which the transport process occurs only from one end and *ii*) two reservoir set-up in which the transport process can occur from both ends.

Different number of experiments have been carried out in which it has been found, using confocal Raman microspectrometry, that the molecular transport process can be monitored *in situ*, yielding valuable information on the kinetics as well as other mechanistic insights (i.e., the shape of the diffusion front and the induction time) of the transport process of α,ω-dibromoalkanes and *n*-alkane molecules within the one-dimensional tunnel architecture of UICs. Furthermore, a preliminary mathematical model has been developed. With this mathematical approach, it can be shown that the dependence of X_0 upon time is linear. The experimental data and the theoretical approach are in good agreement as stated above.

From the results obtained in this work, it appears that the introduction of guest molecules inside the tunnels can be considered as the rate-determining step. Once the guest molecules are inside the tunnels, the rate of transport appears to be constant. The physical explanation of this process is that once the guest molecules are inserted into the urea tunnel, and since it is a linear process, the molecules can only move in one direction (*c* axis in the UIC case). There is no external force applying a backwards movement to the guest molecules since the insertion of an "old" guest molecule is not likely by the fact that: (*i*) DBO guest molecules which are expelled from the tunnel undergo evaporation (i.e., one reservoir experiment) or are diluted in liquid PD or TMP (i.e., two reservoir experiments) and, (*ii*) the process of inserting DBO guest molecules is not an energetically favourable process.

A schematic representation of these three different processes is given in Figure 5.19. As a process itself, the guest molecules are absorbed by the host tunnel and, once they start migrating through the tunnels, the kinetic process is linear with time. Therefore, this molecular transport is neither a classical diffusion nor a single-file process. In essence, the entry of guest molecules into the tunnel is a critical aspect of the process, which may indeed

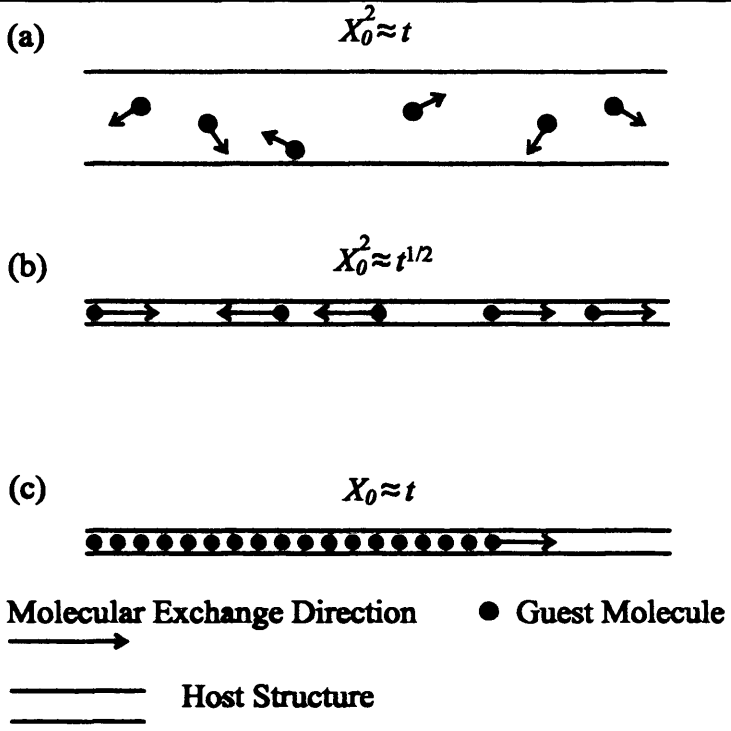

Figure 5.19. Schematic representation of the random walk process in classical diffusion (a), single file diffusion (b) and linear process (c) observed in this experiments.

dictate the kinetics of the entire exchange process. In many other systems exhibiting one-dimensional diffusion, this is not the case.

Crucially, the stability of the urea tunnel structure is an important aspect of the molecular exchange. Therefore, the guest exchange is *only* possible if the tunnels are filled of guest molecules at any time during the molecular exchange. We believe that this structural aspect may have a direct influence upon the kinetics of the molecular transport process (i.e., host-guest interaction).

There is a large dependence of the transport upon the identity (chain length) of the guest molecules. This indicated that the driving force for the molecular exchange to occur is the greater thermodynamic stability of the long-chain guests in UICs. In summary, the preliminary results reported in this work provide direct evidence for the occurrence of alkane-alkane guest exchange in urea inclusion compounds, with the alkane of longer chain length (in this case PD) replacing the alkane of shorter chain length (in this case DD). The confocal Raman microspectrometry technique employed in this work, with appropriate deuteration of one of the alkane guest components, represents a viable strategy for *in situ* characterization of the guest exchange process.

5.11 Future Work

An important aspect of future research will be to carry out an extensive set of experiments for several different combinations of alkane/α,ω-dihalogenalkane guest molecules as a function of chain length. These experiments will give valuable information upon the effect of the chain length of the guest molecules (since in this work only one experiment has been performed), and also information depending on the size and identity of the halogen used (i.e., Cl, F, I). Using a bigger halogen in the guest molecule may have an influence upon the transport process.

Another important aspect is the design and construction of an appropriate cell for *in situ* studying the temperature and pressure dependence of this molecular transport process. With these experiments it will be possible to determine the activation parameters of this process.

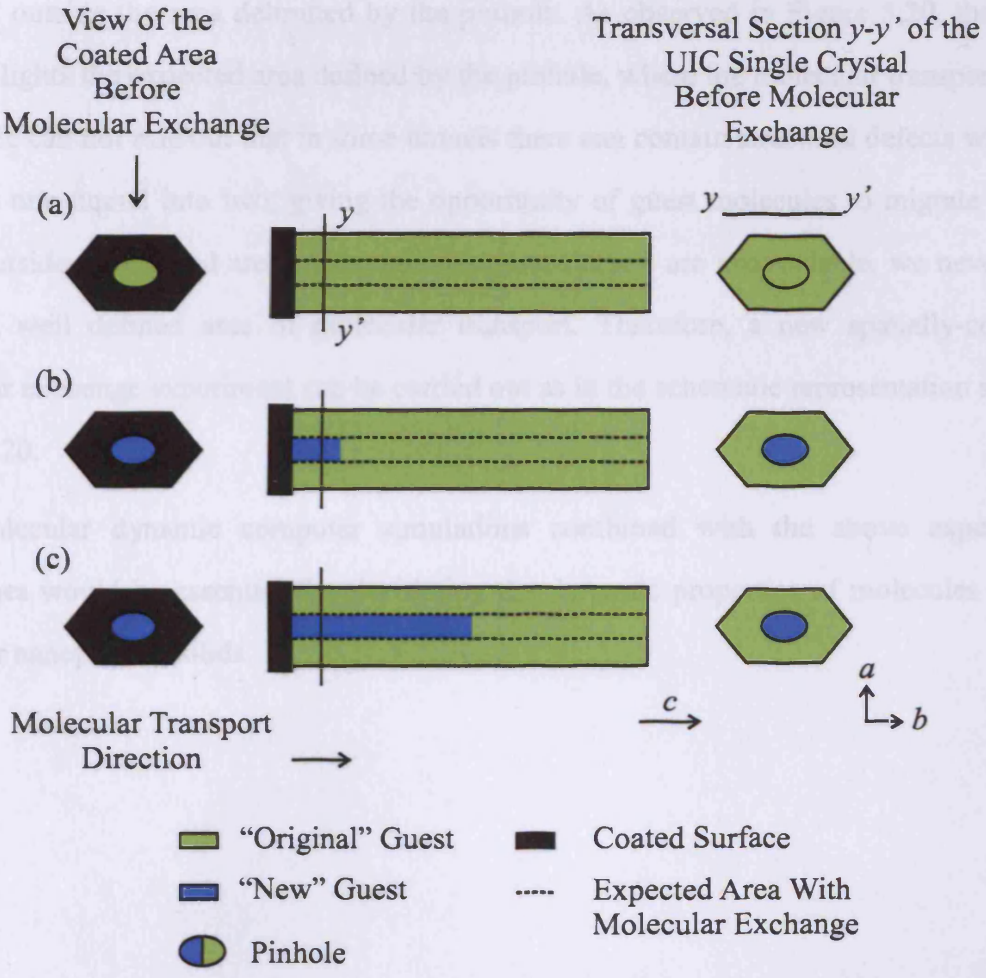

Figure 5.20. Schematic representation concerning the experimental set up using a coated crystal at one end. As observed (blue area) it is expected that the molecular exchange will be observable only in the central area delimited by the dashed lines.

Size and shape of the single crystal used in the experiment may have also some influence upon the molecular exchange. Carrying out an extensive set of experiments for a range of different lengths (long or short) and shapes (flat or round) of single crystals will provide interesting information on the exchange process.

It is believed that the shape of the single crystal that is in contact with the liquid containing the potential "new" guest may have some bearing upon the shape of the diffusion front (see Section 5.7.1). Therefore, if we are able to partially cover the surface of the single crystal which is inside the reservoir, thus leaving a pinhole where the crystal is in contact with the liquid containing "new" guests (for detailed explanation of the experimental set up see Figure 5.20), we can monitor the transport of guest molecules only in a specific area of the crystal. As the tunnels in the UIC are parallel to each other, we would not expect molecular transport outside the area delimited by the pinhole. As observed in Figure 5.20, the dashed line highlights the expected area defined by the pinhole, where the molecular transport should occur. We can not rule out that in some tunnels there can contain structural defects which can bifurcate one tunnel into two, giving the opportunity of guest molecules to migrate to some points outside the dashed area. Although structural defects are unavoidable, we nevertheless expect a well defined area of molecular transport. Therefore, a new spatially-controlled molecular exchange experiment can be carried out as in the schematic representation shown in Figure 5.20.

Molecular dynamic computer simulations combined with the above experimental approaches would be essential for elucidating the dynamic properties of molecules in UICs and other nanoporous solids.

References for Chapter 5

[1] A. Corma, *Chem. Rev.*, **1995**, *95*, 559.

[2] A. Einstein, *Ann. Phys.*, **1905**, *17*, 549.

[3] E. J. Harris, *Transport and Accumulation in Biological Systems*, Butterworths Scientific, London, **1960**.

[4] B. Alberts et al., *Molecular Biology of the Cell*, Garland, New York, **1994**.

[5] J. Karger and D. M. Ruthven, *Diffusion in Zeolites and other Microporus Solids*, Wiley, New York, **1992**.

[6] N. Y. Chen, T. F. Degnan and C. M. Smith, *Molecular Transport and Reaction in Zeolites*, VCH, New York, **1994**.

[7] J. Kärger, M. Petzold, H. Pfeifer, S. Ernst, and J. Weitkamp, *J. Catal.*, **1992**, *136*, 283.

[8] T. Halpin-Healy and Y. C. Zhang, *Phys. Rep.*, **1995**, *254*, 215.

[9] S. Alexander and P. Pincus, *Phys. Rev. B.*, **1978**, *18*, 2011.

[10] H. van Beijeren, K. W. Kehr and R. Kutner, *Phys. Rev.* B., **1983**, *28*, 5711.

[11] J. Kärger, *Phys. Rev. A.*, **1992**, *45*, 4173.

[12] J. Kärger *Phys. Rev. E.*, **1993**, *47*, 1427.

[13] D. G. Levitt, *Phys. Rev., A*, **1973**, *8*, 3050.

[14] G. Nägle, *Phys. Rep.*, **1996**, *272*, 215.

[15] J. K. G. Dhont, *J. Chem. Phys.*, **1992**, *96*, 4591.

[16] J. Martí-Rujas, A. Desmedt, K.D.M. Harris, F. Guillaume, *J. Am. Chem. Soc.*, **2004**, *126*, 11124.

[17] K.D.M. Harris, *Chem. Soc. Rev.*, **1997**, 26, 279.

[18] K. Hahn, J. Kärger and V. Kukla, *Phys Rev. Lett.*, **1996**, *76*, 2762.

Chapter 6 Design of Urea, *p*-Phenylenediamine and α,ω-Dihydroxyalkanes Co-Crystals

6.1 Introduction

In this chapter, the crystal structures and packing of nine new co-crystals are presented. These new co-crystals can be described in terms of two major types of hydrogen-bonded array motif between OH and NH_2 groups: the double-stranded ribbon motif and the infinite chain geometry. The prediction of homologous structures based on crystal engineering grounds has been achieved with the design of these new co-crystals.

6.2 Crystal Engineering

The absence of a direct correspondence between molecular functionality and crystal structure is a great challenge in the design and engineering of molecular crystals.[1,2] Therefore, the supramolecular behaviour of a functional group in a molecule depends on the location of the other functional groups. Crystal structures arise, therefore, from a complex convolution of recognition events.[3-5] The definition of well-defined interaction motifs in crystals leads[6] to a simplification of this complexity, based on the fact that these motifs are reproduced from structure to structure and can be found within a family of molecules. Much of the fundamental work in current crystal engineering is geared towards developing a reliable understanding of preferred interaction motifs, judged by the frequency of occurrence of specific intermolecular interactions and connectivities.[7]

Alcohol and primary amine molecules do not by themselves, completely satisfy, their potential for hydrogen bonding. This follows simply from the fact that the number of respective donors and acceptors are different. While the hydroxyl function can donate one H atom to a hydrogen bond and receive two hydrogen bonds as acceptor (the two oxygen lone pairs), the amino group involves two donor H atoms but only one acceptor size.

With regard to hydrogen bonding, alcohols and amines are obviously complementary, both stoichiometrically and geometrically. Interchange of hydrogen bond donors and acceptors transforms the bonding pattern of the hydroxyl group into that of the amino group,

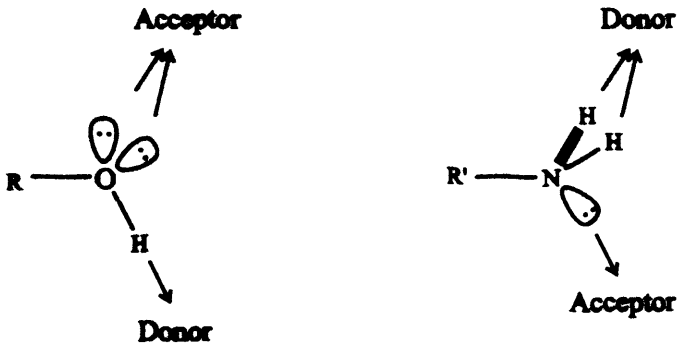

Figure 6.1. H – Bond donor-acceptor complementarity of alcohols and amines.

and *vice versa*, and in both cases the geometric disposition of the valencies is tetrahedral (Figure 6.1). Therefore, molecular recognition may be expected between alcohols and primary amines, since complementarities represent the crucial prerequisite supporting favourable interactions between molecular partners.

Recently, a new crystal structure formed between urea and 1,4-dihydroxybutane has been reported.[8] In this structure, the amino groups from the urea molecules form a hydrogen-bonded network with double-stranded ribbons that run parallel to the *a*-axis. The two strands of the ribbon are linked by a network of N – H···O hydrogen bonds between urea molecules, involving the C = O group and one NH_2 of each urea molecule. The other NH_2 group of each urea molecule protrudes from the edge of the ribbon. For these NH_2 groups, each N – H bond is engaged in a N – H···O hydrogen bond with the OH group of 1,4-dihydroxybutane molecule, and each OH group is involved in two N – H···O hydrogen bonds with different urea molecules.

By examining this structure, the question arose as to whether this structure could be reproduced with longer α,ω-dihydroxyalkanes (a homologous structure) and whether it would be possible to prepare the same type of molecular arrangement by exchanging two urea molecules by one molecule of *p*-phenylenediamine, as it may be expected that this change will not strongly affect the molecular arrangement of the co-crystal (see Figure 6.2b). To study this question, we have prepared different co-crystals with the following compounds: urea (U), *p*-phenylenediamine (PDA) and a series of different α,ω-dihydroxyalkanes: 1,5-dihydroxypentane (1,5-DHP), 1,6-dihydroxyhexane (1,6-DHH_x), 1,7-dihydroxyheptane (1,7-DHH_p), 1,8-dihydroxyoctane (1,8-DHO), 1,9-dihydroxynonane (1,9-DHN), 1,10-dihydroxydecane (1,10-DHD), 1,12-dihydroxydodecane (1,12-DHDD), 1,16-

dihydroxyhexadecane (1,16-DHHD), and 1,4-dihydroxycyclohexane (1,4-DHCH) (see Figure 6.2a). The formation and structures of these complexes are governed by the principles of amine-hydroxy recognition.[9]

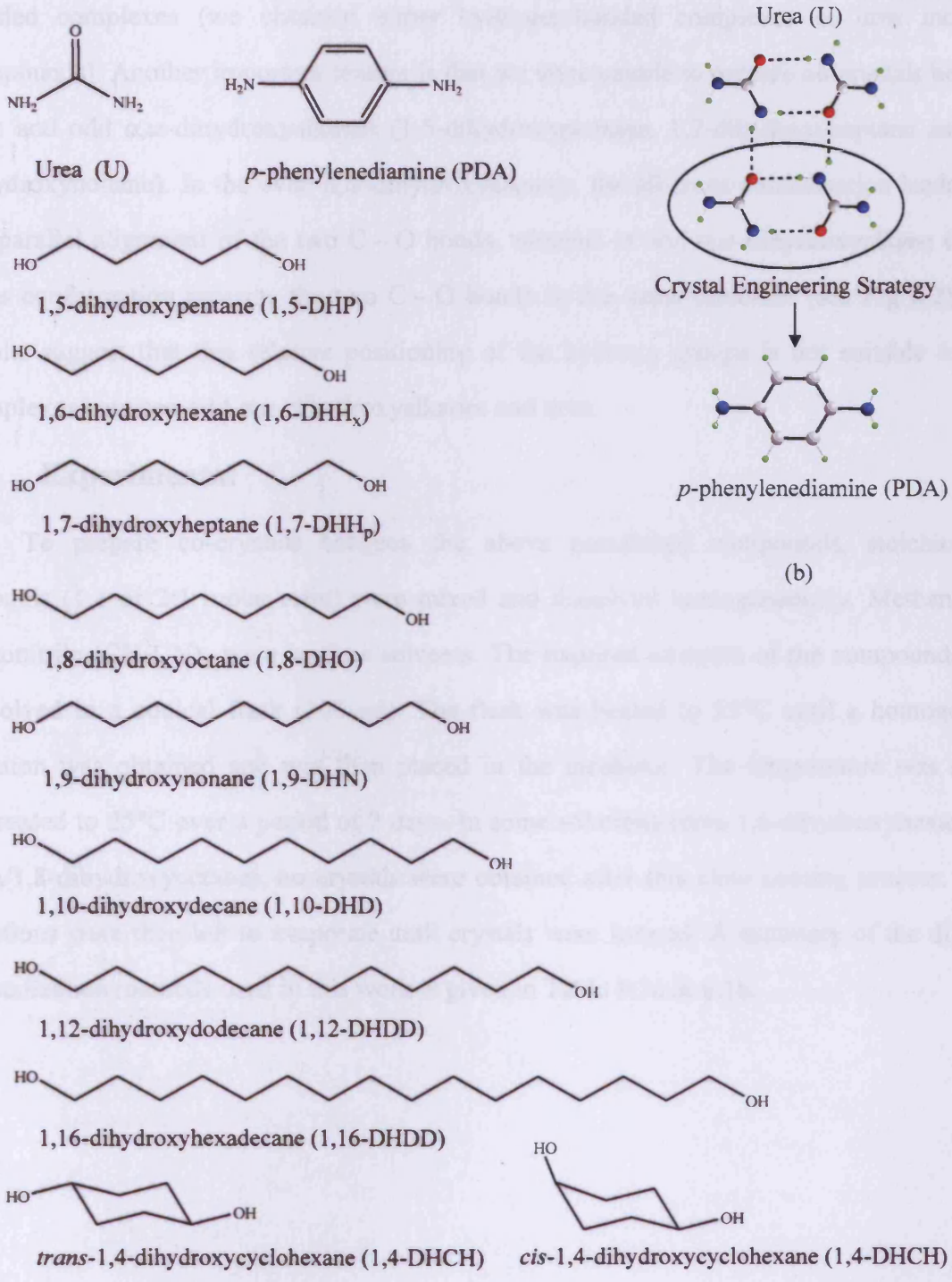

Figure 6.2. (a) List of molecules used in this work and (b) proposed molecular substitution based on crystal engineering grounds.

In the attempts to prepare complexes between urea and α,ω-dihydroxyalkanes, we sometimes also obtained conventional urea inclusion compounds (UICs). Interestingly, these urea inclusion compounds did not crystallize together in the same solution with the hydrogen-bonded complexes (we obtained either hydrogen-bonded complexes or urea inclusion compounds). Another important feature is that we were unable to prepare co-crystals between urea and odd α,ω-dihydroxyalkanes (1,5-dihydroxypentane, 1,7-dihydroxyheptane and 1,9-dihydroxynonane). In the even α,ω-dihydroxyalkanes, the all-*trans* conformation leads to an antiparallel alignment of the two C – O bonds, whereas in odd α,ω-dihydroxyalkane the all-trans conformation projects the two C – O bonds in the same direction (see Fig 6.2).[7] Our results suggest that this relative positioning of the hydroxy groups is not suitable to form complexes between odd α,ω-dihydroxyalkanes and urea.

6.3 Experimental

To prepare co-crystals between the above mentioned compounds, stoichiometric amounts (1:1 or 2:1 molar ratio) were mixed and dissolved homogeneously. Methanol and acetonitrile (CH_3CN) were used as solvents. The required amounts of the compounds were dissolved in a conical flask (100 ml). The flask was heated to 55°C until a homogeneous solution was obtained and was then placed in the incubator. The temperature was slowly decreased to 25°C over a period of 2 days. In some solutions (urea/1,6-dihydroxyhexane and urea/1,8-dihydroxyoctane), no crystals were obtained after this slow cooling process. These solutions were then left to evaporate until crystals were formed. A summary of the different crystalization methods used in this work is given in Table 6.1a & 6.1b.

Table 6.1a. Summary of all experimental methods used to synthesize the single crystals.

A	B	Solvent	Ratio	Crystallization Method	Crystal Type
Urea	1,4-DHCH	CH_3CN	1:1	Slow cooling	Urea
		CH_3CN	2:1	Slow cooling	No crystallization
		MeOH	1:1	Slow cooling	No crystallization
		MeOH	2:1	Slow cooling	Co-crystal
Urea	1,5-DHP	CH_3CN	1:1	Slow cooling	Urea
		CH_3CN	2:1	Slow cooling	No crystallization
		MeOH	1:1	Slow cooling	UIC
		MeOH	2:1	Slow cooling	Urea
Urea	1,6-DHH_x	CH_3CN	1:1	Slow cooling	Urea
		CH_3CN	2:1	Slow cooling	1,6-DHH_x
		MeOH	1:1	Evaporation	Urea
		MeOH	2:1	Evaporation	Co-crystal
Urea	1,7-DHH_p	CH_3CN	1:1	Slow cooling	No crystallization
		CH_3CN	2:1	Slow cooling	No crystallization
		MeOH	1:1	Slow cooling	Urea
		MeOH	2:1	Slow cooling	Urea
Urea	1,8-DHO	CH_3CN	1:1	Evaporation	Urea
		CH_3CN	2:1	Evaporation	Urea
		MeOH	1:1	Evaporation	Urea
		MeOH	2:1	Evaporation	Co-crystal
Urea	1,9-DHN	CH_3CN	1:1	Slow cooling	1,9-DHN
		CH_3CN	2:1	Slow cooling	Urea
		MeOH	1:1	Slow cooling	UIC
		MeOH	2:1	Slow cooling	Urea
Urea	1,10-DHD	CH_3CN	1:1	Slow cooling	No crystallization
		CH_3CN	2:1	Slow cooling	No crystallization
		MeOH	1:1	Slow cooling	UIC
		MeOH	2:1	Slow cooling	Co-crystal
Urea	1,12-DHDD	CH_3CN	1:1	Slow cooling	1,12-DHDD
		CH_3CN	2:1	Slow cooling	1,12-DHDD
		MeOH	1:1	Evaporation	UIC
		MeOH	2:1	Evaporation	Co-crystal

Table 6.1b. Summary of all experimental methods used to synthesize the single crystals.

A	B	Solvent	Ratio	Crystallization Method	Crystal Type
PDA	1,4-DHCH	CH_3CN	1:1	Slow cooling	Co-crystal
		CH_3CN	2:1	Slow cooling	PDA
		MeOH	1:1	Slow cooling	No crystallization
		MeOH	2:1	Slow cooling	No crystallization
PDA	1,5-DHP	CH_3CN	1:1	Slow cooling	PDA
		CH_3CN	2:1	Slow cooling	PDA
		MeOH	1:1	Slow cooling	No crystallization
		MeOH	2:1	Slow cooling	No crystallization
PDA	1,7-DHHp	CH_3CN	1:1	Slow cooling	PDA
		CH_3CN	2:1	Slow cooling	PDA
		MeOH	1:1	Slow cooling	No crystallization
		MeOH	2:1	Slow cooling	No crystallization
PDA	1,8-DHO	CH_3CN	1:1	Slow cooling	Co-crystal
		CH_3CN	2:1	Slow cooling	PDA
		MeOH	1:1	Slow cooling	No crystallization
		MeOH	2:1	Slow cooling	No crystallization
PDA	1,9-DHN	CH_3CN	1:1	Slow cooling	1,9-DHN
		CH_3CN	2:1	Slow cooling	PDA
		MeOH	2:1	Slow cooling	No crystallization
		MeOH	1:1	Slow cooling	No crystallization
PDA	1,10-DHD	CH_3CN	1:1	Slow cooling	Co-crystal
		CH_3CN	2:1	Slow cooling	PDA
		MeOH	2:1	Slow cooling	No crystallization
		MeOH	1:1	Slow cooling	No crystallization
PDA	1,12-DHDD	CH_3CN	1:1	Slow cooling	Co-crystal
		CH_3CN	2:1	Slow cooling	PDA
		MeOH	2:1	Slow cooling	No crystallization
		MeOH	1:1	Slow cooling	No crystallization

All crystalline samples collected were characterized first by powder X-ray diffraction (PXRD) at ambient temperature on a Bruker D8 diffractometer (operating in transmission mode using Ge-monochromated Cu($K_{\alpha 1}$) radiation with a linear position-sensitive detector covering 12° in 2θ). The powder diffractograms were recorded in the range 3.5-50° using a step size 0.017°. Crystal structures were determined by single crystal X-ray diffraction. Data were collected on an Enraf-Nonius Kappa CCD diffractometer at 150 K using monochromated Mo($K_{\alpha 1}$) radiation ($\lambda = 0.71073$ Å) and for the experiments carried out at room temperature, single crystal X-ray diffraction was performed using graphite-monochromated Cu-Kα radiation ($\lambda = 1.54178$ Å) on a Bruker SMART diffractometer equipped with a CCD area detector. Differential scanning calorimetric (DSC) data were recorded for all samples on a TA differential scanning calorimeter.

6.4 Results

6.4.1 Optical Microscopy Investigations

Initially, the single crystals were examined by optical microscopy. For the complexes formed between urea and diols, we can distinguish between: (i) long, thin needles and (ii) eight-sided prisms. All of these samples were colourless. The crystals prepared between *p*-phenylenediamine and diols are brown in colour. In this case, all the crystals collected were eight-sided flat plates. Colourless hexagonal needles and flat hexagonal plates for conventional urea inclusion compounds were also obtained.

6.4.2 Preliminary Characterisation by Powder X-Ray Diffraction

All the samples prepared were initially characterized by PXRD. The diffractograms showed that it is possible to obtain co-crystals between urea and diols as well as conventional urea inclusion compounds. Although urea inclusion compounds were formed, we did not study them, as our main interest here was to study the hydrogen-bonded complexes network between urea and diols. In all the new complexes formed, we did not observe any impurity of urea inclusion compounds in the PXRD pattern. Complexes between *p*-phenylenediamine and diols were also prepared. Figure 6.3 shows the PXRD pattern for a conventional urea inclusion compound with 1,10-dihydroxydecane as the guest component. Figure 6.4 shows the PXRD pattern for the sample obtained by crystallization of urea and 1,10-dihydroxydecane from methanol solution. Clearly, the sample obtained by crystallization of urea and 1,10-dihydroxydecane from methanol solution is not a conventional urea inclusion compound.

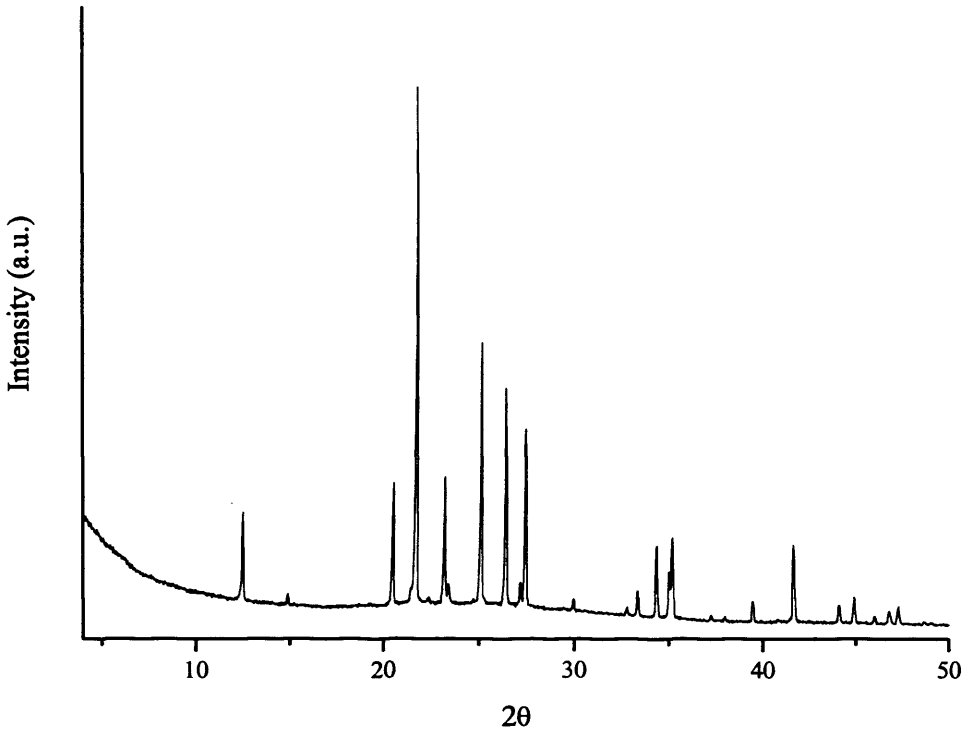

Figure 6.3. PXRD pattern recorded at ambient temperature ($K_{\alpha 1}$(Cu) radiation) for the sample prepared between urea and 1,10-dihydroxydecane from methanol solution. A typical pattern of UICs is clearly observed.

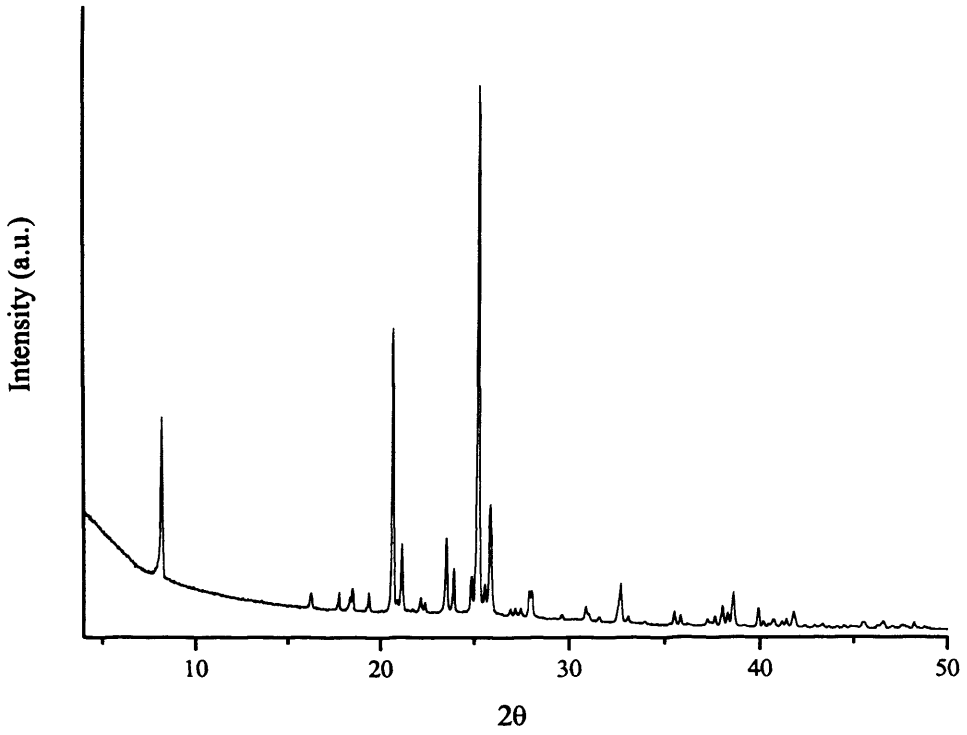

Figure 6.4. PXRD pattern recorded at ambient temperature ($K_{\alpha 1}$(Cu) radiation) for the sample prepared between urea and 1,10-dihydroxydecane from methanol solution.

6.4.3 Structural Properties

This section discusses first the crystal structures of the hydrogen-bonded complexes formed between urea and diols. Secondly, all the structural information for the complexes formed between *p*-phenylenediamine and diols is presented. A detailed description of the crystal packing for each hydrogen-bonded complex is given (heavy atom-heavy atom distances are measured). Following the preliminary characterization described in the previous section, all crystal structures were solved by single crystal X-ray diffraction. These investigations reveal that urea and *p*-phenylenediamine can form complexes with different alcohols. Due to experimental conditions, three of the crystal structures have been determined at room temperature, whereas the other six structures were determined at 150 K. We note that DSC has shown that there is no phase transition on going from room temperature to 150 K in any of the hydrogen-bonded complexes. In all cases, the powder XRD pattern simulated from the known crystal structure is identical to the experimental powder XRD pattern, and therefore the single crystal selected for the single crystal XRD experiments is representative of the bulk phase.

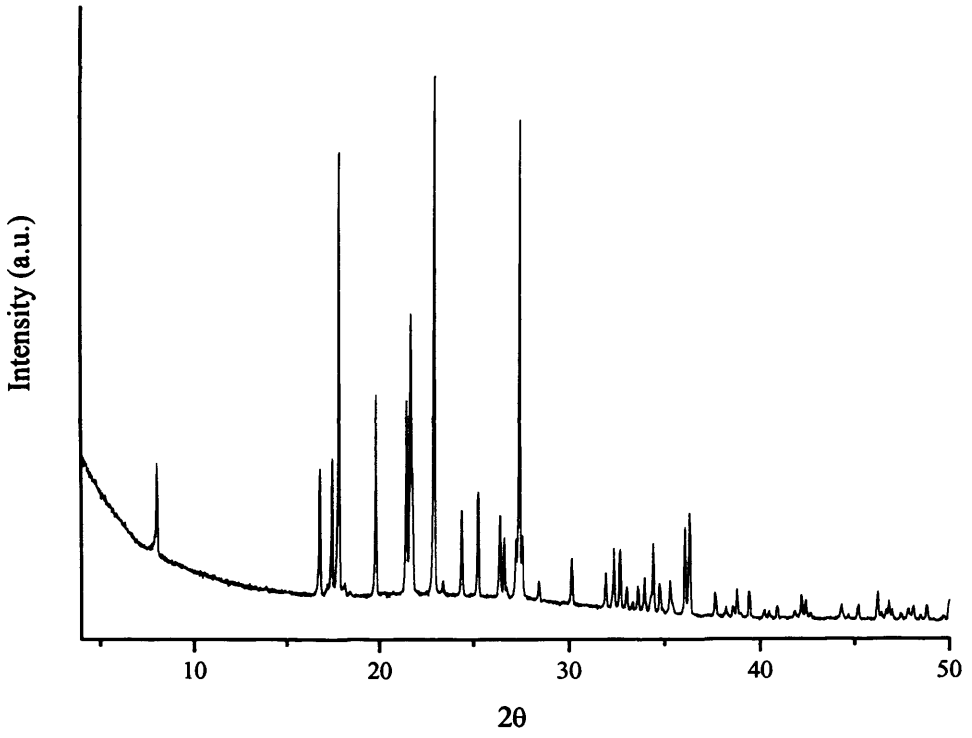

Figure 6.5. PXRD diffractogram recorded for the urea/1,4-cyclohexanediol.

6.4.3.1 Urea/1,4-Dihydroxycyclohexane Co-Crystal

The structure of the urea/1,4-dihydroxycyclohexane complex was solved by single crystal X-ray diffraction at 150 K. The crystal structure is triclinic (space group $P\bar{1}$; $a = 5.140(2)$ Å, $b = 5.372(2)$ Å, $c = 11.158(6)$ Å; $\alpha = 96.940(2)°$, $\beta = 99.185(3)°$, $\gamma = 100.942(3)°$; $V = 294.96(25)$ Å^3; $Z = 1$; $D_c = 1.330$ mg m^{-3}; $R = 0.0403$). The PXRD shows no evidence of urea inclusion compounds (Figure 6.5). Structural parameters are listed in the Appendix, Tables A1 & A2.

The crystal structure contains urea and 1,4-dihydroxycyclohexane in a 2:1 ratio. In this structure, urea molecules are hydrogen bonded to each other to form double-stranded ribbons that run parallel to the *a*-axis (Figure 6.6). The two strands of the ribbon are linked by a network of N – H···O hydrogen bonds between urea molecules, involving the C = O group and one NH_2 group of each molecule, containing two different types of cyclic hydrogen-bonded array ($R_2^2(8)$ and $R_4^2(8)$ in graph set notation[10-12]) alternating along the centre of the ribbon. The urea molecules are in a head-to-tail alignment, linked by an inversion centre. The geometry of these hydrogen bonds are N – H_U···O_U: 2.992 Å, 160.1° and N – H_U···O_U: 2.896 Å, 141.7°.

The other NH_2 group of each urea molecule protrudes from the edge of the ribbon with a periodic spacing of 5.140 Å. For the pendant NH_2 groups, each N – H bond is engaged in an

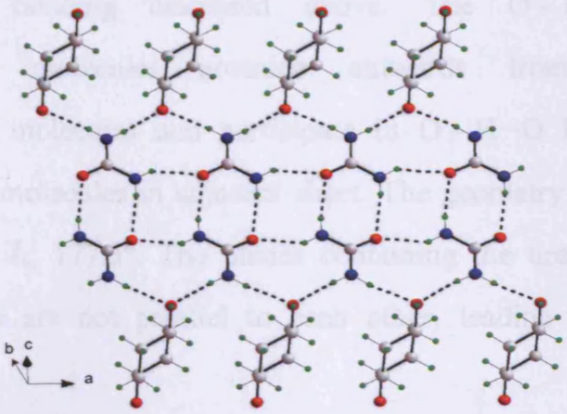

Figure 6.6. Molecular arrangement of urea/1,4-dihydroxycyclohexane showing the urea molecules propagating along the *a*-axis. The dotted lines represent the hydrogen-bonding network between urea-urea molecules and between urea and 1,4-dihydroxycyclohexane molecules. Red, blue, grey and green show oxygen, nitrogen, carbon and hydrogen atoms respectively.

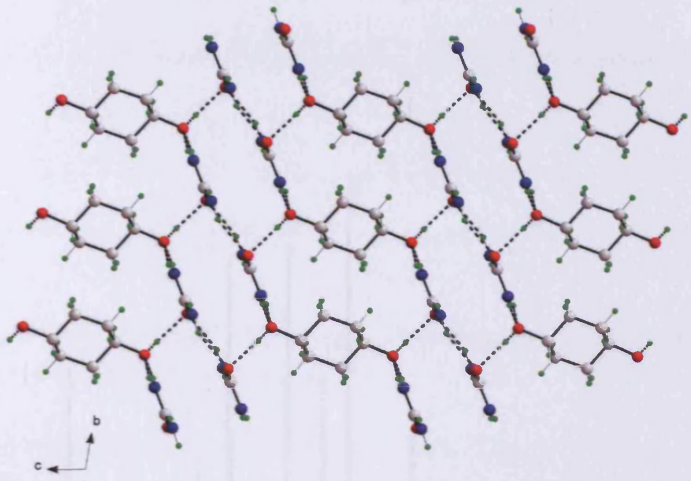

Figure 6.7. View of the urea/1,4-dihydroxycyclohexane viewed perpendicular to the *bc* plane with the urea ribbons running parallel to the *a* axis.

N – H···O hydrogen bond with the OH group of a 1,4-dihydroxycyclohexane molecule and each OH group is involved in two N – H···O hydrogen bonds of this type with two different urea molecules. The geometry of these hydrogen bonds is: N – H_U···O_{DHCH}: 2.984 Å, 172.6°, and N – H_U···O_{DHCH}: 3.020 Å, 169.9°.

The 1,4-dihydroxycyclohexane molecules that form hydrogen bonds with the NH_2 groups along a given edge of a urea ribbon are themselves arranged in a planar ribbon-like manner, with OH groups running along each edge of the ribbon. Each edge of the urea ribbon is linked to the edge of a 1,4-dihydroxycyclohexane ribbon and, vice versa, by means of the N – H···O hydrogen bonding discussed above. The O – H bonds of the 1,4-dihydroxycyclohexane molecules protrude outwards from the sheet of 1,4-dihydroxycyclohexane molecules and participate in O – H···O hydrogen bonds with the oxygen atoms of urea molecules in adjacent sheet. The geometry of this hydrogen bond is: O – H_{DHCH}···O_U: 2.715 Å, 177.3°. The planes containing the urea molecules and the 1,4-dihydroxycyclohexanes are not parallel to each other, leading to a corrugated sheet as observed in Figure 6.7.

6.4.3.2 Urea/1,6-dihydroxyhexane Co-Crystal

The crystal structure corresponding to the urea/1,6-dihydroxyhexane complex was solved by single crystal X-ray diffraction, measured at room temperature. The crystal structure is triclinic (space group $P\bar{1}$; a = 5.164(2) Å, b = 7.495(3) Å, c = 8.434(3) Å;

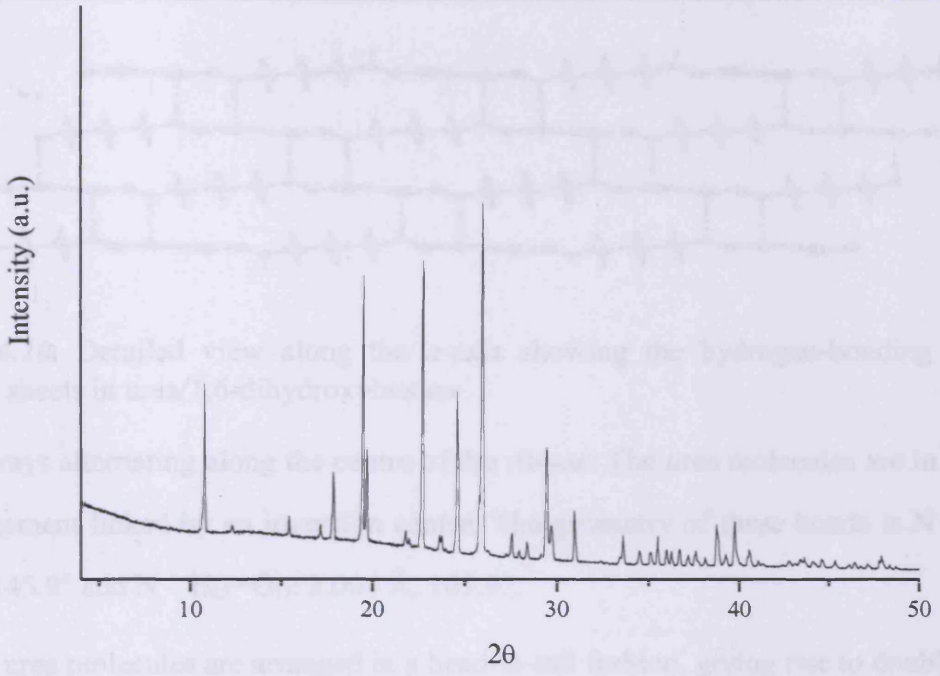

Figure 6.8. PXRD diffractogram recorded for the urea/1,6-dihydroxyhexane co-crystal.

$\alpha = 94.823(2)°$, $\beta = 96.022(3)°$, $\gamma = 101.486(3)°$; $V = 316.258(2)$ Å^3; $Z = 1$; $D_c = 1.251$ mg m^{-3}; R = 0.053). The PXRD diffractogram does not show any evidence of UICs (Figure 6.8). Structural parameters are listed in the Appendix, Tables A4 & A5.

Urea and 1,6-dihydroxyhexane forms a complex in a 2:1 ratio. The urea motif in this structure is based on a hydrogen-bond network that form double-stranded ribbons running nearly parallel to the *a*-axis (Figure 6.9). The two strands of the ribbon are linked by a network of N – H···O hydrogen bonds between urea molecules involving the C = O group and one NH_2 group of each urea molecule and containing two different types of cyclic hydrogen

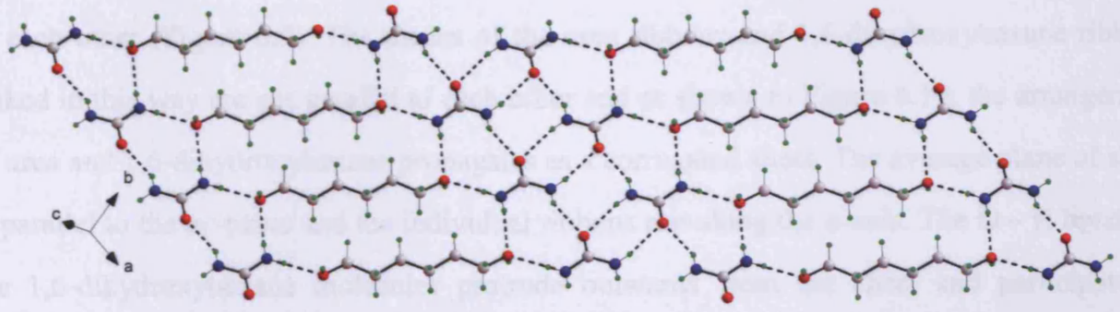

Figure 6.9. View of the urea/1,6-dihydroxyhexane viewed perpendicular to the sheet formed by the urea ribbons.

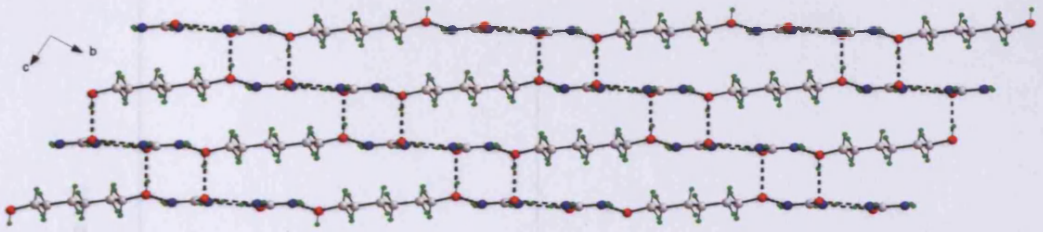

Figure 6.10. Detailed view along the *a*-axis showing the hydrogen-bonding between different sheets in urea/1,6-dihydroxyhexane.

bonded arrays alternating along the centre of the ribbon. The urea molecules are in a head-to-tail arrangement linked by an inversion centre. The geometry of these bonds is N – H_U···O_U: 2.944 Å, 145.9° and N – H_U···O_U: 3.004 Å, 165.9°.

The urea molecules are arranged in a head-to-tail fashion, giving rise to double-stranded ribbons of the urea molecules. The two other NH_2 groups protrude from the edge of the urea ribbon (with a periodic distance of 5.16 Å). For these NH_2 groups, each N – H bond is engaged in an N – H···O hydrogen bond with the OH group of a 1,6-dihydroxyhexane molecule and each OH group is involved in two N – H···O hydrogen bonds of this type with two different urea molecules N – H_U···O_{DHH}: 3.038 Å, 158.3° and N – H_U···O_{DHH}: 2.978 Å, 168.5°.

The 1,6-dihydroxyhexane molecules that form hydrogen bonds with NH_2 groups along each edge of the ribbon are themselves arranged in a planar, ribbon-like manner, with OH groups running along each edge of the ribbon. Each edge of the urea ribbon is linked to the edge of a 1,6-dihydroxyhexane ribbon, and *vice versa*, by means of the N – H···O hydrogen bonds discussed above. The 1,6-dihydroxyhexane molecules of adjacent ribbons are parallel to each other (Figure 6.9). The planes of the urea ribbons and 1,6-dihydroxyhexane ribbons linked in this way are not parallel to each other and as shown in Figure 6.10, the arrangement of urea and 1,6-dihydroxyhexane propagates as a corrugated sheet. The average plane of sheet is parallel to the *ac*-plane and the individual ribbons run along the *a*-axis. The O – H bonds of the 1,6-dihydroxyhexane molecules protrude outwards from the sheet and participate in O – H···O hydrogen bonds with the oxygen atoms of urea molecules in an adjacent sheet. Each urea oxygen atom is involved in one hydrogen bond of this type. The geometry of these hydrogen bonds is O – H_{DHH}···O_U: 2.815 Å, 172.1°.

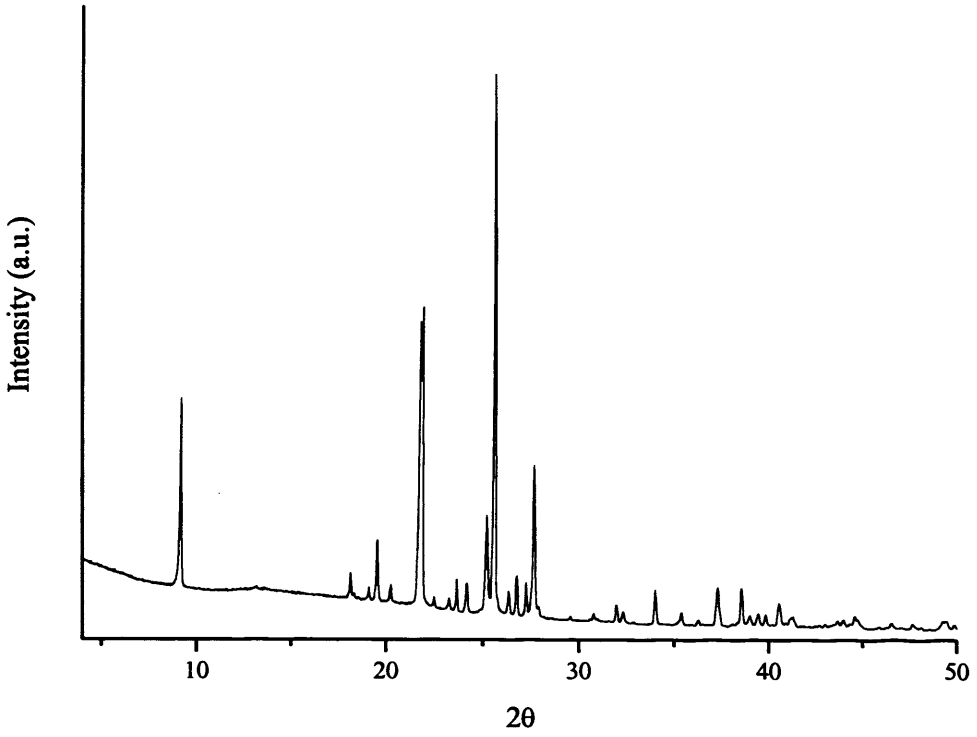

Figure 6.11. PXRD diffractogram recorded for the urea/1,8-dihydroxyoctane co-crystal.

6.4.3.3 Urea/1,8-Dihydroxyoctane Co-Crystal

The crystal structure of the urea/1,8-dihydroxyoctane complex was solved by single crystal X-ray diffraction, measured at 150 K. The crystal structure is monoclinic (space group $P2_1/c$; $a = 10.430(2)$ Å, $b = 5.170(10)$ Å, $c = 14.132(3)$ Å; $\alpha = 90°$, $\beta = 111.66(3)°$, $\gamma = 90°$; $V = 708.2(2)$ Å^3; $Z = 4$; $D_c = 1.249$ mg m^{-3}; $R = 0.0403$). The PXRD diffractogram indicates that no UICs were formed (Figure 6.11). Structural parameters are listed in the Appendix, Tables A5 & A6.

The urea/1,8-dihydroxyoctane complex has a 2:1 ratio. The urea motif in this structure is based on a hydrogen-bonded network that forms double-stranded ribbons running parallel to the *b*-axis (Figure 6.12). The two strands of the ribbon are linked by a network of N – H···O hydrogen bonds between urea molecules including the C = O group and one NH_2 group of each urea molecule and containing two different types of cyclic hydrogen bonded array alternating along the centre of the ribbon. The urea molecules of the two strands of the double-stranded ribbons are in a parallel orientation, linked by a 2_1 screw axis. The geometry of these bonds are N – H_U···O_U: 2.952 Å, 165.3° and N – H_U···O_U: 2.916 Å, 136.5°.

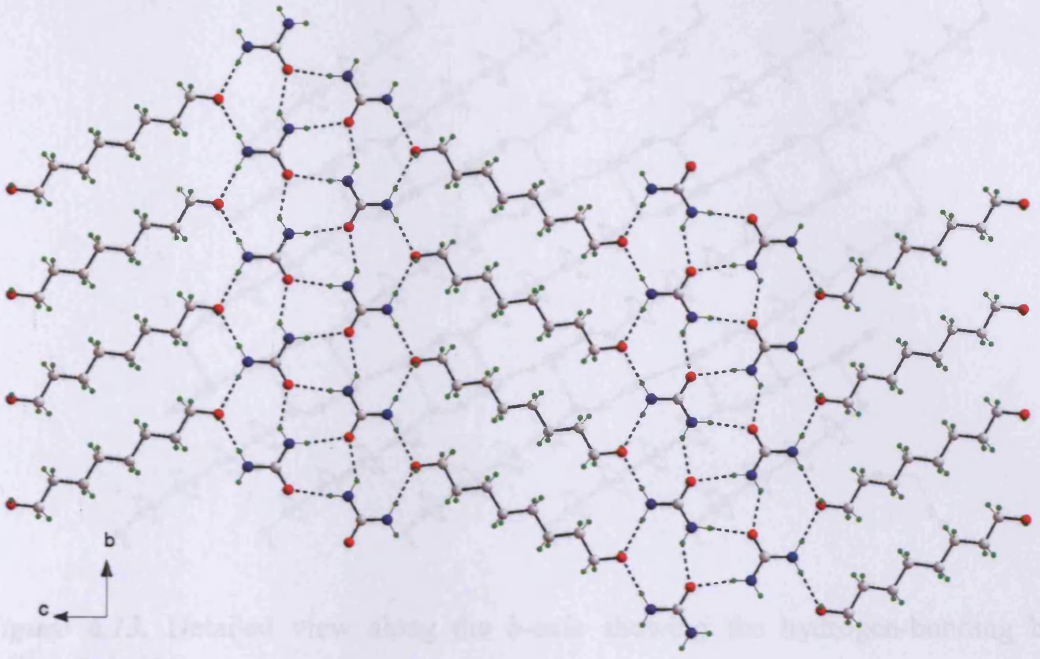

Figure 6.12. View of the urea/1,8-dihydroxyoctane viewed perpendicular to the *bc* plane with the urea ribbons running in the horizontal direction.

The urea molecules in each strand of the ribbon are parallel whereas in the urea/1,6-dihydroxyhexane complex these urea molecules are oriented anti-parallel. The other NH_2 group of each molecule bulges from the edge of the urea ribbon (with a periodic repeat distance of 5.17 Å). For these pendant NH_2 groups, each N – H bond is engaged in an N – H···O hydrogen bond with the OH group of a 1,8-dihydroxyoctane molecule and each OH group is involved in two N – H···O hydrogen bonds of this type with two different urea molecules. The geometries of these hydrogen bonds are $N - H_U \cdots O_{DHO}$: 2.952 Å, 164.9° and $N - H_U \cdots O_{DHO}$: 2.986 Å, 157.8°.

The 1,8-dihydroxyoctane molecules that form hydrogen bonds with NH_2 groups along each edge of the ribbon are themselves arranged in a planar, ribbon-like manner, with OH groups running along each edge of the ribbon. Each edge of the urea ribbon is linked to the edge of a 1,8-dihydroxyoctane ribbon, and *vice versa*, by means of the N – H···O hydrogen bonds discussed above. The 1,8-dihydroxyoctane molecules of adjacent ribbons are not parallel to each other (Figure 6.12). The planes of the urea ribbons and 1,8-dihydroxyoctane ribbons linked in this way are also not parallel and, as shown in Figure 6.13, the arrangement of urea and 1,8-dihydroxyoctane propagates as a corrugated sheet. The average plane of sheet

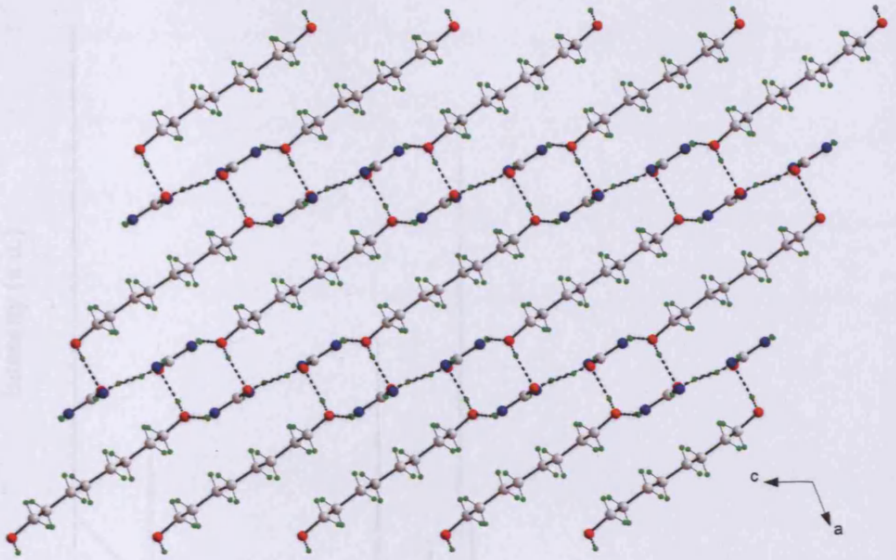

Figure 6.13. Detailed view along the *b*-axis showing the hydrogen-bonding between different sheets.

is parallel to the *ac*-plane and the individual ribbons run along the *b*-axis. The O – H bonds of the 1,8-dihydroxyoctane molecules protrude outwards from the sheet and participate in O – H···O hydrogen bonds, with the oxygen atoms of urea molecules in an adjacent sheet. Each urea oxygen atom is involved in one hydrogen bond of this type. The geometry of these hydrogen bonds is: O – H_{DHO} ···O_U: 2.770 Å, 173.4°.

6.4.3.4 Urea/1,10-dihydroxydecane Co-Crystal

The crystal structure of this new complex was solved by single crystal X-ray diffraction, measured at 150 K. The crystal structure is triclinic (space group $P\bar{1}$; $a = 5.163(3)$ Å, $b = 7.367(5)$ Å, $c = 11.101(8)$ Å; $\alpha = 98.618(2)°$, $\beta = 96.302(3)°$, and $\gamma = 102.01(3)°$; $V = 403.98(5)$ Å^3; Z = 1; $D_c = 1.210$ mg m^{-3}; R = 0.0487). Powder X-ray diffraction (Figure 6.14) revealed that there is no presence of UICs. Structural parameters are listed in the Appendix, Tables A7 & A8.

The crystal structure contains urea and 1,10-dihydroxydecane in a 2:1 ratio. In this structure, the urea molecules are hydrogen bonded to each other to form double-stranded ribbons. These ribbons run approximately parallel to the *a*-axis (Figure 6.15). The two strands of the ribbon are linked by a network of N – H···O hydrogen bonds between urea molecules, involving the C = O group and one NH_2 group of each molecule and containing two different

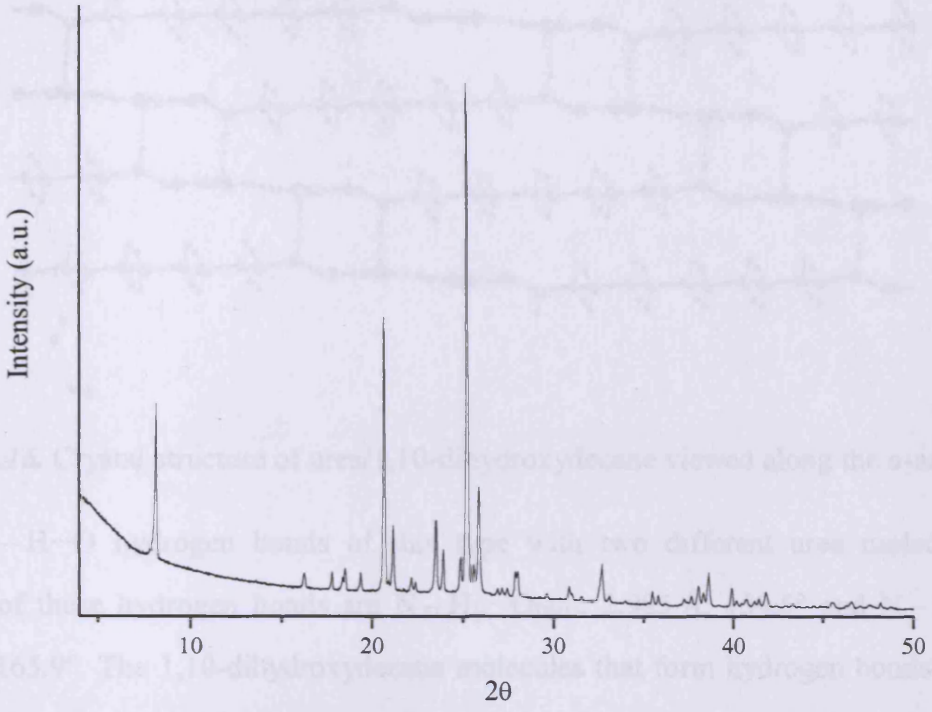

Figure 6.14. PXRD diffractogram corresponding to the complex formed between urea and 1,10-dihydroxydecane.

types of cyclic hydrogen-bonded arrays alternating along the centre of the ribbon. In this structure, as in urea/1,4-dihydroxycyclohexane, the urea molecules are in a head-to-tail arrangement across an inversion centre. The geometry of these hydrogen bonds are N – H_U···O_U: 2.996 Å, 166.81° and N – H_U···O_U: 2.923 Å, 146.01°. The other NH_2 group of each urea molecule protrudes from the edge of the ribbon with a periodic spacing of 5.16 Å.

For the pendant NH_2 groups, each N – H bond is engaged in an N – H···O hydrogen bond with the OH group of a 1,10-dihydroxydecane molecule and each OH group is involved

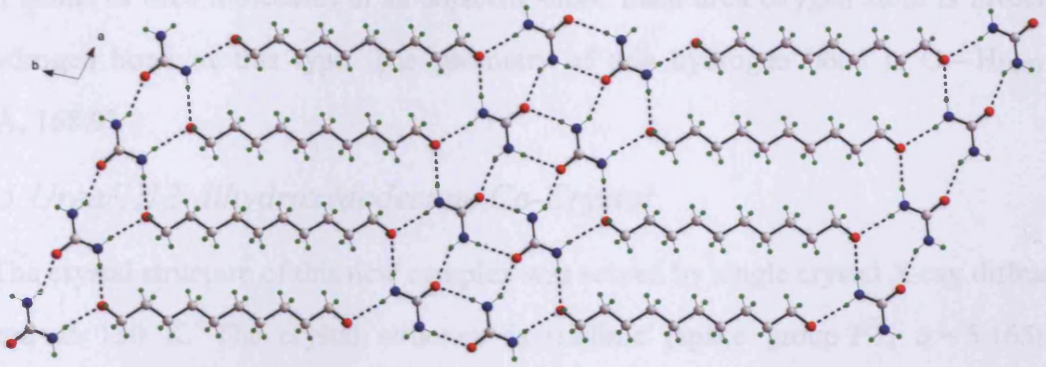

Figure 6.15. View of the urea/1,10-dihydroxydecane viewed perpendicular to the *ab* plane with the urea ribbons running in the horizontal direction.

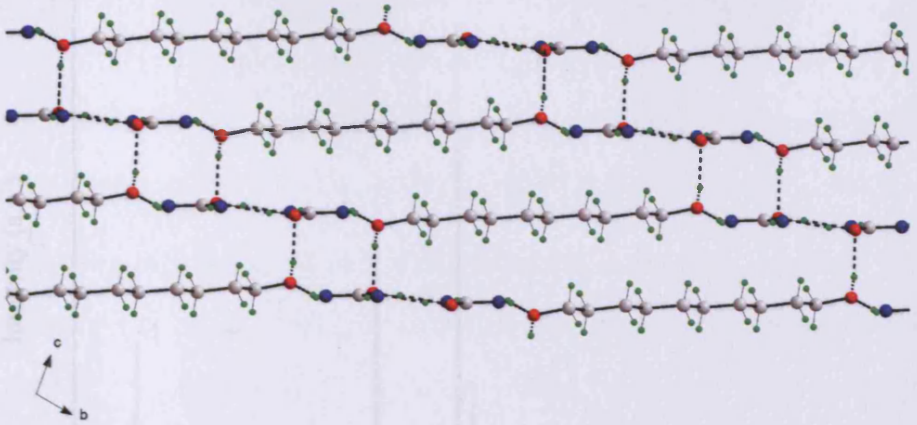

Figure 6.16. Crystal structure of urea/1,10-dihydroxydecane viewed along the *a*-axis.

in two N – H···O hydrogen bonds of this type with two different urea molecules. The geometry of these hydrogen bonds are $N-H_U\cdots O_{DHD}$: 2.985 Å, 159.5° and $N-H_U\cdots O_{DHD}$:2.995 Å, 165.9°. The 1,10-dihydroxydecane molecules that form hydrogen bonds with NH_2 groups along each edge of the ribbon are themselves arranged in a planar ribbon-like manner, with OH groups running along each edge of the ribbon.

Each edge of the urea ribbon is linked to the edge of a 1,10-dihydroxydecane ribbon, and *vice versa*, by means of the N – H···O hydrogen bonds discussed above. The 1,10-dihydroxydecane molecules of adjacent ribbons are parallel to each other. The planes of the urea ribbons and 1,10-dihydroxyoctane ribbons linked in this way are not parallel to each other and, as shown in Figure 6.16, the arrangement of urea and 1,10-dihydroxydecane propagates as a corrugated sheet. The O – H bonds of the 1,10-dihydroxyoctane molecules protrude outwards from the sheet and participate in O – H···O hydrogen bonds with the oxygen atoms of urea molecules in an adjacent sheet. Each urea oxygen atom is involved in one hydrogen bond of this type. The geometry of this hydrogen bond is $O-H_{DHD}\cdots O_U$: 2.780 Å, 168.9°.

6.4.3.5 Urea/1,12-dihydroxydodecane Co-Crystal

The crystal structure of this new complex was solved by single crystal X-ray diffraction, measured at 150 K. The crystal structure is triclinic (space group $P\bar{1}$; $a = 5.165(5)$ Å, $b = 12.262(12)$ Å, $c = 14.561(16)$ Å; $\alpha = 88.518(4)°$, $\beta = 81.9(3)°$, $\gamma = 79.27(5)°$; $V = 897.02(95)$ Å^3; $Z = 1$; $D_c = 1.194$ mg m^{-3}; $R = 0.2309$). Figure 6.17 indicates that no

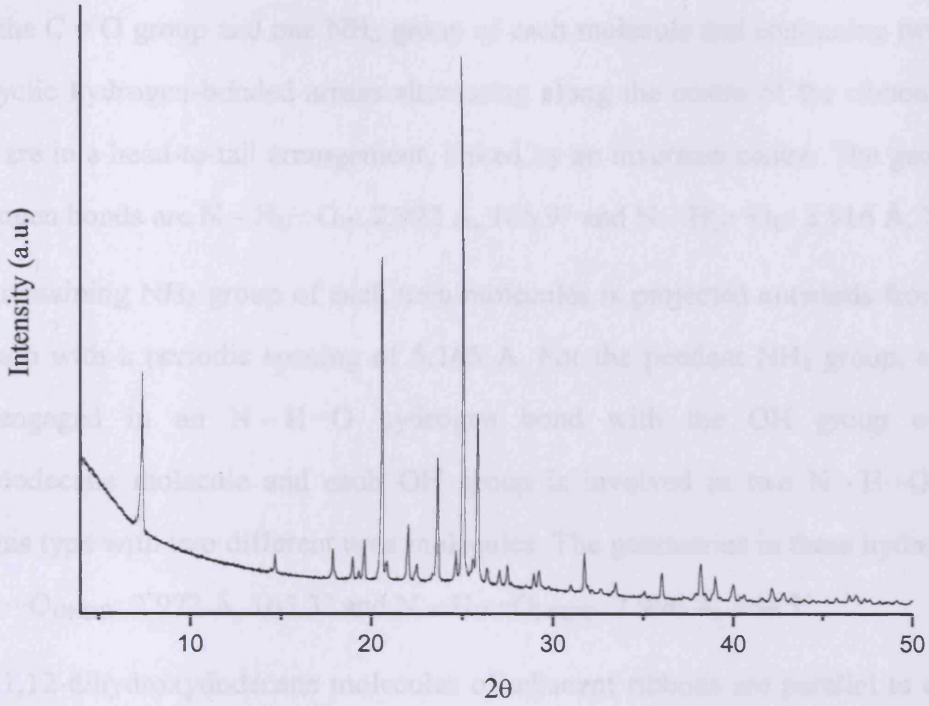

Figure 6.17. PXRD diffractogram corresponding to the complex formed between urea and 1,12-dihydroxydodecane.

UICs were detected by PXRD. Structural parameters are listed in the Appendix, Tables A9 & A10.

The crystal structure of the co-crystal formed between urea and 1,12-dihydroxydodecane contains urea and 1,12-dihydroxydodecane in a 2:1 ratio. In this structure, as in the previous structures, urea molecules are hydrogen bonded to each other to form double-stranded ribbons that run parallel to the *a*-axis (Figure 6.18). Again, the two strands of the ribbon are linked by a network of N – H···O hydrogen bonds between urea molecules,

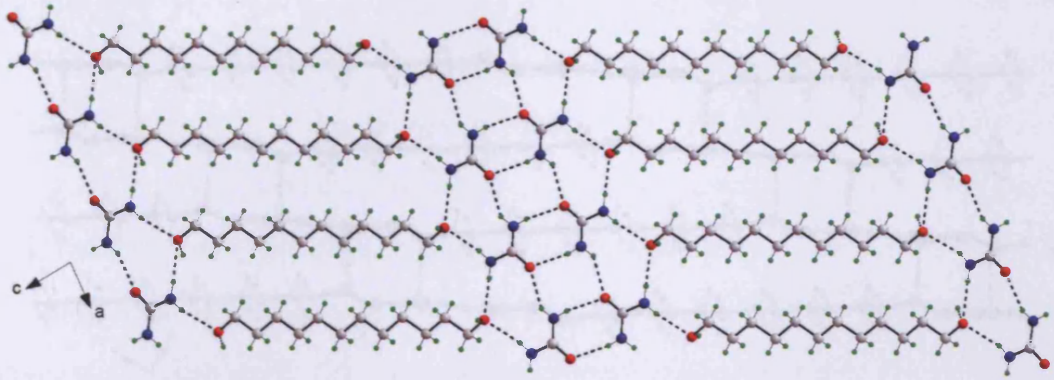

Figure 6.18. Crystal structure of urea/1,12-dihydroxydodecane viewed along the *b*-axis.

involving the C = O group and one NH_2 group of each molecule and containing two different types of cyclic hydrogen-bonded arrays alternating along the centre of the ribbon. The urea molecules are in a head-to-tail arrangement, linked by an inversion centre. The geometries of these hydrogen bonds are N – H_U···O_U: 2.992 Å, 166.9° and N – H_U···O_U: 2.916 Å, 140.4°.

The remaining NH_2 group of each urea molecules is projected outwards from the edge of the ribbon with a periodic spacing of 5.165 Å. For the pendant NH_2 group, each N – H bond is engaged in an N – H···O hydrogen bond with the OH group of a 1,12-dihydroxydodecane molecule and each OH group is involved in two N – H···O hydrogen bonds of this type with two different urea molecules. The geometries in these hydrogen bonds are N – H_U···O_{DHDD}: 2.972 Å, 163.3° and N – H_U···O_{DHDD}: 2.990 Å, 164.5°.

The 1,12-dihydroxydodecane molecules of adjacent ribbons are parallel to each other. Along each boundary of the urea ribbon, these molecules form hydrogen bonds with the amino groups (NH_2) and hydroxyl groups (OH) running along each edge of the ribbon. As in the previous compounds formed between urea and 1,6-dihydroxyhexane, urea and 1,8-dihydroxyoctane, and urea and 1,10-dihydroxydecane, the planes of the urea ribbons and 1,12-dihydroxydodecane ribbons are not parallel to each other and, as shown in Figure 6.19, the arrangement of urea and 1,12-dihydroxydodecane ribbons propagates as a corrugated sheet. The O – H bonds of the 1,12-dihydroxydodecane molecules are projected outwards from the sheet and participate in O – H···O hydrogen bonds with the oxygen atoms of urea molecules in an adjacent sheet. Each urea oxygen atom is involved in one hydrogen bond of this type. The geometry of this hydrogen bond is O – H_{DHDD}···O_U: 2.820 Å, 164.5°.

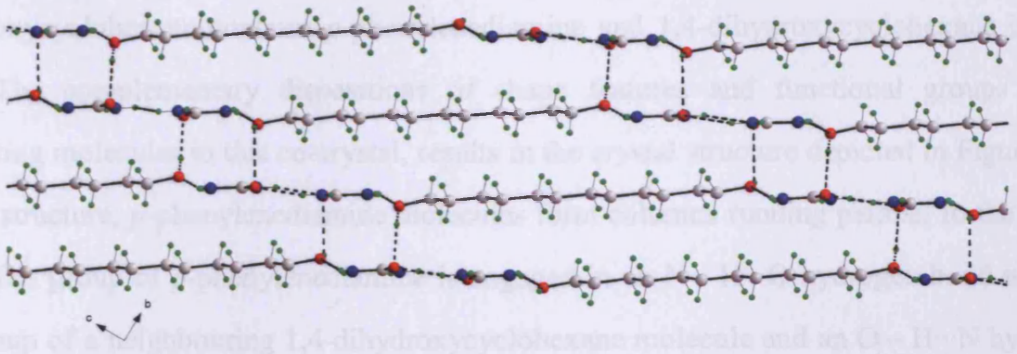

Figure 6.19. Crystal structure of urea/1,12-dihydroxydodecane viewed along the *a*-axis.

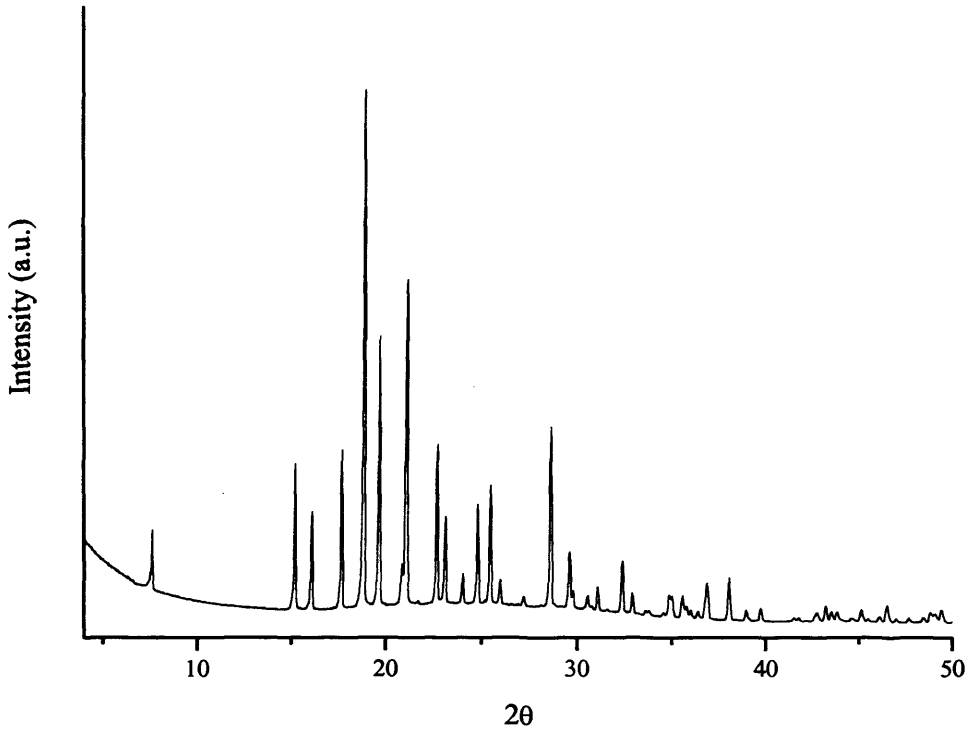

Figure 6.20. PXRD diffractogram corresponding to the complex formed between *p*-phenilenediamine and 1,4-dihydroxycyclohexane.

6.4.3.6 p-Phenylenediamine/1,4-dihydroxycyclohexane Co-Crystal

The crystal structure of this new complex was solved by single crystal X-ray diffraction, measured at room temperature. Powder X-ray diffraction shows that there is no presence of starting materials in the powered sample (Figure 6.20). The crystal structure is monoclinic (space group $P2_1/a$; cell parameters $a = 8.503(5)$ Å, $b = 6.208(4)$ Å, $c = 11.781(8)$ Å; $\beta = 95.638(3)°$; $V = 625.95(7)$ Å^3; $Z = 2$; $D_c = 1.190$ mg m^{-3}; $R = 0.0641$). Structural parameters are listed in the Appendix, Tables A11 & A12.

The crystal structure of the co-crystal formed between *p*-phenylenediamine and 1,4-dihydroxycyclohexane contains *p*-phenylenediamine and 1,4-dihydroxycyclohexane in a 1:1 ratio. The complementary dispositions of shape features and functional groups in the interacting molecules in this co-crystal, results in the crystal structure depicted in Figure 6.21. In this structure, *p*-phenylenediamine molecules form columns running parallel to the *a*-axis. Each NH_2 group of *p*-phenylenediamine is engaged in an N – H···O hydrogen bond with the OH group of a neighbouring 1,4-dihydroxycyclohexane molecule and an O – H···N hydrogen bond with the OH group of another 1,4 dihydroxycyclohexane molecule to give rise to an infinite hydrogen bonded chain O – H···N – H···O – H···N – H.

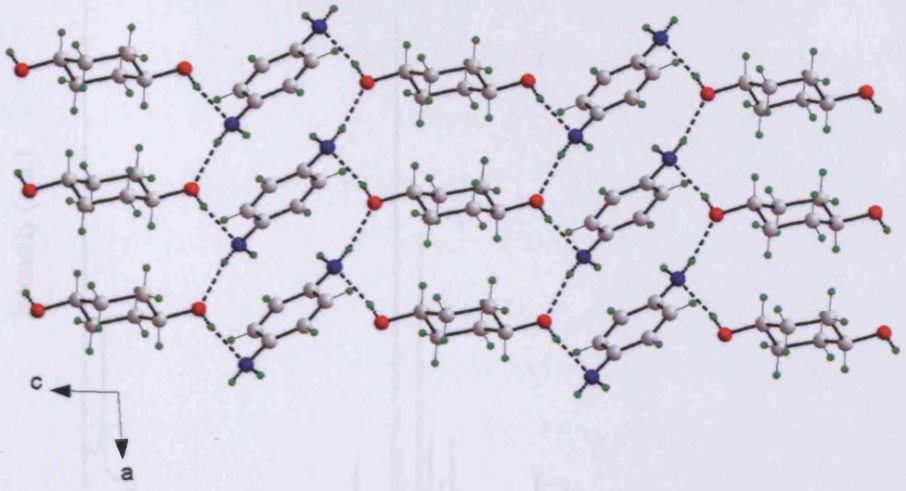

Figure 6.21. Crystal structure of *p*-phenilenediamine and 1,4-dihydroxycyclohexane viewed along the *b*-axis.

The geometry of these hydrogen bonds are N – H_{PDA}···O_{DHCH}: 2.985 Å, 170.9° and O – H_{DHCH}···N_{PDA}: 2.806 Å, 171.9°. The 1,4-dihydroxycyclohexane molecules, like the *p*-phenylenediamine, are arranged in a column running parallel to the *a*-axis. Adjacent *p*-phenylenediamine columns are parallel to each other. As shown in Figure 6.21, the infinite hydrogen bonded chains control the molecular arrangement of this crystal structure. The planes of *p*-phenylenediamine molecules and 1,4-dihydroxycyclohexane in their respective columns are not parallel to each other.

6.4.3.7 p-Phenylenediamine/1,8-Dihydroxyoctane Co-Crystal

Following the preliminary characterization by PXRD (Figure 6.22), single crystal X-ray diffraction was used to solve this crystal structure. Data were collected at 150 K. The crystal structure is monoclinic (space group *C*2/*c*; $a = 36.185(5)$ Å, $b = 5.093(5)$ Å, $c = 8.124(5)$ Å; $\beta = 101.105(5)°$; $V = 1469.1(17)$ Å^3; $Z = 8$; $D_c = 1.150$ mg m^{-3}; $R = 0.0581$). Structural parameters are listed in Appendix, Tables *A13* & *A14*.

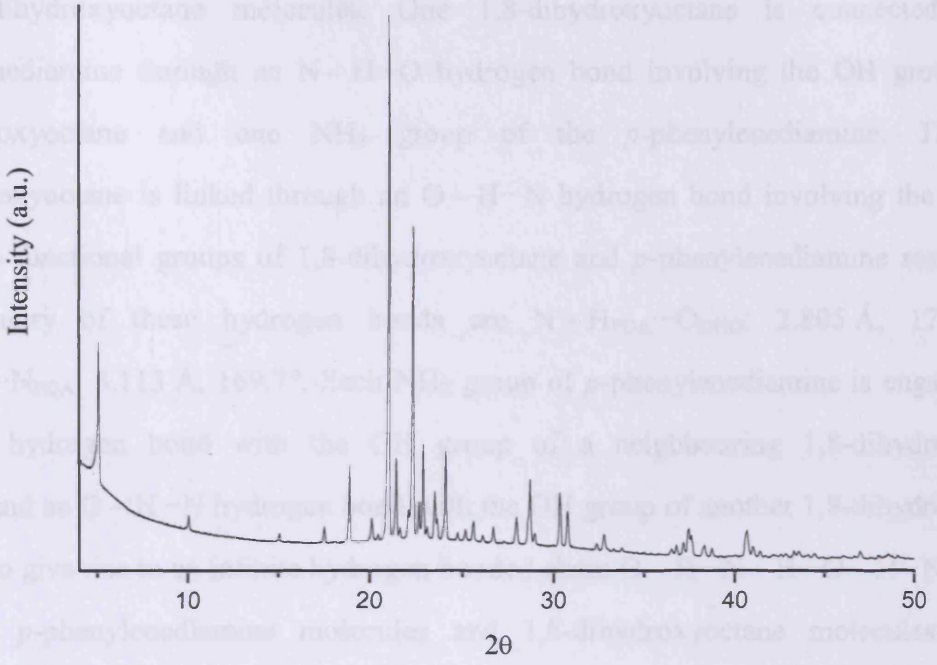

Figure 6.22. PXRD diffractogram corresponding to the complex formed between *p*-phenilenediamine and 1,8-dihydroxyoctane.

The crystal structure of the co-crystal formed between *p*-phenylenediamine and 1,8-dihydroxyoctane contains *p*-phenylenediamine and 1,8-dihydroxyoctane in a 1:1 ratio. The molecular arrangement in this co-crystal is very similar to that observed in the *p*-phenylenediamine and 1,4-dihydroxycyclohexane complex. The *p*-phenylenediamine molecules form single columns and the 1,8-dihydroxyoctane molecules form columns along the *c*-axis (Figure 6.23). Each NH_2 group of the *p*-phenylenediamine forms hydrogen bonds to

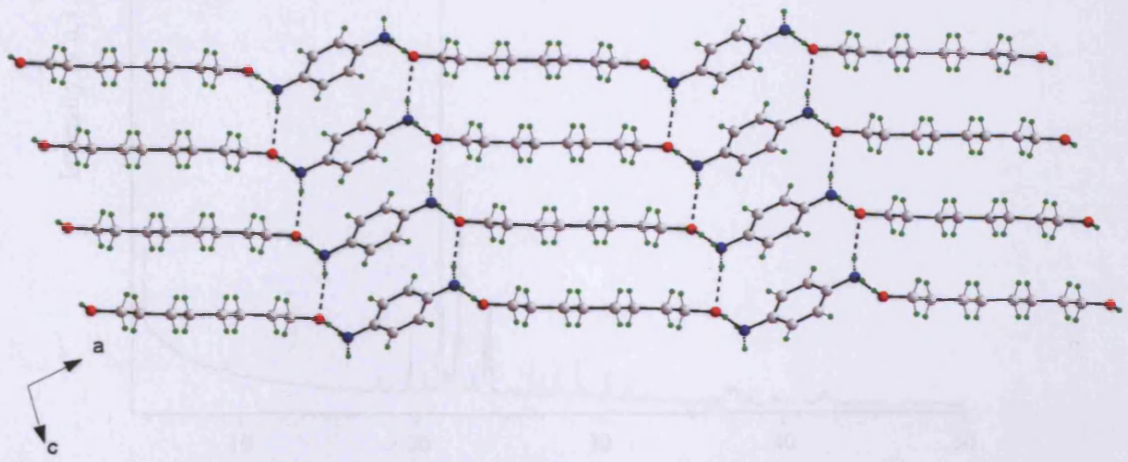

Figure 6.23. Crystal structure of *p*-phenilenediamine/1,8-dihydroxyoctane viewed along the *b*-axis. The *p*-phenilenediamine and 1,8-dihydroxyoctane are in a corrugated sheet conformation.

two 1,8-dihydroxyoctane molecules. One 1,8-dihydroxyoctane is connected to the *p*-phenylenediamine through an N – H···O hydrogen bond involving the OH group of the 1,8-dihydroxyoctane and one NH_2 group of the *p*-phenylenediamine. The other 1,8-dihydroxyoctane is linked through an O – H···N hydrogen bond involving the hydroxyl and amino functional groups of 1,8-dihydroxyoctane and *p*-phenylenediamine respectively. The geometry of these hydrogen bonds are $N-H_{PDA}\cdots O_{DHO}$: 2.805 Å, 175.4° and $O-H_{DHO}\cdots N_{PDA}$: 3.113 Å, 169.7°. Each NH_2 group of *p*-phenylenediamine is engaged in an N – H···O hydrogen bond with the OH group of a neighbouring 1,8-dihydroxyoctane molecule and an O – H···N hydrogen bond with the OH group of another 1,8-dihydroxyoctane molecule to give rise to an infinite hydrogen bonded chain O – H···N – H···O – H···N – H. The planes of *p*-phenylenediamine molecules and 1,8-dihydroxyoctane molecules in their respective columns are not parallel to each other and, as shown in Figure 6.23.

6.4.3.8 p-Phenylenediamine/1,10-dihydroxydecane Co-Crystal

The crystal structure of the *p*-phenylenediamine/1,10-dihydroxydecane co-crystal was solved by single crystal X-ray diffraction, measured at room temperature. Powder X-ray diffraction (Figure 6.24) showed that there is no presence of starting materials in the samples

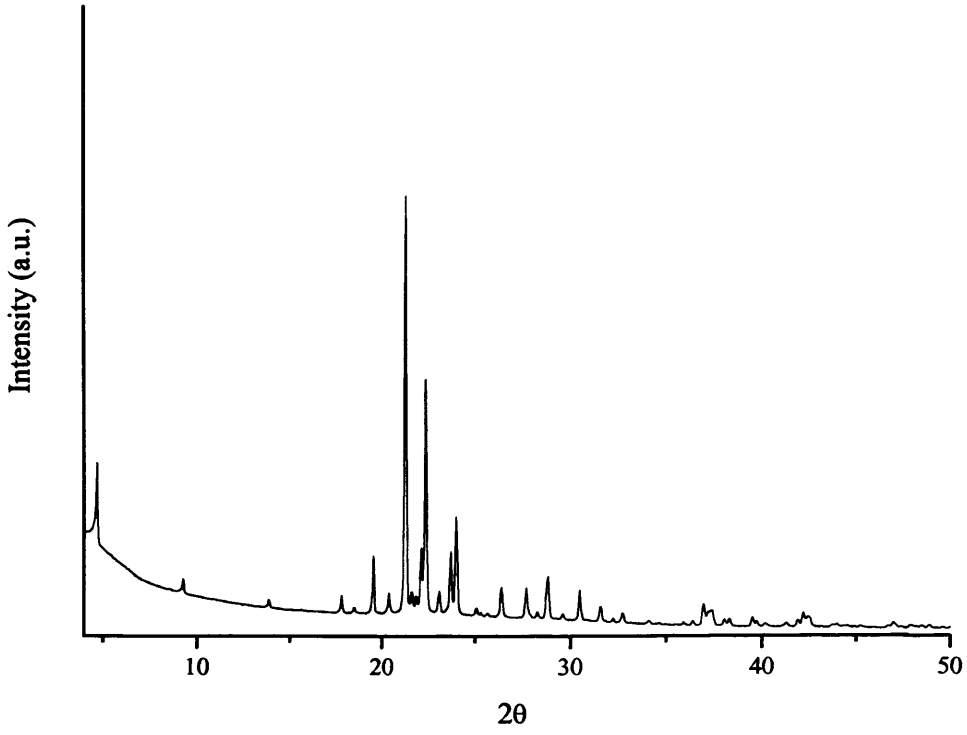

Figure 6.24. PXRD diffractogram corresponding to the complex formed between *p*-phenilenediamine and 1,10-dihydroxydecane.

analyzed. The crystal structure is monoclinic (space group $P2_1/a$; cell parameters $a = 8.265(6)$ Å, $b = 5.188(3)$ Å, $c = 19.534(13)$ Å; $\beta = 99.01(0)°$; $V = 827.29(9)$ Å^3; $Z = 2$; $D_c = 1.134$ mg m^{-3}; $R = 0.111$). Structural parameters are listed in the Appendix, Tables A15 & A16.

The structure of this co-crystal is very similar to that observed for *p*-phenilenediamine/1,8-dihydroxyoctane. The crystal structure of the co-crystal formed between *p*-phenylenediamine and 1,10-dihydroxydecane contains *p*-phenylenediamine and 1,10-dihydroxyoctane in a 1:1 ratio. The *p*-phenylenediamine molecules and the 1,10-dihydroxydecane molecules form columns running along the *a*-axis (Figure 6.25). Each NH_2 group of the *p*-phenylenediamine forms hydrogen bonds to two 1,10-dihydroxydecane molecules. One 1,10-dihydroxydecane is connected to the *p*-phenylenediamine through an N – H···O hydrogen bond involving the OH group of the 1,10-dihydroxydecane and one NH_2 group of the *p*-phenylenediamine. The other 1,10-dihydroxydecane is linked through an O – H···N hydrogen bond involving the hydroxyl and amino functional groups of 1,10-dihydroxydecane and *p*-phenylenediamine respectively. The geometry of these hydrogen bonds are N – H_{PDA}···O_{DHO}: 3.201 Å, 167.3° and O – H_{DHD}···N_{PDA}: 3.202 Å, 174.4. Each NH_2 group of *p*-phenylenediamine is engaged in an N – H···O hydrogen bond with the OH group of a neighbouring 1,10-dihydroxydecane molecule and an O – H···N hydrogen bond with the OH group of another 1,10-dihydroxydecane molecule to give rise to an infinite hydrogen bonded chain O – H···N – H···O – H···N – H. The planes of *p*-phenylenediamine molecules and 1,10-dihydroxydecane molecules in their respective columns are not parallel to each

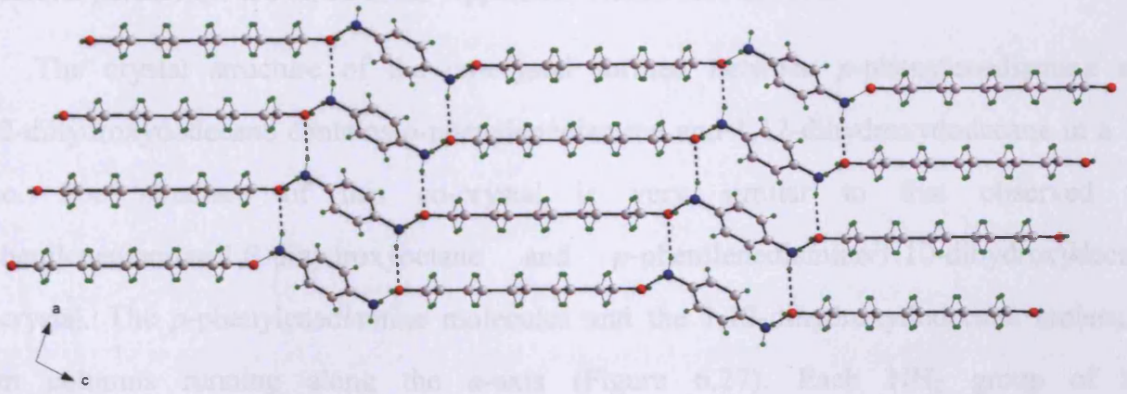

Figure 6.25. Crystal structure of viewed along the *b*-axis. The *p*-phenilenediamine and 1,10-dihydroxydecane is in a corrugated sheet conformation.

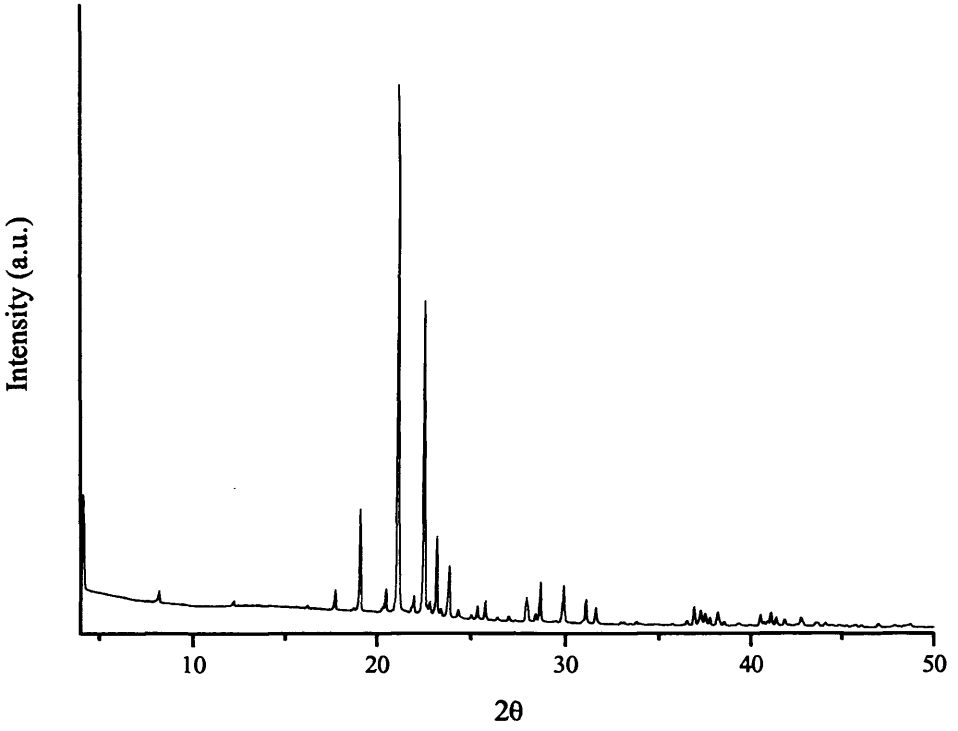

Figure 6.26. PXRD diffractogram corresponding to the complex formed between *p*-phenilenediamine and 1,12-dihydroxydodecane.

other , as shown in Figure 6.25.

6.4.3.9 p-Phenilenediamine/1,12-dihydroxydodecane Co-Crystal

The crystal structure of the *p*-phenylenediamine 1,12-dihydroxydodecane co-crystal was solved by single crystal X-ray diffraction, measured at 150 K. Powder X-ray diffraction (Figure 6.26) showed that there is no presence of starting materials in the samples analyzed. The crystal structure is monoclinic (space group $P2_1/a$; $a = 8.085(2)$ Å, $b = 5.136(3)$ Å, $c = 22.156(9)$ Å; $\beta = 96.136(2)°$; $V = 914.75(17)$ Å^3; $Z = 4$; $D_c = 1.12$ mg m^{-3}; $R = 0.1243$). Structural parameters are listed in the Appendix, Tables A17 & A18.

The crystal structure of the co-crystal formed between *p*-phenylenediamine and 1,12-dihydroxydodecane contains *p*-phenylenediamine and 1,12-dihydroxydodecane in a 1:1 ratio. The structure of this co-crystal is very similar to that observed for *p*-phenilenediamine/1,8-dihydroxyoctane and *p*-phenilenediamine/1,10-dihydroxydecane co-crystal. The *p*-phenylenediamine molecules and the 1,12-dihydroxydodecane molecules form columns running along the *a*-axis (Figure 6.27). Each NH_2 group of the *p*-phenylenediamine forms hydrogen bonds to two 1,12-dihydroxydodecane molecules. One 1,12-dihydroxydodecane is connected to the *p*-phenylenediamine through an N – H···O

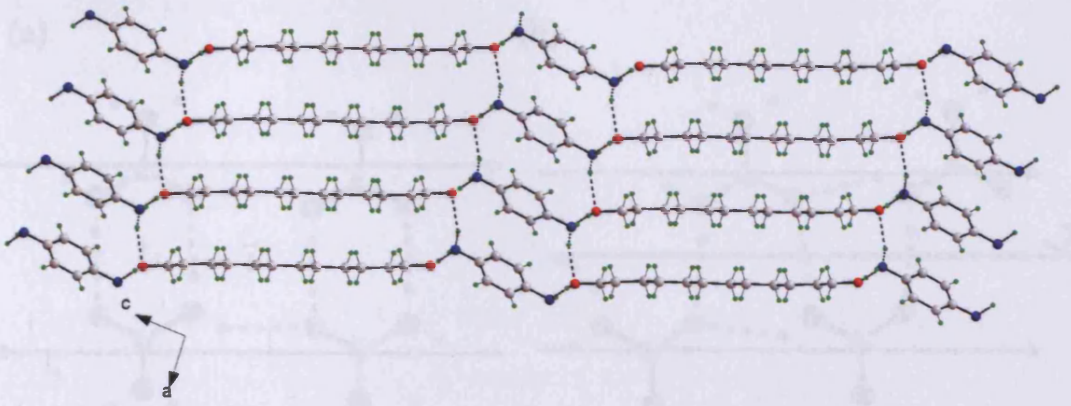

Figure 6.27. Crystal structure of viewed along the *b*-axis. The *p*-phenilenediamine and 1,12-dihydroxydodecane are in a corrugated sheet conformation.

hydrogen bond involving the OH group of the 1,12-dihydroxydodecane and one NH_2 group of the *p*-phenylenediamine. The other 1,12-dihydroxydodecane is linked through an O – H···N hydrogen bond involving the hydroxyl and amino functional groups of 1,12-dihydroxydodecane and *p*-phenylenediamine respectively. The geometry of these hydrogen bonds are $N - H_{PDA} \cdots O_{DHDD}$: 2.810, Å, 176.5°. Each NH_2 group of *p*-phenylenediamine is engaged in an N – H···O hydrogen bond with the OH group of a neighbouring 1,12-dihydroxydodecane molecule and an O – H···N hydrogen bond with the OH group of another 1,12-dihydroxydodecane molecule to give rise to an infinite hydrogen bonded chain O – H···N – H···O – H···N – H. The planes of *p*-phenylenediamine molecules and 1,12-dihydroxydodecane molecules in their respective columns are not parallel to each other, as shown in Figure 6.27.

6.4.4 Comparison of Crystal Structures

For the group of complexes formed with urea and diols, the double-stranded ribbon of urea molecules is the principal hydrogen bonded array observed, whereas, for the complexes formed with *p*-phenylenediamine and diols, the infinite chain is the only hydrogen bonded array and there is no hydrogen bonding between adjacent sheets containing *p*-phenylenediamine and diols. For those complexes formed between urea and diols, the motif adopted by urea molecules is based on double-stranded ribbons. This motif is observed in all the structures except urea/1,8-dihydroxyoctane. All the other crystal structures are triclinic ($P\bar{1}$), whereas the urea/1,8-dihydroxyoctane crystal structure is monoclinic ($P2_1/c$). In the

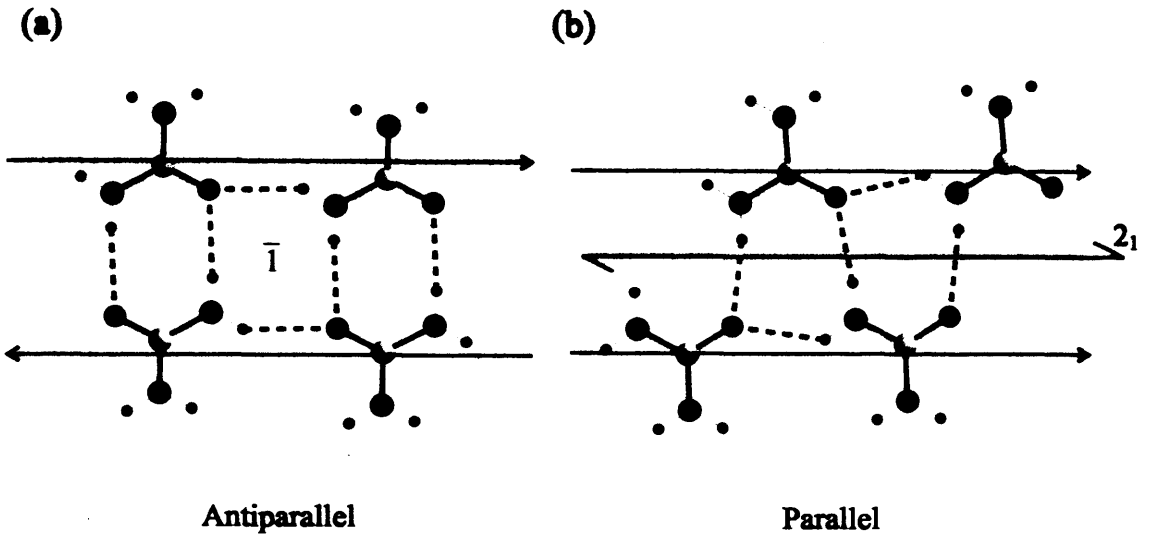

Figure 6.28. Schematic representation of the two urea motifs observed in the crystal structures formed between urea and α,ω-dihydroxyalkanes: (a) antiparallel orientation of urea strands with inversion centre, and (b) parallel orientation of urea strands with 2_1 screw axis.

triclinic structures, the inversion centre, $\bar{1}$, is in the middle of the double-stranded ribbon of urea molecules. This inversion centre leads to an antiparallel orientation for the two strands of the ribbon (Figure 6.28a).

In urea/1,8-dihydroxyoctane, the inversion centre on the ribbon is replaced by a 2_1 screw axis which leads to a parallel orientation of the two strands of the double-stranded ribbons. This alteration also affects the relative orientations of the 1,8-dihydroxyoctane molecules within adjacent sheets (Figure 6.28b). A summary of all the structural parameters obtained in the crystal structures formed between urea and α,ω-dihydroxyalkanes and 1,4-dihydroxycyclohexane is given in Table 6.2.

Interestingly, we observed that, in all the structures, there is a common repeat distance of ~5.16 Å which corresponds to the periodicity of the urea molecules in the double-stranded ribbons. In all the structures formed with urea and diols, the planes containing the urea ribbons and the α,ω-dihydroxyalkane molecules are not parallel to each other and, as shown in previous figures, the planes containing the arrangement of urea and α,ω-dihydroxyalkane ribbons propagate as a corrugated sheets.

This work provides a good example of the even-odd effect in substituted *n*-alkanes. This effect was first studied by Bayer in 1877, who noted that *n*-alkane dicarboxylic acids with

even *n* melt at higher temperatures than those with odd *n*.[13] This phenomenon has since been observed in many other *n*-alkanes and terminally-substituted *n*-alkanes. In particular, detailed studies have been carried out by Boese and co-workers.[14-17] The phenomenon of alternation in solid-state properties has been attributed to crystal packing factors, so that even *n*-alkanes pack more efficiently than odd *n*-alkanes. In our series, the even-odd effect is apparent from the inability to obtain co-crystals between urea/*p*-phenylenediamine and odd α,ω-dihydroxyalkanes, and for the *cis*-isomer of 1,4-dihydroxycyclohexane.

Table 6.2. Structural parameters for structures formed between urea and ω,α-dihydroxyalkanes and 1,4-dihydroxycyclohexane molecules.

	U/1,4-DHCH	U/1,6-DHH$_x$	U/1,8-DHO	U/1,10-DHD	U/1,12-DHDD
Crystal system	triclinic	triclinic	monoclinic	triclinic	triclinic
a (Å)	5.140(2)	5.164(2)	10.430(2)	5.163(3)	5.165(5)
b (Å)	5.372(2)	7.495(3)	5.170(10)	7.367(5)	12.262(12)
c (Å)	11.158(6)	8.434(3)	14.132(3)	11.101(8)	14.561(16)
α (°)	96.940(2)	94.823(2)	90	98.618(2)	88.518(4)
β (°)	99.185(2)	96.022(3)	111.66(3)	96.302(3)	81.9(3)
γ (°)	100.942(3)	101.486(3)	90	102.007(3)	79.267(5)
Space group	$P\bar{1}$	$P\bar{1}$	$P2_1/c$	$P\bar{1}$	$P\bar{1}$
Volume (Å^3)	294.96(25)	316.26(2)	708.21(2)	403.98(5)	897.02(95)
Z	1	1	4	1	1
Dc (mg m^{-3})	1.330	1.251	1.249	1.210	1.194
Ratio	2:1	2:1	2:1	2:1	2:1
M.P. (°C)	137	120	129	131	134

For the even diols, the all-*trans* conformation leads to an antiparallel projection of the two C – O groups, whereas in odd diols the two C – O groups are projected in the same direction.[18] This is also an efficient method to separate the *trans* isomer from the *cis* isomer of 1,4-dihydroxycyclohexane. In the preparation of the complex between urea and 1,4-dihydroxycyclohexane, the starting material was a mixture of both *cis* and *trans* isomers, whereas in our experiments only co-crystals containing the *trans* conformation of the 1,4-dihydroxycyclohexane were obtained.

Our interpretation of the fact that co-crystals are not formed for odd α,ω-dihydroxyalkanes is based on the impossibility to form parallel double stranded ribbons of urea molecules when the α,ω-dihydroxyalkanes have an odd chain length. In the even case, the C – O groups are nearly oriented perpendicular to the double stranded ribbons of urea molecules (viewed perpendicular to the *bc* plane), so that the CH_2 group next to the C – O bond is well oriented to avoid repulsive forces from the NH_2 group (see Figure 6.29). In the odd case, the orientation of the C – O groups are not perpendicular to the urea ribbons and the CH_2 and NH_2 groups are too close to each other. In order to maintain the optimum distances between the CH_2 and NH_2 groups, the odd α,ω-dihydroxyalkanes would have to rotate. However, by doing this rotation, the double stranded ribbons of urea molecules will no longer be in a parallel orientation with the adjacent urea ribbons (Figure 6.30). As observed in Figure 6.30, the rotation of diols will also create a gap (shadow area in Fig. 6.30) in some regions of the structure, thus with the impossibility of establishing a hydrogen bonding network between urea and α,ω-dihydroxyalkanes. Therefore, it is not possible to form a co-crystal with urea and odd α,ω-dihydroxyalkanes.

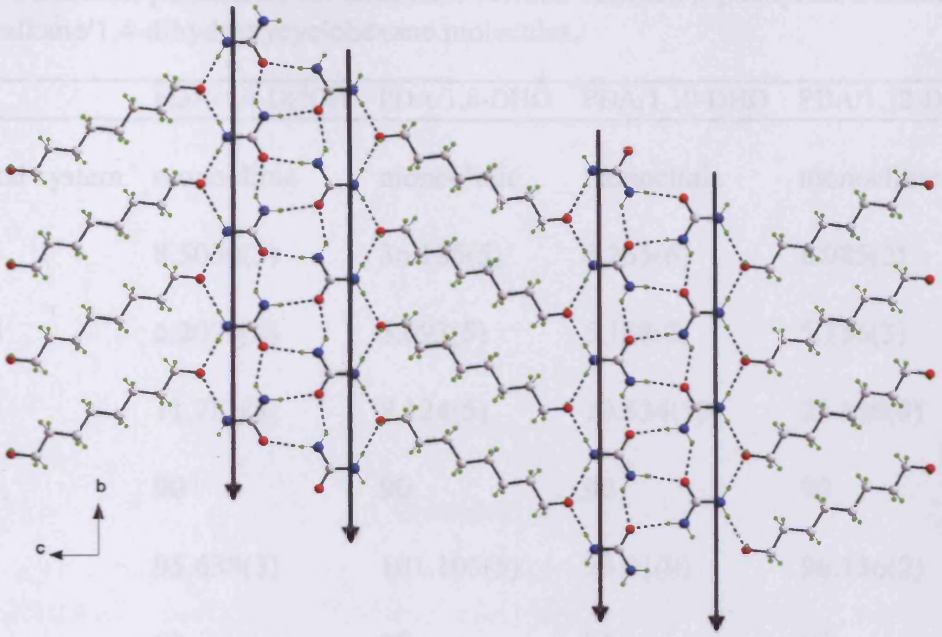

Figure 6.29. In the even-ω,α-dihydroxyalkanes case the C – O bond is oriented nearly perpendicular to the urea ribbons and the distances between CH_2 and NH_2 are large enough to avoid repulsive forces. The arrows indicates the parallel disposition between adjacent double-stranded urea ribbons

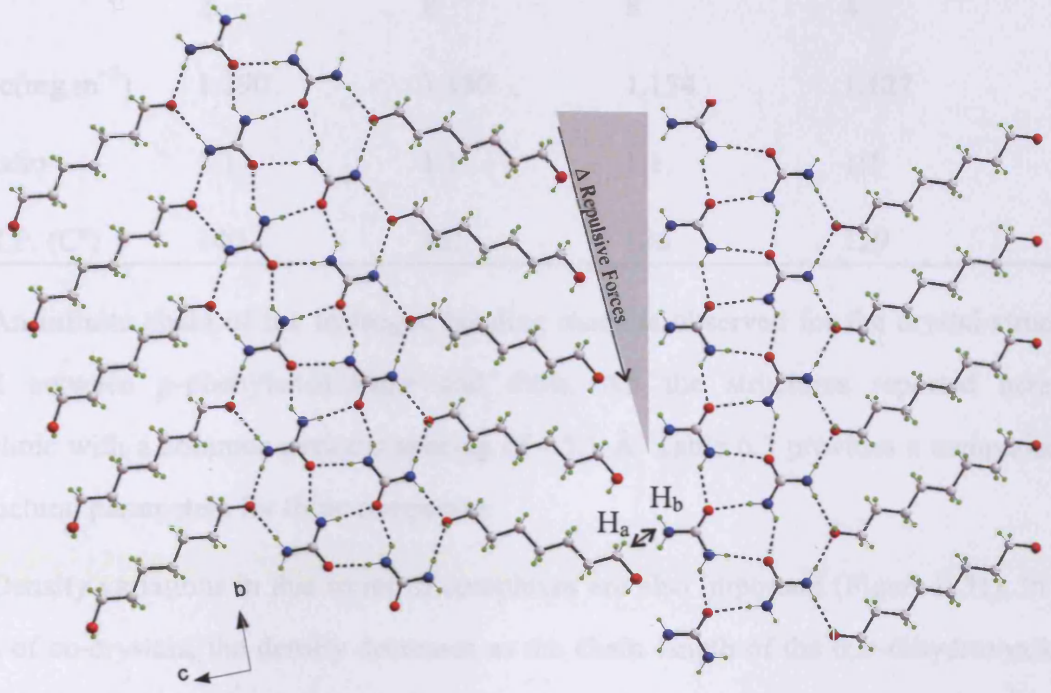

Figure 6.30. Schematic representation of the co-crystal between urea and odd ω,α-dihydroxyalkane (1,7-dihydroxyheptane). In this figure, the rotation of the OH groups does not allow formation of a hydrogen bond network with urea molecules. The adjacent double stranded urea ribbons are not in a parallel disposition. The CH_2 and NH_2 groups (H_a and H_b respectively) are in a good orientation in one molecule, but clearly not in the other ones (shadow area).

Table 6.3. Structural parameters for structures formed between *p*-phenylenediamine and α,ω-dihydroxyalkane/1,4-dihydroxycyclohexane molecules.

	PDA/1,4-DHCH	PDA/1,8-DHO	PDA/1,10-DHD	PDA/1,12-DHDD
Crystal system	monoclinic	monoclinic	monoclinic	monoclinic
a (Å)	8.5030(5)	36.185(5)	8.265(6)	8.085(2)
b (Å)	6.2079(4)	5.093(5)	5.188(3)	5.136(3)
c (Å)	11.781(8)	8.124(5)	19.534(13)	22.156(9)
α (°)	90	90	90	90
β (°)	95.638(3)	101.105(5)	99.01(0)	96.136(2)
γ (°)	90	90	90	90
Space group	$P2_1/a$	$C2/c$	$P2_1/a$	$P2_1/a$
Volume $Å^3$	625.95(7)	1469.1(17)	827.29(10)	914.75(17)
Z	2	8	8	4
Dc(mg m^{-3})	1.190	1.150	1.134	1.127
Ratio	1:1	1:1	1:1	1:1
M.P. (C°)	140	121	126	129

An infinite chain of the hydrogen bonding motif is observed for the crystal structures formed between *p*-phenylenediamine and diols. All the structures reported here are monoclinic with a common periodic spacing of ~ 5.1 Å. Table 6.3 provides a comparison of the structural parameters for these complexes.

Density variations in this series of complexes are also important (Figure 6.31). In both groups of co-crystals, the density decreases as the chain length of the α,ω-dihydroxyalkanes increases. For the complexes formed with urea, the variation is more significant than that for the complexes formed containing *p*-phenylenediamine. Melting point variations have also been analysed for the different compounds. In both cases, the melting point increases as the length of the dihydroxyalkane increases (Figure 6.32).

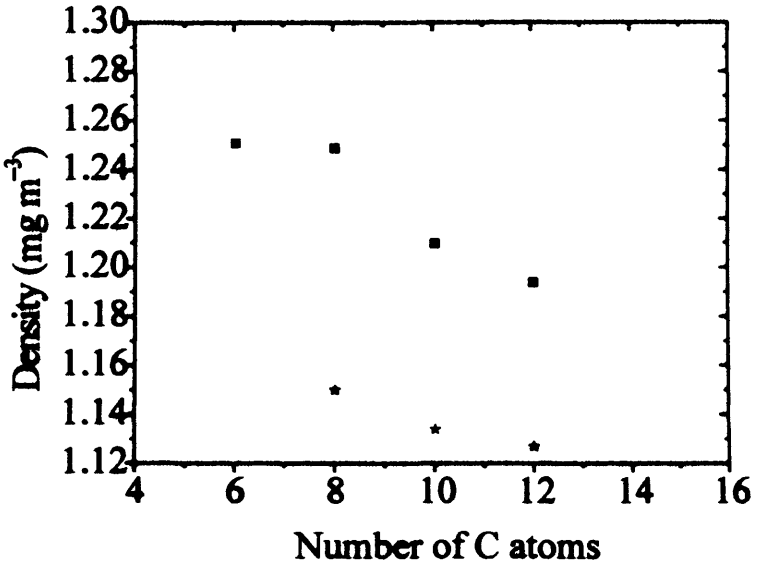

Figure 6.31. Density variation as a function of chain length for the *p*-phenylenediamine/α,ω-dihydroxyalkane co-crystals (star symbol) and urea/α,ω-dihydroxyalkane co-crystals (square symbol). (Note that measurements carried out at room temperature are shown in red).

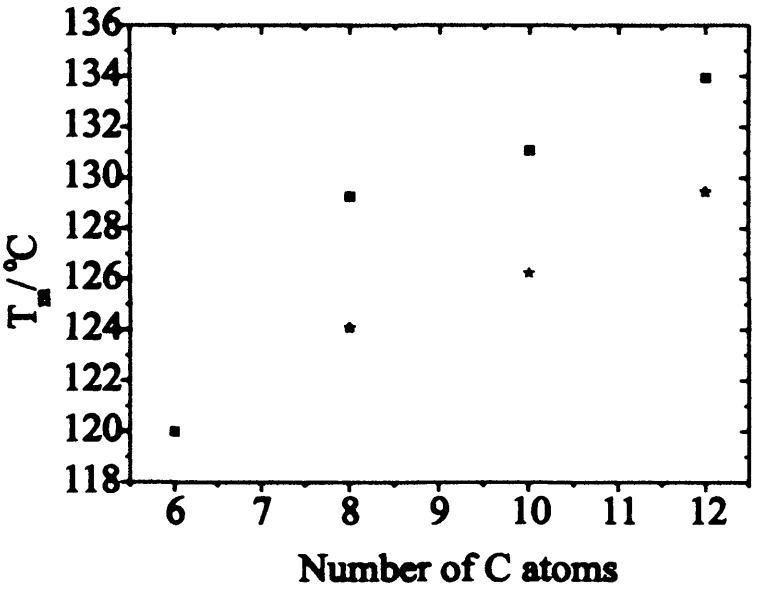

Figur 6.32. Melting point variation as a function of the chain length for the *p*-phenylenediamine/α,ω-dihydroxyalkane co-crystals (star symbol) and for the urea/α,ω-dihydroxyalkane co-crystals (square symbol). (Note that measurements carried out at room temperature are shown in red).

In this work, we were able to prepare urea inclusion compounds with certain α,ω-dihydroxyalkanes (Table 6.4). For urea/1,5-dihydroxypentane, the UIC was unstable at room temperature. The short chain for the 1,5-dihydroxypentane is such that this guest readily escapes from the tunnel structure of the UICs and the urea host structure

recrystallized as a pure urea. The other UICs obtained were stable at room temperature. Interestingly, for all the UICs formed, except that formed with 1,16-dihydroxyhexadecane, the crystal had needle-like morphology. For the urea/1,16-dihydroxyhexadecane inclusion compound, on the other hand, the single crystal formed was, instead, a flat hexagonal shape. Powder X-ray diffraction data revealed that new co-crystals between urea/1,16-dihydroxyhexadecane and *p*-phenylenediamine/1,16-dihydroxyhexadecane were formed, but are too small to use single crystal X-ray diffraction to determine the crystal structure. Therefore, using PXRD technique, these two crystal structures will be investigated in further investigations.

Table 6.4. Series of conventional urea inclusion compounds obtained during the preparation of complexes between urea and ω,α-dihydroxyalkanes.

UICs	Morphology
Urea/1,5-dihydroxypentane	long hexagonal crystals
Urea/1,9-dihydroxynonane	long hexagonal crystals
Urea/1,10-dihydroxydecane	long hexagonal crystals
Urea/1,12-dihydroxydodecane	long hexagonal crystals
Urea/1,16-dihydroxyhexadecane	flat hexagonal crystals

6.5 Conclusions and Further Work

The single crystal X-ray diffraction results reported in this chapter have proved that, by applying crystal engineering principles, a new family of co-crystal structures have been prepared. It has been shown how it is possible to predict a crystal structure by replacing two urea molecules by one molecule of *p*-phenylenediamine. The double-stranded ribbon of urea molecules has been substituted by a *p*-phenylenediamine column, giving rise to another family of crystal structures.

A good level of understanding has now been obtained for the urea/diol and *p*-phenylenediamine/diol systems. Nevertheless, from this work, a number of further avenues of investigation have been opened. In the structures containing urea and diols, we have observed a common pattern for the urea molecules but in the case of urea/1,8-

dihydroxyoctane, the structure is significantly different. Is the urea/1,8-dihydroxyoctane a polymorph? Could polymorphism eventually be found in this family of structures? With the correspondence between molecular and crystal structure now being understood for this group of materials, we conclude that urea and *p*-phenylenediamine are amenable to the principles of crystal engineering.

References for Chapter 6

[1] G. R. Desiraju, *Crystal Engineering. The Design of Organic Solids*; Elsevier: Amsterdam, **1989**

[2] W. J. Steed and J. L. Atwood, *Supramolecular Chemistry*, Vol. 11, pp 389 – 463.Wiley: Chichester, **2000.**

[3] A. Gavezzotti, *Acc. Chem. Res.*, **1994**, *27*, 309.

[4] T. Beyer, T. Lewis, and S.L Price, *CrystEngCom*, **2001**, *3*, 178.

[5] J. D. Dunitz, *Chem Commun.*, **2003**, 545.

[6] G. R. Desiraju, *Angew. Chem. Int. Ed. Engl.*, **1995**, *34*, 2311.

[7] C. B. Aakeröy, A. M. Beatty and B. A. Helfrich, *J. Am. Chem. Soc.*, **2002**, *124*, 14425.

[8] S. O. Lee, B. M. Kariuki and K. D. M. Harris, *New. J. Chem.*, **2005**, *29*, 1266.

[9] O. Ermer and A. Eling, *J. Chem. Soc. Perkin Trans.*, 2, **1994**, 925.

[10] M. C. Etter, Acc. *Chem. Res.*, **1990**, *23*, 120.

[11] M. C. Etter, J. C. MacDonald and J. Bernstein, *Acta Crystallogr. B*, **1990**, *46*, 256.

[12] J. Bernstein, R. E. Davis, L. Shimoni and N. L. Chang, *Angew. Chemie Int. Ed.*, **1995**, *34*, 1555.

[13] A. Baeyer, Ber. *Chem. Ges.*, **1877**, *10*, 1286.

[14] V. R. Thalladi, M. Nüsse and R. J. Boese, *J. Am. Chem. Soc.*, **2000**, *122*, 9227.

[15] V. R. Thalladi and R. J. Boese, *New J. Chem.*, **2000**, *24*, 579.

[16] V. R. Thalladi, R. J. Boese, H. C. Weiss, *J. Am. Chem. Soc.*, **2000**, *122*, 1186.

[17] V. R. Thalladi, R. J. Boese, H. C. Weiss, *Angew. Chemie Int. Ed.*, **1999**, *38*, 988.

[18] V. R. Thalladi, R. J. Boese, H. C. Weiss, *Angew. Chemie Int. Ed.*, **2000**, *39*, 918.

Appendix

Additional crystallographic and structural information for the co-crystals described in Chapter 6 is given in this appendix.

Table A1. Crystal data and structure refinement for U/1,4-DHCH.

Crystal Data	
Formula sum	$C_8\ H_{20}\ N_4\ O_4$
Formula weight	236.27
Crystal system	triclinic
Space group	$P\bar{1}$
Unit cell dimensions	$a = 5.1400(2)$ Å
	$b = 5.3720(2)$ Å
	$c = 11.1580(6)$ Å
	$\alpha = 96.94(2)°$
	$\beta = 99.18(3)°$
	$\gamma = 100.94(3)°$
Cell volume	294.96(25) $Å^3$
Density	1.330 g/cm^3
Pearson code	aP36
Formula type	NOP2Q5
Wyckoff sequence	i18

Table A2. Fractional coordinates and isotropic displacement parameters for U/1,4-DHCH.

Atom	x	y	z	U_{iso}/Å
C1	0.13610(3)	0.85579(3)	0.12018(1)	0.018(1)
C2	-0.14772(3)	0.48838(3)	0.37419(1)	0.018(1)
C3	-0.21141(3)	0.27093(3)	0.44718(1)	0.022(1)
C4	0.14538(2)	0.62963(3)	0.41443(1)	0.022(1)
N1	0.21919(2)	1.09453(2)	0.18220(1)	0.023(1)
N2	0.32063(2)	0.73527(3)	0.08223(1)	0.027(1)
O1	-0.10904(2)	0.74357(2)	0.10142(1)	0.020(1)
O2	-0.20650(2)	0.37810(2)	0.24635(1)	0.022(1)

Table A3. Crystal data and structure refinement for U/1,6-DHH$_x$

Crystal Data	
Formula sum	$C_4\ H_{11}\ N_2O_2$
Formula weight	238.30
Crystal system	triclinic
Space group	$P\bar{1}$
Unit cell dimensions	$a = 5.1642(2)$Å
	$b = 7.4945(3)$Å
	$c = 8.4337(3)$Å
	$\alpha = 94.82(2)°$
	$\beta = 96.02(3)°$
	$\gamma = 101.49(3)°$
Cell volume	316.26(2) Å^3
Z	1
Density	1.251 g/cm^3
RAll	0.053
Pearson code	aP38
Formula type	N2O2P4Q11
Wyckoff sequence	i19

Table A4. Fractional coordinates and isotropic displacement parameters for U/1,6-DHH$_x$.

Atom	x	y	z	U_{iso}
C1	-0.4279(3)	0.7242(2)	-0.84455(19)	0.042(5)
C2	-0.1494(3)	0.8023(2)	-0.87714(19)	0.040(5)
C3	-0.1402(3)	0.9549(2)	-0.98660(18)	0.040(5)
C4	0.0110(3)	0.24761(19)	-0.60938(17)	0.035(4)
N1	0.0165(3)	0.39050(18)	-0.69474(17)	0.046(4)
N2	-0.2224(2)	0.15931(18)	-0.57402(17)	0.046(5)
O1	-0.4379(2)	0.59237(14)	-0.72981(14)	0.045(4)
O2	0.2228(2)	0.19739(14)	-0.56395(13)	0.044(4)

Table A5. Crystal data and structure refinement for U/1,8-DHO

Crystal Data	
Formula sum	$O_5\ N_2\ H_{13}\ C_2$
Formula weight	532.68
Crystal system	monoclinic
Space group	$P2_1/c$
Unit cell dimensions	$a = 10.430(2)$ Å
	$b = 5.170(1)$ Å
	$c = 14.132(3)$ Å
	$\beta = 111.66(3)$ °
Cell volume	708.23(2) $Å^3$
Density	1.249 g/cm^3
Pearson code	mP88
Formula type	N2O2P5Q13
Wyckoff sequence	e22

Table A6. Fractional coordinates and isotropic displacement parameters for U/1,8-DHO.

Atom	x	y	z	U_{iso}
O1	0.94504(1)	0.21089(2)	0.63675(1)	0.023(1)
N2	0.82759(1)	0.42550(2)	0.49077(1)	0.023(1)
C1	0.90374(1)	0.42148(2)	0.59073(1)	0.017(1)
N1	0.93318(1)	0.64761(2)	0.64003(1)	0.022(1)
O2	0.80992(1)	0.57070(2)	0.88334(1)	0.023(1)
C2	0.71244(2)	0.54196(3)	0.78086(1)	0.021(1)
C3	0.67154(2)	0.79807(3)	0.72621(1)	0.021(1)
C4	0.57710(2)	0.76410(3)	0.61503(1)	0.023(1)
C5	0.54373(2)	1.01807(3)	0.55613(1)	0.024(1)

Table A7. Crystal data and structure refinement for U/1,10-DHD

Crystal Data	
Formula sum	$C_{12}\ H_{30}\ O_4\ N_4$
Formula weight	294.39
Crystal system	triclinic
Space group	$P\bar{1}$
Unit cell dimensions	$a = 5.1630(3)$Å
	$b = 7.3670(5)$Å
	$c = 11.1010(8)$Å
	$\alpha = 98.62(2)°$
	$\beta = 96.302(3)°$
	$\gamma = 102.01°(3)$
Cell volume	403.98(5) $Å^3$
Density (calculated)	1.210 g/cm^3
Pearson code	aP50
Formula type	N2O2P6Q15
Wyckoff sequence	i25

Table A8. Fractional coordinates and isotropic displacement parameters for U/1,10-DHD.

Atom	x	y	z	U_{iso}
C1	0.42374(3)	0.21291(2)	0.41376(2)	0.021(1)
C2	0.29836(4)	0.34583(2)	0.76246(2)	0.025(1)
C3	0.08569(3)	0.45219(2)	0.79098(2)	0.023(1)
C4	0.19998(3)	0.64114(2)	0.87648(2)	0.025(1)
C5	-0.00932(4)	0.75257(2)	0.90470(2)	0.025(1)
C6	0.10515(4)	0.94453(2)	0.98524(2)	0.027(1)
O1	0.23334(2)	0.28304(2)	0.44679(1)	0.026(1)
O2	0.19290(2)	0.17387(2)	0.67442(1)	0.027(1)
N1	0.37691(3)	0.03891(2)	0.34881(1)	0.026(1)
N2	0.67668(3)	0.31182(2)	0.44460(1)	0.026(1)

Table A9. Crystal data and structure refinement for U/1,12-DHDD

Crystal Data	
Formula sum	$C_{14}\ H_{34}\ O_4\ N_4$
Formula weight	644.89
Crystal system	triclinic
Space group	$P\bar{1}$ (no. 2)
Unit cell dimensions	$a = 5.1650(5)$ Å
	$b = 12.2620(12)$ Å
	$c = 14.5610(16)$ Å
	$\alpha = 88.52(4)°$
	$\beta = 81.9(3)°$
	$\gamma = 79.27(5)°$
Cell volume	897.02(95) $Å^3$
Density	1.194 g/cm^3
Pearson code	aP112
Formula type	N2O2P7Q17
Wyckoff sequence	i56

Table A10. Fractional coordinates and isotropic displacement parameters for U/1,12-DHDD.

Atom	x	y	z	U_{iso}
C1	1.54668(16)	0.07731(7)	-0.13155(6)	0.032(1)
C2	1.95067(16)	-0.07545(6)	-0.36905(6)	0.027(1)
C3	1.92996(15)	0.76467(7)	-0.61131(6)	0.036(1)
C4	1.67167(15)	0.73955(6)	-0.56202(5)	0.030(1)
C5	1.71164(15)	0.66037(6)	-0.47795(6)	0.032(2)
C6	1.45586(15)	0.63798(7)	-0.42790(6)	0.035(2)
C7	1.48841(15)	0.56391(6)	-0.34476(6)	0.029(2)
C8	1.22943(15)	0.53960(6)	-0.29173(6)	0.035(2)
C9	1.26811(15)	0.46490(7)	-0.20676(6)	0.038(2)
C10	1.00916(17)	0.43797(7)	-0.15614(6)	0.045(2)
C11	1.05239(17)	0.36378(6)	-0.07089(6)	0.034(2)
C12	0.78940(15)	0.33728(7)	-0.01797(6)	0.029(2)
C13	0.82714(15)	0.26360(7)	0.06330(6)	0.035(2)
C21	0.56734(15)	0.23673(6)	0.11482(6)	0.033(2)
O1	1.33355(11)	0.04806(4)	-0.10482(4)	0.041(2)
O3	0.60659(11)	0.15641(4)	0.18681(3)	0.032(2)
O4	1.89577(10)	0.84322(5)	-0.68664(5)	0.045(2)
N1	1.75912(11)	0.05186(5)	-0.08370(4)	0.023(2)
N2	1.57469(13)	0.13641(5)	-0.20785(5)	0.041(2)
N3	1.92645(12)	-0.13507(5)	-0.28853(5)	0.033(2)
O2	2.17343(10)	-0.04984(4)	-0.40303(4)	0.029(1)
N4	1.73920(15)	-0.04868(6)	-0.40755(5)	0.048(2)

Table A11. Crystal data and structure refinement for PDA/1,4-DHCH.

Crystal Data	
Formula sum	$C_{12}\ H_{20}\ O_2\ N_2$
Formula weight	448.60
Crystal system	monoclinic
Space group	$P2_1/a$
Unit cell dimensions	$a = 8.5030(5)$ Å
	$b = 6.2790(4)$ Å
	$c = 11.7810(8)$ Å
	$\beta = 95.64(3)°$
Cell volume	625.95(7) $Å^3$
Density	1.190 g/cm^3
Pearson code	mP72
Formula type	NOP6Q10
Wyckoff sequence	e18

Table A12. Fractional coordinates and isotropic displacement parameters for PDA/1,4-DHCH.

Atom	x	y	z	U_{iso}
C1	0.52492(3)	0.29148(4)	0.45150(2)	0.048(1)
C2	0.53558(3)	0.49019(4)	0.38061(2)	0.043(1)
C3	0.43332(3)	0.66484(4)	0.42221(2)	0.050(1)
C4	0.04030(3)	0.30402(4)	-0.03939(2)	0.045(1)
C5	0.10840(2)	0.37067(4)	0.06560(2)	0.042(1)
C6	0.06648(3)	0.56936(4)	0.10485(2)	0.047(1)
O1	0.48499(2)	0.45350(3)	0.26364(1)	0.062(1)
N1	0.20974(2)	0.23556(3)	0.13637(2)	0.052(1)

Table A13. Crystal data and structure refinement for PDA/1,8-DHO.

Crystal Data	
Formula sum	$C_7H_{13}N_1O_1$
Formula weight	1017.49
Crystal system	monoclinic
Space group	*C*2/*c*
Unit cell dimensions	$a = 36.185(5)$ Å
	$b = 5.093(5)$ Å
	$c = 8.124(5)$ Å
	$\beta = 101.11(5)°$
Cell volume	1469.14(17) $Å^3$
Density (calculated)	1.150 g/cm^3
Pearson code	mC176
Formula type	NOP7Q13
Wyckoff sequence	f22

Table A14. Fractional coordinates and isotropic displacement parameters for PDA/1,8-DHO.

Atom	x	y	z	U_{iso}
O1	0.85748(1)	0.34671(3)	0.17864(3)	0.030(1)
N1	0.82802(1)	-0.20222(4)	0.00276(3)	0.027(1)
C2	0.95668(1)	0.22138(4)	0.40861(3)	0.028(1)
C6	0.78847(1)	-0.22123(4)	-0.00115(3)	0.021(1)
C1	0.97975(1)	-0.02673(5)	0.45815(3)	0.029(1)
C7	0.77025(1)	-0.04883(4)	0.08791(3)	0.023(1)
C3	0.91643(1)	0.16773(4)	0.31989(3)	0.027(1)
C5	0.76776(1)	-0.42394(4)	-0.08950(3)	0.024(1)
C4	0.89465(1)	0.41374(4)	0.26363(3)	0.029(1)

Table A15. Crystal data and structure refinement for PDA/1,10-DHD.

Crystal Data	
Formula sum	$C_8\ H_{15}\ N_1\ O_1$
Formula weight	282.42
Crystal system	monoclinic
Space group	$P2_1/a$
Unit cell dimensions	$a = 8.2649(6)$Å
	$b = 5.1883(3)$Å
	$c = 19.5336(13)$Å
	$\beta = 99.01(0)°$
Cell volume	827.29(10) $Å^3$
Z	2
Density	1.134 g/cm^3
RAll	0.111
Pearson code	mP25
Formula type	NOP8Q15

Table A16. Fractional coordinates and isotropic displacement parameters for PDA/1,10-DHD.

Atom	x	y	z	U_{iso}
C1	0.2794(4)	0.3939(6)	0.23360(13)	0.0426(7)
C2	0.2347(4)	0.6526(5)	0.20068(13)	0.0428(7)
C3	0.1492(4)	0.6331(6)	0.12640(13)	0.0416(7)
C4	0.1092(4)	0.8901(6)	0.09121(13)	0.0420(7)
C5	0.0227(4)	0.8711(5)	0.01711(13)	0.0410(7)
C6	0.5094(3)	-0.0176(5)	0.42923(13)	0.0349(7)
C7	0.5921(3)	0.1723(5)	0.46930(13)	0.0396(7)
C8	0.4157(3)	-0.1895(6)	0.46059(14)	0.0405(7)
N1	0.5121(3)	-0.0276(5)	0.35659(11)	0.0450(7)
O1	0.3542(3)	0.4310(4)	0.30334(9)	0.0543(7)

Table A17. Crystal data and structure refinement for PDA/1,12-DHDD.

Crystal Data	
Formula sum	$C_9H_{17}N_1O_1$
Formula weight	620.96
Crystal system	monoclinic
Space group	$P2_1/a$
Unit cell dimensions	$a = 8.085(2)$Å
	$b = 5.136(3)$Å
	$c = 22.156(9)$Å
	$\beta = 96.14(2)°$
Cell volume	914.75(17)Å^3
Density	1.127 g/cm^3
Pearson code	mP112
Formula type	NOP9Q17
Wyckoff sequence	e28

Table A18. Fractional coordinates and isotropic displacement parameters for PDA/1,12-DHDD.

Atom	x	y	z	U_{iso}
O1	0.12973(5)	0.40770(7)	0.67270(2)	0.025(1)
N1	0.46904(6)	0.54550(9)	0.62578(2)	0.021(1)
C1	0.40357(6)	0.32451(10)	0.52862(2)	0.020(1)
C6	0.32381(7)	0.55644(11)	0.83101(2)	0.025(1)
C3	0.57854(6)	0.70162(10)	0.53276(2)	0.020(1)
C5	0.24728(7)	0.60074(11)	0.76547(2)	0.026(1)
C4	0.19999(7)	0.34932(10	0.73274(2)	0.023(1)
C8	0.42900(7)	0.76895(11)	0.93186(2)	0.025(1)
C7	0.36173(7)	0.81064(11)	0.86567(2)	0.026(1)
C9	0.46573(7)	1.02052(11)	0.96687(2)	0.027(1)
C2	0.48300(6)	0.52715(10)	0.56209(2)	0.020(1)